UNIVERSITY OF SOUTHAMPTON

Femtosecond Laser Induced Forward Transfer Techniques for the Deposition of Nanoscale, Intact, and Solid-Phase Material

by

David Paul Banks

A thesis submitted in partial fulfillment for the
degree of Doctor of Philosophy

in the
Faculty of Engineering, Science, and Maths
Optoelectronics Research Centre

November 2008

Declaration of Authorship

I, David Paul Banks, declare that this thesis titled, 'Femtosecond Laser Induced Forward Transfer Techniques for the Micro-Deposition of Nanoscale, Intact, and Solid-Phase Material' and the work presented in it are my own. I confirm that:

- This work was done wholly or mainly while in candidature for a research degree at this University
- Where any part of this thesis has previously been submitted for a degree or any other qualification at this University or any other institution, this has been clearly stated
- Where I have consulted the published work of others, this is always clearly attributed
- Where I have quoted from the work of others, the source is always given. With the exception of such quotations, this thesis is entirely my own work
- I have acknowledged all main sources of help
- Where the thesis is based on work done by myself jointly with others, I have made clear exactly what was done by others and what I have contributed myself

Signed: ____

Date: ____

“An important scientific innovation rarely makes its way by gradually winning over and converting its opponents: What does happen is that the opponents gradually die out.”

Max Planck

UNIVERSITY OF SOUTHAMPTON

Abstract

Faculty of Engineering, Science, and Maths
Optoelectronics Research Centre

Doctor of Philosophy

by David Paul Banks

The subject of this thesis is the study of the Laser Induced Forward Transfer (LIFT) technique with femtosecond duration pulses. In principle, femtosecond-LIFT should offer a number of advantages over traditional nanosecond-LIFT in terms of achievable resolution and transferring intact and solid phase material.

The first important results are the deposition of 300 nm nanodroplets of Cr. These droplets represent the smallest reported LIFT-fabricated structures to date and were around 40% smaller than the previous record. The ability to deposit multiple nanodroplets to form micron-period arrays has also been studied, with the conclusion that the minimum achievable period was limited by the laser spot size.

Femtosecond-LIFT with Dynamic Release Layers (DRLs) has also been investigated. Solid phase pellets of a gadolinium gallium oxide film have been transferred using polymeric and metallic DRLs. It was found that polymeric DRLs produced better results than metallic layers in terms of reproducibility and absence of residual DRL after transfer. A specially designed triazene polymer produced the best results, but commercially available photoresist also displayed promise in this area.

A new DRL-free technique has been developed that has been seen to allow for the forward transfer of solid, contiguous segments of a Cr film without evidence of significant melting. The technique, which relies on simple beam shaping and multiple low energy pulses, has been used to transfer $\approx 10\ \mu$m structures.

A novel solid phase etching technique that uniquely allows for simultaneous deposition of the etched material, also in solid phase, has been presented. Micron deep holes and trenches have been produced in Si and silica substrates by the generation of large shocks in a thin Cr layer by absorption of femtosecond pulses. The shock initiated the propagation of cracks in the bulk substrates that ultimately lead to etching of whole sections of material.

Acknowledgements

Many thanks to Rob for his invaluable support throughout this project, both scientific and personal. Without his contributions in suggesting experiments, discussing ideas, suggesting collaborators, and thorough proof-reading, this thesis would have been much thinner, far less interesting, and not as well written. Thanks also to Christos and John for their help in the femtosecond lab, especially in the early days when I was finding my feet. Thanks to Kamal for her help with experiments and for listening as I tried to explain my experiments, thus often helping me to get things clearer in my own head. Thanks to Ioanna for her input to my early work on nanoscale structures. Thanks to Rossana, Tim, Romain, and Tom for providing samples for me to blow to bits. Thanks to Ali for allowing me to use his FFT Matlab code. Thanks to Mark and Rob for interesting discussions. Thanks to Simon and Tim for making bits of kit for me, for teaching me AutoCAD, and whose sarcasm ensured I thoroughly thought through exactly what I wanted before going to talk to them. Finally, thanks to all my friends at the ORC who kept me sane during my PhD.

Special thanks to Xu for taking care of me, particularly during the hectic final few weeks of thesis writing when I was too busy to feed myself. Thanks also to my parents for their constant, unequivocal support.

Finally, a curse on whoever kept stealing tools from my lab resulting in numerous precious hours being lost hunting for spanners, Allen keys, and screw drivers.

Contents

List of Figures

List of Tables

Abbreviations

2ω	frequency-doubled
3ω	frequency-tripled
4ω	frequency-quadrupled
AC	**A**ctive **C**arrier
AC-LIFT	**A**ctive **C**arrier-**L**aser **I**nduced **F**orward **T**ransfer
AFA-LIFT	**A**bsorbing **F**ilm **A**ssisted-**L**aser **I**nduced **F**orward **T**ransfer
AFM	**A**tomic **F**orce **M**icroscopy
BLAST	**B**allistic **L**aser **A**ssisted **S**olid **T**ransfer
CCD	**C**harge **C**oupled **D**evice
DRL	**D**ynamic **R**elease **L**ayer
DRL-LIFT	**D**ynamic **R**elease **L**ayer-**L**aser **I**nduced **F**orward **T**ransfer
DRL-fs-LIFT	**DRL-LIFT** with **fs** pulses
DW	**D**irect **W**rite
EDX	**E**nergy **D**ispersive **X**-ray Analysis
FFT	**F**ast **F**ourier **T**ransform
iFFT	**I**nverse **F**ast **F**ourier **T**ransform
fs	femtosecond
FWHM	**F**ull-**W**idth **H**alf-**M**aximum
GdGaO	**G**a**d**olinium **Ga**llium **O**xide
HA-LIFT	**H**ydrogen **A**ssisted-**L**aser **I**nduced **F**orward **T**ransfer
IR	**I**nfra-**R**ed
LIFT	**L**aser **I**nduced **F**orward **T**ransfer
LIMIT	**L**aser **I**nduced **M**olecular **I**mplantation **T**echnique
LISE	**L**aser **I**nduced **S**olid **E**tching
LITI	**L**aser **I**nduced **T**hermal **I**maging

LMI	**L**aser **M**olecular **I**mplantation
LP-LIFT	**L**ong **P**ulsed-**L**aser **I**nduced **F**orward **T**ransfer
LTHC	**L**ight **T**o **H**eat **C**onversion Layer
MAPLE	**M**atrix **A**ssisted **P**ulsed **L**aser **E**vaporation
MAPLE-DW	**M**atrix **A**ssisted **P**ulsed **L**aser **E**vaporation-**D**irect **W**rite
NA	**N**umerical **A**perture
Nd:YAG	**N**eodymium-doped **Y**ttrium **A**luminium **G**arnet
ns	nanosecond
PLD	**P**ulsed **L**aser **D**eposition
PMMA	**P**oly(**M**ethyl **M**eth**A**crylate)
ps	picosecond
SEM	**S**canning **E**lectron **M**icroscopy
SGL	**S**hock **G**eneration **L**ayer
TP	**T**riazene **P**olymer
TTM	**T**wo **T**emperature **M**odel
UV	**U**ltra-**V**iolet
WD	**W**orking **D**istance

Symbols

a	aperture diameter	m
ap	function defining aperture	
b	function defining input beam	
c_e	electron specific heat	J/m^{3}K
c_i	ion specific heat	J/kgK
d	thickness of target	m
D	thermal diffusion coefficient	
d_{air}, $d_{air}(x)$	donor-receiver separation in LIFT setup	m
d_j	thickness of layer j	m
d_{scan}	separation between successive exposures	m
E_{In}	incident electric field amplitude	
$E_{In,j}$	effective electric field amplitude incident on layer j	
$\mathbf{E}^{+}_{\mathbf{j,i}}(\mathbf{z})$	electric field propagating in positive z-direction in layer j	
$\mathbf{E}^{-}_{\mathbf{j,i}}(\mathbf{z})$	electric field propagating in negative z-direction in layer j	
	- i distinguishes multiple reflections	
$\mathbf{E}_{\mathbf{j}}(\mathbf{z})$	total electric field in layer j	
f	fringe number	
F	associated frequency scale of FFT	rads^{-1}
G	electron-phonon coupling constant	W/m^{3}K
H	transfer function	
$\mathbf{I}_{\mathbf{j}}(\mathbf{z})$	intensity in layer j	W/m^2
I_{Max}	maximum intensity	W/m^2
I_{peak}	peak intensity	W
J	fluence	J/m^2
J_{th}	threshold fluence for LIFT	J/m^2

k_j	propagation constant in layer j	m^{-1}
l_d	thermal diffusion length	m
n	refractive index	
$\mathbf{n_j}$	complex refractive index of layer j	
n_j	real part of refractive index of layer j	
N_p	number of pulses	
P_{800}	incident power at $\lambda = 800$ nm	W
P_{SC}	power in supercontinuum after AC	W
r	amplitude reflection coefficient	
$r(x)$	optical path length	m
r_{ij}	reflection coefficient from layer i to layer j	
r'_{ij}	effective reflection coefficient at Γ_{ij}	
r^*_{ij}	as r'_{ij} but looking in opposite direction $(= -r'_{ij})$	
S	Summation of multiple reflections	
S_{laser}	term governing laser heating	$\mathrm{W/m^3K^2}$
t	time	s
T_e	electron temperature	K
T_i	ion temperature	K
t_{ij}	transmission coefficient from layer i to layer j	
t'_{ij}	effective transmission coefficient at Γ_{ij}	
t_p	laser pulse FWHM duration	s
w	gaussian beam parameter	
x, y, z	spatial co-ordinates	m
X_j	Term relating $r'_{j,j+1}$ and $r'_{j-1,j}$	
Y_j	Term relating $r{*}_{j,j-1}$ and $r{*}_{j+1,j}$	
z_F	distance from best image plane	m
z_j	depth in layer j	m

α_j	absorption coefficient of layer j	
Γ_{ij}	interface between layers i and j	
δ	skin depth	m
δ_b	electron ballistic range	m
κ_e	electron thermal conductivity	W/mK

κ_i	ion thermal conductivity	W/mK
κ_j	imaginary part of refractive index of layer j	
λ	wavelength	m
λ_0	incident wavelength into AC	m
ω	angular frequency	rads^{-1}
ρ_i	ion/lattice density	$\mathrm{kg/m}^3$
τ_{ei}	electron-ion coupling time	s
τ_j	internal transmittance of layer j	

Dedicated to Tim

Chapter 1

Introduction and Synopsis

1.1 Microfabrication

The ability to deposit a wide variety of materials with micron and sub-micron resolution is desirable in many fields from microelectronics and integrated optics to the fabrication of biological molecule microarrays. The requirements of the deposition technique vary with application, but generally include some or all of: high resolution, control of deposition size and thickness, maintenance of material properties following deposition, high spatial accuracy, simplicity, low cost, and quick processing time.

Many techniques have been developed to address these challenges, each with their own advantages and disadvantages. Photolithographic methods allow the production of complicated structures from a wide range of materials with very high resolutions (10's of nm [Mappes et al., 2007; Merriam et al., 2007; Robinson et al., 1999]); but can be complex, expensive, and time-consuming multiple-step processes. Laser-induced dissociation from various chemical precursors is another method that allows high resolution [Haight et al., 2003], but the necessity to use high temperatures and a lack of suitable precursors limits the number of materials that can be deposited in this manner. For the deposition of delicate molecules, e.g. proteins, DNA, and polymeric materials, gentler methods that can be used in an ambient atmosphere are often necessary. Ink-jet printing, pin-spotting and immobilisation techniques are commonly used (see [Blawas and Reichert, 1998; Heller, 2002]), but these usually suffer from limited resolution of 10's-100's of μm. A complete discussion of microfabrication techniques with the relative merits of each would run to longer than this thesis. For good general discussions of the subject see, for example [Franssila, 2004; Madou, 2002].

One family of processes that are of great interest for microfabrication are direct-write (DW) techniques. DW methods are so-called because pattern definition and material

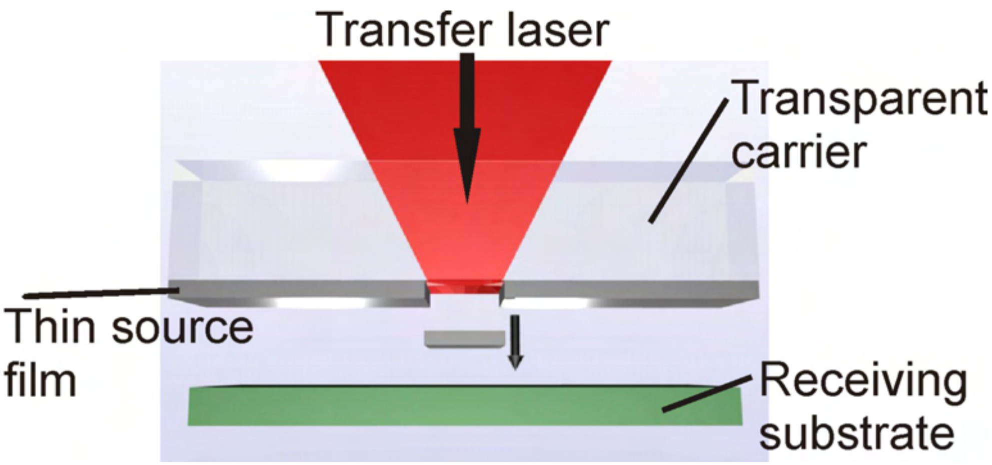

Figure 1.1: Artistic representation of laser-induced forward transfer.

patterning are performed simultaneously. Although the best achievable resolution with DW methods (≈100 nm [Haight et al., 2003]) is typically less than that with lithography, the wide range of materials that can be patterned, the inherent simplicity and quick processing times, and the ability to pattern non-planar substrates offer versatile capabilities not readily available lithographically. There are also DW techniques that offer better resolution (e.g. e-beam or ion beam machining), but these require expensive equipment and high vacuum environments.

1.2 Laser-Induced Forward Transfer

A significant majority of DW techniques are laser-based. Such techniques typically combine good resolution with simplicity and rapid processing times. An important subgroup are Laser-Induced Forward Transfer (LIFT) methods, which use a laser to transfer material on a pixel-by-pixel basis from a thin film precursor to a receiving substrate (see fig. 1.1).

LIFT was first reported by Bohandy et al. [Bohandy et al., 1986] and has since been used for the micron-scale deposition of a variety of metals, semiconductors, superconductors, dielectrics, and biomaterials (a more complete history follows in the next chapter). The extreme simplicity of the technique, which can be performed in ambient atmosphere and offers deposited feature sizes of 100's of nm - 100's of μm, relative to many other microfabrication methods led to it being intensively studied during the late 1980's and early 1990's.

LIFT was originally proposed as a quick and simple method of repairing damaged photomasks. However, the potential to micro-deposit virtually any material that could be prepared in thin film form was quickly recognised. Unfortunately, an inherent limitation of the technique is that the material to be patterned is required to act as its own propellant for transfer, which in practice limited the materials that could be transferred. Hence, a number of complementary techniques have been developed to expand the range of applications, including:

- Matrix-Assisted Pulsed Laser Evaporation-Direct Write (MAPLE-DW) [Pique et al., 1999]
- Dynamic Release Layer LIFT (DRL-LIFT) [Tolbert et al., 1993]
- Laser Induced Thermal Imaging (LITI) [Blanchet et al., 2003]
- Laser Molecular Implantation (LMI) [Fukumura et al., 1994]

More will be said about these processes in chapter 2.

Recently, the use of femtosecond duration pulses for LIFT has begun to attract attention [Banks et al., 2006, 2008a; Bera et al., 2007; Yang et al., 2006; Zergioti et al., 2005, 1998]. The advantages of using femtosecond pulses for ablation applications is well known and, as LIFT is essentially an ablation-driven transfer process, it seems reasonable to suspect that LIFT may also benefit from the use of such pulses. Indeed early femtosecond studies have already reported smaller feature sizes than in the nanosecond regime [Banks et al., 2006], transfer of intact biomaterial [Karaiskou et al., 2003; Zergioti et al., 2005], transfer in solid phase [Banks et al., 2008a], and a reduction in the spreading out of material during transfer [Papazoglou et al., 2002; Zergioti et al., 2003].

The subject of this project was the femtosecond LIFT technique. In particular, we were interested in the deposition of sub-micron structures and the transfer of material intact and in solid-phase. Nanoscale structures could have applications for example in plasmonics, whilst solid and intact transfer might allow for the deposition of complex materials displaying long-range order, such as single-crystals, single-domain, or oriented films. The LIFT of such materials has not previously been possible due to the particulate or molten nature of the transfer process.

1.3 Significant Achievements

Below is a summary of the key achievements of this project in the order they appear in this thesis.

1.3.1 Nanoscale Structures

In chapter 4 the LIFT of nanoscale structures is presented. In that chapter we present the successful and reproducible transfer of droplets ≈ 300 nm in diameter. These are the smallest structures reported by LIFT to date, with the previous best being around 0.5 μm with both nanosecond [Narazaki et al., 2008] and femtosecond [Papakonstantinou et al., 1999] duration pulses.

We also investigate the deposition of these nanodroplets in micron period arrays. The periodicity of such arrays is vital for plasmonic applications. We find that the nearest spacing of such deposits is, perhaps not unsurprisingly, limited to around half the laser spot size (i.e. when successive transfer pulses begin to overlap).

Elements of the work in chapter 4 have been published as [Banks et al., 2006].

1.3.2 Intact Transfer and Transparent Films

In chapters 5 and 6, the DRL-LIFT process using femtosecond pulses is studied for the first time. Using a specially designed triazene polymer [Nagel et al., 2007], transfer of solid and intact discs of a gadolinium gallium oxide film is achieved. Despite the fact that neither the polymer nor the oxide film absorbed the laser linearly, the high intensity femtosecond pulses allowed for nonlinear absorption and transfer of very clean and undamaged segments of the oxide films. The transfer experiments are presented in chapter 5 and selected results have been published as [Banks et al., 2008b].

We also identified a problem in the LIFT of transparent films. It was realised that back reflection from the various film-air-substrate interfaces, especially a relatively reflective material such as Si which is often deposited onto, would lead to the formation of a standing wave pattern in the film or films. Such a pattern could result in locally high intensities that could damage the transferred material. A theoretical model of standing wave formation in a LIFT setup is developed in chapter 6. The results of the model are compared with the oxide film depositions and a clear influence of the standing wave on the resultant depositions is observed in the amount of damage sustained during transfer. This is the first time the role of standing waves in LIFT has been considered.

1.3.3 Solid Phase Transfer

In chapter 7, initial results of a new forward transfer technique developed as part of this project are presented. The technique has been named Ballistic Laser-Assisted Solid Transfer (BLAST) and involves the use of multiple, low energy pulses to gently transfer material without significant melting or fragmentation. BLAST represents a new method of achieving forward transfer of intact and solid phase material; something that was previously only achievable with DRL-LIFT. Such a process has potential applications in forward transfer of complex materials that must remain as a single, solid phase, contiguous piece to retain their properties. Selected elements of this work have been published as [Banks et al., 2008a].

1.3.4 Solid Phase Etching

In work closely related to BLAST, chapter 8 presents results of another new technique developed during the project. So-called Laser-Induced Solid Etching (LISE) is unique in that it allows for the etching of material from bulk substrates in a single, solid-phase piece that can be deposited onto another nearby substrate. Thus, LISE is unique as a simultaneous solid phase etching and deposition process. Potential applications including the DW fabrication of strip loaded waveguides [Grivas et al., 2004] have been identified and will be pursued shortly.

1.4 Thesis Structure

The first two chapters cover important background. In chapter 2 a review of laser-induced forward transfer techniques is presented. The chapter covers conventional LIFT, MAPLE-DW, DRL-LIFT, LITI, LMI, and some other, less commonly applied techniques, and summarises the relative merits of each. Chapter 3 begins with a discussion on the interaction of femtosecond pulses with matter before the envisaged benefits of using femtosecond duration pulses for LIFT are considered.

The experimental results obtained during this project are presented in the remaining chapters. Chapter 4 covers the results of experiments to deposit the smallest possible nanodroplets, and microarrays. Descriptions of the femtosecond laser system, beam delivery apparatus, and LIFT experimental setup are included here too.

Chapter 5 is the first of two chapters dedicated to femtosecond DRL-LIFT. In this chapter, the transfer of discs of a gadolinium gallium oxide film is presented and a qualitative model of the transfer process is described. In chapter 6 a semi-quantitative model of the standing wave patterns present during LIFT or DRL-LIFT of transparent films is developed. Detrimental effects arising from the standing waves are predicted due to local high intensities. The model is compared to results from the previous chapter to explain experimental observations of damage to the transferred oxide material.

Chapter 7 describes various attempts to achieve solid phase forward transfer using femtosecond pulses without requiring a DRL. These include basic femtosecond LIFT, BLAST, and beam shaping results. The relative merits of a number of techniques are discussed in terms of their ability to produce solid phase transfer of single, contiguous pieces of the thin film.

Initial results of the LISE technique are presented in chapter 8. The quality of etched and deposited structures in silica and Si targets as functions of various experimental parameters is investigated and a qualitative model for the etching process is described.

Finally, chapter 9 concludes the thesis and discusses potential future work to follow on from the results presented here.

Bibliography

Banks, D., Grivas, C., Mills, J., Zergioti, I., and Eason, R. (2006). Nanodroplets deposited in microarrays by femtosecond ti:sapphire laser induced forward transfer. *Appl. Phys. Lett.*, 89:193107.

Banks, D., Grivas, C., Zergioti, I., and Eason, R. (2008a). Ballistic laser-assisted solid transfer (blast) from a thin film precursor. *Opt. Express*, 16:3249–3254.

Banks, D., Kaur, K., Gazia, R., Fardel, R., Nagel, M., Lippert, T., and Eason, R. (2008b). Triazene photopolymer dynamic release layer-assisted femtosecond laser-induced forward transfer with an active carrier substrate. *Europhys. Lett.*, 83:38003.

Bera, S., Sabbah, A., Yarbrough, J., Allen, C., Winters, B., Durfee, C., and Squier, J. (2007). Optimization study of the femtosecond laser-induced forward-transfer process with thin aluminium films. *Appl. Opt.*, 46(21):4650–4659.

Blanchet, G., Loo, Y.-L., Rogers, J., Gao, F., and Fincher, C. (2003). Large area, high resolution, dry printing of conducting polymers for organic electronics. *Appl. Phys. Lett.*, 82(3):463–465.

Blawas, A. and Reichert, W. (1998). Protein patterning. *Biomaterials*, 19:595–609.

Bohandy, J., Kim, B., and Adrian, F. (1986). Metal deposition from a supported metal film using an excimer laser. *J. Appl. Phys.*, 60(1):1538–1539.

Franssila, S. (2004). *Introduction to Microfabrication.* Wiley, Hoboken, NJ, USA.

Fukumura, H., Kohji, Y., Nagasawa, K., and Masuhara, H. (1994). Laser implantation of pyrene molecules into poly(methyl methacrylate) films. *J. Am. Chem. Soc.*, 116:10304–10305.

Grivas, C., May-Smith, T., Shepherd, D., Eason, R., Pollnau, M., and Jelinek, M. (2004). Broadband single-transverse-mode fluorescence sources based on ribs fabricated in pulsed laser deposited ti:sapphire waveguides. *Appl. Phys. A*, 79:1195–1198.

Haight, R., Longo, P., and Wagner, A. (2003). Metal deposition with femtosecond light pulses at atmospheric pressure. *J. Vac. Sci. Technol. A*, 21(3):649–652.

Heller, M. (2002). Dna microarray technology: Devices, systems, and applications. *Annu. Rev. Biomed. Eng.*, 4:129–153.

Karaiskou, A., Zergioti, I., Fotakis, C., Kapsetaki, M., and Kafetzopoulos, D. (2003). Microfabrication of biomaterials by the sub-ps laser-induced forward transfer process. *Appl. Surf. Sci.*, 208-209:245–249.

Madou, M. (2002). *Fundamentals of microfabrication: the science of miniaturization.* CRC Press, Boca Raton, FL, USA.

Mappes, T., Achenbach, S., and Mohr, J. (2007). X-ray lithography for devices with high aspect ratio polymer submicron structures. *Microelectron. Eng.*, 84:12351239.

Merriam, A., Bethune, D., Hoffnagle, J., Hinsberg, W., Jefferson, C., Jacob, J., and Litvin, T. (2007). A solid-state 193-nm laser with high spatial coherence for sub-40-nm interferometric immersion lithography. *Proc. SPIE*, 6520:65202Z.

Nagel, M., Hany, R., Lippert, T., Molberg, M., Nuesch, F., and Rentsch, D. (2007). Aryltriazene photopolymers for uv-laser applications: Improved synthesis and photodecomposition study. *Macromol. Chem. Phys.*, 208:277–286.

Narazaki, A., Sato, T., Kurosaki, R., Kawaguchi, Y., and Niino, H. (2008). Nano- and microdot array formation of fesi$_2$ by nanosecond excimer laser-induced forward transfer. *Appl. Phys. Exp.*, 1:057001.

Papakonstantinou, P., Vainos, N., and Fotakis, C. (1999). Microfabrication by uv femtosecond laser ablation of pt, cr and indium oxide thin films. *Appl. Surf. Sci.*, 151:159–170.

Papazoglou, D., Karaiskou, A., Zergioti, I., and Fotakis, C. (2002). Shadowgraphic imaging of the sub-ps laser-induced forward transfer process. *Appl. Phys. Lett.*, 81(9):1594–1596.

Pique, A., Chrisey, D., Auyeung, R., Fitz-Gerald, J., Wu, H., McGill, R., Lakeou, S., Wu, P., Nguyen, V., and Duignan, M. (1999). A novel laser transfer process for direct writing of electronic and sensor materials. *Appl. Phys. A [Suppl.]*, 69:S279–S284.

Robinson, A., Palmer, R., Tada, T., Kanayama, T., amd J.A. Preece, M. A., and Harris, K. (1999). 10 nm scale electron beam lithography using a triphenylene derivative as a negative/positive tone resist. *J. Phys. D: Appl. Phys.*, 32(16):L75–L78.

Tolbert, W., Lee, I., Doxtader, M., Ellis, E., and Dlott, D. (1993). High-speed color imaging by laser ablation transfer with a dynamic release layer: fundamental mechanisms. *J. Imag. Sci. Tech.*, 37(4):411–421.

Yang, L., Wang, C., Ni, X., Wang, Z., Jia, W., and Chai, L. (2006). Microdroplet deposition of copper film by femtosecond laser-induced forward transfer. *Appl. Phys. Letts*, 89:161110.

Zergioti, I., Karaiskou, A., Papazoglou, D., Fotakis, C., Kapsetaki, M., and Kafetzopoulos, D. (2005). Femtosecond laser microprinting of biomaterials. *Appl. Phys. Lett.*, 86:163902.

Zergioti, I., Mailis, S., Vainos, N., Papakonstantinou, P., Kalpouzos, C., Grigoropoulos, C., and Fotakis, C. (1998). Microdeposition of metal and oxide structures using ultrashort laser pulses. *Appl. Phys. A*, 66:579–582.

Zergioti, I., Papazoglou, D., Karaiskou, A., Fotakis, C., Gamaly, E., and Rode, A. (2003). A comparative schlieren imaging study between ns and sub-ps laser forward transfer of cr. *Appl. Surf. Sci.*, 208-209:177–180.

Chapter 2

The History of Laser Forward Transfer Techniques

This thesis is concerned primarily with the LIFT process using femtosecond pulses (fs-LIFT) and its potential for the direct-writing of nanoscale features of a variety of materials, and for achieving solid phase and intact material transfer. This chapter provides an overview of the LIFT process and some related techniques that have evolved from LIFT to meet new processing requirements. Section 2.1 describes the basic LIFT technique before section 2.2 then introduces other forward transfer methods closely related to LIFT. Finally, section 2.3 reviews forward transfer results reported to date in terms of feature size, materials patterned, and devices produced.

2.1 Laser-Induced Forward Transfer: An Introduction

The LIFT technique [Bohandy et al., 1986; Kyrkis et al., 2006], shown schematically in fig. 2.1, involves the pixelated transfer of material from a thin film precursor (the *donor*). The donor is coated onto one face of a transparent *carrier* and is placed in close contact with a *receiver* substrate. Material transfer from the donor to the receiver occurs when a laser pulse of sufficient intensity is focused or demagnified through the carrier onto the carrier-donor interface. Absorption of the laser energy heats the donor material and forward transfer typically occurs when either the donor melts through and droplets form on the free-surface [Willis and Grosu, 2005], or ablation at the carrier-donor interface provides an explosive thrust [Adrian et al., 1987]. The technique allows for 2D and 3D DW of a wide range of materials on scales from sub-micron [Banks et al., 2006; Narazaki et al., 2008; Papakonstantinou et al., 1999; Zergioti et al., 1998] to 0.5 mm [Fardel et al.,

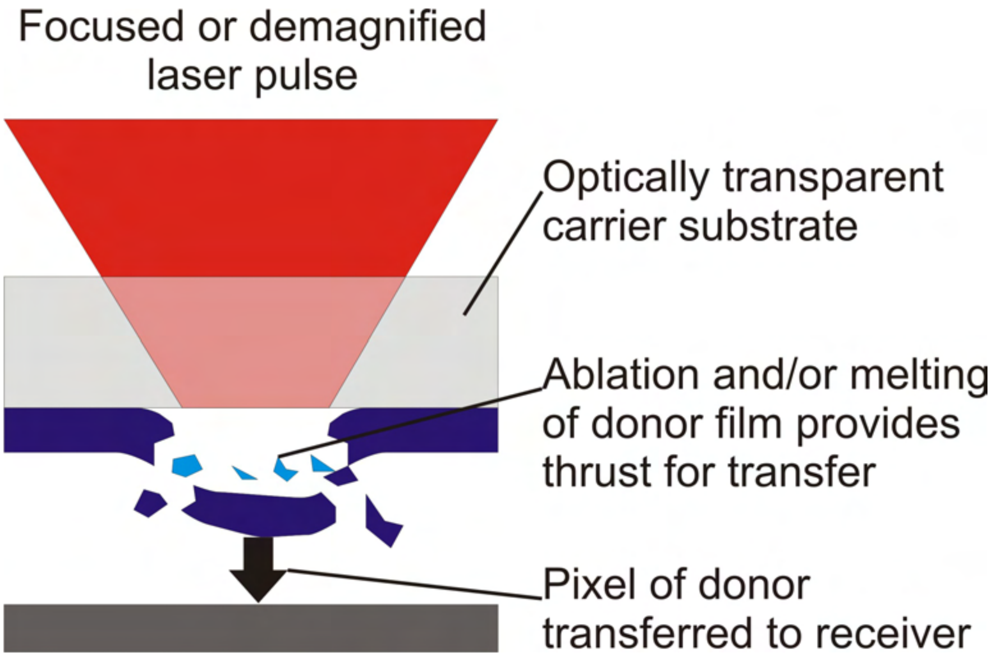

FIGURE 2.1: Illustration of the Laser-Induced Forward Transfer technique.

2007b], is easily integrated with micromachining methods [Pique et al., 1999], and can be performed in an ambient atmosphere [Banks et al., 2006].

LIFT was first proposed by Bohandy et al. [Bohandy et al., 1986] as a method for repairing damaged photomasks. To demonstrate the technique, they deposited lines of Cu 40-60 μm wide onto Si using an ArF laser (193 nm, 15 ns). It was observed that there was a threshold laser fluence for forward transfer. The optimum laser fluence, at which the material deposition was relatively uniform across the irradiated region, was found to be slightly above the transfer threshold. The threshold and optimum fluences were found to increase with donor film thickness, with better quality deposits obtained using thinner films and lower laser powers.

In Bohandy's initial report, it was hypothesised that material removal from the carrier occurred when the donor film reached the boiling temperature with explosive ablation driving forward transfer. This was subsequently supported by a finite difference model developed by Adrian and coworkers [Adrian et al., 1987] and a finite element model by Baseman et al [Baseman and Froberg, 1990]. More recent works on LIFT initiated by tightly focused laser pulses have demonstrated that it is also possible to get forward transfer of micro- and nano-droplets by careful control of melting of the donor film [Willis and Grosu, 2005].

What both these regimes have in common is that direct and significant heating of the donor material is necessary to achieve transfer. Whilst this does not represent a problem for the microdeposition of metals and other 'strong' materials not easily damaged by heating, for delicate materials, LIFT is not a viable option. Absorption of the laser energy in such materials may induce photo-chemical or photo-thermal reactions. Also, long-range order of the donor can easily be lost by melting or fracturing of the material during transfer. To combat these challenges, a number of related techniques have been developed and studied. The techniques are described in the next section and key results are presented in section 2.3.

2.2 Other Laser Forward Transfer Techniques: Complementing LIFT

2.2.1 Matrix-Assisted Pulsed Laser Evaporation-Direct Write

The Matrix-Assisted Pulsed Laser Evaporation-Direct Write (MAPLE-DW) technique [Pique et al., 1999] is a hybrid of Matrix-Assisted Pulsed Laser Evaporation (MAPLE) (fig. 2.2(a) and [Pique et al., 2008]) and LIFT. MAPLE is a variant of the Pulsed Laser Deposition (PLD) technique [Eason, 2007] for the deposition of thin films of complex (usually organic) molecules that cannot be processed via conventional PLD. In MAPLE, the material to be deposited is dissolved or mixed in particulate form into a solvent matrix material. The solution is coated onto a support substrate or frozen (depending on the volatility of the solvent) to form a target. A pulsed laser is then used to induce rapid evaporation of the matrix and release the donor material. Kinetic energy imparted to the donor material by the evaporating matrix is sufficient to transfer material to a receiver substrate placed nearby on which a thin film is grown.

MAPLE-DW, shown in fig. 2.2(b), combines MAPLE with the direct-write capabilities of LIFT for the microdeposition of a variety of materials. The solution containing the donor material is coated as a thin film onto a carrier substrate to form the donor in a geometry analogous to conventional LIFT; the film is not usually frozen as the carrier provides the necessary support. A pulsed laser is focused through the carrier (as in LIFT) and evaporates the matrix (as in MAPLE) imparting sufficient thrust to the donor material to propel small amounts to a receiver substrate.

MAPLE-DW is distinguished from other forward transfer techniques in that it is a pyrolytic method for the matrix material only. The matrix material is normally volatile so only a small amount of heating is required for evaporation and significant heating of the donor material can be avoided. Using MAPLE-DW, various metals [Modi et al., 2001], organics [Pique et al., 1999], and biomaterials [Ringeisen et al., 2002] have been forward-transferred.

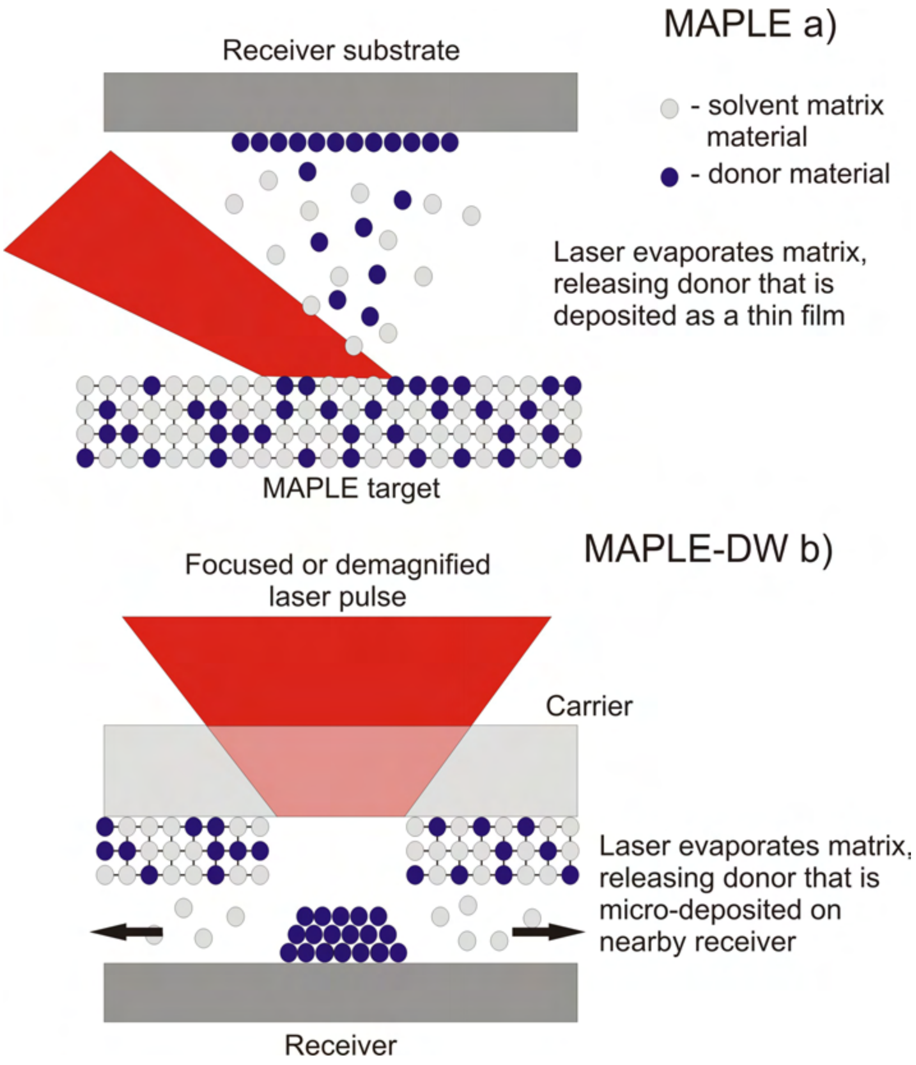

FIGURE 2.2: Illustrations of the MAPLE (a) and MAPLE-DW (b) techniques.

2.2.2 Dynamic Release Layer-LIFT

An alternative approach for protecting the donor material during LIFT is to insert a sacrificial propulsive layer between the carrier and the donor. It is then this layer that is exposed to the laser and ablated to provide the driving force for LIFT (see fig. 2.3). LIFT with a sacrificial layer was referred to as LIFT with a Dynamic Release Layer (DRL-LIFT) [Tolbert et al., 1993] originally, but is also known as Absorbing Film Assisted LIFT (AFA-LIFT) [Hopp et al., 2004]. In this thesis we will use the more widely accepted name: DRL-LIFT.

DRL-LIFT is a very versatile variant on LIFT allowing for the forward transfer of a donor film without having to expose the donor material to the laser directly. In this way 'hard', e.g. metals and ceramics, and 'soft', e.g. polymers and liquids, materials can be transferred without damage and do not need to be combined with a sacrificial

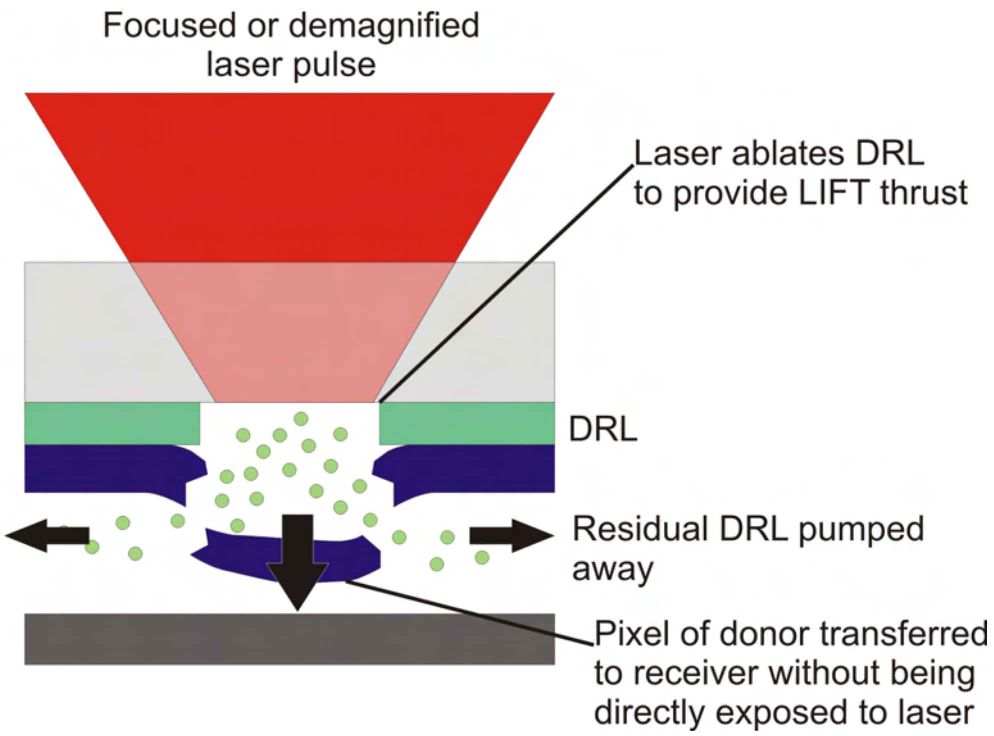

FIGURE 2.3: Illustration of the DRL-LIFT technique.

matrix. However, it is important to remember that DRL and donor material must be compatible, i.e. it must be possible to grow the desired donor onto the chosen DRL. Plus there is always the possibility of residual DRL contamination of the deposited material if the DRL is not completely evaporated in the process.

Most commonly, thin metal films have been used for DRL applications. Such films don't place many limitations on the possible donor materials that can be used, but there is the potential contamination of the transferred material with residual DRL that is not evaporated by the laser. Smausz et al have observed nanoparticles of metallic DRL that are transferred to the receiver during DRL-LIFT with a water donor film [Smausz et al., 2006]. To combat the residual DRL issue, many recent works have used a specially designed triazene polymer (TP) as the DRL material that dissociates upon UV irradiation into gaseous fragments. The TP appears to leave little or no residue following DRL-LIFT (see e.g. [Banks et al., 2008b; Fardel et al., 2007a]), however because it decomposes at a relatively low temperature (≈250 ^{o}C [Nagel et al., 2007]) some limitations are placed on what materials can be grown on the TP as donors. Whilst metallic DRLs have routinely been used for the deposition of biomaterials (see e.g. [Hopp et al., 2004; Serra et al., 2004a]), TP-DRLs have also shown promise in this area (see e.g. [Doraiswamy et al., 2006]). In chapter 5, TP-DRL-LIFT is performed with femtosecond duration pulses for the first time.

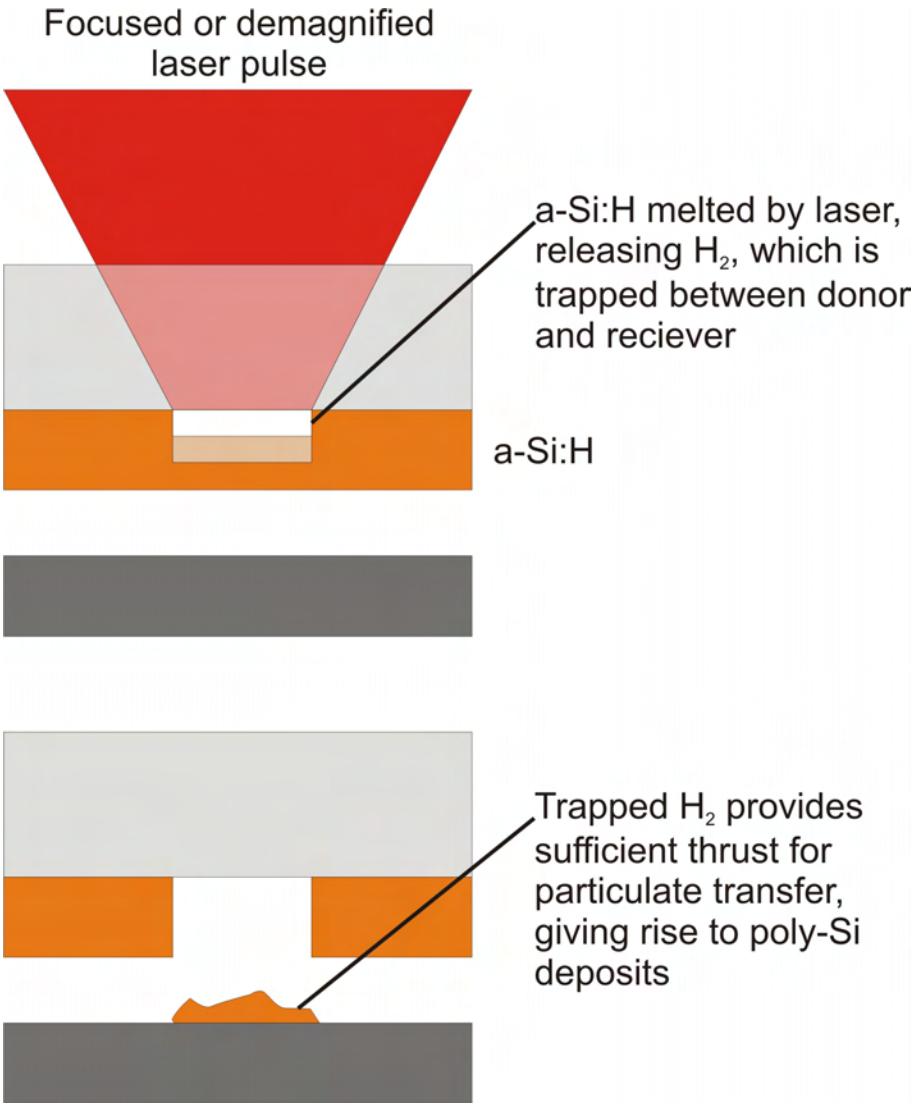

FIGURE 2.4: Illustration of laser transfer by explosive hydrogen release.

2.2.3 Hydrogen Assisted LIFT

An alternative method of achieving LIFT without direct ablation was proposed by Toet and coworkers [Toet et al., 1999]. In this technique the donor film is hydrogenated amorphous silicon (*a-Si:H*). The thrust for forward transfer comes from the explosive release of hydrogen when the a-Si:H film is melted at the carrier-donor interface. The Si is then transferred in a mixture of molten droplets and particles, and is deposited as a poly-Si pixel. This technique is sometimes known as Hydrogen-Assisted Laser-Induced Forward Transfer (HA-LIFT) and is shown in fig. 2.4.

The a-Si:H films can also be used as DRLs for the deposition of other donor materials, e.g. metals [Toet et al., 2000b]. However, as the HA-LIFT process normally only releases the hydrogen from the a-Si:H film and transfers the Si, contamination of the deposited

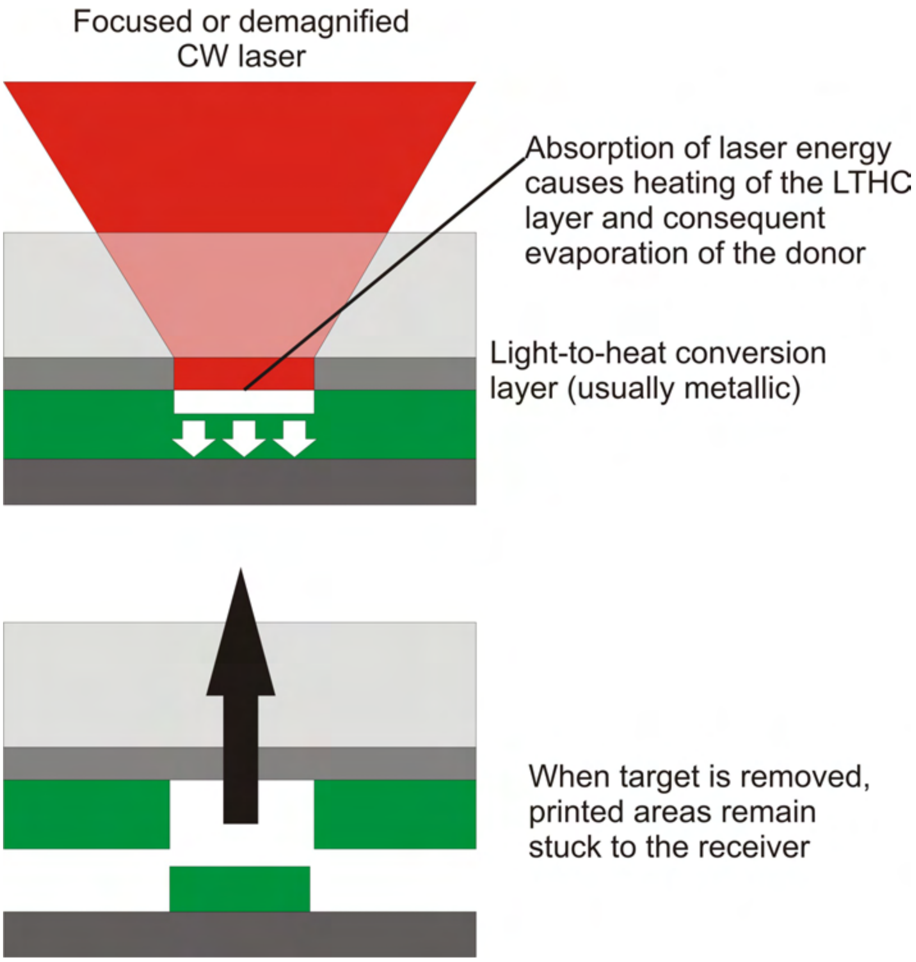

FIGURE 2.5: Illustration of the Laser-Induced Thermal Imaging technique.

donor with poly-Si is a potential issue, one that has not yet been addressed in the literature.

2.2.4 Laser Induced Thermal Imaging

The Laser-Induced Thermal Imaging (LITI) technique, shown in fig. 2.5, is a forward transfer method designed exclusively for the printing of conducting polymers [Blanchet et al., 2003]. As with DRL-LIFT, an extra film, not intended for transfer is included between the carrier and donor layers to protect the donor. However, in the case of LITI, this extra layer is not ablated but instead is designed to absorb the incident laser and heat up sufficiently to decompose surrounding organics into gaseous fragments to provide the LIFT thrust. The layer (typically metallic) is known as a Light-to-Heat Conversion (LTHC) layer in LITI literature.

By not requiring ablation of the LTHC, the issue of contamination of the deposited material by residual LTHC is eliminated. However, to further protect the donor material, a second polymer layer is sometimes included between the LTHC layer and the donor; this layer is then akin to a DRL [Blanchet et al., 2003]. The technique typically uses a continuous wave laser that is either split into individually addressable spots for pixelated transfer or rastered across the target for the transfer of continuous lines and films.

2.2.5 Long-Pulsed LIFT

Long-pulsed LIFT (LP-LIFT) is a name coined here for LIFT with laser pulses on the order of μs or longer. This process displays quite different behaviour from conventional LIFT with nanosecond pulses. The technique was studied by Kantor and co-workers who used an IR laser ($\lambda = 1.064\ \mu$m) to transfer segments of tungsten approximately 5 μm in diameter in solid phase [Kantor and Szorenyi, 1995; Kantor et al., 1994a,b]. The deposits displayed little evidence of melting and adhered well to the receiver substrate, but it was found that there was a distinct pulse duration threshold for transfer of around 500 μs (as well as the usual LIFT fluence threshold). Shorter duration pulses didn't produce transfer; to understand why, it is necessary to consider the suspected transfer process in this pulse duration regime.

Despite the similarities, the transfer dynamics of LP-LIFT are very different from conventional nanosecond LIFT, as shown in fig. 2.6. In LP-LIFT, the donor and receiver are in contact (or at least the separation is on the order of the amount of thermal expansion experienced by the donor). The high temperature in the donor causes a small amount of thermal expansion, bringing the hot donor material into tight contact with the receiver (fig. 2.6(a)). The donor is held at high temperature by the laser for a relatively long period of time, allowing the donor in the irradiated region to anneal to the receiver. When donor and receiver are separated, the annealed regions stay bonded to the receiver, whilst the rest of the rest of the donor film remains on the carrier (fig. 2.6(b)). The pulse duration threshold is believed to exist as the donor must be kept hot long enough to anneal well to the receiver. Hence, LP-LIFT is a thermal process, relying on annealing to achieve solid phase forward transfer. This fact makes it a potentially attractive technique, but only for certain applications, i.e. when donor and receiver are both able to withstand significant heating.

2.2.6 Laser Molecular Implantation

The final forward transfer technique covered in this review differs from the others in that no donor film transfer occurs. Instead, dopant molecules supported in a polymer film (the *source* film) are transferred and implanted into another, undoped polymer film placed in close contact (the *target* film); no transfer of polymer film occurs. This

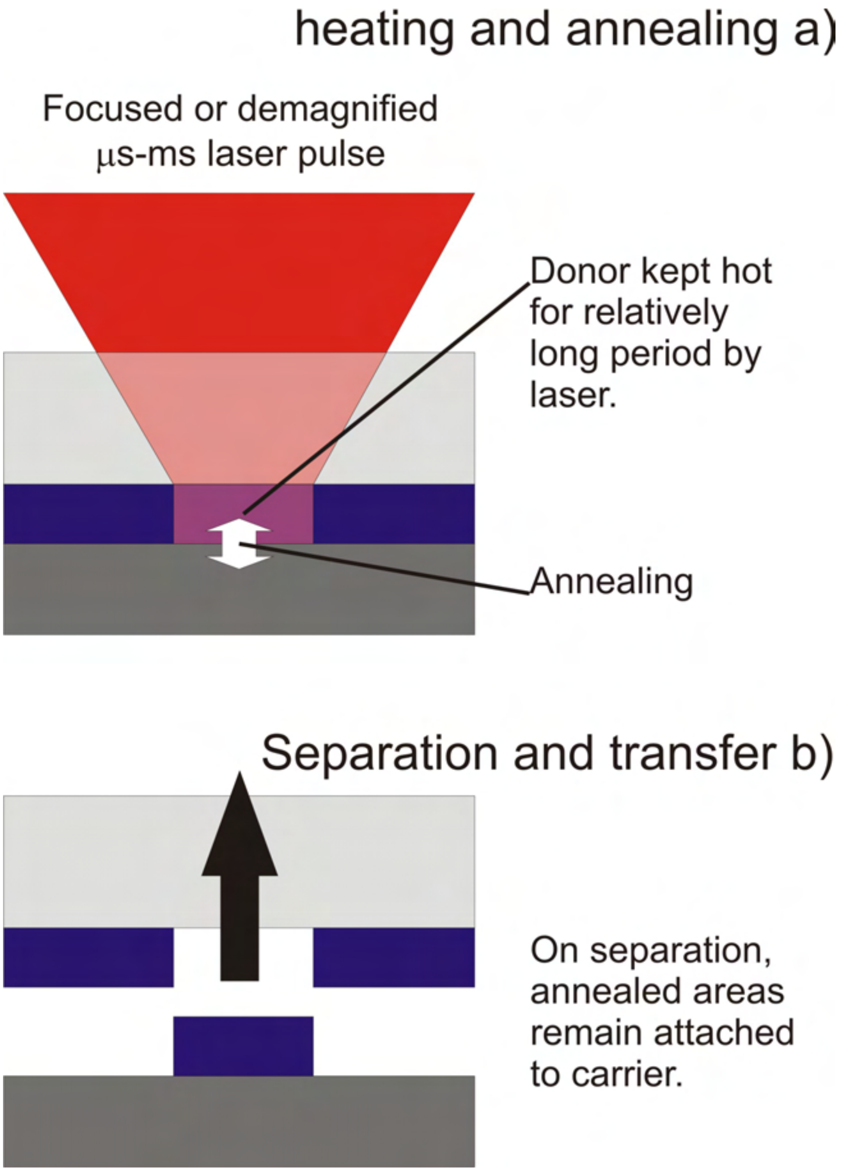

FIGURE 2.6: Illustration of LP-LIFT. Donor material is annealed to the receiver by the laser (a) and remains on the receiver after separation (b).

technique has been developed by Fukumura and coworkers [Fukumura et al., 1996; Goto et al., 2000; Okada et al., 2001] and is known as Laser Molecular Implantation (LMI) or Laser-Induced Molecular Implantation Technique (LIMIT). The technique is illustrated in fig. 2.7.

The transfer mechanism (fig. 2.7) has been proposed to be the absorption of multiple photons by one dopant molecule in the doped polymer matrix, which heats up the surrounding polymer network. The dopant molecule can then be ejected with a high kinetic energy from the expanded polymer into the undoped polymer nearby. The temperatures reached are not sufficient to decompose the dopant or supporting polymer molecules so

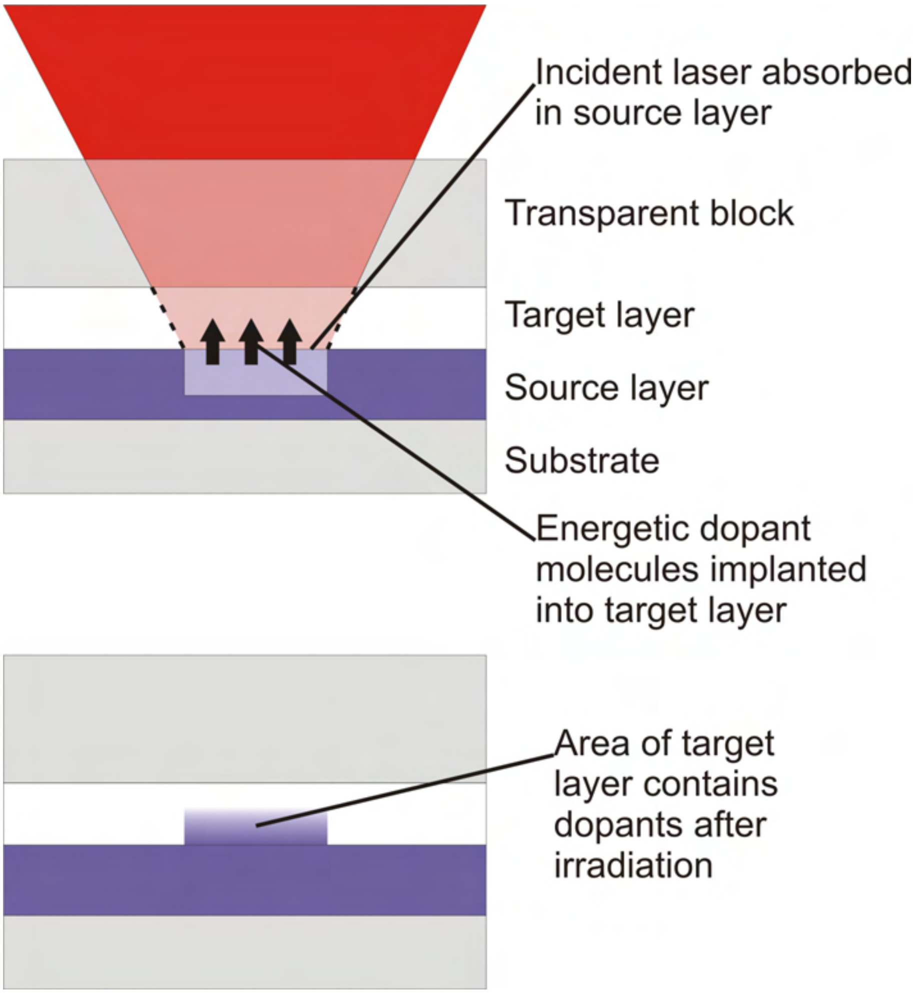

Figure 2.7: Illustration of Laser Molecular Implantation.

there is no explosive expansion-driven transfer. The technique works in forward- [Fukumura et al., 1996] and backward-transfer [Fukumura et al., 1994] geometries, i.e. donor and receiver polymer films are interchangeable.

For high resolution LMI, interferometry, tight focusing, and fibre lasers inside micropipettes have been applied, achieving feature sizes of ≈10 μm [Fukumura et al., 1998], ≈30 μm [Okada et al., 2001], and sub-μm [Goto et al., 2000], respectively. The typical application for LMI has been the spatially-selective implantation of fluorescent molecules into polymer films.

2.3 Significant LIFT achievements

2.3.1 Early Works

Since the first demonstration of LIFT in 1986 by Bohandy et al. [Bohandy et al., 1986], there have been numerous studies of the technique reported in the literature. Alongside fundamental investigations of the processes underlying the technique, significant successes have been achieved in the direct writing of biosensor and organic polymer-based optoelectronic devices. Table 2.1 (at the end of this chapter on page 30) presents a chronological list of laser forward transfer reports in the literature. The list is not exhaustive but covers the most important works. A good review of work up to 2004 is also available in the chapter by Kyrkis et al. (chapter 7) in [Kyrkis et al., 2006].

LIFT was originally developed for the micro-deposition of metals with specific applications in the repair of damaged photomasks [Bohandy et al., 1986, 1988]. Bohandy et al. used an ArF laser (193 nm) to write spots and lines of Cu from a 400 nm donor film onto a Si receiver. They observed significant dependence of the deposited material on the laser fluence. A well-defined transfer threshold fluence was identified, below which no Cu was transferred. For fluence slightly above the threshold, material transfer was relatively uniform across the irradiated region, with the size of deposited features (≈ 30 μm) corresponding well to the patterning laser spot size. Increasing the fluence further resulted in larger deposits that were rougher and surrounded by splattered material extending well beyond the irradiated region.

It was hypothesised that material transfer was the result of explosive ablation at the carrier-donor interface. A numerical model developed by Adrian et al. [Adrian et al., 1987] found that the transfer threshold fluence appeared to approximately correspond with the donor reaching the boiling temperature at the interface, supporting this hypothesis. Similar results were obtained by Baseman et al. using a finite element method [Baseman and Froberg, 1990]. Subsequently, a model developed by Willis and Grosu [Willis and Grosu, 2004] also supported the ablation-driven transfer hypothesis.

2.3.2 Investigations of LIFT

Following the early demonstrations described above, a wide variety of metals [Bahnisch et al., 2000; Banks et al., 2006; Bera et al., 2007; Chakraborty et al., 2007; Claeyssens et al., 2007; Esrom et al., 1995; Germain et al., 2007; Kantor et al., 1994b; Komorita et al., 2003; Koundourakis et al., 2001; Landstrom et al., 2004; Mailis et al., 1999; Mogyorosi et al., 1989; Nakata and Okada, 1999; Papakonstantinou et al., 1999; Sano et al., 2002; Tan et al., 2003; Toth et al., 1990; Willis and Grosu, 2004, 2005; Yang et al., 2006; Zergioti et al., 1998, 2003] amongst others, polymers [Lee et al., 1992], oxides [Chakraborty et al., 2007; Mailis et al., 1999; Papakonstantinou et al., 1999; Papazoglou et al., 2002; Sakata et al., 2005; Zergioti et al., 1998], semiconductors [Mogyorosi et al., 1989], superconductors [Fogarassy et al., 1989], diamond [Pimenov et al., 1995], carbon nanotube field emission cathodes [Chang-Jian et al., 2006], conducting polymers [Thomas et al., 2007], and an adenosine triphosphate sensor fabricated from luciferase [Tsuboi et al., 2007] have now been successfully deposited using LIFT. Many of these studies have observed the same, strict dependence on fluence of the process in the early reports (see e.g. [Banks et al., 2006; Bera et al., 2007; Papakonstantinou et al., 1999; Sano et al., 2002; Willis and Grosu, 2005; Yang et al., 2006]).

Sano et al. [Sano et al., 2002] and Yamada et al. [Yamada et al., 2002] have optimised the process in terms of the donor-receiver separation, observing that tight contact between the donor and receiver reduced the amount of particulate material transferred around the main deposit. Nakata and Okada [Nakata and Okada, 1999] have studied the behaviour of ablated atoms and emissive particles under typical LIFT conditions in terms of laser fluence and atmospheric conditions. Atomic velocities of up to 2 km/s were measured, whilst the emissive particles were much slower, traveling at around 100 m/s. The motion of both species over 100's of μm was observed to be much hampered in air compared to vacuum. The interaction with the transferred material with the receiver was also investigated, with high energy particles observed reflecting off the substrate.

Kantor et al. investigated the process with long laser pulses (100 μs - 1 ms) and compared the results to conventional nanosecond LIFT (recall, this was the process referred to as LP-LIFT earlier). They found that adherence of the transferred material to the receiver was much improved in the longer pulsed regime. The material was transferred in solid phase, and there was a lack of surrounding particulate material but, for reasons described above, it is believed that the process is only applicable to the LIFTing of high-melt temperature films.

In 2005, Willis and Grosu [Willis and Grosu, 2005] identified another transfer mechanism not driven by ablation. They found that, by careful control of the laser fluence such that thin Al and Ni donors were just melted through, it was possible to transfer single, micron-sized droplets. These droplets were around 3 μm in diameter; an order of magnitude less than the spot size. Similar (and smaller, ≈ 0.5 μm) droplets had already been reported by Zergioti et al. [Zergioti et al., 1998] and Papakonstantinou et al. [Papakonstantinou et al., 1999], but Willis and Grosu were the first to identify the droplet transfer as a different process from the conventional ablation driven method. It was hypothesised that the small size of the droplets was the result of melt-though of the donor only occurring in the centre due to the Gaussian intensity distribution of the laser. However, recently we reported similar droplets of 300 nm diameter, again an order of magnitude smaller than the laser spot, using a top-hat intensity distribution [Banks et al., 2006]. Hence, it is now believed that droplet formation is the result of hydrodynamic flow when the irradiated area is fully melted through [Willis and Grosu, 2007], in a process akin to that reported by Seifert et al. for free surface ablation with low energy pulses [Seifert and Betz, 1998; Seifert et al., 1996]. A number of authors have now reported droplet transfer in both nanosecond [Narazaki et al., 2008] and femtosecond [Banks et al., 2006; Bera et al., 2007; Papakonstantinou et al., 1999; Yang et al., 2006; Zergioti et al., 1998] LIFT experiments; the smallest features are around 500 nm (nanosecond [Narazaki et al., 2008]) and 300 nm (femtosecond [Banks et al., 2006]). An interesting recent report by Narazaki et al. [Narazaki et al., 2008] identified the formation of crystalline $FeSi_2$ in the droplets during transfer.

A recent report by Stoian et al. [Stoian et al., 2005] identified benefits in terms of the quality of ablated features produced using multiple femtosecond pulses separated by a few picoseconds over the process with single pulses. An investigation of using similarly separated pulses for femtosecond LIFT by Klini et al. did not demonstrate any obvious benefits over the conventional, single pulsed process [Klini et al., 2008].

2.3.3 Forward Transfer with Release Layers

In 1993, Tolbert et al. [Tolbert et al., 1993] proposed a variation of the LIFT technique in which a sacrificial material was inserted between the carrier and the donor to protect the delicate donor during transfer. An Al layer, which was termed a Dynamic Release Layer (DRL), was used to absorb Nd:YAG (1064 nm) laser pulses. Ablation of the DRL was used to provide the propellant for the forward transfer of PMMA doped with coloured dyes. The authors coined the term DRL-LIFT for their technique. Hopp et al. would later refer to the technique also as Absorbing Film Assisted LIFT (AFA-LIFT) [Hopp et al., 2004; Smausz et al., 2006].

One area where DRL-LIFT has had particular success has been in the deposition of biomaterials. The micron scale deposition of biomaterials is desirable for the development of micro-assays which would have medical diagnostic applications [Blawas and Reichert, 1998; Heller, 2002]. This goal has been pursued extensively by the group of Serra et al. who have produced a number of works dedicated to the preparation of biomolecule, particularly DNA, microarrays [Colina et al., 2006, 2005; Fernandez-Pradas et al., 2004; Serra et al., 2004a,b]. Hopp et al. [Hopp et al., 2004] have also applied the DRL-LIFT technique for the forward transfer of living fungi. Typically metal layers have been used as DRLs, however these can present a problem as the deposited material is often contaminated by residual DRL, as Smausz et al. observed using Ag DRLs of various thicknesses to DRL-LIFT a water donor [Smausz et al., 2006].

In the last few years, a new DRL material has appeared in the literature. The triazene polymer (TP) [Nagel et al., 2007] has emerged as a highly suitable DRL material that requires only low fluences to ablate, and is completely decomposed during DRL-LIFT. The TP has been used for the DRL-LIFT of PMMA [Mito et al., 2001], mammalian cells [Doraiswamy et al., 2006], quantum dots [Xu et al., 2007], and organic LEDs [Fardel et al., 2007a]. Two chapters of this thesis are dedicated to DRL-LIFT with the TP, representing the first studies of this process with femtosecond duration pulses.

Kattamis et al. [Kattamis et al., 2007] proposed the use of thick, commercially available polyimide polymers as DRLs for the DRL-LIFT of materials that cannot withstand the mechanical shocks inherent with other forward transfer processes. Using a 4 μm thick polyimide DRL, they were able to demonstrate viable, contamination-free transfer of living mammalian embryonic stem cells.

Other release-layer based forward transfer techniques have also been demonstrated. In 2003, Blanchet et al. [Blanchet et al., 2003] demonstrated the forward transfer of conducting polymers using a metallic layer to convert the incident laser energy to heat. The hot metal layer caused evaporation of a solvent leading to forward transfer of the polymer. However, the metal was not ablated so there was no risk of contaminating the polymer with redeposited metal. This was the LITI technique described previously. Further reports of light-emitting polymer transfer were presented by Lee et al. [Lee and Lee, 2004].

In 1999, Toet et al. [Toet et al., 1999] demonstrated the forward transfer deposition of poly-Si using the explosive release of trapped hydrogen in an amorphous hydrogenated silicon layer (the HA-LIFT technique). They observed that the transferred material was very rough, but could be smoothed by a secondary scan of the laser, and also that adhesion of the transferred material was good for applied fluence $\geq$ 400 mJ/cm^2. In follow-on work, the group presented a numerical model of the technique [Toet et al., 2000a], and then used the a-Si:H as a DRL for the transfer of Al [Toet et al., 2000b].

2.3.4 MAPLE-DW and LMI

The MAPLE-DW technique was first described by Pique et al. [Pique et al., 1999] who used it deposit various electronic and sensor materials. A number of electronic components were produced, including conductive lines, resistors, and capacitors. The devices were functional but, due to the unavoidably porous nature of the deposited material, the resistivities of the electronics were $\approx 10^3$ times the bulk value. A chemically sensitive resistor, with applications in chemical detection, was also produced.

MAPLE-DW has been applied by a number of authors for the production of high definition displays [Fitz-Gerald et al., 2000], Li-ion microbatteries [Wartena et al., 2004], and solar cells [Kim et al., 2004]. The transfer of eukaryotic cells with MAPLE-DW has also been achieved [Pique et al., 2002; Wu et al., 2001], as has the writing of various oxide materials [Arnold et al., 2004], and e-coli [Ringeisen et al., 2002].

It is now also relatively common practice to combine MAPLE and DRL-LIFT. The DRL acts as a propulsion layer as usual, whilst the (now liquid) matrix protects and keeps alive the delicate cells during transfer. This technique has been successfully applied to the transfer of single mammalian cells per laser shot [Barron et al., 2005, 2004; Doraiswamy et al., 2006].

LMI has been used to implant a range of organic molecules into polymer films. A particularly successful avenue of research has been the implantation of photochromic molecules to form optical devices and rewritable memories [Fukumura et al., 1996, 1994, 1998; Karnakis et al., 1998a; Okada et al., 2001]. LMI has also been combined with the triazene polymer commonly used for DRL applications [Karnakis et al., 1998b]. In this study the TP was doped with pyrene to form the source film. Recent work has focused on producing sub-micron patterns of organic molecules on polymer films and other organic substrates [Goto et al., 2004, 1999, 2000; Kishimoto et al., 2001; Pihosh et al., 2005].

2.3.5 Femtosecond LIFT

The use of femtosecond duration pulses for LIFT has recently been attracting much attention (see e.g. [Banks et al., 2006, 2008a,b; Bera et al., 2007; Claeyssens et al., 2007; Germain et al., 2007; Koundourakis et al., 2001; Mailis et al., 1999; Papazoglou et al., 2002; Thomas et al., 2007; Yang et al., 2006; Zergioti et al., 2005, 1998]. The works have included the transfer of biomaterials and polymers intact, nanoscale structures, and solid phase patterning. However, we shall leave a full discussion of the history of femtosecond LIFT to the next chapter on femtosecond light-matter interactions.

Table 2.1: Overview of laser forward transfer work

Technique	Material transferred	Matrix or release layer material	Feature size (μm)	Laser type (λ (nm))	References
LIFT	Cu	N/A	50-70	ArF (193)	[Bohandy et al., 1986]
LIFT	Cu, Ag	N/A	15-50	2ω-Nd:YAG (532)	[Bohandy et al., 1988]
LIFT	YBaCuO, BiSrCaCuO	N/A	100	Nd:YAG (1064)	[Fogarassy et al., 1989]
LIFT	V, Cr, Ti, Ge, Sn	N/A		Ruby (694), XeCl (308)	[Mogyorosi et al., 1989]
LIFT	Ti, Cr, Ge/Se	N/A		Ruby (694)	[Toth et al., 1990]
LIFT	PMMA/IR-165 dye	N/A		Nd:YAG (1064)	[Lee et al., 1992]
DRL-LIFT	PMMA/coloured dyes	Al		Nd:YAG (1064)	[Tolbert et al., 1993]
LIFT	W	N/A	5-10	Nd:YAG (1064)	[Kantor and Szorenyi, 1995; Kantor et al., 1994b]
LIFT	PMMA	N/A		4ω-Nd:YAG (266)	[Blanchet, 1995]
LIFT	Pd	N/A	150	ArF, KrF, KrCl, XeCl, XeF (193, 248, 222, 308, 351)	[Esrom et al., 1995]
LIFT	Diamond/photoresist	N/A	10	KrF (248), Cu (510)	[Pimenov et al., 1995]

Continued

Overview of laser forward transfer work - continued

Technique	Material transferred	Matrix or release layer material	Feature size (μm)	Laser type (λ (nm))	References
LMI	PMMA/diphenyl anthracene (5.5 wt%), PMMA/pyrene (3.5 wt%)	N/A	200	(248, 351)	[Fukumura et al., 1996, 1998; Karnakis et al., 1998a,b]
LIFT	Pt, Cr, In_2O_3	N/A	0.7-5	KrF (248)	[Koundourakis et al., 2001; Mailis et al., 1999; Papakonstantinou et al., 1999; Zergioti et al., 1998]
LIFT	Al	N/A		Ti:sapph (1053)	[Bullock and Bolton, 1999]
LMI	Zinc tetraphenyl porphyrin (ZnTPP)	PMMA	2-100	(248)	[Goto et al., 2004, 1999; Pihosh et al., 2005]
LIFT	Au	N/A		dye laser (440)	[Nakata and Okada, 1999]
MAPLE-DW	Ag, Au, NiCr, $BaTiO_3$, Y_3FeO_12	PBMA	20-30	KrF (248)	[Pique et al., 1999]
a-Si:H	p-Si, Al	H_2	5	XeCl (308)	[Toet et al., 2000a,b, 1999]
LIFT	Au/Sn	N/A	30	Ti:sapph (775)	[Bahnisch et al., 2000]

Continued

Overview of laser forward transfer work - continued

Technique	Material transferred	Matrix or release layer material	Feature size (μm)	Laser type (λ (nm))	References
MAPLE-DW, DRL-LIFT	Phosphor powders Y_2O_3 and Zn_2SiO_4:Mn	Au (DRL), glycerin-isopropanol-$LaNO_2$-$Mg_2(NO_3)_2$ (matrix)	100	KrF (248)	[Fitz-Gerald et al., 2000]
LIMIT	Dicyanoanthracene	N/A	1	Nd:YAG (355, 420, 3ns)	[Goto et al., 2000]
MAPLE-DW	Ag, graphite	PTF epoxy resin	400	(355, 5ns)	[Modi et al., 2001; Pique et al., 2002]
DRL-LIFT	PMMA/Pyrene	Triazene polymer	100	(248, 30ns)	[Mito et al., 2001]
MAPLE-DW	polyethylene, eukaryotic cells	Volatile solvents (water, methanol, chloroform)	10	(193, 20ns)	[Pique et al., 2002; Wu et al., 2001]
LIFT	In_2O_3	N/A		dye laser/KrF (248, 0.5ps)	[Papazoglou et al., 2002]
LIFT/DRL-LIFT	Rhodamine 610 laser dye	Au	300	Nd:YAG (532)	[Nakata et al., 2002]
LIFT	Au, Ni	N/A	150	KrF (248, 30ns)	[Sano et al., 2002]
LIFT	Ni	N/A	150	KrF (248, 30ns)	[Yamada et al., 2002]

Continued

Overview of laser forward transfer work - continued

Technique	Material transferred	Matrix or release layer material	Feature size (μm)	Laser type (λ (nm))	References
MAPLE-DW	E-coli	Luria-Bertani broth	100-150	ArF (193)	[Ringeisen et al., 2002]
MAPLE-DW	$BaTiO_3$	α-terpineol		3ω-Nd:YAG (355, 150ns)	[Young et al., 2002]
LITI	DNNSA-PANI, SWNT	N/A	2.5-5	(780nm, CW)	[Blanchet et al., 2003]
MAPLE-DW	Ruthenium oxide	sulfuric acid	$\geq$1000	3ω-Nd:YAG (355, 150ns)	[Arnold et al., 2003]
LIFT	Lambda phage DNA	N/A	150	dye laser/KrF (248, 0.5ps)	[Karaiskou et al., 2003]
LIFT	Sn	N/A	200	KrF (248, 30ns)	[Komorita et al., 2003]
MAPLE-DW	Ag, MnO_2, Ag_2O	Glycerol		3ω-Nd:YAG (355, 150ns)	[Pique et al., 2003]
LIFT	Au	N/A	2-4	Ti:sapph (400, 150fs)	[Tan et al., 2003]
LIFT	Cr	N/A		dye/KrF (248, 0.5ps), KrF (248, 30ns)	[Zergioti et al., 2003]
DRL-LIFT, MAPLE-DW	Mammalian cells	Glycerol (matrix), Ti (DRL)	120	4ω-Nd:YAG (266, 5ns)	[Barron et al., 2005, 2004]

Continued

Overview of laser forward transfer work - continued

Technique	Material transferred	Matrix or release layer material	Feature size (μm)	Laser type (λ (nm))	References
MAPLE-DW	Zn, Ag_2O	PVDF-HFP binder	$\geq$1000	3ω-Nd:YAG (355, 10ns)	[Arnold et al., 2004]
DRL-LIFT, MAPLE-DW	DNA, proteins	Ti (DRL), phosphate buffer solution (matrix)	30-100	ArF (193, 20ns), 3ω-Nd:YAG (355, 10ns)	[Colina et al., 2006, 2005; Fernandez-Pradas et al., 2004; Serra et al., 2004a,b]
DRL-LIFT	Fungi (trichoderma conidia)	Ag	300-500	KrF (248, 30ns)	[B.Hopp et al., 2005; Hopp et al., 2004]
LITI	Light emitting and inert polymers	N/A	50	Nd:YAG (CW)	[Lee and Lee, 2004]
LIFT	Au, Al	N/A	1-5	KrF (248, 28ns)	[Landstrom et al., 2004]
MAPLE-DW	C, $LiCoO_2$	Binder	40-60	3ω-Nd:YAG (355)	[Wartena et al., 2004]
LIFT	Al, Ni	N/A	1-25	Nd:YAG (1064, 7ns)	[Willis and Grosu, 2004, 2005]
LIFT	TiO_2-Au nanocomposite	N/A	200	Nd:YAG (1064, 10ns)	[Sakata et al., 2005]
LIFT	Cr	N/A	0.3	Ti:sapph (800, 130fs)	[Banks et al., 2006]
LIFT	Carbon nanotubes	N/A	10	Nd:YAG (1064, 10ns)	[Chang-Jian et al., 2006]
DRL-LIFT	Mammalian cells	Triazene polymer	20	ArF (193, 30ns)	[Doraiswamy et al., 2006]
DRL-LIFT	Water	Ag	$\geq$200	KrF (248, 30ns)	[Smausz et al., 2006]

Continued

Overview of laser forward transfer work - continued

Technique	Material transferred	Matrix or release layer material	Feature size (μm)	Laser type (λ (nm))	References
LIFT	Cu	N/A	1.5	(775, 150fs)	[Yang et al., 2006]
DRL-LIFT	OLED components	Triazene polymer	500	XeCl (308, 30ns)	[Fardel et al., 2007a,b]
LIFT	Al	N/A	5	(785, 45fs)	[Bera et al., 2007]
LIFT	V_2O_5	N/A	300	2ω-Nd:YAG (532)	[Chakraborty et al., 2007]
LIFT	Au	N/A	1	Ti:sapph (800, 110fs)	[Germain et al., 2007]
DRL-LIFT	Quantum dot emitters	Triazene polymer	800	(193)	[Xu et al., 2007]
LIFT	Luciferase	N/A	200	Nd:YAG (355, 266, 10ns)	[Tsuboi et al., 2007]
LIFT	N/A (theoretical)	N/A	N/A	N/A	[Willis and Grosu, 2007]
DRL-LIFT, MAPLE-DW	Embryonic cells	polyimide (DRL), glycerol (matrix)	5-20	3ω-Nd:YVO_4 (355, 15ns)	[Kattamis et al., 2007]
LIFT	Zn	N/A	5	(248, 450fs)	[Claeyssens et al., 2007]
LIFT	PEDOT-PSS (poly(3,4-ethylenedioxythiophene)-poly(styrenesulfonate))	N/A	200-300	(248, 532, 1025, 1064 - 25ns, 8ns, 50ps, 400fs)	[Thomas et al., 2007]
BLAST	Cr	N/A	10	Ti:sapph (800, 130fs)	[Banks et al., 2008a]
LIFT	$FeSi_2$	N/A	0.5	KrF (248, 20ns)	[Narazaki et al., 2008]
DRL-LIFT	GdGaO	Triazene polymer	8-10	Ti:sapph (800, 130fs)	[Banks et al., 2008b]

Bibliography

Adrian, F., Bohandy, J., Kim, B., Jette, A., and Thompson, P. (1987). A study of the mechanism of metal deposition by the laser-induced forward transfer process. *J. Vac. Sci. Technol. B*, 5(5):1490–1494.

Arnold, C., Kim, H., and Pique, A. (2004). Laser direct write of planar alkaline microbatteries. *Appl. Phys. A*, 79:417–420.

Arnold, C., Wartena, R., Swider-Lyons, K., and Pique, A. (2003). Direct-write planar microultracapacitors by laser engineering. *J. Electrochem. Soc.*, 150(5):A571–A575.

Bahnisch, R., Gross, W., and Menschig, A. (2000). Single-shot, high repetition rate metallic pattern transfer. *Microelectron. Eng.*, 50:541–546.

Banks, D., Grivas, C., Mills, J., Zergioti, I., and Eason, R. (2006). Nanodroplets deposited in microarrays by femtosecond ti:sapphire laser induced forward transfer. *Appl. Phys. Lett.*, 89:193107.

Banks, D., Grivas, C., Zergioti, I., and Eason, R. (2008a). Ballistic laser-assisted solid transfer (blast) from a thin film precursor. *Opt. Express*, 16:3249–3254.

Banks, D., Kaur, K., Gazia, R., Fardel, R., Nagel, M., Lippert, T., and Eason, R. (2008b). Triazene photopolymer dynamic release layer-assisted femtosecond laser-induced forward transfer with an active carrier substrate. *Europhys. Lett.*, 83:38003.

Barron, J., Krizman, D., and Ringeisen, B. (2005). Laser printing of single cells: statistical analysis, cell viability and stress. *Ann. Biomed. Eng.*, 33(2):121–130.

Barron, J., Spargo, B., and Ringeisen, B. (2004). Biological laser printing of three dimensional cellular structures. *Appl. Phys. A*, 79:1027–1030.

Baseman, R. and Froberg, N. (1990). Minimum fluence for laser blow-off of thin gold films at 248 and 532 nm. *Appl. Phys. Lett.*, 56(15):1412–1414.

Bera, S., Sabbah, A., Yarbrough, J., Allen, C., Winters, B., Durfee, C., and Squier, J. (2007). Optimization study of the femtosecond laser-induced forward-transfer process with thin aluminium films. *Appl. Opt.*, 46(21):4650–4659.

B.Hopp, Smausz, T., Barna, N., Vass, C., Antal, Z., Kredics, L., and Chrisey, D. (2005). Time-resolved study of absorbing film assisted laser induced forward transfer of trichoderma longibrachiatum conidia. *J. Phys. D: Appl. Phys.*, 38:833–837.

Blanchet, G. (1995). Deposition of poly(methyl-methacrylate) films by uv laser ablation. *Macromolecules*, 28(13):4603–4607.

Blanchet, G., Loo, Y.-L., Rogers, J., Gao, F., and Fincher, C. (2003). Large area, high resolution, dry printing of conducting polymers for organic electronics. *Appl. Phys. Lett.*, 82(3):463–465.

Blawas, A. and Reichert, W. (1998). Protein patterning. *Biomaterials*, 19:595–609.

Bohandy, J., Kim, B., and Adrian, F. (1986). Metal deposition from a supported metal film using an excimer laser. *J. Appl. Phys.*, 60(1):1538–1539.

Bohandy, J., Kim, B., Adrian, F., and Jette, A. (1988). Metal deposition at 532 nm using a laser transfer technique. *J. Appl. Phys.*, 63(4):1158–1162.

Bullock, A. and Bolton, P. (1999). Laser-induced back ablation of aluminium thin films using picosecond laser pulses. *J. Appl. Phys.*, 85(1):460–465.

Chakraborty, S., Sakata, H., Yokoyama, E., Wakaki, M., and Chakravorty, D. (2007). Laser-induced forward transfer technique for maskless patterning of amorphous v_2o_5 thin film. *Appl. Surf. Sci.*, 254:638–643.

Chang-Jian, S., Ho, J., Cheng, J., and Sung, C. (2006). Fabrication of carbon nanotube field emission cathodes in patterns by a laser transfer method. *Nanotechnology*, 17:1184–1187.

Claeyssens, F., Klini, A., Mourka, A., and Fotakis, C. (2007). Laser patterning of zn for zno nanostructure growth: Comparison between laser induced forward transfer in air and in vacuum. *Thin Solid Films*, 515:8529–8533.

Colina, M., Duocastella, M., Fernandez-Pradas, J., Serra, P., and Morenza, J. (2006). Laser-induced forward transfer of liquids: study of the droplet ejection process. *J. Appl. Phys.*, 99:084909.

Colina, M., Serra, P., Fernandez-Pradas, J., Sevilla, L., and J.L.Morenza (2005). Dna deposition through laser induced forward transfer. *Biosens. Bioelectron.*, 20:1638–1642.

Doraiswamy, A., Narayan, R., Lippert, T., Urech, L., Wokaun, A., Nagel, M., Hopp, B., Dinescu, M., Modi, R., Auyeung, R., and Chrisey, D. (2006). Excimer laser forward transfer of mammalian cells using a novel triazene absorbing layer. *Appl. Surf. Sci.*, 252:4743–4747.

Eason, R. (2007). *Pulsed Laser Deposition of Thin Films.* Wiley-Interscience, John Wiley and Sons, Inc., Hoboken, New Jersey, USA.

Esrom, H., Zhang, J., Kogelschatz, U., and Pedraza, A. (1995). New approach of a laser-induced forward transfer for deposition of patterned thin metal films. *Appl. Surf. Sci.*, 86:202–207.

Fardel, R., Nagel, M., Nuesch, F., Lippert, T., and Wokaun, A. (2007a). Fabrication of organic light-emitting diode pixels by laser-assisted forward transfer. *Appl. Phys. Lett.*, 91:061103.

Fardel, R., Nagel, M., Nuesch, F., Lippert, T., and Wokaun, A. (2007b). Laser forward transfer using a sacrificial layer: influence of the material properties. *Appl. Surf. Sci.*, 254:1322–1326.

Fernandez-Pradas, J., Colina, M., Serra, P., Dominguez, J., and Morenza, J. (2004). Laser-induced forward transfer of biomolecules. *Thin Solid Films*, 453-454:27–30.

Fitz-Gerald, J., Pique, A., Chrisey, D., Rack, P., Zeleznik, M., Auyeung, R., and Lakeou, S. (2000). Laser direct writing of phosphor screens for high-definition displays. *Appl. Phys. Lett.*, 76(11):1386–1388.

Fogarassy, E., Fuchs, C., Kerherve, F., Hauchecorne, G., and Perriere, J. (1989). Laser-induced forward transfer of high-T_c ybacuo and bisrcacuo superconducting thin films. *J. Appl. Phys.*, 66(1):457–459.

Fukumura, H., Kohji, Y., and Masuhara, H. (1996). Laser implantation of fluorescent molecules into polymer films. *Appl. Surf. Sci.*, 96-98:569–571.

Fukumura, H., Kohji, Y., Nagasawa, K., and Masuhara, H. (1994). Laser implantation of pyrene molecules into poly(methyl methacrylate) films. *J. Am. Chem. Soc.*, 116:10304–10305.

Fukumura, H., Uji-i, H., Banjo, H., Masuhara, H., Karnakis, D., Ichinose, N., Kawanishi, S., Uchida, K., and Irie, M. (1998). Laser implantation of photochromic molecules into polymer films: a new approach towards molecular device fabrication. *Appl. Surf. Sci.*, 127-129:761–766.

Germain, C., Charron, L., Lilge, L., and Tsui, Y. (2007). Electrodes for microfluidic devices produced by laser induced forward transfer. *Appl. Surf. Sci.*, 253:8328–8333.

Goto, M., Hobley, J., Oishi, T., Kasahara, A., Tosa, M., Yoshihara, K., Kishimoto, M., and Fukumura, H. (2004). Micro-patterning of multiple organic molecules by laser implantation. *Appl. Phys. A*, 79:157–160.

Goto, M., Ichinose, N., Kawanishi, S., and Fukumura, H. (1999). Implantation of organic molecules into biotissue by pulsed laser irradiation. *Jpn. J. Appl. Phys.*, 38:L87–L88.

Goto, M., Kawanishi, S., and Fukumura, H. (2000). Laser implantation of dicyanoanthracene in poly(methyl methacrylate) from a 100-nm aperture micropipette. *Appl. Surf. Sci.*, 154-155:701–705.

Heller, M. (2002). Dna microarray technology: Devices, systems, and applications. *Annu. Rev. Biomed. Eng.*, 4:129–153.

Hopp, B., Smausz, T., Antal, Z., Kresz, N., Bor, Z., and Chrisey, D. (2004). Absorbing film assisted laser induced forward transfer of fungi (trichoderma conidia). *J. Appl. Phys.*, 96(6):3478–3481.

Kantor, Z. and Szorenyi, T. (1995). Dynamics of long-pulse laser transfer of micrometer-sized metal patterns as followed by time-resolved measurements of reflectivity and transmittance. *J. Appl. Phys.*, 78(4):2775–2781.

Kantor, Z., Toth, Z., and Szorenyi, T. (1994a). Metal pattern deposition by laser-induced forward transfer. *Appl. Surf. Sci.*, 86:196–201.

Kantor, Z., Toth, Z., Szorenyi, T., and Toth, A. (1994b). Deposition of micrometer-sized tungsten patterns by laser transfer technique. *Appl. Phys. Lett.*, 64(25):3506–3508.

Karaiskou, A., Zergioti, I., Fotakis, C., Kapsetaki, M., and Kafetzopoulos, D. (2003). Microfabrication of biomaterials by the sub-ps laser-induced forward transfer process. *Appl. Surf. Sci.*, 208-209:245–249.

Karnakis, D., Goto, M., Ichinose, N., Kawanishi, S., and Fukumura, H. (1998a). Forward-transfer laser implantation of pyrene molecules in a solid polymer. *Appl. Phys. Lett.*, 73(10):1439–1441.

Karnakis, D., Lippert, T., Ichinose, N., Kawanishi, S., and Fukumura, H. (1998b). Laser induced molecular transfer using ablation of a triazeno-polymer. *Appl. Surf. Sci.*, 127-129:781–786.

Kattamis, N., Purnick, P., Weiss, R., and Arnold, C. (2007). Thick film laser induced forward transfer for deposition of thermally and mechanically sensitive materials. *Appl. Phys Lett.*, 91:171120.

Kim, H., Kushto, G., Arnold, C., Kafafi, Z., and Pique, A. (2004). Laser processing of nanocrystalline tio$_2$ films for dye-sensitized solar cells. *Appl. Phys. Lett.*, 85(3):464–466.

Kishimoto, M., Hobley, J., Goto, M., and Fukumura, H. (2001). Microscopic laser patterning of functional organic molecules. *Adv. Mater.*, 13(15):1155–1158.

Klini, A., Loukakos, P., Gray, D., Manousaki, A., and Fotakis, C. (2008). Laser induced forward transfer of metals by temporally shaped femtosecond laser pulses. *Opt. Express*, 16(15):11300–11309.

Komorita, K., Sano, T., Yamada, H., and Miyamoto, I. (2003). Oxidation state control of micro metal oxide patterns produced by using laser-induced forward transfer technique. *Proc. SPIE*, 4830:20–24.

Koundourakis, G., Rockstuhl, C., Papazoglou, D., Klini, A., Zergioti, I., Vainos, N., and Fotakis, C. (2001). Laser printing of active optical microstructures. *Appl. Phys. Lett.*, 78(7):868–870.

Kyrkis, K., Andreadaki, A., Papazoglou, D., and Zergioti, I. (2006). *Recent advances in laser processing of materials*, chapter 7, pages 213–240. European Materials Research Society. Elsevier, Burlington, MA 01803, USA.

Landstrom, L., Klimstein, J., Schrems, G., Piglmayer, K., and Bauerle, D. (2004). Single-step patterning and the fabrication of contact masks by laser-induced forward transfer. *Appl. Phys. A*, 78:537–548.

Lee, I., Tolbert, W., Dlott, D., Doxtader, M., Foley, D., Arnold, D., and Ellis, E. (1992). Dynamics of laser ablation transfer imaging investigated by ultrafast microscopy. *J. Imag. Sci. Tech.*, 36(2):180–187.

Lee, J. and Lee, S. (2004). Laser-induced thermal imaging of polymer light emitting materials on poly(3,4-ethylenedioxythiophene): silane hole-transport layer. *Adv. Mater.*, 16(1):51–54.

Mailis, S., Zergioti, I., Koundourakis, G., Ikiades, A., Patentalaki, A., Papakonstantinou, P., Vainos, N., and Fotakis, C. (1999). Etching and printing of diffractive optical microstructures by a femtosecond excimer laser. *Appl. Opt.*, 38(11):2301–2308.

Mito, T., Tsujita, T., Masuhara, H., Hayashi, N., and Suzuki, K. (2001). Hollowing and transfer of polymethyl methacrylate film propelled by laser ablation of triazeno polymer film. *Jpn. J. Appl. Phys.*, 40:L805–L806.

Modi, R., Wu, H., Auyeung, R., Gilmore, C., and Chrisey, D. (2001). Direct writing of polymer thick film resistors using a novel laser transfer technique. *J. Mater. Res.*, 16(11):3214–3222.

Mogyorosi, P., Szorenyi, T., Ball, K., Toth, Z., and Hevesi, I. (1989). Pulsed laser ablative deposition of thin metal films. *Appl. Surf. Sci.*, 36:157–163.

Nagel, M., Hany, R., Lippert, T., Molberg, M., Nuesch, F., and Rentsch, D. (2007). Aryltriazene photopolymers for uv-laser applications: Improved synthesis and photodecomposition study. *Macromol. Chem. Phys.*, 208:277–286.

Nakata, Y. and Okada, T. (1999). Time-resolved microscopic imaging of the laser-induced forward transfer process. *Appl. Phys. A [Suppl.]*, 69:S275–S278.

Nakata, Y., Okada, T., and Maeda, M. (2002). Transfer of laser dye by laser-induced forward transfer. *Jpn. J. Appl. Phys.*, 41:L839–L841.

Narazaki, A., Sato, T., Kurosaki, R., Kawaguchi, Y., and Niino, H. (2008). Nano- and microdot array formation of fesi$_2$ by nanosecond excimer laser-induced forward transfer. *Appl. Phys. Exp.*, 1:057001.

Okada, T., Hatanaka, K., Hobley, J., Fukumura, H., and Kishimoto, M. (2001). Laser-induced molecular implantation at the focus of an objective lens: a comparative study among anthracene derivatives. In *Technical Digest. CLEO/Pacific Rim 2001. 4th Pacific Rim Conference on Lasers and Electro-Optics (Cat. No.01TH8557)*, pages 56 – 57, Chiba, Japan.

Papakonstantinou, P., Vainos, N., and Fotakis, C. (1999). Microfabrication by uv femtosecond laser ablation of pt, cr and indium oxide thin films. *Appl. Surf. Sci.*, 151:159–170.

Papazoglou, D., Karaiskou, A., Zergioti, I., and Fotakis, C. (2002). Shadowgraphic imaging of the sub-ps laser-induced forward transfer process. *Appl. Phys. Lett.*, 81(9):1594–1596.

Pihosh, Y., Oishi, T., Goto, M., Kasahara, A., and Tosa, M. (2005). Preparation of coumarin 6 and zntpp micro dots on pbma films by laser molecular implantation. *Appl. Surf. Sci.*, 241:205–208.

Pimenov, S., Shafeev, G., Smolin, A., Konov, V., and Vodolaga, B. (1995). Laser-induced forward transfer of ultra-fine diamond particles for selective deposition of diamond films. *Appl. Surf. Sci.*, 86:208–212.

Pique, A., Arnold, C., Wartena, R., Weir, D., Pratap, B., Swider-Lyons, K., Kant, R., and Chrisey, D. (2003). Laser-induced forward transfer direct-write of miniature sensor and microbattery systems. *Proc. SPIE*, 4830:182–188.

Pique, A., Chrisey, D., Auyeung, R., Fitz-Gerald, J., Wu, H., McGill, R., Lakeou, S., Wu, P., Nguyen, V., and Duignan, M. (1999). A novel laser transfer process for direct writing of electronic and sensor materials. *Appl. Phys. A [Suppl.]*, 69:S279–S284.

Pique, A., Chrisey, D., Spargo, B., Bucaro, M., Vachet, R., Callahan, J., McGill, R., Leonhardt, D., and Mlsna, T. (2008). Use of matrix assisted pulsed laser evaporation (maple) for the growth of organic thin films. In *Proceedings of the 1998 MRS Spring Symposium*, pages 421–426, San Francisco, CA, USA. MRS, Warrendale, PA, USA.

Pique, A., Weir, D., Wu, P., Pratap, B., Arnold, C., Ringeisen, B., McGill, R., Auyeung, R., Kant, R., and Chrisey, D. (2002). Direct-write of sensor devices by a laser forward transfer technique. *Proc. SPIE*, 4637:361–368.

Ringeisen, B., Chrisey, D., Pique, A., Young, H., Modi, R., Bucaro, M., Jones-Meehan, J., and Spargo, B. (2002). Generation of mesoscopic patterns of viable escherichia coli by ambient laser transfer. *Biomaterials*, 23:161–166.

Sakata, H., Chakraborty, S., Yokoyama, E., Wakaki, M., and Chakravorty, D. (2005). Laser-induced forward transfer of tio-au nanocomposite films for maskless patterning. *Appl. Phys. Lett.*, 86:114104.

Sano, T., Yamada, H., Nakayama, T., and Miyamoto, I. (2002). Experimental investigation of laser induced forward transfer process of metal thin films. *Appl. Surf. Sci.*, 186:221–226.

Seifert, N. and Betz, G. (1998). Computer simulations of laser-induced ejection of droplets. *Appl. Surf. Sci.*, 133:189194.

Seifert, N., Betz, G., and Husinsky, W. (1996). Droplet formation on metallic surfaces during low-fluence laser irradiation. *Appl. Surf. Sci.*, 103:63–70.

Serra, P., Colina, M., Fernandez-Pradas, J., Sevilla, L., and Morenza, J. (2004a). Preparation of functional dna microarrays through laser-induced forward transfer. *Appl. Phys. A*, 85(9):1639–1641.

Serra, P., Fernandez-Pradas, J., Berthet, F., Colina, M., Elvira, J., and Morenza, J. (2004b). Laser direct writing of biomolecule arrays. *Appl. Phys. A*, 79:949–952.

Smausz, T., Hopp, B., Kecskemeti, G., and Bor, Z. (2006). Study on metal microparticle content of the material transferred with absorbing film assisted laser induced forward transfer when using silver absorbing layer. *Appl. Surf. Sci.*, 252:4738–4742.

Stoian, R., Mermillod-Blondin, A., Winkler, S., Rosenfeld, A., Hertel, I., Spyridaki, M., Koudoumas, E., Tzanetakis, P., Fotakis, C., Burakov, I., and Bulgakova, N. (2005). Temporal pulse manipulation and consequences for ultrafast laser processing of materials. *Opt. Eng.*, 45(5):051106.

Tan, B., Venkatakrishnan, K., and Tok, K. (2003). Selective surface texturing using femtosecond pulsed laser induced forward transfer. *Appl. Surf. Sci.*, 207:365–371.

Thomas, B., Alloncle, A., Delaporte, P., Sentis, M., Sanaur, S., Barret, M., and Collot, P. (2007). Experimental investigations of laser-induced forward transfer process of organic thin films. *Appl. Surf. Sci.*, 254:1206–1210.

Toet, D., Smith, P., Sigmon, T., and Thompson, M. (2000a). Experimental and numerical investigations of a hydrogen-assisted laser-induced materials transfer procedure. *J. Appl. Phys.*, 87(7):3537–3546.

Toet, D., Smith, P., Sigmon, T., and Thompson, M. (2000b). Spatially selective materials deposition by hydrogen-assisted laser-induced transfer. *Appl. Phys. Lett.*, 77(2):307–309.

Toet, D., Thompson, M., Smith, P., and Sigmon, T. (1999). Laser-assisted transfer of silicon by explosive hydrogen release. *Appl. Phys. Lett.*, 74(15):2170–2172.

Tolbert, W., Lee, I., Doxtader, M., Ellis, E., and Dlott, D. (1993). High-speed color imaging by laser ablation transfer with a dynamic release layer: fundamental mechanisms. *J. Imag. Sci. Tech.*, 37(4):411–421.

Toth, Z., Kantor, Z., Mogyorosi, P., and Szorenyi, T. (1990). Surface patterning by pulsed laser induced transfer of metals and compounds. *Proc. SPIE*, 1279:150–157.

Tsuboi, Y., Furuhata, Y., and Kitamura, N. (2007). A sensor for adenosine triphosphate fabricated by laser-induced forward transfer of luciferase onto a poly(dimethylsiloxane) microchip. *Appl. Surf. Sci.*, 253:8422–8427.

Wartena, R., Curtright, A., Arnold, C., Pique, A., and Swider-Lyons, K. (2004). Li-ion microbatteries generated by a laser direct-write method. *J. Power Sources*, 126:193–202.

Willis, D. and Grosu, V. (2004). Evaporation and phase explosion during laser-induced forward transfer of aluminium. *Proc. SPIE*, 5339:304–312.

Willis, D. and Grosu, V. (2005). Microdroplet deposition by laser-induced forward transfer. *Appl. Phys. Lett.*, 86:244103.

Willis, D. and Grosu, V. (2007). The effect of melting-induced volumetric expansion on initiation of laser-induced forward transfer. *Appl. Surf. Sci.*, 253:4759–4763.

Wu, P., Ringeisen, B., Callahan, J., Brooks, M., Bubb, D., Wu, H., Pique, A., Spargo, B., McGill, R., and Chrisey, D. (2001). The deposition, structure, pattern deposition, and activity of biomaterial thin-films by matrix-assisted pulsed-laser evaporation (maple) and maple direct write. *Thin Solid Films*, 398-399:607–614.

Xu, J., Liu, J., Cui, D., Gerhold, M., Wang, A., Nagel, M., and Lippert, T. (2007). Laser-assisted forward transfer of multi-spectral nanocrystal quantum dot emitters. *Nanotechology*, 18:025403.

Yamada, H., Sano, T., Nakayama, T., and Miyamoto, I. (2002). Optimization of laser-induced forward transfer process of metal thin films. *Appl. Surf. Sci.*, 197-198:411–415.

Yang, L., Wang, C., Ni, X., Wang, Z., Jia, W., and Chai, L. (2006). Microdroplet deposition of copper film by femtosecond laser-induced forward transfer. *Appl. Phys. Letts*, 89:161110.

Young, D., Auyeung, R., Pique, A., Chrisey, D., and Dlott, D. (2002). Plume and jetting regimes in a laser based forward transfer process as observed by time-resolved optical microscopy. *Appl. Surf. Sci.*, 197-198:181–187.

Zergioti, I., Karaiskou, A., Papazoglou, D., Fotakis, C., Kapsetaki, M., and Kafetzopoulos, D. (2005). Femtosecond laser microprinting of biomaterials. *Appl. Phys. Lett.*, 86:163902.

Zergioti, I., Mailis, S., Vainos, N., Papakonstantinou, P., Kalpouzos, C., Grigoropoulos, C., and Fotakis, C. (1998). Microdeposition of metal and oxide structures using ultrashort laser pulses. *Appl. Phys. A*, 66:579–582.

Zergioti, I., Papazoglou, D., Karaiskou, A., Fotakis, C., Gamaly, E., and Rode, A. (2003). A comparative schlieren imaging study between ns and sub-ps laser forward transfer of cr. *Appl. Surf. Sci.*, 208-209:177–180.

Chapter 3

Femtosecond Laser-Matter Interactions: Fundamentals and Implications for LIFT

3.1 Introduction

The main aim of this PhD was to investigate the LIFT process with femtosecond-duration pulses (from hereon referred to as *fs-LIFT*). The interesting questions were whether fs-LIFT offered advantages over LIFT with longer duration pulses (referred to as *ns-LIFT* as most studies involved nanosecond-duration laser pulses) in terms of depositing the smallest structures or transferring intact and solid-phase material.

The benefits of using femtosecond pulses for various material processing applications are well known (see, for example [Dausinger et al., 2004; Misawa and Juodkazis, 2006]). In particular, micromachining and ablation benefit from the reduced thermal effects, minimal collateral damage, and ability to directly process virtually any material.

For similar reasons, we may expect LIFT to benefit from using femtosecond-duration pulses also. To understand how, let us first consider briefly the fundamentals of femtosecond laser-matter interactions (numerous discussions of this complex field exist in the literature; see for example [Chowdhury and Xu, 2003; Gamaly et al., 2002; Hohlfeld et al., 2000]). Then we will discuss the potential advantages of fs-LIFT over ns-LIFT.

3.2 Laser-Matter Interactions on Femtosecond Timescales

Laser-matter interactions when the pulse duration is on the order of femtoseconds or shorter can be drastically different from longer pulse regimes. The explanation for these differences is that the pulse duration is shorter than the characteristic electron-ion coupling time in the target material, τ_{ei}. Although τ_{ei} is material dependent, reported values are typically around $\tau_{ei} \approx 1-10$ ps ([Elsayed-Ali et al., 1987; Gamaly et al., 2002; Schoenlein et al., 1987] and references therein). Hence, for sub-picosecond pulses, the electronic and ionic distributions in the target are not in thermal equilibrium, and the behaviour of the electrons during the heating pulse must be considered to understand the process.

Two distinct intensity regimes can be identified for femtosecond interactions. The first is a low intensity regime (although, when considering femtosecond pulses, the use of 'low' is something of a misnomer), where the pulse peak intensity, I_{peak}, is $\lesssim 10^{13}$ W/cm^2. The other is a high intensity regime with $I_{peak} > 10^{13}$ W/cm^2. The high intensity regime is discussed briefly first as, for reasons that will be explained shortly, this regime is not of interest for fs-LIFT.

3.2.1 High Intensity Femtosecond Interactions

At laser intensities of $> 10^{13}$ W/cm^2, virtually any target material, whether metallic or dielectric, transparent or absorbing, is fully ionised by multi-photon absorption within ≈20 fs of the onset of irradiation [Gamaly et al., 2002]. Thus the behaviour of all target materials is qualitatively similar in this regime.

Free electrons (either from the conduction band in metallic targets or created by multi-photon ionisation in dielectrics) within the target skin depth, δ, absorb multiple photons via inverse Bremsstrahlung, becoming highly energetic. These electrons may either travel ballistically deeper into the target with a characteristic range, δ_b, or be photoelectrically emitted from the surface, as shown in fig. 3.1(a). The value of δ_b has been estimated by a number of authors to be approximately equal to the equilibrium mean free path of the electrons [Hohlfeld et al., 2000]. Electrons remaining in the target may then diffuse, driven by thermal gradients before cooling via Coulomb collisions.

It is believed that, at these intensities, the dominant ablation mechanism is electrostatic [Bulgakova et al., 2004; Gamaly et al., 2002; Stoian et al., 2002]. Following irradiation, the skin layer is positively charged and there is a cloud of electrons close to the surface that have been photoelectrically emitted (see fig. 3.1(b)). This results in a strong accelerating voltage that can pull ions out of the target [Gamaly et al., 2002]. Thermal

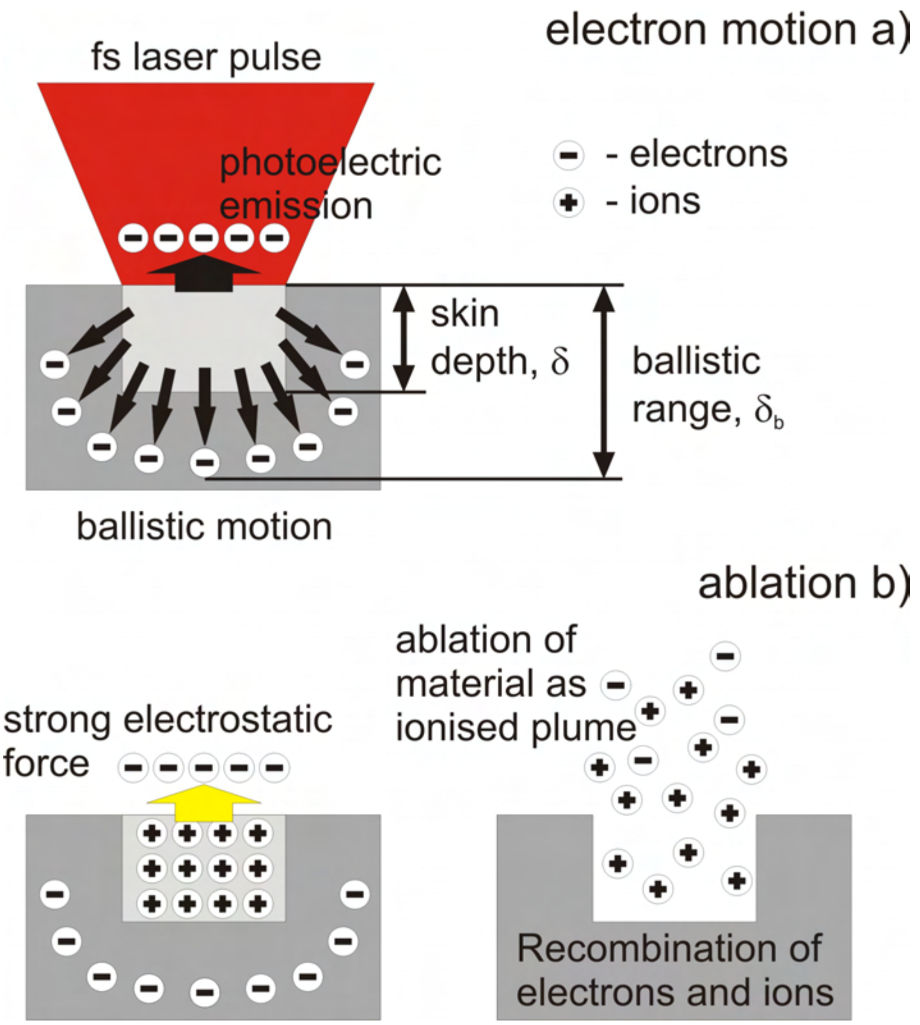

FIGURE 3.1: Electron behaviour (a) and electrostatic ablation process (b) following high intensity femtosecond irradiation.

effects in the target are minimised because most of the pulse energy is carried away by the photoelectrons and is never deposited as heat. This, in turn, allows for the excellent quality of ablated features usually observed with femtosecond pulses.

Despite the evident advantages of the high intensity femtosecond regime for materials processing, such high intensities cannot be used for fs-LIFT. This is because, as was discussed previously, all materials are ionised and absorb at these intensities. Hence, the carrier substrate would absorb most of the laser energy in this regime before it could reach the donor film. Whilst we could then, in principle, use ablated carrier as the propellant for LIFT (much like a DRL; see section 2.2.2), it is likely that the carrier would be a far from optimal DRL material (see chapter 5 for a discussion on DRL materials). Thus we are compelled to limit ourselves to the low intensity regime.

3.2.2 Low Intensity Femtosecond Interactions

For irradiation with femtosecond pulses possessing lower intensity, the probability for multi-photon ionisation occurring is much lower. Instead the dominant mechanism is impact or avalanche ionisation, where atoms are ionised by a collision with an energetic free electron. In a metallic target the initial free electrons are already present, but in a dielectric they must be created somehow by the laser. If the dielectric is absorbing, gradual ionisation by the absorption of a number of successive photons is possible, but if it is transparent we are reliant on absorption at defects, or the very small probability of multi-photon ionisation, to generate the initial electrons. Consequently, absorption of femtosecond pulses at these intensities in transparent media is low, and so such intensities can be used for fs-LIFT.

The ablation mechanism in this regime is not electrostatic as the photoelectrically emitted electrons do not possess sufficient extra energy to overcome the ionic binding energy, necessary to pull ions from the target surface. Instead, ablation for bulk targets is predominantly a thermal process as in the longer pulsed regime, although there are still some advantages to using the shorter pulses as will be described below. For thin film targets, the generation of strong shock waves, specifically reflection of these waves at film-substrate interfaces, due to the extremely rapid absorption of the laser pulse energy is believed to play a role in the ablation process also [Hare et al., 1995; Zergioti et al., 2005b].

The temperature of the target in the low intensity regime is well described by the two-temperature model (TTM) [Chowdhury and Xu, 2003]. In the TTM, the electronic and ionic temperature profiles, $T_e(x,y,z,t)$ and $T_i(x,y,z,t)$ respectively, are considered as two separate thermally diffusive systems which are somehow coupled to each other. It is conventional to assume linear coupling of the two systems, so that the diffusion equations are of the form [Chowdhury and Xu, 2003]

$$\textbf{Electrons}: \quad c_e\big(T_e(x,y,z,t)\big)\frac{\partial T_e(x,y,z,t)}{\partial t} = \nabla\Big(\kappa_e(x,y,z,t)\big(\nabla T_e(x,y,z,t)\big)\Big) \\ -G\Big(T_e(x,y,z,t)-T_i(x,y,z,t)\Big)+S_{laser},$$

$$\textbf{Ions}: \quad \rho_i c_i\big(T_i(x,y,z,t)\big)\frac{\partial T_i(x,y,z,t)}{\partial t} = \nabla\Big(\kappa_i(x,y,z,t)\big(\nabla T_i(x,y,z,t)\big)\Big) \\ +G\Big(T_e(x,y,z,t)-T_i(x,y,z,t)\Big)$$

where c_e and c_i are the electron and ion specific heats (in J/m^{3}K and J/kgK, respectively), κ_e and κ_i are the thermal conductivities (in W/mK), and G is the electron-ion coupling coefficient (in W/m^{3}K). The first equation describes the electron temperature profile and the second describes the ion temperature profile. The left hand-side and

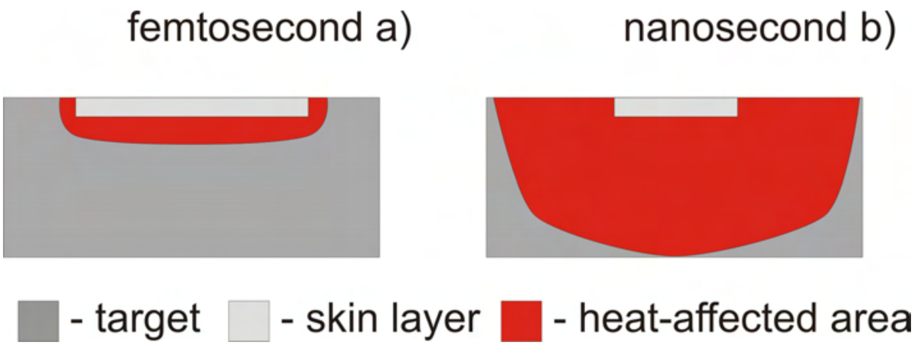

FIGURE 3.2: Illustrative comparison of the heat affected volume in identical targets irradiated by femtosecond (a) and nanosecond duration (b) pulses.

first term on the right hand-side of both equations describe energy flow due to thermal diffusion. The second term on the right is the coupling term between the two systems. The laser heating of the electrons is accounted for by the heat source term, S_{laser} in the first equation, which can be written as [Chowdhury and Xu, 2003]

$$S_{laser} = \frac{0.94(1-r)J}{\delta_b t_p \Big(1 - exp\big(-\frac{d}{\delta+\delta_b}\big)\Big)} exp\Big(-\Big(\frac{z}{\delta}\Big) - ln2\Big(\frac{t}{t_p}\Big)^2\Big)$$

where r is the target amplitude reflection coefficient, J is the laser fluence in J/m^2, t_p is the FWHM pulse duration, d is the thickness of the target material, and z is the depth into the target (assuming $z = 0$ at the illuminated surface).

The electron diffusion length is relatively small as τ_{ei} is very short. Hence, in the femtosecond regime, when electron-ion coupling occurs, the laser energy is approximately confined to the ballistic range (typically ≤ 150 nm [Hohlfeld et al., 2000]). In the longer pulsed regime, the pulse duration is long enough that significant thermal diffusion can occur during the pulse. The diffusion length during the pulse, l_d, can be estimated from [Papakonstantinou et al., 1999]

$$l_d = \frac{1}{2}\sqrt{\pi D t_p}$$

where D is the diffusion coefficient. Taking Cr as an example ($D = 28.3 \times 10^{-6}$ [Papakonstantinou et al., 1999]), for a 10 ns pulse, $l_d \approx 0.5$ μm. Hence, energy has already diffused significantly more at the end of the laser pulse in this regime than in the femtosecond regime. Figure 3.2 illustrates the relative difference in heated volumes in targets irradiated by femtosecond (a) and nanosecond (b) duration pulses.

After the end of the pulse and electron-ion recombination, thermal diffusion in the target is the dominant process in both pulse duration regimes. However, because of the much larger heated volume, greater pulse energies are required to initiate the same phase changes with longer pulses. The higher pulse energies result in an overall larger heated area and more violent heating process, giving rise to the crack formation and collateral damage typically seen with long-pulsed ablation. Conversely, femtosecond duration pulses require only relatively low pulse energies to vaporise and ablate the skin layer. Hence, the process is less violent and the heat affected area smaller, even though the ablation process is also thermal in nature. A number of results in the literature suggest a detectable heated zone with nanosecond duration lasers to extend 10's of μm beyond the irradiated area. With femtosecond pulses, this spread has been consistently found to be $\leq 2\ \mu$m (see, for example [Chichkov et al., 1996; Harzic et al., 2002; Hirayama and Obara, 2005] amongst many others).

3.3 The Potential Benefits of Using Femtosecond Pulses for LIFT

The three main objectives for LIFT are;

1. deposition of the smallest possible structures,
2. transfer of material intact, and
3. transfer of material in solid phase.

We will now consider each of these objectives separately and discuss how using fs-LIFT may offer advantages over ns-LIFT for each.

3.3.1 fs-LIFT for the Smallest Structures

The smallest structures deposited by LIFT to date involve the transfer of single droplets of molten donor with fluence approximately equal to the material transfer threshold. The growth process of these droplets will be discussed in more detail in chapter 4, but briefly they are believed to be the result of hydrodynamic flow when the donor film is just melted through [Willis and Grosu, 2005]. The droplets can be sub-micron in diameter with the smallest feature sizes reported to date around 500-700 nm for ns-LIFT [Narazaki et al., 2008] and 300 nm for fs-LIFT ([Banks et al., 2006] and chapter 4).

The fact that smaller droplets are obtainable with fs-LIFT should be no surprise. The smaller heat affected area (and, hence, melted region) with femtosecond pulses has already been discussed, with obvious implications for smaller droplets (see fig. 3.3(a)). Also, the lower pulse energies required for fs-LIFT (200-500 mJ/cm^2 [Banks et al., 2006;

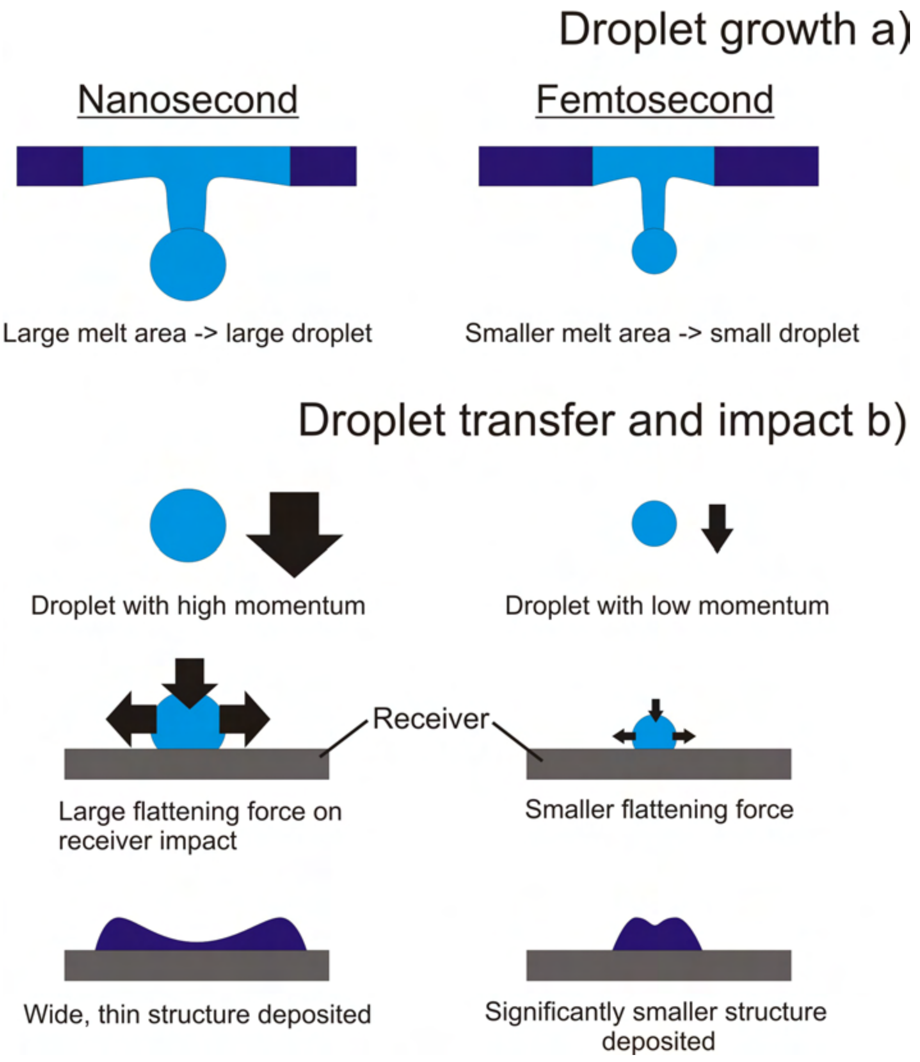

FIGURE 3.3: Schematic of the droplet transfer process with nanosecond (left) and femtosecond (right) pulses. Differences in droplet size (a) and the droplet momentum (b) imply femtosecond pulses should yield smaller droplets.

Bera et al., 2007] c.f. several J/cm^2 for ns-LIFT [Narazaki et al., 2008; Willis and Grosu, 2005]) and hence, less violent process, suggest that the droplet transfer and impact on the receiver should be 'gentler' with fs-LIFT. As the droplets are transferred in liquid phase, they typically flatten somewhat upon impact at the receiver, with a resulting increase in diameter. Lower momentum impact arising from a gentler transfer can be expected to lead to less flattening and hence smaller deposited features (as shown in fig. 3.3(b)).

Given the apparent advantages of fs-LIFT over ns-LIFT it is perhaps reasonable to wonder why, so far, the smallest fs-LIFT droplets are only about half the size of those with ns-LIFT. Seifert et al have studied a similar droplet growth process in the free surface ablation of targets and suggested there exists a material-dependent minimum size for these droplets [Seifert and Betz, 1998; Seifert et al., 1996]. They predicted a theoretical minimum diameter around 200 nm for Au, in pretty good agreement with the smallest features reported with fs-LIFT of ≈ 300 nm for Cr, allowing for flattening upon receiver impact ([Banks et al., 2006] and chapter 4). Hence, it appears that fs-LIFT offers some, but not dramatic, potential for reducing the achievable structure size. Our results on using fs-LIFT for depositing nanoscale droplets have been reported in [Banks et al., 2006] and are described in more detail in the next chapter.

3.3.2 fs-LIFT for Intact Transfer

The transfer of intact material is, arguably, the most important objective for LIFT (and indeed any microfabrication technique). After all, it is pointless being able to deposit micron-scale structures of functional materials if the deposition process destroys or alters the behaviour of the material. Many materials can withstand the high temperatures and violent nature of the ns-LIFT process. However, for materials sensitive to photolytic or thermolytic damage, the ns-LIFT process tends to lead to modification or destruction of the donor during transfer. This is why complementary techniques such as MAPLE-DW and DRL-LIFT were developed, to allow for the deposition of sensitive materials.

Photolytic damage of the donor is, for obvious reasons, confined to the skin layer of the film. Thermolytic damage can occur wherever the donor is significantly heated. As has been discussed previously, the heated volume with nanosecond pulses extends 10's of μm beyond the skin layer, whilst with femtosecond pulses, the detectable heated range is only $\lesssim 2\ \mu$m. It stands to reason therefore, that if the donor thickness is also on the order of a few microns, then a significant portion might not be significantly heated during the fs-LIFT process. Hence, it is not unreasonable to expect that fs-LIFT may be capable of intact transfer without having to use any sacrificial materials, as indicated in fig. 3.4.

The intact transfer of viable biomaterial using fs-LIFT with an 800 nm thick donor film has already been demonstrated by Zergioti et al. [Karaiskou et al., 2003; Zergioti et al., 2005a]. With ns-LIFT, some form of protective matrix or DRL has always been necessary for transfer of sensitive donors (see e.g. [Kim et al., 2004; Pique et al., 1999; Ringeisen et al., 2002; Serra et al., 2004; Wartena et al., 2004]). Zergioti et al. [Zergioti et al., 2005b] also observed, using schlieren imaging, the behaviour of shock waves in thin films after nanosecond and femtosecond duration irradiation through a carrier. In the femtosecond regime, the shock wave could be seen in their results as an almost planar structure propagating in air after traveling through the film. In contrast, the shock wave in the nanosecond regime was observed to be almost hemispherical. These

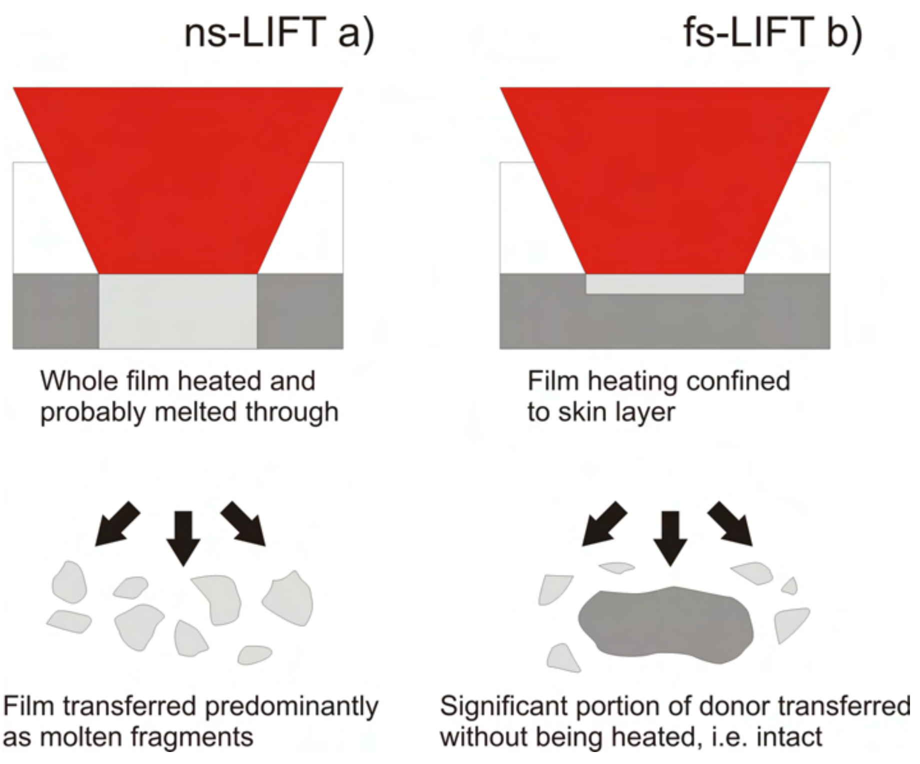

FIGURE 3.4: Schematic of the transfer process in ns-LIFT (a) and fs-LIFT (b), showing the envisaged potential benefits of fs-LIFT for intact transfer.

results suggested that removal of donor material from the carrier in the femtosecond regime appeared to be, at least in part, driven by shock wave effects, whilst with longer pulses, film removal was by conventional thermal ablation. Similar results have been reported by the group for metallic [Zergioti et al., 2003] and oxide donors [Papazoglou et al., 2002].

3.3.3 fs-LIFT for Solid Transfer

The transfer of donor material in single, solid segments (or *pellets*) is an area that has received very little attention in the literature. The only notable results to date that did not require a DRL (besides our own reported in [Banks et al., 2008] and chapter 7) are those of Kantor et al. [Kantor and Szorenyi, 1995; Kantor et al., 1994a,b], where W pellets were transferred using LP-LIFT. However, due to the nature of the technique (see section 2.2.5), these results relied on significant heating of the donor to anneal it to the receiver and so LP-LIFT would not be applicable for the deposition of heat sensitive donors.

Solid-phase transfer alone does not have many obvious applications, save perhaps for non-porous metallic structures for electrical connections or the forward transfer of donors

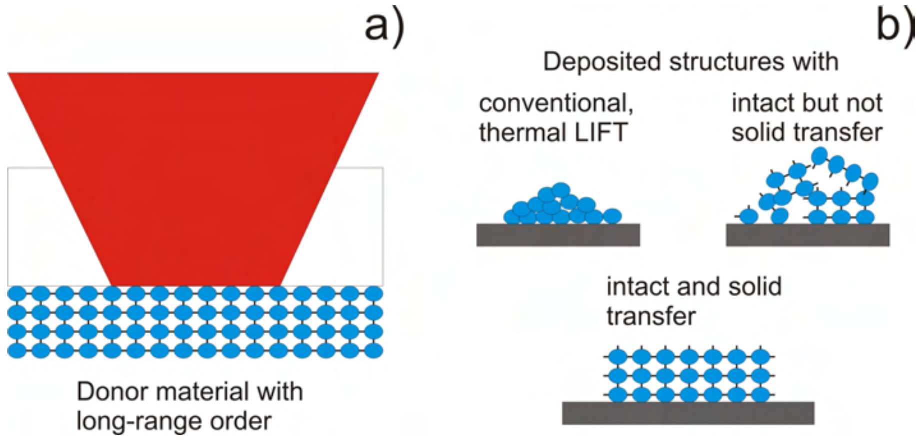

FIGURE 3.5: Schematic of LIFT of complex materials (a) and the deposited structures with conventional (thermally-driven) LIFT, intact transfer, and, the ultimate goal, solid and intact transfer (b).

with pre-existing structures written into them. However, if solid and intact transfer could be combined, without requiring a DRL material, this would represent a powerful new capability for forward transfer techniques. Consider, for example, the LIFT of single crystal, single domain, or oriented donors (fig. 3.5(a)). Many such materials cannot be grown onto commonly used DRL materials (e.g. polymers), but if they are to be LIFTed, then this must be done with the donor remaining intact AND in a single, solid-phase pellet to maintain the long-range order of the original film (fig. 3.5(b)).

Such transfer is clearly a challenge. However, it is known that fs-LIFT is capable of intact transfer with the correct choice of experimental parameters. Hence, 'all' that remains is to achieve solid-phase transfer simultaneously. Here we may be able to utilise the reduced heated volume and shock-induced transfer available with fs-LIFT. Chapter 7 presents the results of experiments attempting to use fs-LIFT for solid transfer of donor films using Cr as an example material.

Bibliography

Banks, D., Grivas, C., Mills, J., Zergioti, I., and Eason, R. (2006). Nanodroplets deposited in microarrays by femtosecond ti:sapphire laser induced forward transfer. *Appl. Phys. Lett.*, 89:193107.

Banks, D., Grivas, C., Zergioti, I., and Eason, R. (2008). Ballistic laser-assisted solid transfer (blast) from a thin film precursor. *Opt. Express*, 16:3249–3254.

Bera, S., Sabbah, A., Yarbrough, J., Allen, C., Winters, B., Durfee, C., and Squier, J. (2007). Optimization study of the femtosecond laser-induced forward-transfer process with thin aluminium films. *Appl. Opt.*, 46(21):4650–4659.

Bulgakova, N., Stoian, R., Rosenfeld, A., Hertel, I., and Campbell, E. (2004). Electronic transport and consequences for material removal in ultrafast pulsed laser ablation of materials. *Phys. Rev. B*, 69:054102.

Chichkov, B. N., Momma, C., Nolte1, S., Alvensleben, F., and Tunnermann, A. (1996). Femtosecond, picosecond and nanosecond laser ablation of solids. *Appl. Phys. A*, 63(2):109–115.

Chowdhury, I. and Xu, X. (2003). Heat transfer in femtosecond laser processing of metal. *Numer. Heat Tr. A-Appl.*, 44:219–232.

Dausinger, F., Lichtner, F., and Lubatschowski, H. (2004). *Femtosecond Technology for Technical and Medical Applications*. Springer, New York, USA.

Elsayed-Ali, H., Norris, T., Pessot, M., and Mourou, G. (1987). Time-resolved observation of electron-phonon relaxation in copper. *Phys. Rev. Lett.*, 58(12):1212–1215.

Gamaly, E., Rode, A., Luther-Davies, B., and Tikhonchuk, V. (2002). Ablation of solids by femtosecond lasers: Ablation mechanism and ablation thresholds for metals and dielectrics. *Phys. Plamsmas*, 9(3):949–957.

Hare, D., Franken, J., and Dlott, D. (1995). Coherent raman measurements of polymer thin-film pressure and temperature during picosecond laser ablation. *J. Appl. Phys.*, 77(11):5950–5960.

Harzic, R. L., Huot, N., Audoaurd, E., Jonin, C., Laporte, P., Valette, S., Fraczkiewicza, A., and Fortunier, R. (2002). Comparison of heat-affected zones due to nanosecond and femtosecond laser pulses using transmission electronic microscopy. *Appl. Phys. Letts*, 80(21):3886–3888.

Hirayama, Y. and Obara, M. (2005). Heat-affected zone and ablation rate of copper ablated with femtosecond laser. *J. Appl. Phys.*, 97:064903.

Hohlfeld, J., Wellershoff, S.-S., Gudde, J., Conrad, U., Jahnke, V., and Matthias, E. (2000). Electron and lattice dynamics following optical excitation of metals. *Chem. Phys.*, 251:237–258.

Kantor, Z. and Szorenyi, T. (1995). Dynamics of long-pulse laser transfer of micrometer-sized metal patterns as followed by time-resolved measurements of reflectivity and transmittance. *J. Appl. Phys.*, 78(4):2775–2781.

Kantor, Z., Toth, Z., and Szorenyi, T. (1994a). Metal pattern deposition by laser-induced forward transfer. *Appl. Surf. Sci.*, 86:196–201.

Kantor, Z., Toth, Z., Szorenyi, T., and Toth, A. (1994b). Deposition of micrometer-sized tungsten patterns by laser transfer technique. *Appl. Phys. Lett.*, 64(25):3506–3508.

Karaiskou, A., Zergioti, I., Fotakis, C., Kapsetaki, M., and Kafetzopoulos, D. (2003). Microfabrication of biomaterials by the sub-ps laser-induced forward transfer process. *Appl. Surf. Sci.*, 208-209:245–249.

Kim, H., Kushto, G., Arnold, C., Kafafi, Z., and Pique, A. (2004). Laser processing of nanocrystalline tio$_2$ films for dye-sensitized solar cells. *Appl. Phys. Lett.*, 85(3):464–466.

Misawa, H. and Juodkazis, S. (2006). *3D Laser Microfabrication, Principles and Applications*. Wiley-VCH, Weinheim, Germany.

Narazaki, A., Sato, T., Kurosaki, R., Kawaguchi, Y., and Niino, H. (2008). Nano- and microdot array formation of fesi$_2$ by nanosecond excimer laser-induced forward transfer. *Appl. Phys. Exp.*, 1:057001.

Papakonstantinou, P., Vainos, N., and Fotakis, C. (1999). Microfabrication by uv femtosecond laser ablation of pt, cr and indium oxide thin films. *Appl. Surf. Sci.*, 151:159–170.

Papazoglou, D., Karaiskou, A., Zergioti, I., and Fotakis, C. (2002). Shadowgraphic imaging of the sub-ps laser-induced forward transfer process. *Appl. Phys. Lett.*, 81(9):1594–1596.

Pique, A., Chrisey, D., Auyeung, R., Fitz-Gerald, J., Wu, H., McGill, R., Lakeou, S., Wu, P., Nguyen, V., and Duignan, M. (1999). A novel laser transfer process for direct writing of electronic and sensor materials. *Appl. Phys. A [Suppl.]*, 69:S279–S284.

Ringeisen, B., Chrisey, D., Pique, A., Young, H., Modi, R., Bucaro, M., Jones-Meehan, J., and Spargo, B. (2002). Generation of mesoscopic patterns of viable escherichia coli by ambient laser transfer. *Biomaterials*, 23:161–166.

Schoenlein, R., Lin, W., Fujimoto, J., and Eesley, G. (1987). Femtosecond studies of nonequilibrium electronic processes in metals. *Phys. Rev. Lett.*, 58(16):1680–1683.

Seifert, N. and Betz, G. (1998). Computer simulations of laser-induced ejection of droplets. *Appl. Surf. Sci.*, 133:189194.

Seifert, N., Betz, G., and Husinsky, W. (1996). Droplet formation on metallic surfaces during low-fluence laser irradiation. *Appl. Surf. Sci.*, 103:63–70.

Serra, P., Colina, M., Fernandez-Pradas, J., Sevilla, L., and Morenza, J. (2004). Preparation of functional dna microarrays through laser-induced forward transfer. *Appl. Phys. A*, 85(9):1639–1641.

Stoian, R., Rosenfeld, A., Ashkenasi, D., Hertel, I., Bulgakova, N., and Campbell, E. (2002). Surface charging and impulsive ion ejection during ultrashort pulsed laser ablation. *Phys. Rev. Lett.*, 88(9):097603.

Wartena, R., Curtright, A., Arnold, C., Pique, A., and Swider-Lyons, K. (2004). Li-ion microbatteries generated by a laser direct-write method. *J. Power Sources*, 126:193–202.

Willis, D. and Grosu, V. (2005). Microdroplet deposition by laser-induced forward transfer. *Appl. Phys. Lett.*, 86:244103.

Zergioti, I., Karaiskou, A., Papazoglou, D., Fotakis, C., Kapsetaki, M., and Kafetzopoulos, D. (2005a). Femtosecond laser microprinting of biomaterials. *Appl. Phys. Lett.*, 86:163902.

Zergioti, I., Karaiskou, A., Papazoglou, D., Fotakis, C., Kapsetaki, M., and Kafetzopoulos, D. (2005b). Time resolved schlieren study of sub-pecosecond and nanosecond laser transfer of biomaterials. *Appl. Surf. Sci.*, 247:584589.

Zergioti, I., Papazoglou, D., Karaiskou, A., Fotakis, C., Gamaly, E., and Rode, A. (2003). A comparative schlieren imaging study between ns and sub-ps laser forward transfer of cr. *Appl. Surf. Sci.*, 208-209:177–180.

Chapter 4

Femtosecond LIFT of Tiny Structures: Nanodroplets and Microarrays

4.1 Introduction

LIFT is, first and foremost, a microfabrication technology. Hence, the most obvious question to be asked is "what are the smallest features that can be produced"? Early LIFT studies found that there was a well-defined fluence threshold for forward transfer and that, below this threshold no donor was transferred. Around the threshold, transfer was patchy and incomplete across the irradiated region with the deposited material consisting of a number of independent structures that appeared to have been transferred in the form of liquid droplets. The optimal fluence, in terms of uniformity of deposited material across the irradiated area, was found to be slightly above this transfer threshold. Further increasing the fluence resulted in an increase in the deposited feature size to greater than the laser spot size [Bohandy et al., 1986].

Later, work concerned with depositing the smallest possible features, concentrated on using tightly focused lasers and fluence around the transfer threshold to try and deposit a single liquid droplet per laser pulse. A number of groups have had success in this area with nanosecond [Narazaki et al., 2008; Willis and Grosu, 2005] and femtosecond lasers [Bera et al., 2007; Papakonstantinou et al., 1999; Yang et al., 2006]. The smallest reported deposited droplet sizes in the literature in both pulse duration regimes are around 0.5 μm [Narazaki et al., 2008; Papakonstantinou et al., 1999]. Such droplets have become known as *nanodroplets* and can be an order of magnitude smaller than the patterning laser spot size.

In this chapter, we begin with a discussion of the current understanding of the processes of nanodroplet growth and transfer in section 4.2. Next, in section 4.3, the experimental setup used for all the forward transfer experiments in this thesis is described. The results of our nanodroplet studies, including the smallest droplets reported to date, are presented in section 4.4. Finally, the results of attempts to produce large area microarrays of nanodroplets complete the chapter in section 4.5.

4.2 Nanodroplet Growth and Transfer

The ejection of liquid droplets from targets irradiated by low fluence lasers is a well-known phenomenon in both standard ablation (i.e. target material directly exposed to a laser) and forward transfer geometries. The process for conventional ablation with nanosecond duration laser pulses has been studied theoretically by Seifert et al. [Seifert and Betz, 1998; Seifert et al., 1996]. In their work it was found that droplet growth from the surface appeared to be a hydrodynamic effect dependent on the surface tension and inertial forces acting on the molten region. Their theory predicted that the smallest droplet size was limited by the surface tension of the material in the molten state (for the case of Au, a minimum diameter of ≈ 200 nm was given), and that droplets would only form for surface tensions between $\approx 0.2 - 5$ Nm^{-1}. They also demonstrated that multiple laser shots were required to release a droplet from the surface; for their studies 8-10 shots were required. A schematic of droplet ejection based on the results of Seifert et al. is shown in fig. 4.1.

Clearly, therefore, the droplet-ejection process in a forward transfer geometry is different from that encountered in conventional ablation. The obvious difference is that droplet formation and ejection occurs with only 1 laser pulse. The process for forward transfer geometries is only partially understood. Willis and Grosu have suggested that, when Gaussian intensity distributions are used, the melt front in the donor film may only reach the free surface in the centre of the irradiated region, thus explaining the sub-spot size droplets [Willis and Grosu, 2005, 2007]. However, the fact that droplets are also obtained with close to top-hat beam profiles suggests that this is not the explanation (see e.g. [Narazaki et al., 2008; Papakonstantinou et al., 1999] and section 4.4).

Willis and Grosu [Willis and Grosu, 2005] and Narazaki et al. [Narazaki et al., 2008] have also observed, for fluence just below the transfer threshold in each case, the appearance of domed structures in the donor film. These domed structures have been attributed by Narazaki et al. to be the result of a small amount of vaporisation of the donor at the donor-carrier interface, providing a pressure away from the carrier. In Willis and Grosu's work, the domed structure exhibited a further feature: a sharp protrusion in

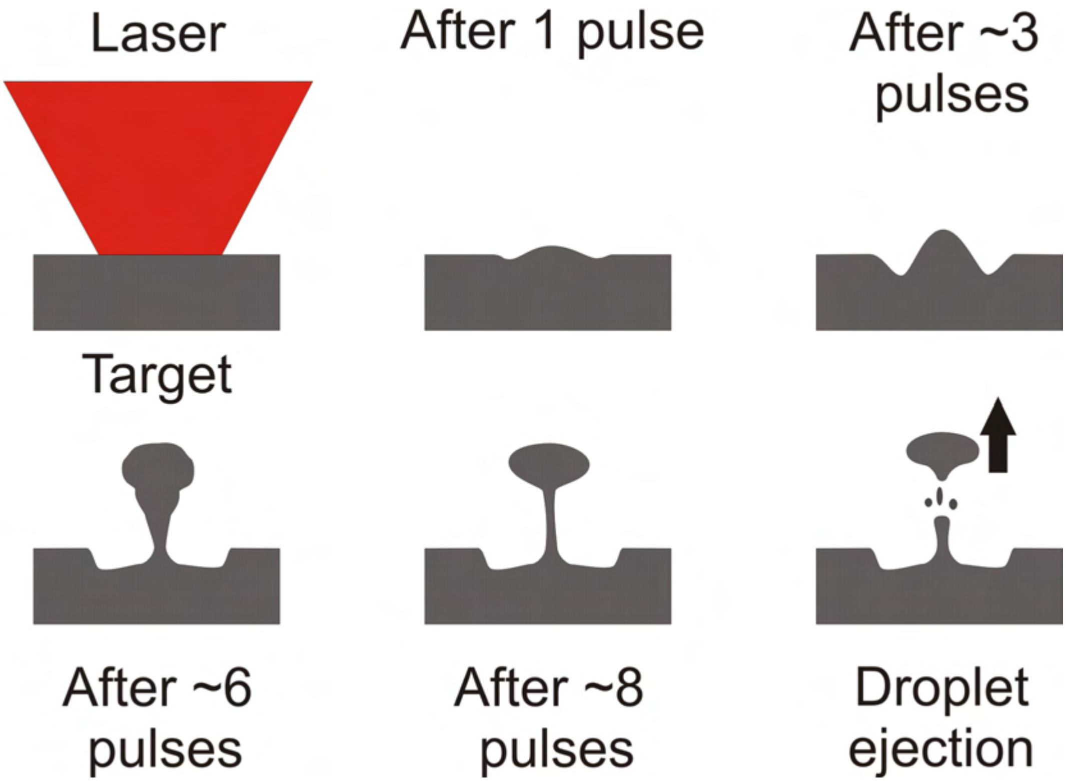

FIGURE 4.1: Diagrammatic representation of how droplets grow on the surface of a target material exposed to multiple, low fluence nanosecond laser pulses (based on [Seifert and Betz, 1998]).

the centre topped by a relatively large droplet. The obtained features closely resembled the structures obtained theoretically by Seifert et al. prior to droplet ejection from a free surface [Seifert and Betz, 1998].

Figure 4.2 shows the envisaged transfer process based on the experimental and theoretical observations described previously. Absorption of laser energy in the donor causes it to partially melt through (a). It is possible that a small amount of vaporisation occurs at the carrier-donor interface, causing a bulge to form in the film (b). This process may occur when the film is only partially melted through, resulting in a solidified bulge after irradiation (c). If the film is completely melted in the irradiated region (d), hydrodynamic flow drives the formation of a free-standing structure topped by a droplet (e), which can be transferred to the receiver (f). It is most likely that the small amount of evaporation at the carrier-donor interface drives the production of nanodroplets with a single pulse in a forward transfer setup. In direct ablation, any evaporation is at the free surface so would not be expected to significantly affect droplet growth.

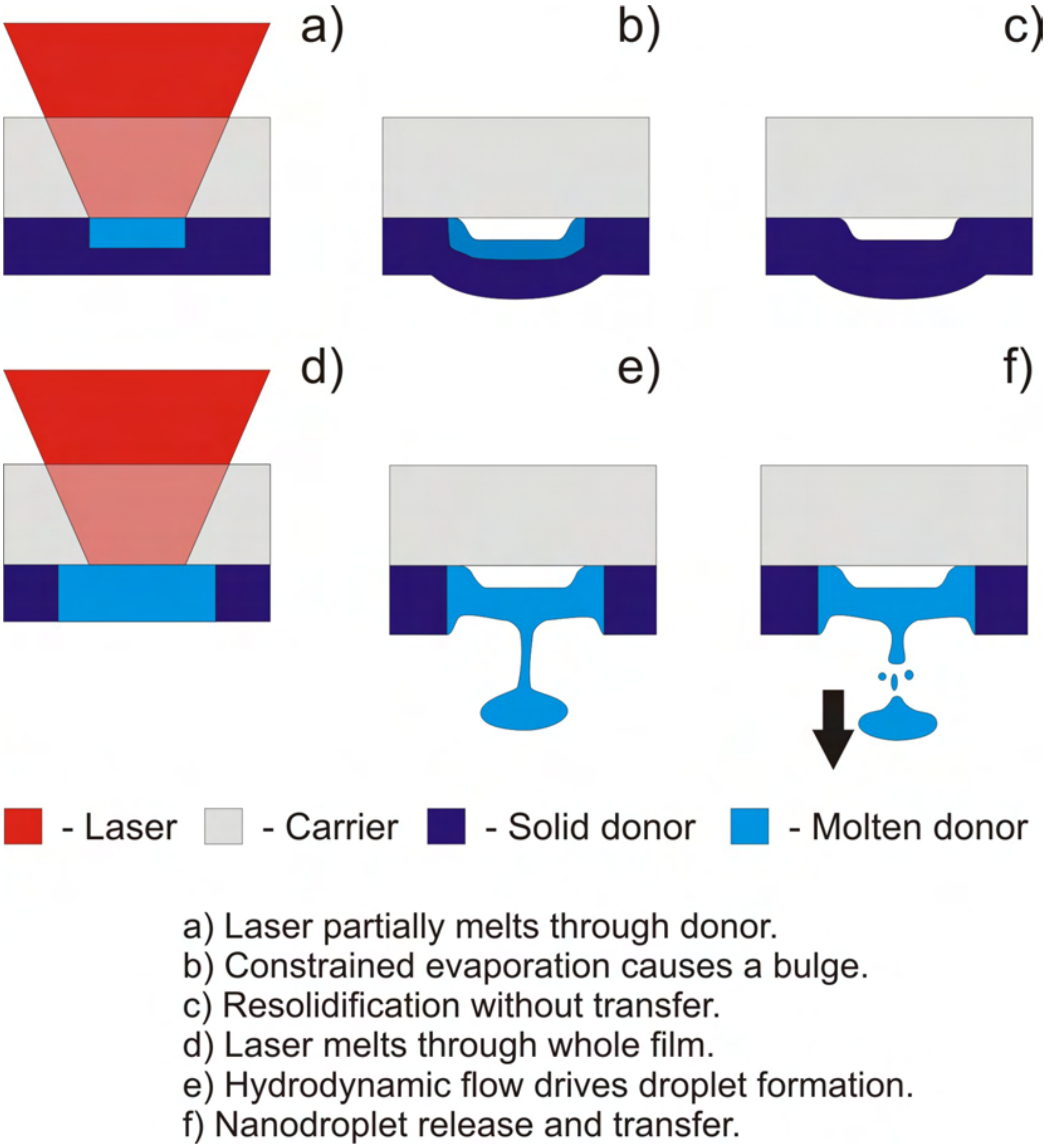

a) Laser partially melts through donor.
b) Constrained evaporation causes a bulge.
c) Resolidification without transfer.
d) Laser melts through whole film.
e) Hydrodynamic flow drives droplet formation.
f) Nanodroplet release and transfer.

FIGURE 4.2: Diagrammatic representation of nanodroplet growth and transfer in a forward transfer setup.

4.3 Experimental LIFT Setup

In this section, the experimental setup used in these, and all subsequent LIFT experiments is presented. The setup consisted of three parts, a femtosecond Ti:sapphire laser, described in section 4.3.1, a commercial micromachining workstation (section 4.3.2), and a vacuum chamber, detailed in section 4.3.3. The elements specific to the nanodroplet experiments are covered last in section 4.3.4.

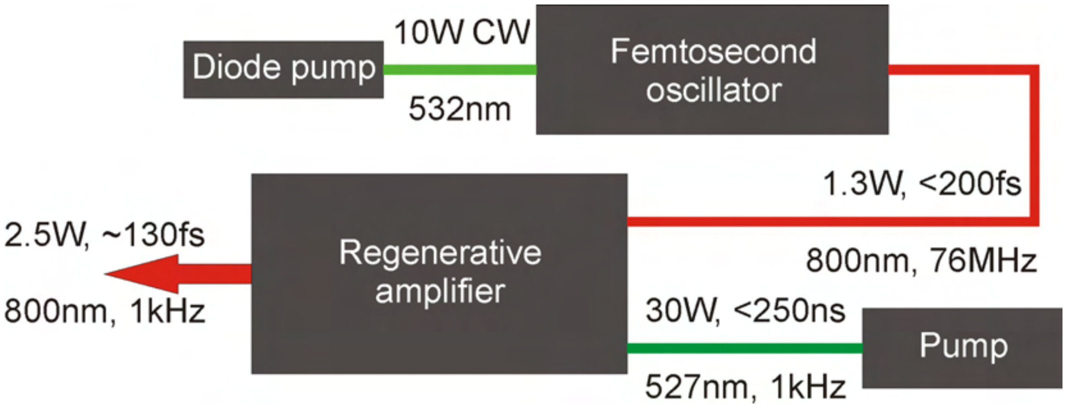

FIGURE 4.3: Sketch of the layout of the main components and laser properties in the femtosecond system.

4.3.1 Femtosecond Laser System

The laser used for forward transfer experiments was a commercial Ti:sapphire femtosecond system based around an oscillator and regenerative amplifier. A schematic of the system is shown in fig. 4.3. The Ti:sapphire oscillator (Coherent MIRA 900) was pumped by a diode laser (Coherent Verdi V10) providing 10W of CW light at 532 nm. The oscillator, shown in fig. 4.4, was passively mode-locked by Kerr lensing in the laser medium, producing 800 nm (700-980 nm tunable), ≈ 11 nm bandwidth, sub-200 fs, nJ energy pulses at 76 MHz with an average power of 1.3W.

60% of the oscillator output was used as the seed for a high power regenerative amplifier (Coherent Legend-F), shown in fig. 4.5; the other 40% was used as the seed for a high repetition rate amplifier not used for forward transfer experiments. Seed pulses into the amplifier were initially stretched to picosecond duration in a 4-pass stretcher. The

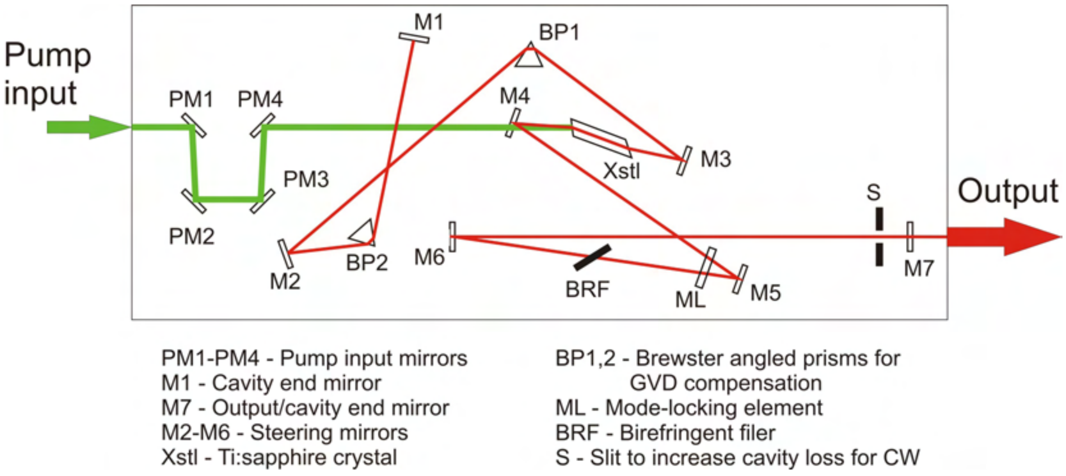

FIGURE 4.4: Schematic of the Coherent MIRA 900 oscillator.

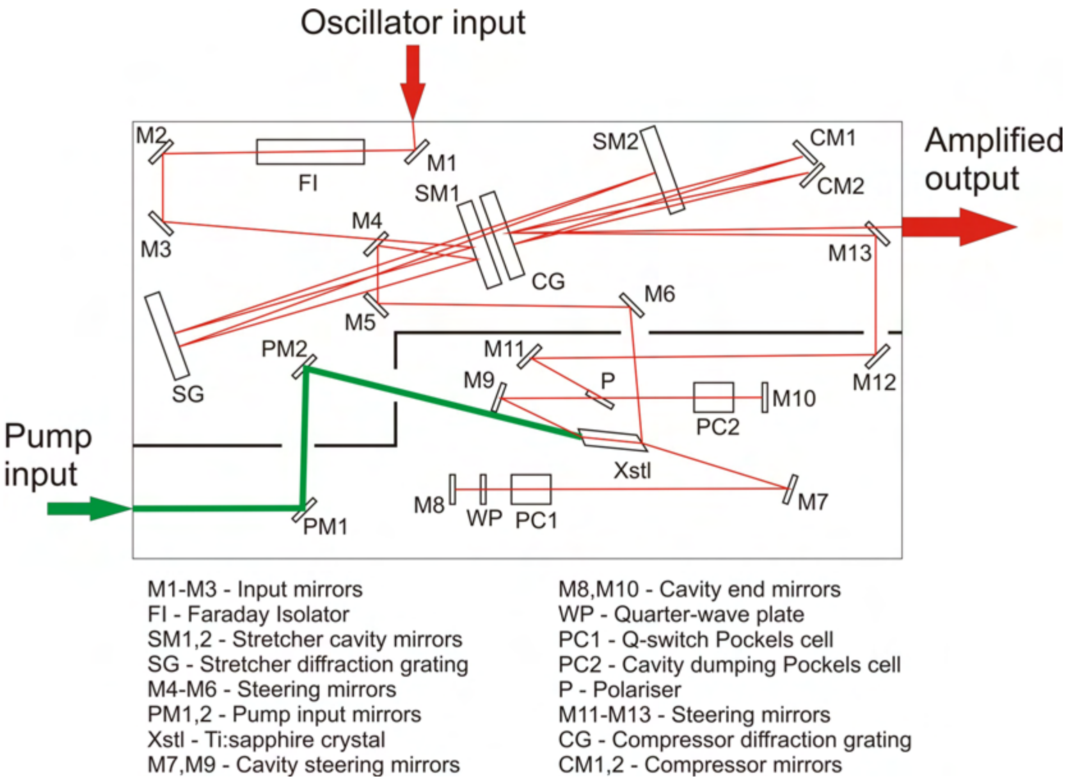

FIGURE 4.5: Schematic of the Coherent Legend-F regenerative amplifier.

amplification cavity consisted of 2 high-speed Pockels cells, a quarter-wave plate, a polariser, and a Ti:sapphire amplification medium. The Ti:sapphire crystal was pumped by a green (527 nm) Q-switched, diode-pumped laser (Coherent Evolution-30) delivering sub-250 ns pulses at 1 kHz with 30W of average power. The injection of a single seed pulse from the oscillator train into the amplification cavity was synchronised with a pulse from the pump laser to ensure maximum amplification efficiency.

The amplification cavity design (fig. 4.6(a)) was akin to that of Pax and Weston [Pax and Weston, 1991] with the one difference that the current amplifier lacked an input polariser because the oscillator output was already polarised. Q-switching of the amplifier was performed as shown in fig. 4.6(b-d). With both Pockels cells off (b), the input polarisation of the oscillator seed pulses was rotated 90° by the first double pass through the wave plate, thus passing through the output polariser. Following the second double pass through the wave plate, the polarisation reverted to the initial state and was reflected out of the cavity off the polariser. To trap pulses in the cavity (c), the input/Q-switch Pockels cell was turned on (to its quarter wave voltage) immediately **after** the first double pass of a seed pulse through the cell. When in the 'on' state, the double pass through the input Pockels cell canceled out the effect of the wave plate, and allowed the pulse to pass through the polariser on every cavity round trip. The seed pulse was thus amplified by multiple passes through the Ti:sapphire crystal. To output

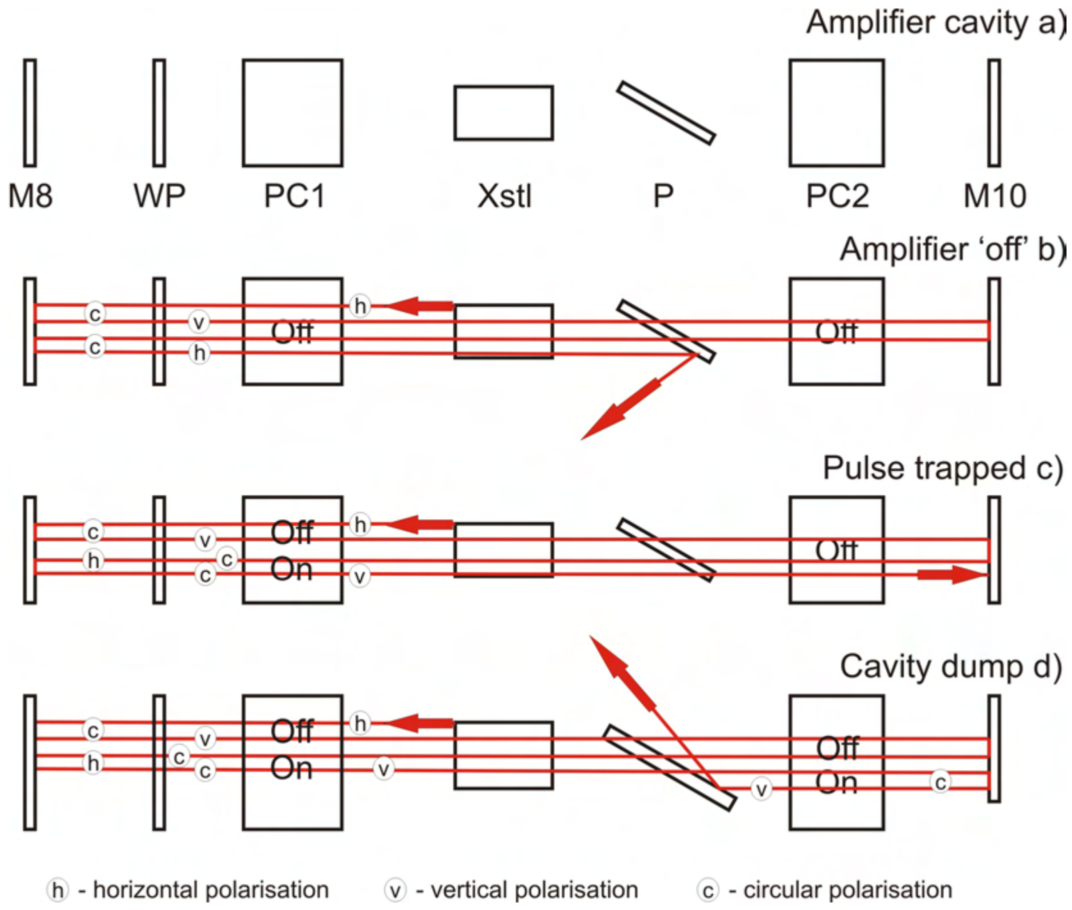

FIGURE 4.6: Principle of operation of the Pockels cells/quarter-wave plate/polariser q-switch used in the regenerative amplifier. (a) amplification cavity components; (b) cavity in 'off' state, i.e. no amplification; (c) trapping an oscillator pulse in the cavity; (d) cavity dumping the amplified pulse.

the amplified pulse (d), the output/cavity dumper Pockels cell was turned on (again, to its quarter wave voltage) when the gain in the Ti:sapphire saturated. The effect of this was to induce a further 90° rotation of the polarisation so that the pulse was reflected out of the cavity the next time it encountered the polariser.

The final step in the amplification process was to recompress the pulse to femtosecond duration. This was accomplished using a 4-pass compressor, resulting in $\approx$ 130 fs pulses. The repetition rate of the regenerative amplifier was adjustable up to 1 kHz, with an average power of 2.5 W at 800 nm. The FWHM diameter of the Gaussian output beam was $\approx$ 10 mm.

4.3.2 Micromachiner

To relay the laser to the LIFT setup, a commercial micromachining workstation (New Wave UP-266) was used (fig. 4.7). The incident laser pulses illuminated an aperture

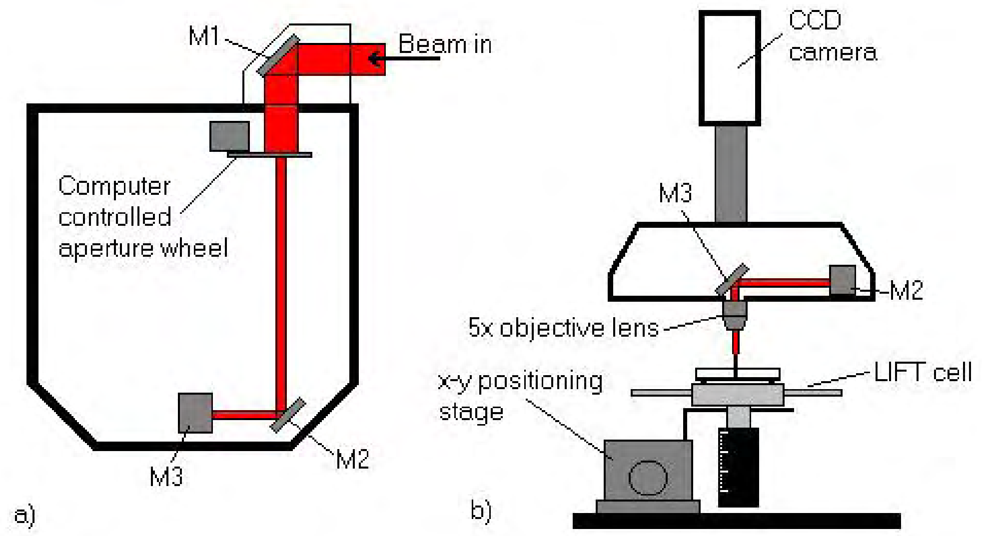

FIGURE 4.7: Layout diagram of the New Wave UP-266 micromachiner used for LIFT experiments.

wheel with a range of possible apertures from ≈ 120 μm to ≥ 2 mm diameter. The micromachiner contained an intermediate lens of focal length ≈ 400 mm and an objective lens. 3 objective lenses were available for use in the micromachiner: a 5x with $\approx 35-40$ mm working distance (WD), a 50x (Nikon LU PLAN ELWD) with 10.1 mm WD and 0.55 numerical aperture (NA), and a 100x (Nikon LU PLAN ELWD) with 3.5 mm WD and NA 0.8.

The micromachiner also featured 3-axis, computer controlled translation stages capable of 1 μm resolution with a maximum scan speed of ≈ 2 mm/s. The vacuum chamber used for forward transfer experiments was mounted on these stages and is described in the next section. A white light source and CCD camera were also included to allow for real-time observations of the workpiece. The best image plane of the CCD could be adjusted by means of a lens to coincide with the best image of the laser. Hence, by adjusting the position of the LIFT apparatus such that the carrier-donor interface was well-imaged on the CCD, then it was known that the laser was also well imaged on the interface.

4.3.3 Forward Transfer Vacuum Chamber

A schematic of the forward transfer vacuum chamber is shown in fig. 4.8. Two valves allowed pumping and venting of the chamber. A sample holder on the end of a linear vacuum feedthrough (MDC miniature series) was used to mount the receiver substrates

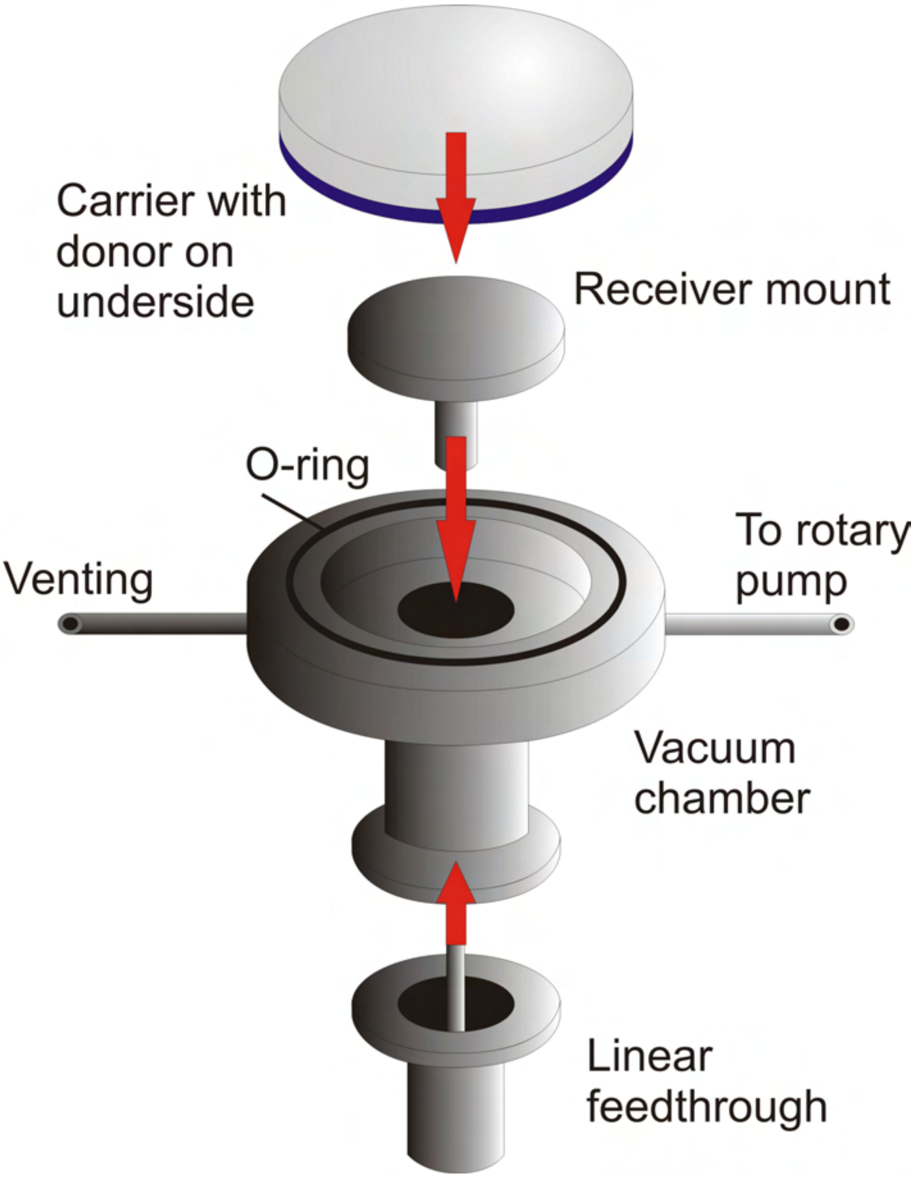

FIGURE 4.8: Representation of the vacuum chamber used for all LIFT experiments.

onto and allowed for control of the donor-receiver separation. The coated carriers could be used also as the lid of the vacuum chamber. In this way, the number of interfaces prior to the carrier-donor interface was minimised. Sometimes forward transfer experiments were carried out at atmospheric pressure. To do this, the receiver mount was simply raised above the body of the vacuum chamber and the carrier placed on top of the receiver. For experiments under vacuum, the chamber was pumped down to ≈ 0.1 mbar using a rotary pump.

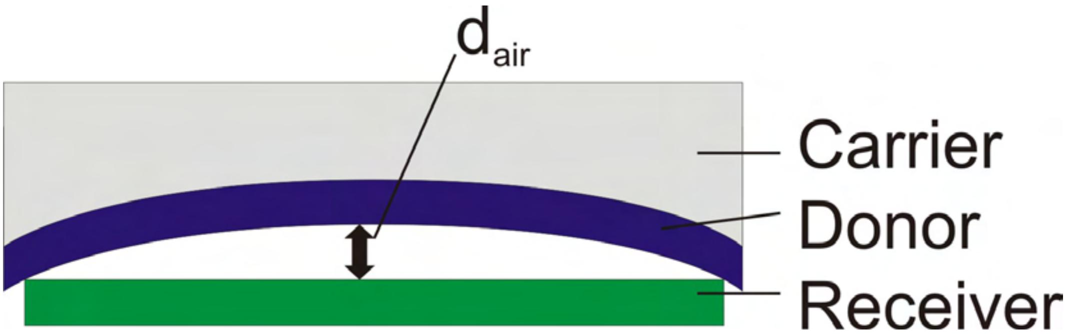

FIGURE 4.9: Diagram of how using long focal length plano-concave lenses as carrier substrates allowed for control of d_{air}.

4.3.4 Setup for Nanodroplet Experiments

For the nanodroplet experiments, single pulses from the Ti:sapphire laser were used. The amplifier output was reduced with a telescope to ≈4 mm diameter (FWHM). This beam illuminated a ≈120 μm diameter circular aperture to give an approximately uniform profile. The aperture was imaged onto the carrier-donor interface using the 100x microscope objective, resulting in a laser spot diameter of ≈4 μm at the film surface, as estimated by the laser-induced damage area on the donor.

Shot-to-shot pulse energy was determined by measuring a known fraction (≈8%) of the incident energy with a callibrated fast photodiode. The laser fluence at the film, J, was then calculated based on the pulse energy, the measured throughput of the micromachiner, the reflectivity of the air-carrier and carrier-donor interfaces, and the spot size.

Borosilicate planoconcave lenses of 1 m focal length were used as carriers; these allowed for the accurate determination of donor-receiver separation, d_{air}, when the carrier was rested, concave face down, on the receiver (see fig. 4.9). In all experiments, d_{air} was kept at or below ≈ 2 μm as previous studies suggested the droplet releasing structures were on the order of a few microns high with much thicker donor films than used here (see e.g. [Willis and Grosu, 2005]). A 30 nm thick film of Cr was evaporated onto the concave face of a carrier lens for the donor film. It was chosen to use significantly thinner films than previous investigations because it might be expected that having less donor material in the irradiated area could result in smaller deposited features. Silicon wafers were used as receivers. All experiments were performed in air at room temperature.

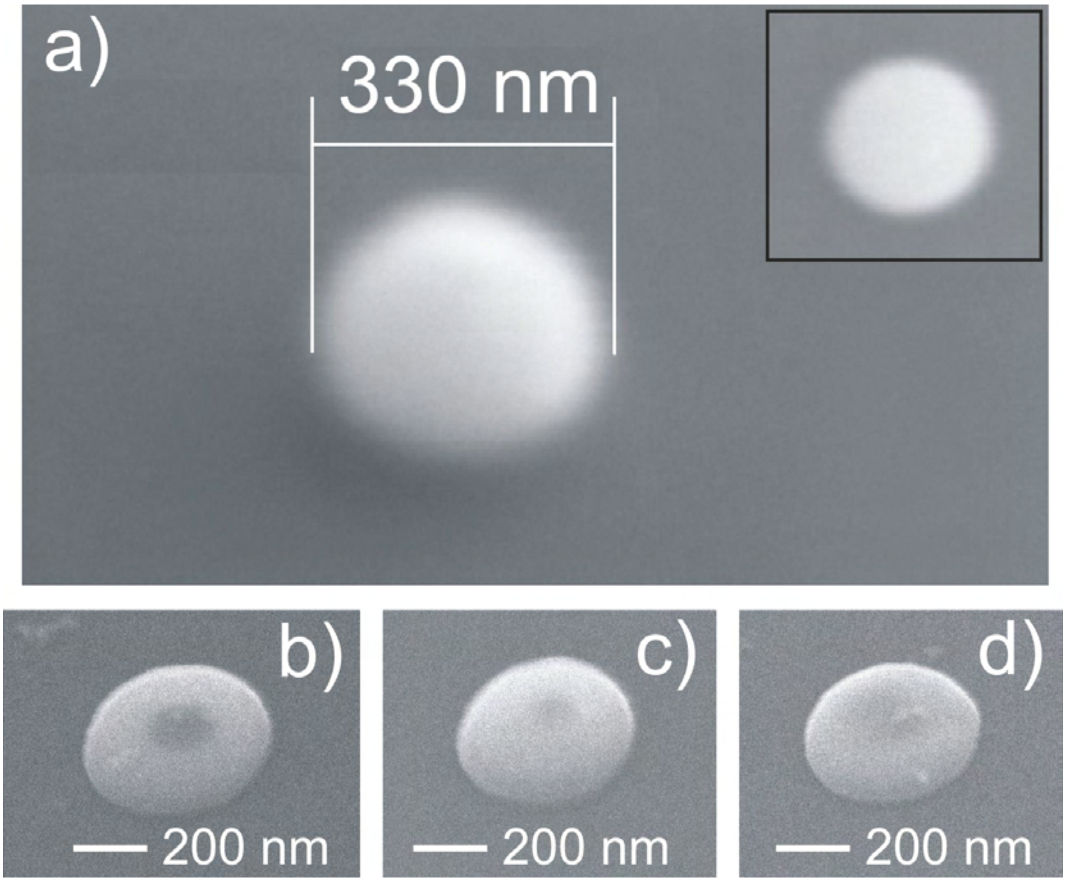

FIGURE 4.10: SEM micrographs of Cr nanodroplets deposited onto a Si receiver using fluence $J = 330 \pm 5$ mJ/cm^2.

4.4 Nanodroplet Results

The first experiment carried out was a thorough fluence scan to determine the threshold for Cr transfer, J_{th}, which was found to be J_{th}=325±5 mJ/cm^2. Figure 4.10(a) shows a typical SEM micrograph of one of the smallest deposits produced with $J \approx J_{th}$; a top down view of the same deposit is shown in the inset to fig. 4.10(a). Other similar droplets are shown in (b-d). The deposits produced around the transfer threshold were highly circular and around 300-350 nm in diameter, significantly less than the laser wavelength and an order of magnitude less than the spot size. These ≈ 300 nm droplets represent the smallest reported structures deposited by LIFT to date. Deposited droplets possessed a domed profile with a peak height of approximately 100 nm or more (estimated from the SEM), substantially greater than the source film thickness.

The speed with which a droplet impacted on the receiver and the mass of film material transferred would be expected to determine the size and morphology of the resulting deposited structure. These parameters depend on the temperature of the source film at the time of droplet release, which itself was a function of the laser fluence. The effect of

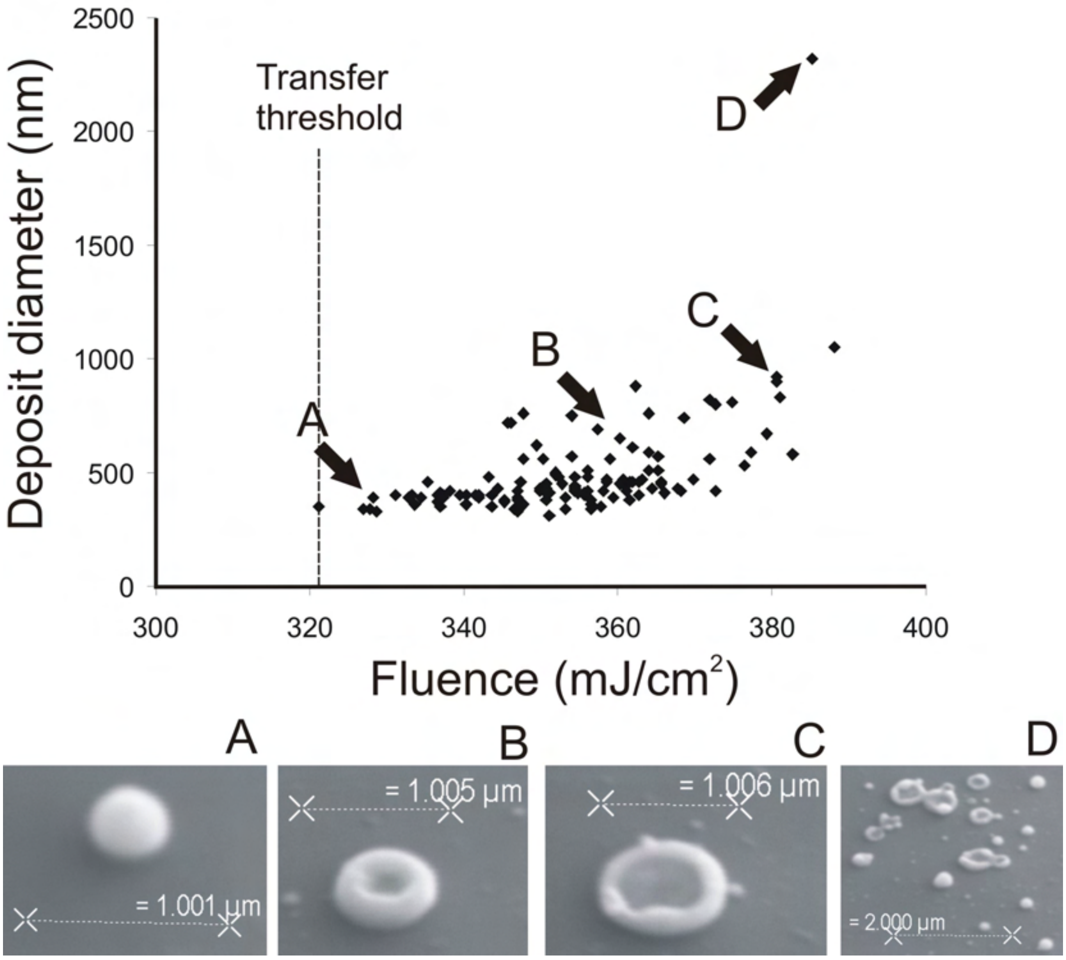

FIGURE 4.11: Plot of the deposited structure diameter as a function of the applied laser fluence. Marked structures on the graph correspond to deposits similar to the corresponding SEM micrographs underneath.

laser fluence on the resultant deposition diameter is shown in fig. 4.11; SEM micrographs of typical deposits around the points marked A-D are shown below the graph. The sharp donor material transfer threshold can be seen clearly at 320-325 mJ/cm^2, below which there were no deposits. Deposition size and shape were observed then to be relatively independent of fluence up to around 345 mJ/cm^2, with reproducible diameters of 300-400 nm and the same domed profile seen in fig. 4.10 (A). The transfer mechanism is believed to have been the same as shown in fig. 4.2.

At around 345 mJ/cm^2 a second fluence threshold can be seen, above which the deposit diameters began to increase more significantly with the applied fluence. Also observed was a larger spread in the obtained deposit diameters. The increase in diameter may be attributed to greater impact momentum of droplets on the receiver when a higher laser fluence was applied. This threshold possibly was due to the onset of significant evaporation at the carrier-donor interface. Depositions produced with fluence greater than this threshold typically possessed diameters from 300 to 500 nm, although a minority with significantly larger diameters, up to ≈800 nm, were also obtained. It is suggested that there were two competing processes in this fluence regime, one being the melt-through LIFT seen at lower fluence that resulted in the smaller depositions, and the other an explosive, and hence more violent, process driven by vaporized film material that resulted in droplets being transferred with more momentum, and hence the larger diameter depositions. Which process was dominant would have been highly sensitive to any weak points (most likely determined by small thickness variations) in the donor film, with weaker areas more susceptible to explosive transfer. The larger diameter deposits also exhibited a central depressed region (B), the diameter and depth of which also increased with applied fluence; again this feature can be attributed to greater momentum of the droplets during transfer, causing a flattening upon impact.

Above 360 mJ/cm^2, the smallest deposits were no longer obtained, and instead most depositions were around 500-700 nm in diameter. A possible reason for this would be the material transfer becoming almost exclusively evaporation driven. As the fluence was increased, the amount of evaporation also increased, and the droplets were transferred with greater momentum. The results of this were that deposited structures exhibited larger diameters and the central flattened region occupied a larger proportion of the deposits. By the time the applied fluence reached ≈380 mJ/cm^2, the deposited structures were almost completely flat (C).

At around 380 mJ/cm^2, yet another fluence threshold was observed, above which multiple deposits were obtained per single laser shot (D). This phenomenon was attributed to phase explosion occurring in the molten donor film. Phase explosion involves the nucleation of gas bubbles throughout a superheated liquid, the number of bubbles being an exponential function of liquid temperature [Song and Xu, 1998]. It is believed that each of the multiple deposits was the result of a gas bubble gaining sufficient internal pressure to propel a piece of the superheated liquid donor film to the receiver.

The number of deposits produced per laser shot is plotted as a function of fluence in fig. 4.12. Obviously there was quite a large error attached to the number of deposits (estimated at ±10%) as it was difficult to determine which deposited structures were unique transfer events and which were just splatter (see deposit marked D in fig. 4.11). Nonetheless, it can be seen that the number of deposits appeared to be increasing exponentially with fluence, supporting the phase explosion hypothesis. Unfortunately, because a value for the temperature of the superheated molten Cr film as a function of fluence is currently not available, it was not possible to compare the experimental values to theory.

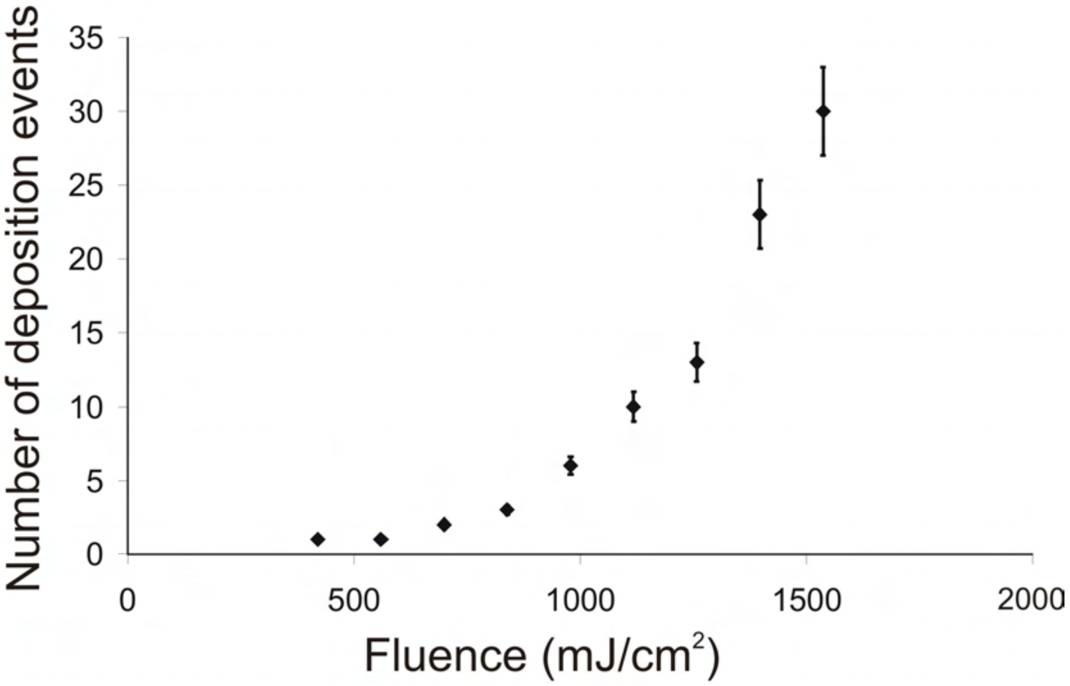

Figure 4.12: Plot of the number of separate deposition events as a function of applied fluence for fluences well above the transfer threshold. Error estimated to be ±10% of the total value.

Adhesion of deposited material to the receiver is a challenge with LIFT. Throughout the fluence scan, deposit adhesion was seen to improve with increasing applied laser fluence, i.e. as the area of deposited material in contact with the receiver increased. The smallest transferred features exhibited very poor adhesion and could easily be removed with less than 1 minute in an ultrasound bath immersed in de-ionised water at 40°C. In comparison, material transferred with fluence $\approx 360 - 370$ mJ/cm^2, i.e. deposits exhibiting significant flattening, were still visible on the receiver after 5 minutes of ultrasound cleaning. Longer times in the ultrasound bath were not attempted.

4.5 Microarrays of Nanodroplets

Having produced sub-spot (and sub-wavelength) size depositions, the next question was how close could successive deposits be placed. Of course, it would always be possible to move carrier and receiver independently to place deposits arbitrarily close, but this would introduce undesirable extra complexity into the printing technique. However, to transfer two droplets from closely separated points on the donor would require the second droplet to be expelled from an area of the donor that had already been modified by the laser, which could affect the droplet growth process. Closely spaced nanodroplets

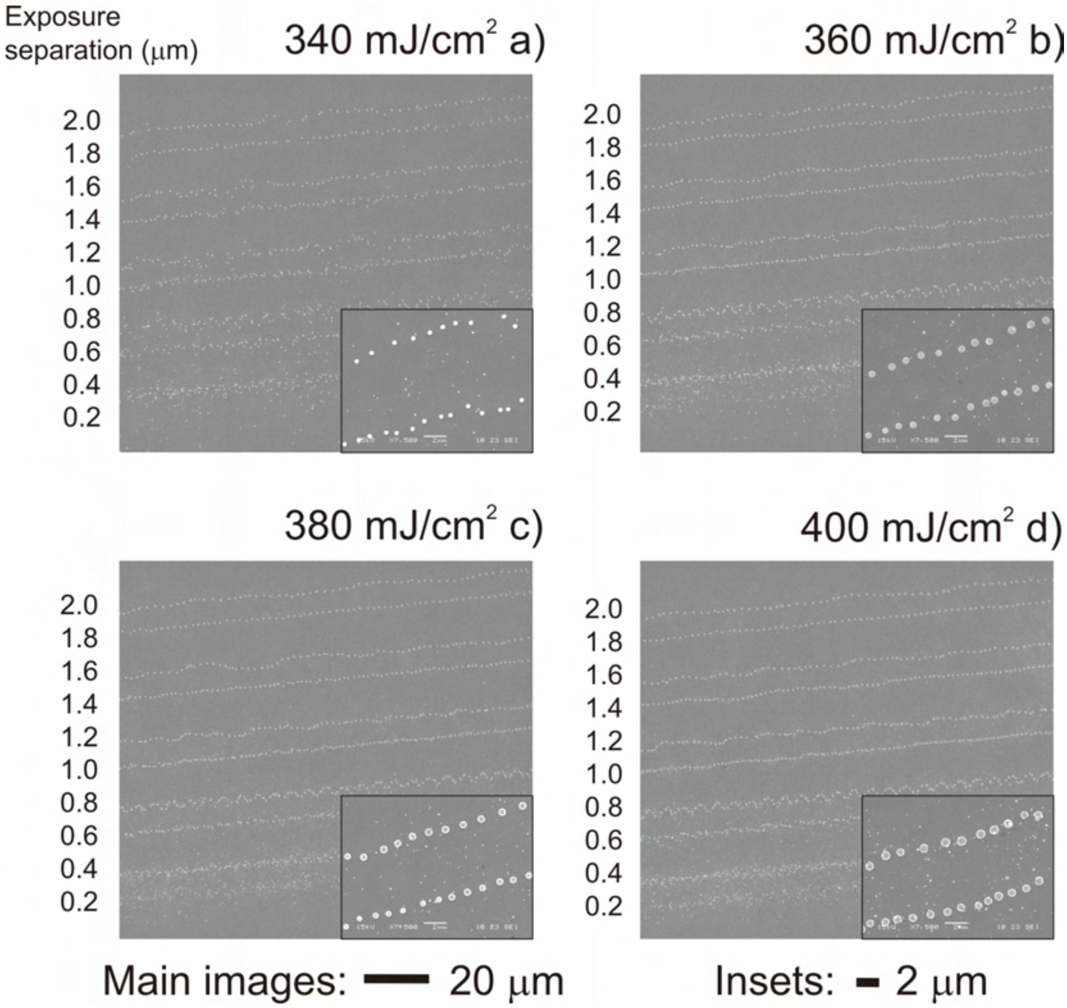

FIGURE 4.13: SEM micrographs of lines of nanodroplets produced with exposure separations from 200 nm - 2 μm for fluence 340 mJ/cm^2 (a), 360 mJ/cm^2 (b), 380 mJ/cm^2 (c), and 400 mJ/cm^2 (d).

could have uses in plasmonic applications and so the objective of this final experiment was to produce arrays of nanodroplets of micron, or even sub-micron, period.

To investigate how closely successive deposits could be positioned, lines of droplets were produced by linearly scanning the micromachiner translation stages perpendicular to the laser beam. The laser repetition was 1 kHz and the stages were scanned at speeds from 200-2000 μm/s, corresponding to exposure separations (N.B. the exposure separation was defined as the distance between the centres of two successive incident pulses) from 0.2-2 μm. The laser fluence was varied from 340-400 mJ/cm^2 in 20 mJ/cm^2 steps.

Figure 4.13 shows SEM micrographs of all the lines produced with the various combinations of fluence and scan speed. The exposure separation decreased from 2 μm for the top lines in the figures to 0.2 μm for the bottom line (this line is hard to see as clean droplets were not transferred). The reason that some of the lines were not straight was due to a problem with the stages and not with the LIFT process, hence why similar variations were seen in separate experiments with the various fluence values. The insets show close-up views of the lines produced with 1.4 μm (lower line) and 1.6 μm (top line) separations at the indicated fluence.

A number of trends were obvious from fig. 4.13. Firstly, it appeared that the minimum separation with the current experimental conditions for which reproducible, round droplets were produced was $\approx$1.5 μm. It was impossible to tell how successful the 0.8 μm separation depositions were due to the fact that the stages exhibited some sort of resonance at this scan speed. For certain, below 0.8 μm separation, the effect of having two successive excessive exposures so close together prevented any clean droplets being transferred. It was also observed that deposits produced with 340 mJ/cm^2, i.e. just above the transfer threshold, displayed significant irregularity in their positions on the receiver, i.e. they weren't arranged in clear lines like the droplets at higher fluence.

Figure 4.14 shows close-up SEM micrographs of lines of deposits produced with 360 mJ/cm^2 and exposure separations of 1-2 μm. At this higher resolution it can be seen that an approximately regular spacing of deposits did not occur until the exposure separation was around 1.4 μm, and even then there was still significant variation for some droplets. It should be noted that, due to the large ($\geq$ 2 m) separation between the laser amplifier and the LIFT apparatus, small beam pointing instabilities may have contributed to the irregular spacing.

Extending the experiments into two dimensions, i.e. true arrays rather than the microlines described so far, further compounded the problem of multiple pulses overlapping (spatially, not temporally) on a single area of the source film. The area of film a droplet was transferred from may also have been exposed to the transfer pulses of its nearest (and next nearest) neighbours previously, if the array periodicity was sufficiently small compared to the spot size.

Figure 4.15 shows microarrays of 2 (fig. 4.15(a)) (i.e. approximately the laser spot radius) and 5 μm (fig. 4.15(b)) ($>>$ than the spot radius) periodicity using $\approx$ 360 mJ/cm^2 (i.e. the exposure separation was 2 and 5 μm, respectively). It is believed that the irregular spacing of the deposits was primarily the result of backlash in the translation stages and beam pointing instabilities, although having many deposits in close proximity may also have been a contributory factor. The advantage of having greater than spot size separation of successive exposures in terms of the amount of debris around the deposited structures was apparent comparing the two arrays.

At the smallest array periodicity of $\approx$ 2 μm, there was significant spatial overlap of successive pulses in between the points where droplets were transferred. Hence, in these

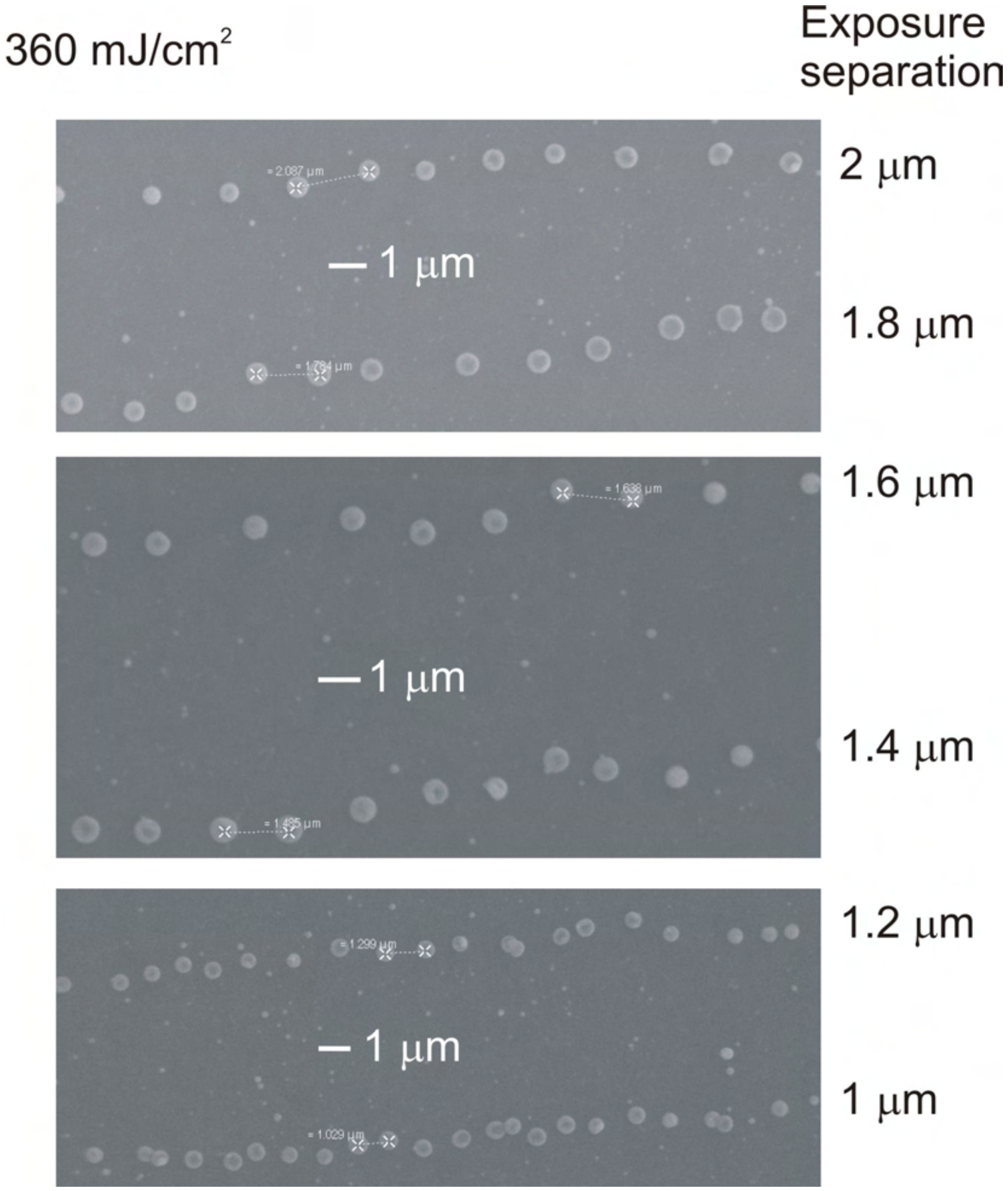

Figure 4.14: Close-in SEM micrographs of lines with indicated exposure separations produced with applied fluence 360 mJ/cm^2.

areas the film became progressively weakened and debris was expelled. If the periodicity was greater than the spot radius, then there was no overlap of successive pulses and debris formation was limited. The droplet size was still quite uniform even at the 2 μm spacing as there wasn't much overlap of successive pulses at the points where droplets were produced. However, smaller periodicity arrays just produced a mess of debris with no obvious nanodroplets because such arrays required droplets to form in areas of the donor already damaged by earlier pulses.

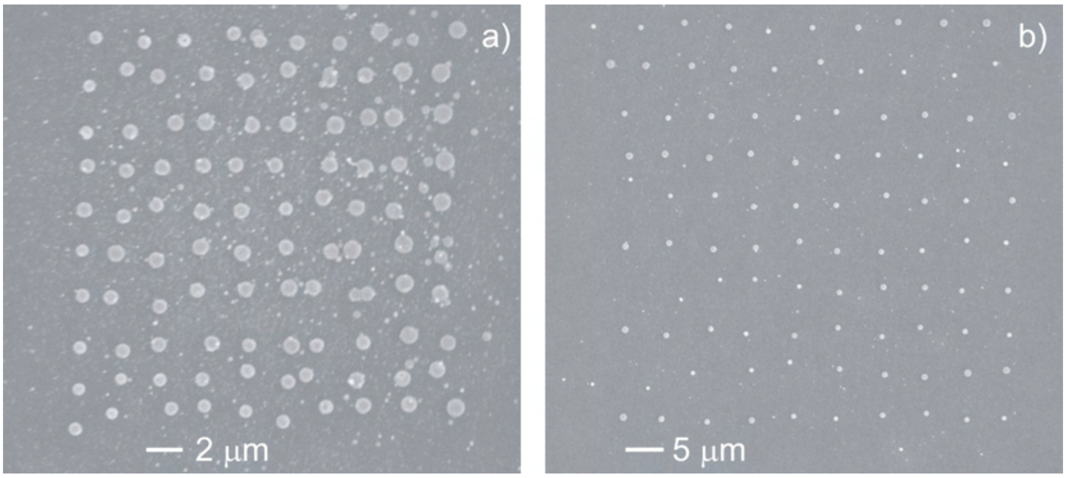

Figure 4.15: SEM micrographs of sub-spot size (2 μm) and greater than spot size (5 μm periodicity microarrays of nanodroplets.

4.6 Conclusions

The deposition of nanodroplets with reproducible diameters around 300 nm using fs-LIFT has been observed. The droplets were an order of magnitude smaller than the spot size and are the smallest known LIFT depositions to date. It was found that such nanodroplets were transferred over a relatively large range of laser fluence. It is believed that the minimum fluence threshold for nanodroplet transfer was when the donor film melted through, and the maximum fluence threshold was when phase explosion began to occur in the superheated molten film, resulting in splashy deposited structures. The size of the deposited droplets was found to increase slightly with fluence, probably in line with an increase of the impact momentum of nanodroplets on the receiver substrate. For the same reason, deposit adhesion to the receiver was found to improve with applied fluence.

The spatial overlapping of pulses on the donor film was found to have a detrimental impact on the transfer process. If the exposure separation was around the laser spot radius, such that there was significant overlap of successive pulses in the areas between droplets, then debris around the deposited features was observed. If the separation was reduced further such that there was overlap of successive pulses at the points where droplets should have formed, no clear nanodroplets were produced at all. Thus it is believed that the smallest microarray periods that can be achieved using this technique are around half the laser spot size.

Bibliography

Bera, S., Sabbah, A., Yarbrough, J., Allen, C., Winters, B., Durfee, C., and Squier, J. (2007). Optimization study of the femtosecond laser-induced forward-transfer process with thin aluminium films. *Appl. Opt.*, 46(21):4650–4659.

Bohandy, J., Kim, B., and Adrian, F. (1986). Metal deposition from a supported metal film using an excimer laser. *J. Appl. Phys.*, 60(1):1538–1539.

Narazaki, A., Sato, T., Kurosaki, R., Kawaguchi, Y., and Niino, H. (2008). Nano- and microdot array formation of fesi$_2$ by nanosecond excimer laser-induced forward transfer. *Appl. Phys. Exp.*, 1:057001.

Papakonstantinou, P., Vainos, N., and Fotakis, C. (1999). Microfabrication by uv femtosecond laser ablation of pt, cr and indium oxide thin films. *Appl. Surf. Sci.*, 151:159–170.

Pax, P. and Weston, J. (1991). Novel large mode volume resonator. *IEEE J. Quantum Elect.*, 27(5):1242–1246.

Seifert, N. and Betz, G. (1998). Computer simulations of laser-induced ejection of droplets. *Appl. Surf. Sci.*, 133:189194.

Seifert, N., Betz, G., and Husinsky, W. (1996). Droplet formation on metallic surfaces during low-fluence laser irradiation. *Appl. Surf. Sci.*, 103:63–70.

Song, K. and Xu, X. (1998). Explosive phase transformation in excimer laser ablation. *Appl. Surf. Sci.*, 127(5):111–116.

Willis, D. and Grosu, V. (2005). Microdroplet deposition by laser-induced forward transfer. *Appl. Phys. Lett.*, 86:244103.

Willis, D. and Grosu, V. (2007). The effect of melting-induced volumetric expansion on initiation of laser-induced forward transfer. *Appl. Surf. Sci.*, 253:4759–4763.

Yang, L., Wang, C., Ni, X., Wang, Z., Jia, W., and Chai, L. (2006). Microdroplet deposition of copper film by femtosecond laser-induced forward transfer. *Appl. Phys. Letts*, 89:161110.

Chapter 5

Femtosecond DRL-LIFT of Microscale Gadolinium Gallium Oxide

5.1 Introduction

The ≈300 nm depositions demonstrated in chapter 4 required that the target film was melted or evaporated to initiate forward transfer. Whilst this presents no problems for the deposition of metallic structures, there are many other photo- and thermo-sensitive materials which would be modified or destroyed by such processes. Also, there are already a great many techniques for direct-writing metals (see e.g. [Herman, 1989] and refs therein), some of which are capable of better resolution than so far demonstrated by LIFT (see e.g. [Haight et al., 2003]). The inherent simplicity and ability to deposit onto virtually any substrate material nonetheless makes LIFT attractive for many applications and so considerable effort has been directed towards modifying the technique to allow for the forward transfer of more delicate materials.

One method that is being successfully applied by a number of groups is DRL-LIFT (see section 2.2 and fig. 5.1). In this chapter the first study of DRL-LIFT using ultrashort lasers (DRL-fs-LIFT) is presented. A number of metallic and polymeric DRL materials are investigated and the physics of the transfer processes with different DRLs will be discussed. A gadolinium gallium oxide (GdGaO) film is used as a sample 'hard' donor material, which is transparent to the laser wavelength.

This chapter begins with a detailed discussion of dynamic release layers and the suitability of certain materials for DRL applications. This is followed by the principle of active

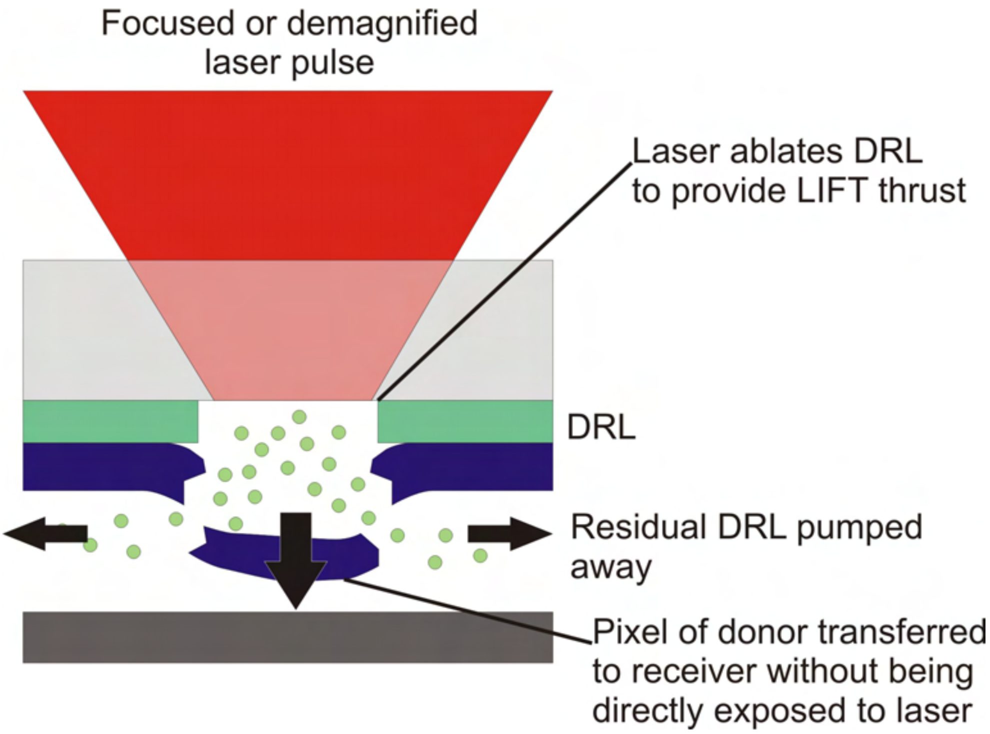

FIGURE 5.1: Illustration of the DRL-LIFT technique (reproduced from chapter 2).

carrier (AC) substrates, which is relevant to many ultrafast LIFT experiments but has not previously been addressed in the literature. Section 5.4 details the experimental setup used to study DRL-fs-LIFT. Section 5.5 presents the results obtained with the various DRL materials. Finally, the physics of the DRL-fs-LIFT process, which differs significantly from the longer pulsed regime, is discussed in section 5.6.

5.2 Dynamic Release Layers

The choice of material to use as a DRL is crucial. To be suitable, a material must have a low ablation threshold, high absorption coefficient at the laser wavelength, and avoid excessive thermalisation of the absorbed photons to facilitate transfer with low thermal impact on the donor. The DRL should dissociate upon irradiation to avoid contamination of the transferred donor with residual DRL material. The DRL should also be able to withstand the donor growth process, which may involve high-temperatures and high-vacuum environments.

Metal films are commonly used as DRLs because of their high absorption coefficients, especially for UV wavelengths (see e.g. [Hopp et al., 2004; Serra et al., 2004; Tolbert et al., 1993]). However, metals do not dissociate but instead melt, evaporate, or undergo phase-explosion (or fragmentation via non-thermal processes, e.g. Coulomb explosion)

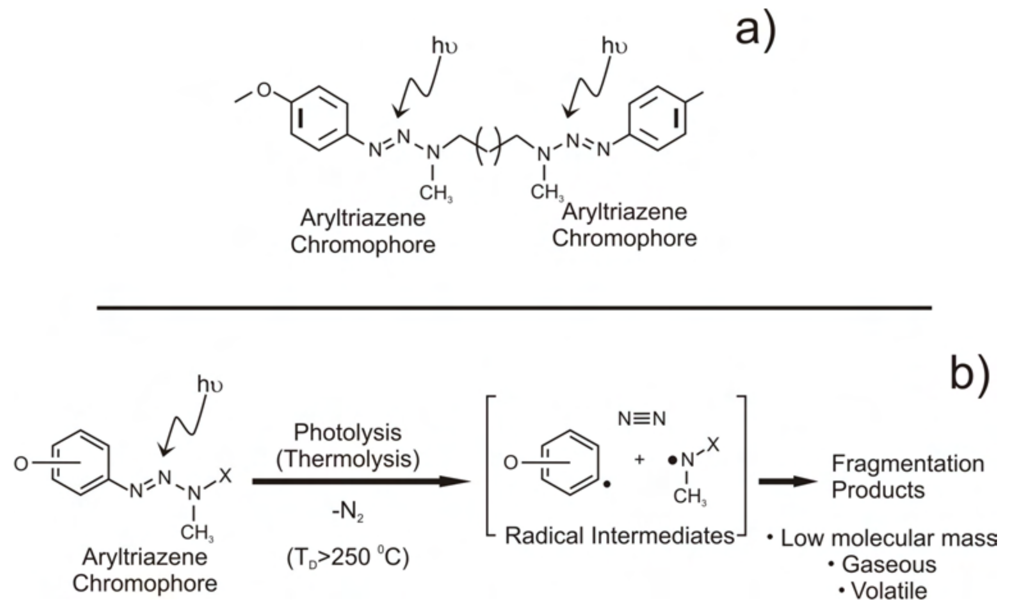

FIGURE 5.2: Structure formula of a triazene polymer repeating unit (a) and nitrogen-liberating decomposition pathway (b). Adapted from [Fardel et al., 2007a].

so there are concerns of residual DRL contamination, as has been observed by Smausz et al. [Smausz et al., 2006].

A particularly well-suited material for DRL applications is the triazene polymer (TP), which exhibits clean and well-defined photofragmentation into small, volatile, gaseous, molecular fragments [Lippert and Dickinson, 2003]. The fragmentation process releases N_2, providing the thrust required for LIFT [Fardel et al., 2007c; Nagel et al., 2007]. This thrust, which originates from the pressure increase, allows a precise "cutting" of well-defined regions from the donor film. The structure of the TP consists of repeating units of 2 photodecomposible aryltriazene chromophore units linked by an alkyl bridge, as shown in fig. 5.2(a) [Fardel et al., 2007a]. Exposure to UV irradiation (or multi-photon at longer wavelengths [Bonse et al., 2005b]) causes photolytic cleavage of the triazene chromophores with simultaneous release of nitrogen. Two unstable intermediates are produced that rapidly decompose into gaseous by-products. The photolytic decomposition pathway of a TP chromophore is shown in fig. 5.2(b) [Fardel et al., 2007a]. An important point to note is that the TP chromophore can also experience the same decomposition pathway if the temperature is raised above ≈250 ^{o}C [Lippert and Dickinson, 2003], which can place limitations on the donor materials that can be deposited on top of the TP. The TP was designed for UV applications and has a very low ablation threshold of 25 mJ/cm^2 under 308 nm irradiation (with ns pulses) meaning that transfer can be achieved with low thermal impact on sensitive donors using UV wavelengths [Karnakis et al., 1998].

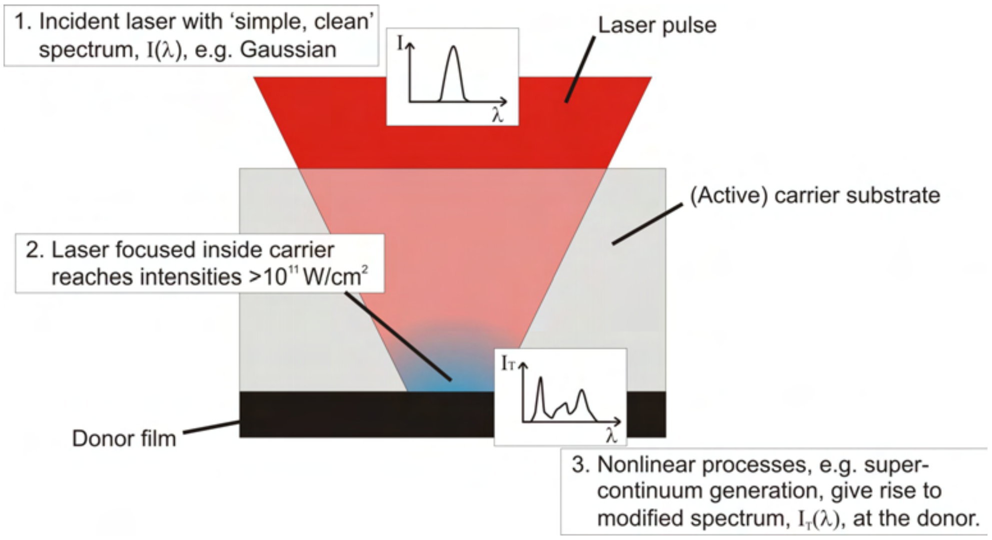

FIGURE 5.3: Schematic of the Active Carrier processes for an incident laser pulse initially having an approximately Gaussian spectrum.

Bonse and coworkers have studied in detail the ablation behavior of the TP at 800 nm in the nanosecond and femtosecond regimes [Bonse et al., 2007, 2005b] and found a strong dependence on the pulse duration (with damage threshold fluence increasing with pulse duration). They observed a two-step ablation behaviour at 800 nm with 130 fs pulses where residual solvent (used during the preparation of the TP film) was boiled-off at sub-ablation threshold fluences around 350−390 mJ/cm^2 due to its lower boiling temperature [Bonse et al., 2005a]. The IR damage threshold of the TP itself was measured to be ≈500 mJ/cm^2 [Bonse et al., 2005a]. Three-photon absorption is believed to be the dominant absorption mechanism at 800 nm. The quality of the structures obtained with fs laser ablation was also quite high, with strong indication that the fs-pulse induced decomposition also produced mainly gaseous ablation products (similar to 308 nm, ns irradiation).

5.3 Active Carriers

This section introduces the phenomenon of active carrier substrates and discusses their possible influence on fs-LIFT experiments with or without a DRL. Here the discussion is limited to possible negative effects, which have more direct relevance to the current DRL experiments. The envisaged positive effects are still highly speculative and have not been experimentally demonstrated; these will be discussed in chapter 9.

5.3.1 Introduction to ACs

The principle of ACs is illustrated in fig. 5.3. The measured ablation threshold of the TP at 800 nm corresponds to an intensity of $\approx 10^{12}$ W/cm^2 [Bonse et al., 2005a]. Reported transfer intensity thresholds for fs-LIFT of various donors without DRLs are also typically $\geq 10^{11}$ W/cm^2 (see e.g. [Bahnisch et al., 2000; Banks et al., 2006; Bera et al., 2007; Papakonstantinou et al., 1999; Zergioti et al., 2003]). It is well-known that, when ultrashort laser pulses are focused inside transparent media, nonlinear processes can occur, resulting in a significant broadening of the laser spectrum [Brodeur and Chin, 1999]. The intensity threshold for the onset of supercontinuum generation with 800 nm in silica has been measured to be $\approx 10^{11-12}$ W/cm^2 and, a spectrum from $\approx$400 - $\geq$1000 nm results [Nagura et al., 2002]. Hence, in a fs-LIFT arrangement it is unavoidable that, at some point within the carrier, the laser intensity will be great enough to induce nonlinear processes. Such a setup, where the normally passive carrier substrate plays an active role by modifying the laser spectrum, may be termed Active Carrier LIFT (AC-LIFT).

An AC can present a challenge for fs-LIFT as the generation of new wavelengths may result in light that can damage the donor or receiver. It is therefore important when performing fs-LIFT (or any forward transfer technique with ultrashort pulses), that the absorption properties of the donor/DRL/matrix etc. material are considered not just at the laser wavelength, but at all wavelengths generated in the AC. For example, there is no point using a DRL to protect a photosensitive donor material during fs-LIFT if the carrier becomes active and generates short wavelengths that are not completely absorbed by the DRL and destroy the donor instead. Figure 5.4(a) illustrates how an AC may cause unexpected damage to a donor material. With an inactive carrier (top) the laser spectrum, shown in red, would typically be chosen to maximise absorbance in the DRL (blue) and minimise it in the donor (black). Note that the DRL and donor absorption spectra shown here are hypothetical. With an active carrier (bottom), the laser spectrum can contain many wavelengths, some of which may not be well absorbed by the DRL but strongly absorbed by the donor, and so can damage the donor material.

So how significant is the AC in a fs-LIFT setup? Firstly, it should be noted that AC processes are an unavoidable consequence of the intensities required for fs-LIFT. Typically the nonlinear effects are not optimised (although potentially they could be tailored for certain applications: see chapter 9). The carrier (usually silica) is not a very nonlinear material and the nonlinear interaction length is not long (on the order of the depth of field of the laser). As such, the nonlinear processes in an AC are not very efficient and the resultant laser spectrum at the donor can vary significantly from one pulse to the next due to small variations in pulse energy and duration. Figure 5.4(b)

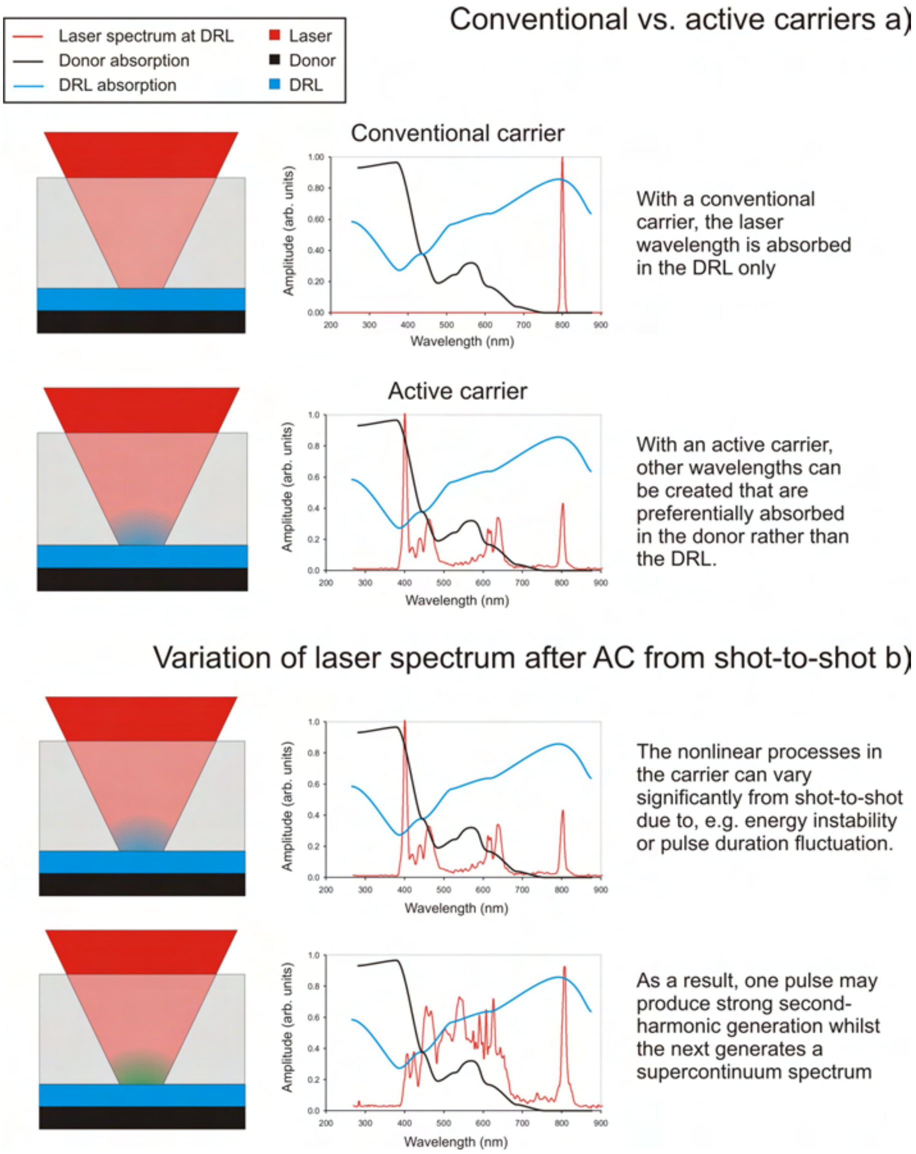

FIGURE 5.4: Illustration of the problems that can arise from having an AC substrate: donor damage (a) and varying pulse-to-pulse spectra (b).

illustrates how the possible variations of the spectrum that can occur may affect the fs-LIFT process. The laser spectra, again shown in red, are actual spectra measured after an AC (see section 5.3.3). The variation in the laser spectrum from shot-to-shot can have significant effects on the absorption properties of the donor and DRL films, which in turn may affect the forward transfer intensity threshold and any photo-induced modifications of the donor material.

5.3.2 Active Carrier Experiments

To measure the spectra of the AC-generated supercontinua, the Ti:sapphire laser was imaged onto the rear surface of an uncoated fused silica carrier in the same geometry as used for all fs-LIFT experiments presented in this thesis (see section 4.3.1 for more details of the laser system). The laser pulses were centrally incident on a 450 μm circular aperture, resulting in an approximately uniform, circular beam; the intensity difference between the centre and the edge of the beam was calculated to be $\leq$5%. A highly demagnified image of the aperture was relayed to the carrier-donor interface, using the micromachining workstation (described in section 4.3.2) resulting in an $\approx$10-12 μm diameter circular spot at the carrier-film interface, as measured by the laser damaged area. As before the image plane of the microscope was adjusted to coincide with the best image of the aperture and the depth of field of the laser was measured to be $\approx$200 μm. Two IR-cut off filters (cut-off wavelength $\approx$670nm; effective overall transmission (800 nm) $\leq$1%, ($\leq$670 nm) $\geq$90%) were inserted after the carrier to remove residual 800 nm light.

The spectrum after the carrier was measured using a CCD spectrometer. The spectrometer was set to detect a single pulse only so that the spectrum of individual pulses could be observed to see the variation. To measure the efficiency of supercontinuum generation, the incident 800 nm laser power before entering the carrier, P_{800}, was measured with a thermal power meter, and the supercontinuum power, P_{SC} measured with a semiconductor detector after the filters. Accurate single pulse energy measurements were not possible with the system so the values recorded for P_{800} and P_{SC} are average powers.

5.3.3 Active Carrier Results

Figure 5.5 shows sample spectra measured after the carrier; note that wavelengths greater than $\approx$670 nm was cut-off by the IR filters. Despite the filters, there was sufficient unshifted energy at the laser wavelength, λ_0, remaining after the AC to be detected. It can be seen that there appear to be a number of competing processes occurring in the AC. For some pulses, a conventional supercontinuum appeared, resulting in a broad spectrum extending down to around 400 nm (fig. 5.5(a,b)), as has been observed by other authors (see e.g. [Brodeur and Chin, 1999; Nagura et al., 2002]. However, for other pulses, there was a very pronounced peak at 400 nm, which must have been the result of second harmonic generation (fig. 5.5(i,j)), and little or no energy at other wavelengths. The 400 nm peak could also exhibit side peaks at around 420, 450, and 470 nm (fig. 5.5(e,f,h,i,j)), which could be Raman in origin, although it has not been possible to

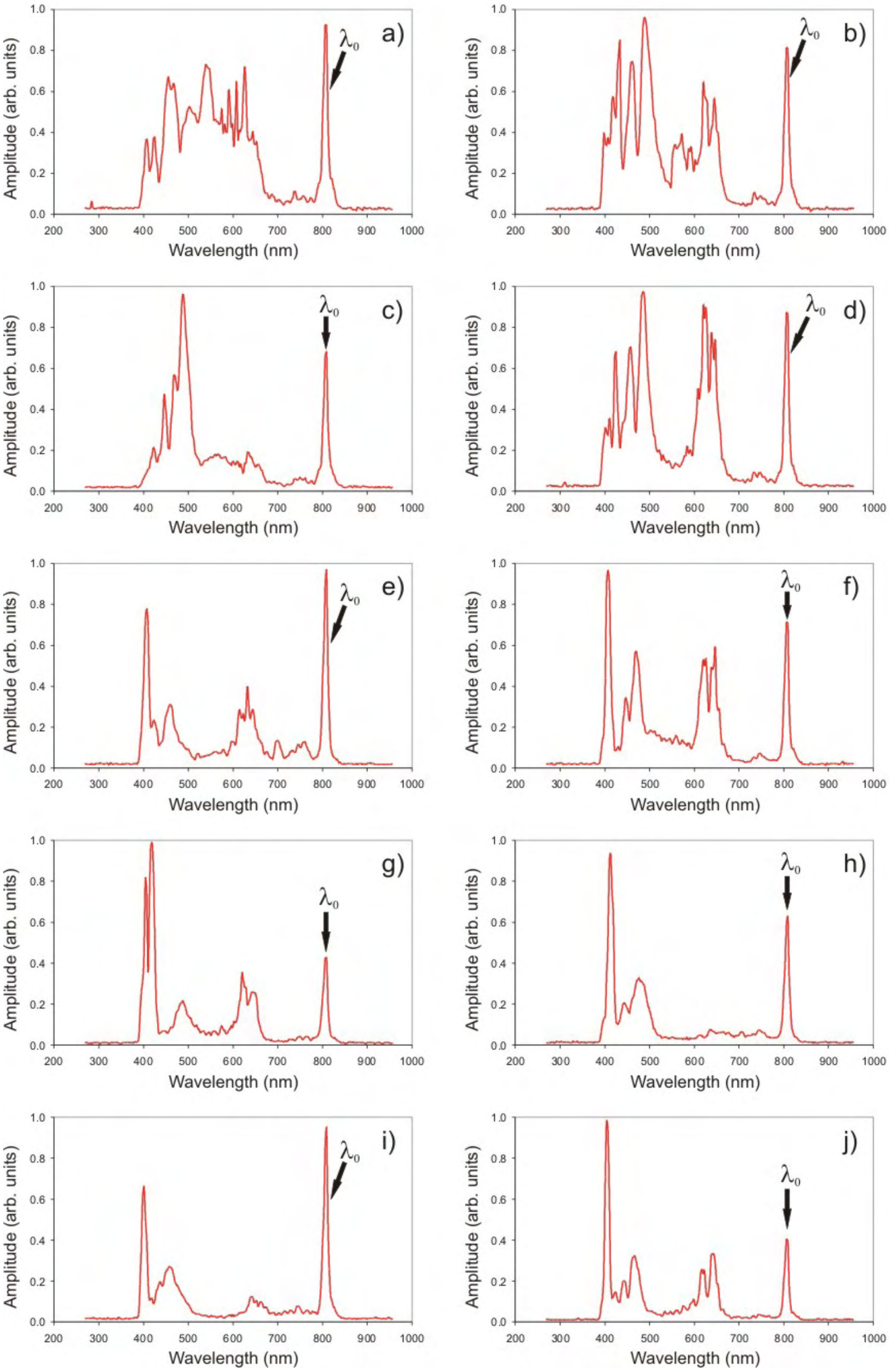

FIGURE 5.5: Sample spectra measured after an active carrier substrate with wavelengths ≥670nm filtered out.

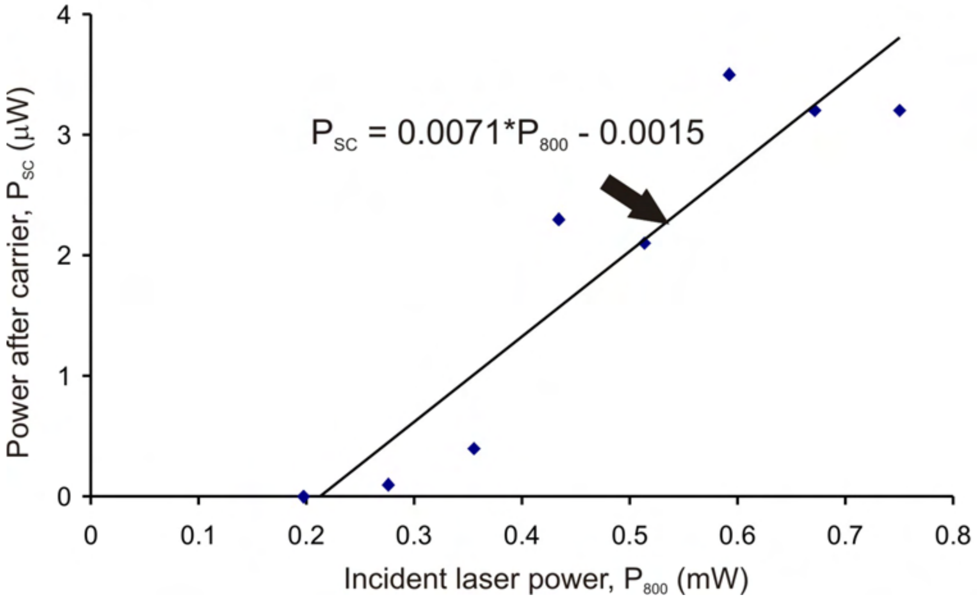

FIGURE 5.6: Plot of the power conversion efficiency in an Active Carrier.

confirm this. Another commonly seen feature of the spectra was a peak around 630nm (fig. 5.5(b,d,e,f,g,i,j)), which may be the short-wavelength tail of a continuum extending from 800 nm with the intermediate wavelengths cut-off by the filters, or some other resonant process (fig. 5.5(j)).

Clearly the nonlinear processes in an AC are complicated. The variation in observed spectra may be attributable to a combination of pulse energy and pulse duration instability affecting at what point inside the carrier the intensity became sufficient to initiate nonlinear processes and hence affecting the nonlinear interaction length. The process requires further study, involving measuring the energy of individual pulses and comparing this with the resultant spectrum, to be fully understood. However, for now it is sufficient to appreciate that the laser spectrum at the carrier/DRL (or donor) interface may include wavelengths as short as ≈ 400 nm.

Figure 5.6 shows a plot of P_{800} vs. P_{SC} for a fused silica carrier. As can be seen the conversion efficiency was around 0.7% and the threshold power for supercontinuum/second-harmonic generation was $\approx 0.2 - 0.25$ mW (approximately equivalent to 110 mJ/cm^2 or 7×10^{11} W/cm^2 at the rear-face of the carrier). The influence (or lack of) of the AC on the current DRL-fs-LIFT experiments will be discussed in section 5.5.1.

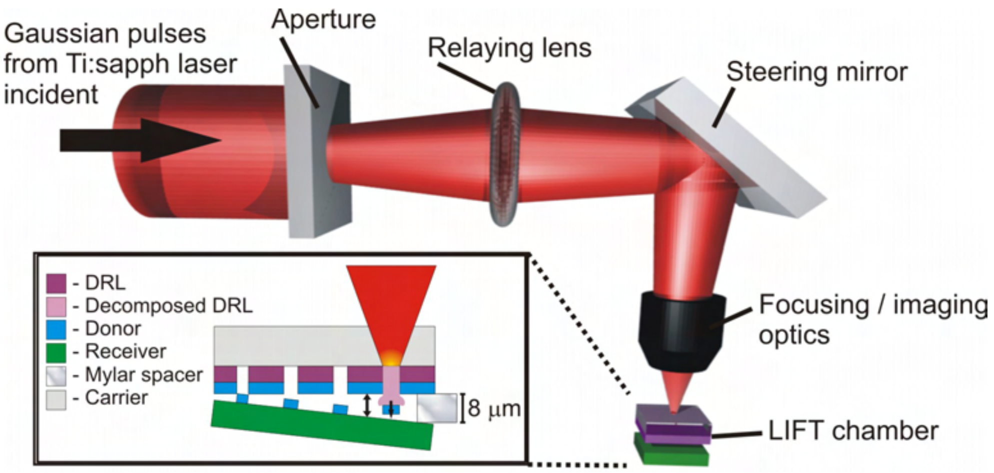

FIGURE 5.7: Experimental setup used to perform DRL-fs-LIFT experiments.

5.4 DRL Experimental Setup

For all DRL-fs-LIFT experiments, the same experimental setup as that described for the AC study (see section 5.3.2) was used. 50 mm diameter, 3 mm thick fused silica discs were used as carriers and the receivers were ≈1 cm square silicon wafers. All experiments were performed under vacuum at ≈0.1 mbar. The separation between the donor film and the receiver, d_{air}, was controlled by the insertion of a single 8 μm thick Mylar spacer. This resulted in a variation of the separation with position across the LIFT setup. A schematic of the setup is shown in fig. 5.7.

To study the performance of different materials for DRL-fs-LIFT applications, metallic and polymeric DRLs were prepared. For the metallic DRL, Al was thermally evaporated to a thickness of ≈ 30 nm. Shipley S1813 photoresist and TP were used as the polymeric DRLs. The S1813 was spin-coated at 10000 rpm (the maximum available) to a thickness of ≈1 μm. The TP was synthesized as described by Nagel et al. [Nagel et al., 2007] and was then prepared by spin coating from a solution in chlorobenzene and cyclohexanone (1:1, w/w). The thickness of the TP was controlled by adjusting the viscosity of the solution and spin speed to yield a DRL with a thickness of ≈100 nm.

On top of each DRL, a donor film of a transparent amorphous GdGaO material was grown by pulsed laser deposition (PLD). It was chosen that the donor film in the centre of the carrier was ≈150 nm thick. However, the nature of the PLD technique is such that the GdGaO film thickness varied considerably across the carrier substrate (see fig. 5.8); at the edge of a carrier, the film thickness was measured (by masking off a small area then using stylus profiling) to be ≈50 nm. The PLD target was single crystal gadolinium gallium garnet ($Gd_3Ga_5O_{12}$). The films were deposited at room temperature and in an oxygen atmosphere at a pressure of 4×10^{-2} mbar. The GdGaO was chosen as a sample

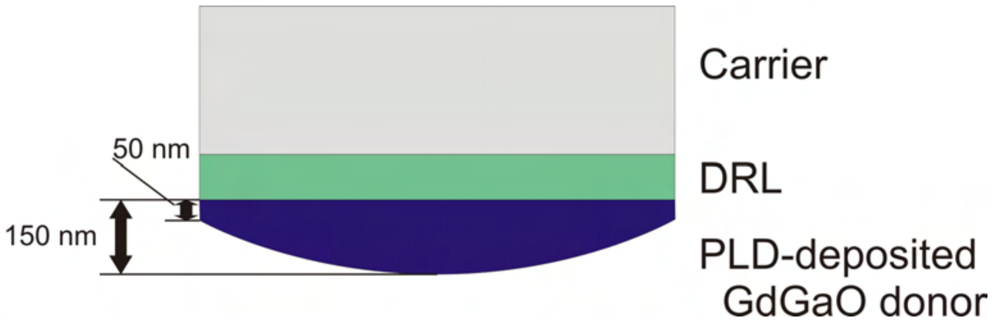

Figure 5.8: Schematic of how the thickness of the PLD-deposited GdGaO donor varied across the carrier.

material to study the DRL-fs-LIFT of ‘hard’ donor films. It is interesting because it can be grown (in an amorphous state) under conditions that do not damage the polymeric DRLs and LIFTed (again in the amorphous state) before post-transfer annealing, which may crystallise it. As such it could provide a template material for the micro-deposition of single-crystals by DRL-fs-LIFT.

5.5 DRL Results

This section describes the results of DRL-fs-LIFT studies at 800 nm of GdGaO donors with and without DRLs. The possible effects of the Active Carriers on the process are considered first before results of GdGaO forward transfer without a DRL, with a metallic DRL, and finally with polymeric DRLs are presented.

5.5.1 Interaction of the Active Carriers with the DRLs

Figure 5.9 shows the absorbance spectra of the 100 nm triazene DRL (black line) and a 1.2 μm thick S1813 film (green line, [Shipley, 2002]). The incident laser spectrum is shown in blue and a typical AC-generated spectrum with a strong 400 nm peak is shown in red. The GdGaO donor film (absorption spectrum shown as a dotted line) was essentially transparent to wavelengths longer than 300 nm; hence the donor could not be damaged either directly by linear absorption the laser or the AC-shifted spectrum. The TP was also essentially transparent to all laser wavelengths that could exist after the AC. Although the cut-off wavelength of TP absorption is known to increase slightly as the polymer ages (due to exposure to room lighting), it is not thought that the absorption at 400 nm is ever significantly greater than at 800 nm; hence, given the $\approx$1% conversion efficiency from 800→400 nm, it can be concluded that the AC did not affect linear absorption of the laser in the TP-DRL. That said, it should be noted that the

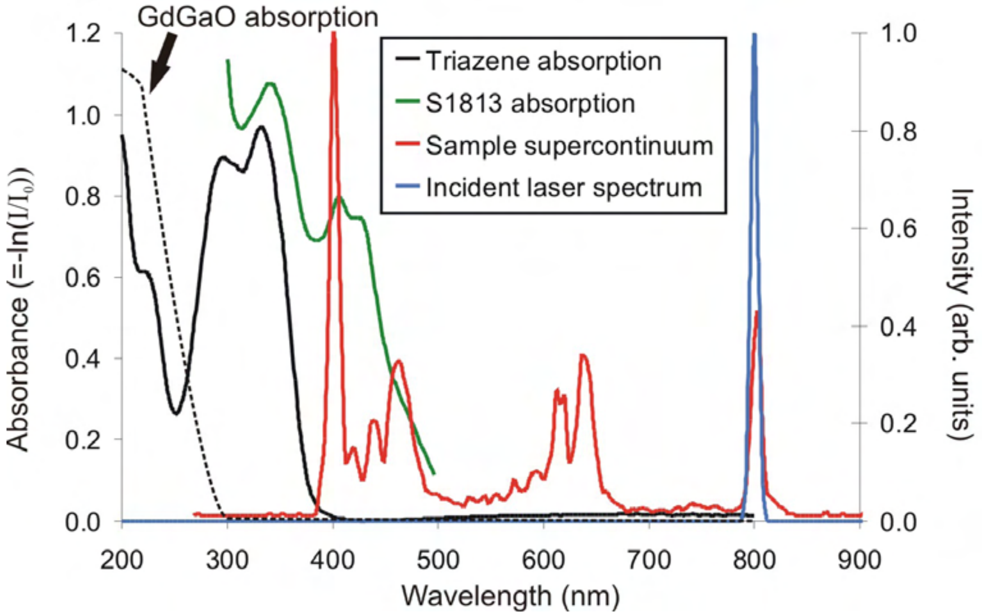

FIGURE 5.9: Absorption spectrum of the polymer DRLs and GdGaO donor, and intensity spectra of the laser before and after the active carrier substrate.

damage threshold of a 100 nm TP film on the backside of a carrier without a donor or receiver in place was measured to be ≈ 330 mJ/cm^2, so there was some process occurring that lowered the damage threshold of the TP in a backwards ablation geometry; what this process might have been is discussed in more detail in section 5.6.2 and the next chapter. Data for the S1813 was only available for $\lambda \leq 500$ nm, but it can be surmised by extrapolating the available data that the photoresist absorbed the short wavelength tail of the supercontinua much more strongly than the incident laser wavelength.

5.5.2 DRL-fs-LIFT Results for GdGaO

The threshold for forward transfer of the GdGaO donor without a DRL was measured to be ≈110 mJ/cm^2. Figure 5.10 shows SEM micrographs of transferred GdGaO material using ≈120 mJ/cm^2 without the DRL; the white bars represent 2 μm. It is evident that the GdGaO experienced significant damage during transfer; the deposits were fragmented and non-uniform across the irradiated region. EDX measurements confirmed that the deposits were GdGaO; the measured atomic percentages of Ga and Gd are listed underneath the micrographs for the indicated points. Although values obtained from the EDX measurements on such thin samples must be treated with caution, it appears the Ga:Gd ratio varied significantly across these deposits, another clear indication that the material properties were altered by the transfer process.

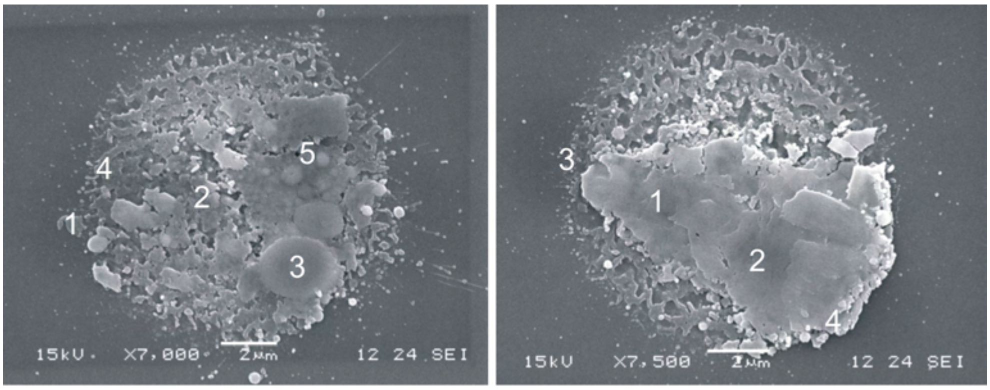

Point	Atomic %		Ga:Gd
	Ga	Gd	
1	0.69	1.16	1:1.68
2	1.35	1.78	1:1.32
3	8.22	11.10	1:1.35
4	0.27	0.00	N/A
5	3.07	6.51	1:2.12

Point	Atomic %		Ga:Gd
	Ga	Gd	
1	5.70	7.52	1:1.32
2	8.16	9.78	1:1.20
3	0.00	0.00	N/A
4	0.97	0.92	1:0.95

FIGURE 5.10: SEM micrographs of GdGaO depositions without a DRL. The white bars represent 2 μm.

5.5.2.1 Metallic DRL

The threshold for forward transfer with the 30 nm Al DRL was measured to be ≈ 400 mJ/cm^2. SEM micrographs of typical structures deposited with fluence slightly above threshold are shown in fig. 5.11. As can be clearly seen, the donor film did not shear

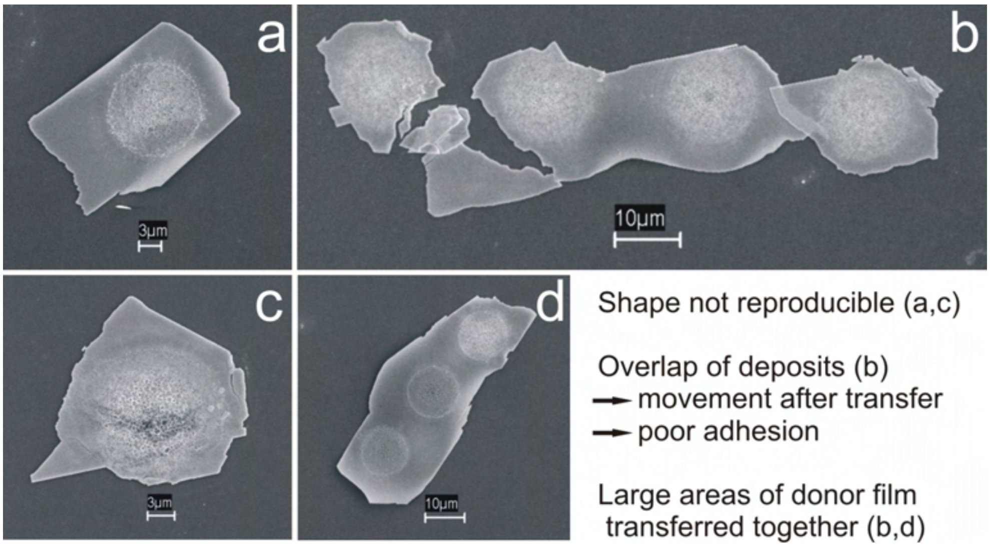

Shape not reproducible (a,c)

Overlap of deposits (b)
→ movement after transfer
→ poor adhesion

Large areas of donor film transferred together (b,d)

FIGURE 5.11: SEM micrographs of GdGaO deposited using the 30 nm Al DRL and fluence just above the transfer threshold.

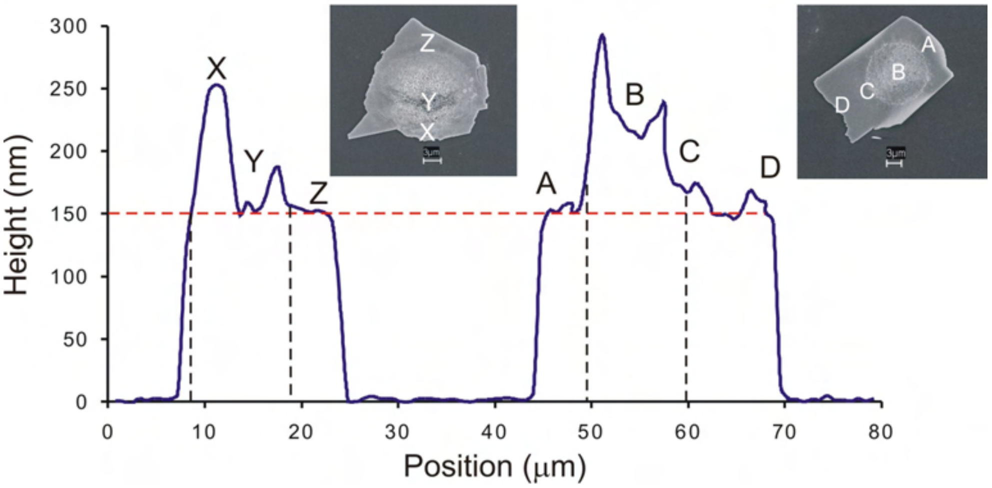

FIGURE 5.12: Stylus profiling measurements of GdGaO deposits using an Al-DRL.

cleanly around the irradiated region upon transfer and so the shape of the resultant deposits was non-uniform (fig. 5.11(a,c)). Indeed, most often single pulses were not able to induce forward transfer and the majority of exposures (≈70-75%) produced no deposition. When deposits were obtained, it was commonly observed that a large piece of donor, covering several exposures, was transferred at once (fig. 5.11(b,d)); it is believed that such deposits are the result of successive weakening of a region of donor film following multiple exposures. Occasionally deposits were observed to be lying on top of each other (see e.g. fig. 5.11(b)); this suggested movement of deposited material after transfer and indicated poor adhesion of the transferred structures.

Figure 5.12 shows sample stylus profiling measurements of Al-DRL assisted depositions. It was apparent that the deposited structures were substantially thicker than the GdGaO donor film, up to 250 nm thick. This result suggested that residual Al-DRL remained on the depositions following forward transfer. Substantial areas of the deposited structures were around 150 nm thick (marked with the red dashed line in fig. 5.12). The thickness and relative uniformity of such regions leads us to surmise that these are unexposed areas of donor material that have been pulled off the DRL by the transferred material.

Other areas of the deposits were substantially thicker, from 200-250 nm, a value that could not be fully accounted for by the combined thickness of donor and DRL. Hence these regions are believed to be the exposed areas, where the DRL had been melted and boiled resulting in a non-uniform, rough surface. The size of these thicker regions was typically around 10 μm, in good agreement with the laser spot size (marked with the black dashed lines), supporting this explanation. Labeled SEM micrographs of Al-DRL deposits are also shown in fig. 5.12 to illustrate the above hypotheses.

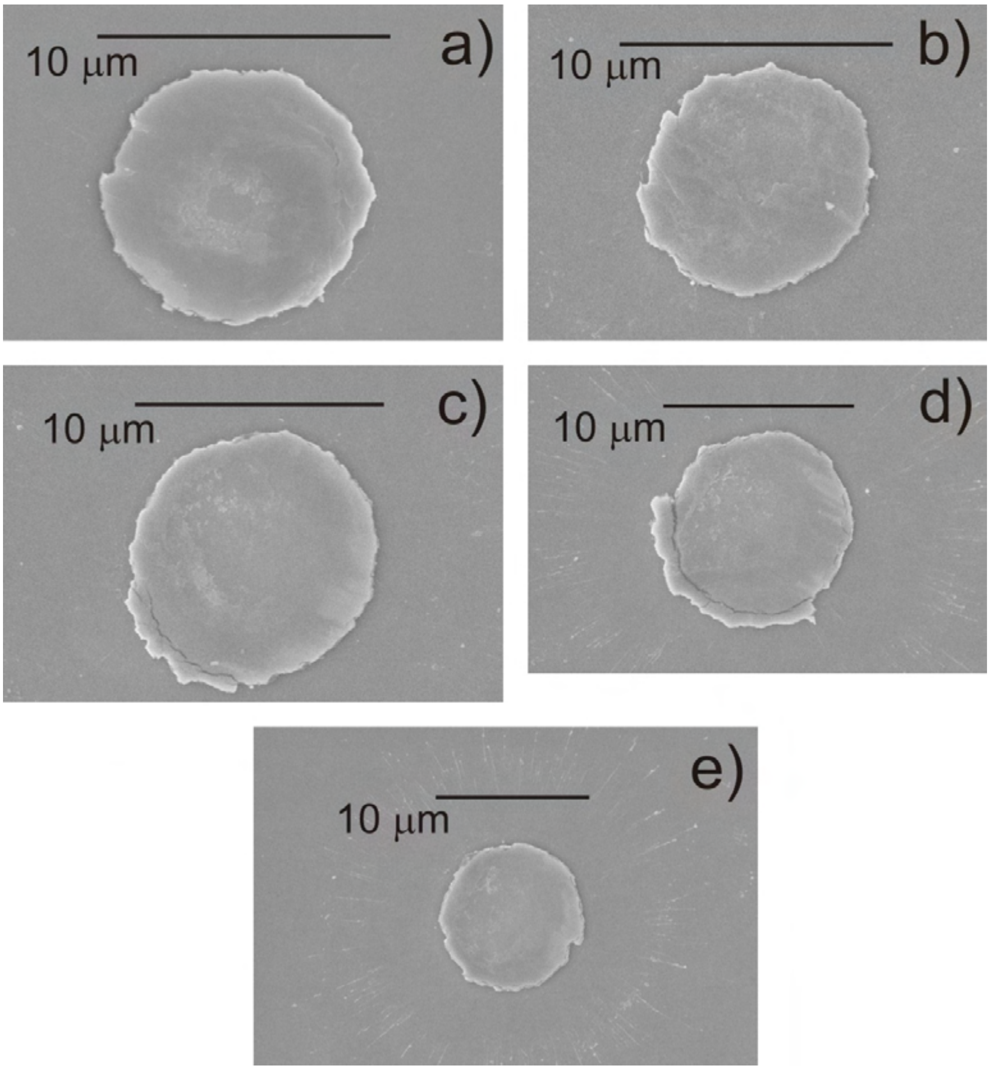

FIGURE 5.13: SEM micrographs of S1813 DRL-assisted GdGaO depositions produced using fluence slightly greater than the transfer threshold (a,b) and 10-15% above threshold (c,d,e).

5.5.2.2 S1813 DRL

Front-side ablation studies of an S1813 DRL without a donor layer were performed to determine the ablation threshold. However, the DRL could not be ablated with a single pulse using the current setup (damage to the optical components occurred first). A reliable ablation threshold value for the S1813 resist with a laser similar to the current one is not known from the literature. Koch et al have reported the ablation threshold of a 1.3-1.9 μm thick Shipley S1813 series photoresist to be ≈ 0.95 J/cm^2 with a sub-30 fs laser at 800 nm (roughly equivalent to 3×10^{13} W/cm^2) [Koch et al., 2006]. However, direct comparison with our experiments, which use a very different pulse duration, would not be expected to give an accurate threshold value. The only conclusion that can be

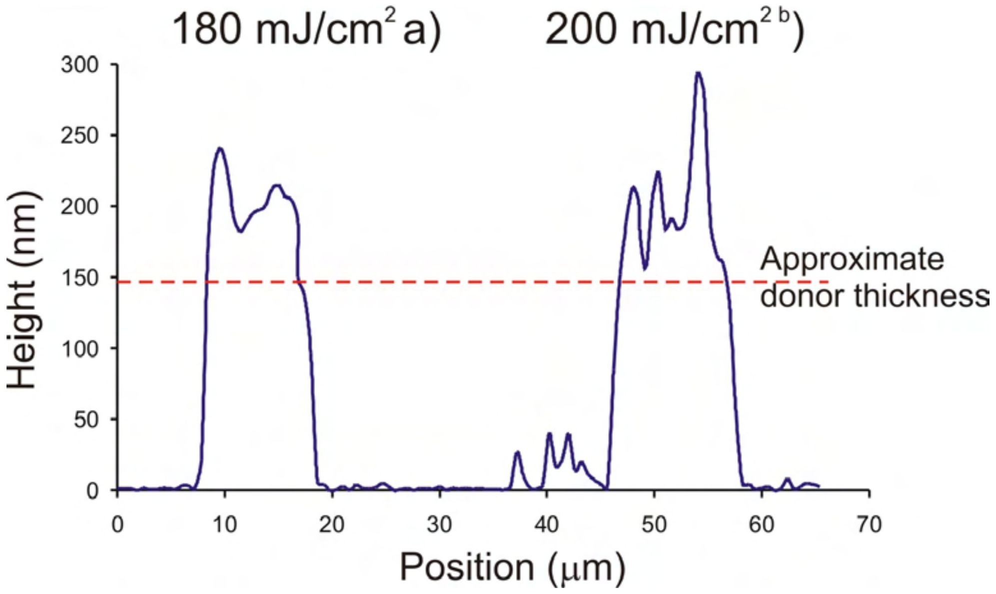

FIGURE 5.14: Stylus profiling measurements of GdGaO deposits using an S1813-DRL.

stated with any certainty is that the ablation threshold of the S1813 was $\geq$500 mJ/cm^2, which was about the maximum fluence that could be achieved using the current setup.

The transfer threshold for GdGaO with the S1813 DRL was measured to be $\approx$ 175 − 180 mJ/cm^2. Figure 5.13 shows SEM micrographs of GdGaO depositions produced using the S1813 DRL with fluences around threshold ($\approx$ 180 mJ/cm^2) (a,b); other depositions obtained with increasing fluence, up to $\approx$ 200 mJ/cm^2, are also shown (c-e). The deposits with the photoresist DRL exhibited a more reproducible circular shape than with the Al-DRL and were around 8-10 μm in diameter, i.e. slightly smaller than the spot size. Around the transfer threshold, the well-defined shape and lack of surrounding debris suggested a relatively gentle transfer process preventing excessive shattering during LIFT (fig. 5.13(a,b,c)). When the fluence was increased, it appeared that the process became more explosively-driven; the deposit shape was still well-defined but a ring of splattered material, believed to be residual photoresist, was evident around the deposits (fig. 5.13(d,e)).

Stylus profiling measurements of deposits were again carried out to look for residual DRL contamination; sample results are shown in fig. 5.14 for a deposit transferred with approximately threshold fluence (a), and with $\approx$ 200 mJ/cm^2 (b). GdGaO deposits around the threshold fluence were typically approximately 200 nm thick; this suggested that a residual layer of DRL remained on the donor after transfer. At higher fluence, the average thickness was still around 200 nm indicating contamination, but the surfaces of such deposits were much rougher, conducive with a more violent transfer process. The

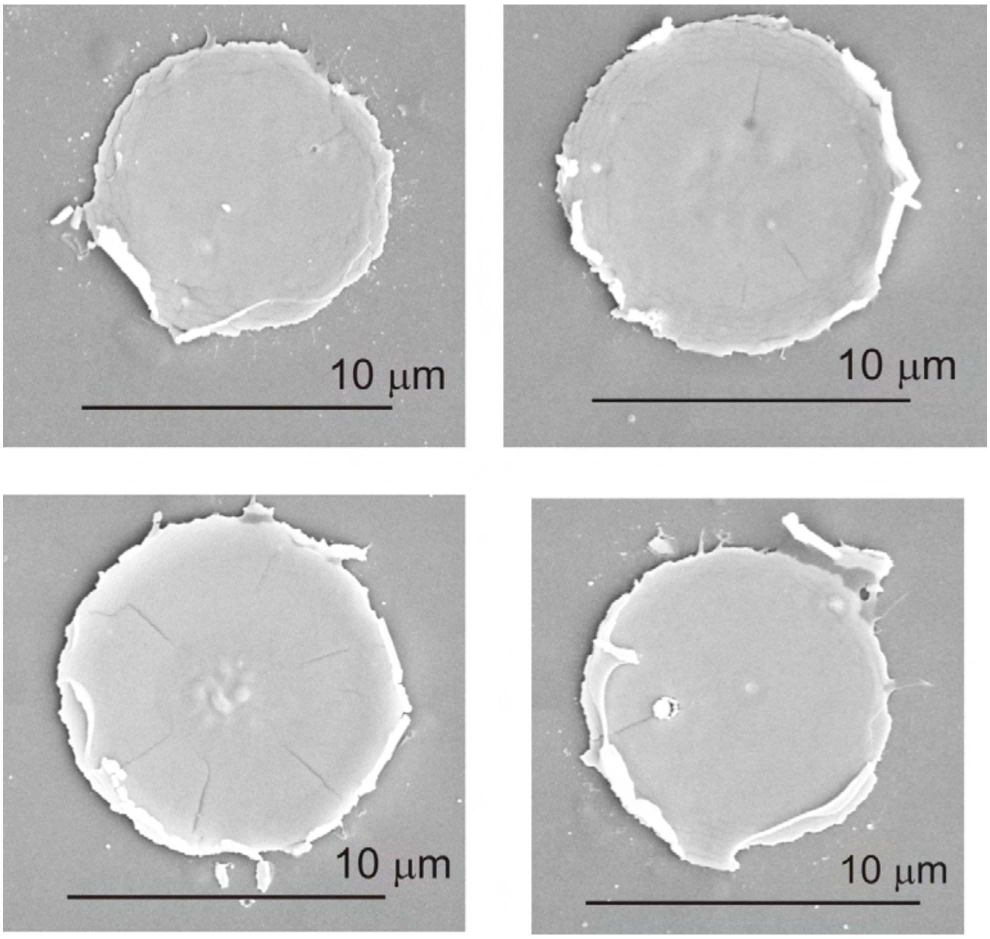

Figure 5.15: SEM micrographs of TP DRL-assisted GdGaO depositions produced using fluence $\approx 90 - 100$ mJ/cm^2.

photoresist splatter seen on the SEM was also visible in the profiling results with higher fluence.

5.5.2.3 TP DRL

The threshold for forward transfer of the GdGaO donor was measured to be ≈90 mJ/cm^2 with the TP-DRL. Figure 5.15 shows SEM micrographs of GdGaO discs deposited with fluence ≈90-100 mJ/cm^2. The reproducible round shape of the deposits was again observed as with the photoresist (c.f. fig. 5.13). Again there was an almost complete absence of surrounding splatter when fluence slightly greater than the transfer threshold was used. The deposits were around 10-12 μm in diameter, corresponding well to the laser spot size.

Stylus profiling results of TP-assisted GdGaO depositions are shown in fig. 5.16. A key feature of all the deposits was a raised area around the edge, which is believed to be

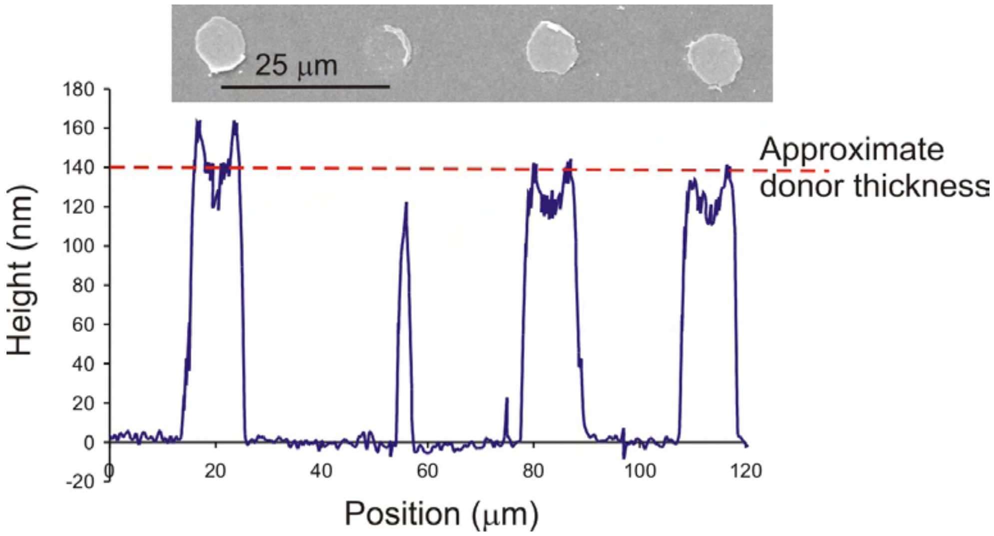

FIGURE 5.16: Stylus profiling measurements of GdGaO deposits using a TP-DRL.

a result of how the deposits were transferred, which will be discussed in section 5.6. The centre of transferred structures was observed to be reproducibly ≈120 nm thick. This result, combined with the SEM observations of a relatively smooth surface of the deposited material, suggested an almost complete lack of residual TP.

A detailed study of the effect of donor-receiver separation, $d_{air}(x)$, on the resultant GdGaO deposits was also performed using the TP DRL. There were a couple of reasons that such a study was only performed with the TP DRL; firstly because the TP-assisted depositions appeared to be the best in terms of shape, smoothness, and lack of residual DRL, but the main reason was because the TP was essentially transparent to visible wavelengths, allowing the donor-receiver separation to be estimated interferometrically using the micromachining workstation's white light source. Figure 5.17(a) shows the principle of the interferometric measurement and fig. 5.17(b) shows typical *in situ* views seen on the micromachiner CCD of the interference fringes with the TP DRL. The Al and S1813 DRLs both absorbed too much of the white light to give visible fringes so $d_{air}(x)$ could not be determined easily with these materials.

As can be seen in fig. 5.17(b), strong coloured fringes were visible when the TP DRL was used. These fringes were believed to be the result of interference between white light being reflected back off the Si receiver and light reflected off one of the carrier-DRL-donor-air/vacuum interfaces. To determine which interface was dominant in terms of back reflection, consider the refractive indices, n, of the materials involved. For the silica carrier, $n \approx 1.46$ and for the TP n has been measured to be ≈1.6-1.8 [Bonse et al., 2005b]. For the GdGaO, n is not known, hence it cannot be stated with certainty whether back reflection off the DRL-donor or donor-air/vacuum ($n_{air/vac} \approx 1$) interface

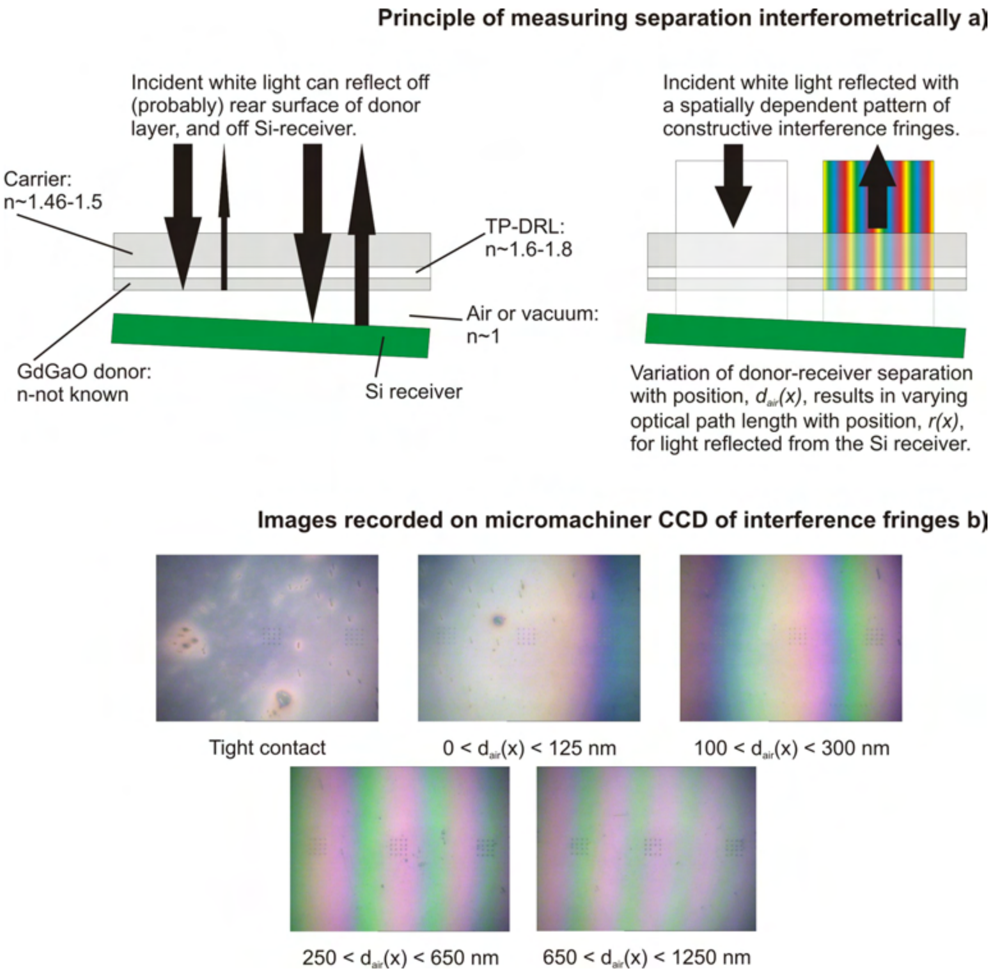

Principle of measuring separation interferometrically a)

Images recorded on micromachiner CCD of interference fringes b)

FIGURE 5.17: Schematic of the interferometric setup for measuring donor-receiver separation with the TP DRL (a) and typical fringes seen on the micromachiner CCD during DRL-fs-LIFT experiments (b).

is stronger. However, when the donor and receiver were in tight contact, i.e. there was no donor-air/vacuum interface, no fringes were visible (see fig. 5.17(b), top-left image), implying that back reflection from the donor-air/vacuum interface was necessary for the formation of fringes.

The optical path difference, $r(x)$, between light reflected from the donor-air/vacuum interface and the Si receiver surface was twice the donor-receiver separation, i.e. $2 \times d_{air}(x)$. Noting the π-phase shift upon refection at the air-receiver interface, constructive interference occurred when $r(x) = f\lambda/2$, where f is the fringe number. Hence each successive green fringe, for example, represented an increase in $r(x)$ of $\approx 250 - 260$ nm, which equates to an increase in $d_{air}(x)$ of $\approx 125 - 130$ nm. Therefore, within the 1^{st} green fringe $f = 1 \rightarrow d_{air}(x) \approx 125$ nm, within the 2^{nd} green fringe $f = 2 \rightarrow d_{air}(x) \approx 250$ nm, and so on. Obviously estimates of $d_{air}(x)$ using a broadband source like the micromachiner's white light are not the most accurate possible and better results could

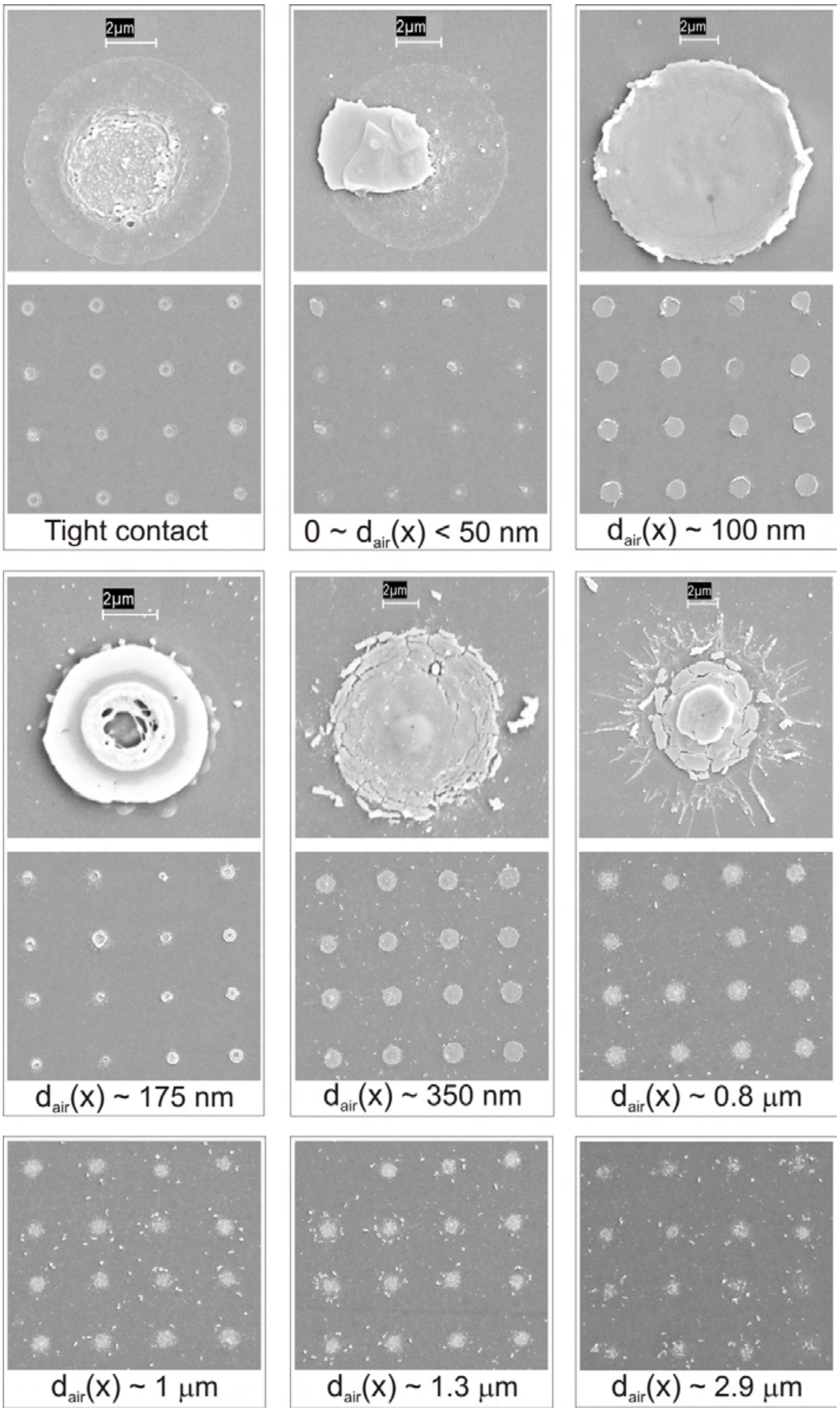

FIGURE 5.18: SEM micrographs of GdGaO deposits obtained as a function of donor-receiver separation; close up views at smaller separations are also shown. Deposit separations in array images were 25 μm, and the white bars in the close up images represent 2 μm.

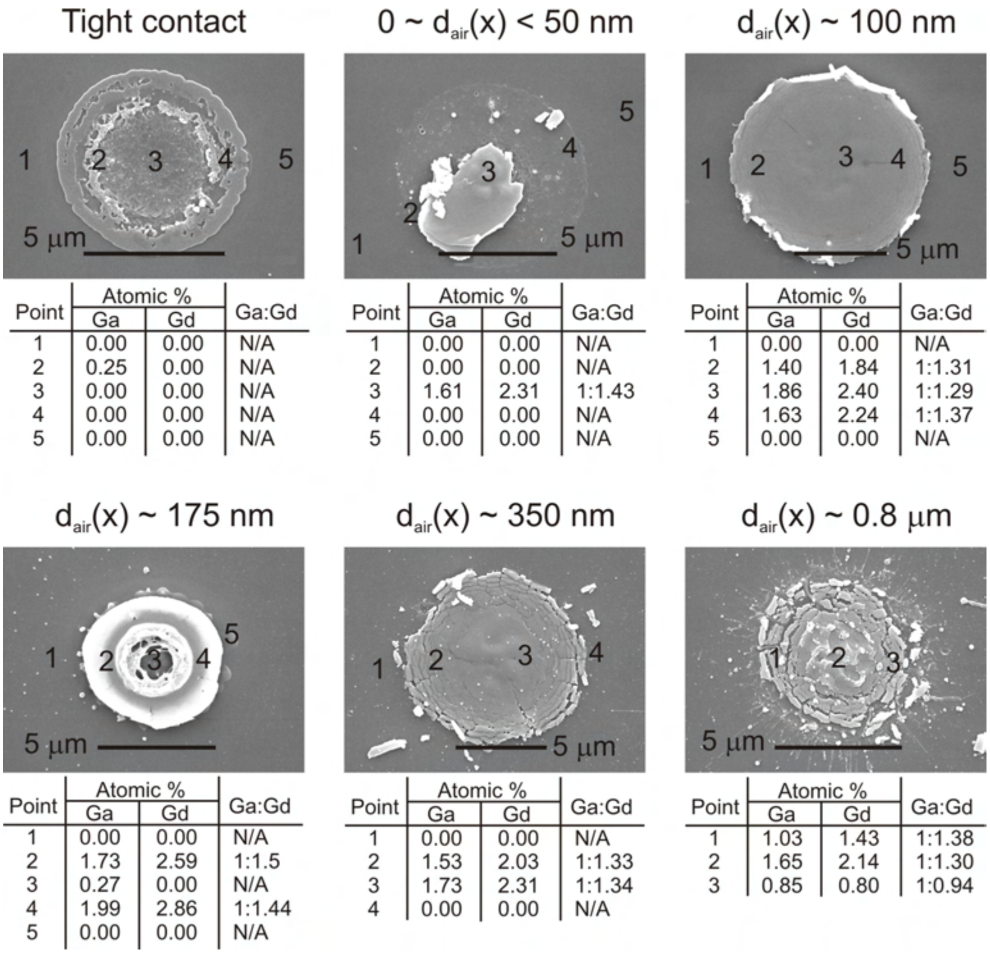

Tight contact

Point	Atomic %		Ga:Gd
	Ga	Gd	
1	0.00	0.00	N/A
2	0.25	0.00	N/A
3	0.00	0.00	N/A
4	0.00	0.00	N/A
5	0.00	0.00	N/A

$0 \sim d_{air}(x) < 50$ nm

Point	Atomic %		Ga:Gd
	Ga	Gd	
1	0.00	0.00	N/A
2	0.00	0.00	N/A
3	1.61	2.31	1:1.43
4	0.00	0.00	N/A
5	0.00	0.00	N/A

$d_{air}(x) \sim 100$ nm

Point	Atomic %		Ga:Gd
	Ga	Gd	
1	0.00	0.00	N/A
2	1.40	1.84	1:1.31
3	1.86	2.40	1:1.29
4	1.63	2.24	1:1.37
5	0.00	0.00	N/A

$d_{air}(x) \sim 175$ nm

Point	Atomic %		Ga:Gd
	Ga	Gd	
1	0.00	0.00	N/A
2	1.73	2.59	1:1.5
3	0.27	0.00	N/A
4	1.99	2.86	1:1.44
5	0.00	0.00	N/A

$d_{air}(x) \sim 350$ nm

Point	Atomic %		Ga:Gd
	Ga	Gd	
1	0.00	0.00	N/A
2	1.53	2.03	1:1.33
3	1.73	2.31	1:1.34
4	0.00	0.00	N/A

$d_{air}(x) \sim 0.8$ μm

Point	Atomic %		Ga:Gd
	Ga	Gd	
1	1.03	1.43	1:1.38
2	1.65	2.14	1:1.30
3	0.85	0.80	1:0.94

FIGURE 5.19: SEM micrographs of GdGaO deposits and EDX measurements of the atomic percentages at the indicated points at various donor-receiver separations.

be obtained using a narrow-band source, e.g. another laser; however, the method used here is believed to be sufficiently accurate for this experiment where determination of the separation to ≈ 50 nm was all that was required.

Figure 5.18 shows SEM micrographs of deposits and arrays obtained as a function of separation for $0 \leq d_{air}(x) \leq 3$ μm and fig. 5.19 shows EDX measurements of the Gd and Ga atomic percentages over the same range; fluence of ≈ 100 mJ/cm^2 was used for all these results. It was immediately apparent that the donor-receiver separation had a very dramatic influence on the resultant deposits. With the donor and receiver in tight contact, virtually no GdGaO was transferred and only a trace Ga signal was recorded in the centre of the irradiated region; also, significant damage was observed to the surface of the receiver. For small separations, $d_{air}(x) \leq 50$ nm, solid donor material was transferred but in small, irregular fragments; damage to the receiver was again visible. The optimal separation was found to be $d_{air}(x) \approx 100 - 125$ nm where the best deposits in terms of shape, uniformity, and lack of surrounding debris were reproducibly obtained. A small increase in separation to about $d_{air}(x) \approx 175 - 200$ nm resulted in a dramatic change in the resultant deposit morphology; the deposited material typically displayed a ring-like shape with significant evidence of molten material. However, EDX measurements indicated that the molten regions did not contain any of the donor film constituents, suggesting that these regions were damaged receiver or residual DRL. Further increasing the separation to $d_{air}(x) \geq 350$ nm saw the disc-like (as opposed to ring-like) morphology of the deposits reappear, but with deposited material being significantly more cracked and damaged than at the optimal separation. Finally, increasing the separation still further to $d_{air}(x) \geq 0.75 - 0.8$ μm resulted in increased shattering of the deposits and evidence of some molten material transfer. At separations $d_{air}(x) \geq 1$ μm the deposited material was completely shattered during transfer and spread over a wide area.

The most unusual results were the deposits at $d_{air}(x) \approx 175 - 200$ nm, which displayed significant evidence of damage to the centre of the transferred material; such features were reproducibly obtained if and apparently only if $d_{air}(x) \approx 175 - 200$ nm. The reason for such features is not known for certain but we can make an hypothesis: with $d_{air}(x) \approx 175 - 200$ nm, the optical path difference between incident laser light, and light reflected back off the Si receiver in the donor film was ≈ 400 nm, i.e half the laser wavelength. Hence, constructive interference of the laser could occur in the donor and, as the donor damage threshold had been previously measured to be not much greater than the TP transfer threshold (see section 5.5.2), it can be concluded that the laser intensity inside the donor layer was sufficient to cause the observed damage. This is a potentially important observation for LIFT or DRL-LIFT of materials that do not absorb the laser well, i.e. that note must be taken of potential interference effects resulting from back reflections that could lead to unexpectedly high intensities and damage delicate materials. This issue is dealt with in more detail in the next chapter.

To complete the study of TP DRL-fs-LIFT, stylus profiling and SEM observations were performed of the holes left in the donor film after transfer. Figure 5.20 shows the results. The SEM micrographs of deposits are also shown for comparison. As can be seen, in tight contact virtually no material was removed from the donor, although obvious damage to the donor had occurred (a). For separations from $\approx 100 - 400$ nm, flat-bottomed holes in the donor were observed (b)&(c). The depth of such holes was reproducibly around 220 nm, conducive with complete removal of DRL and donor from the carrier. Combined with the evidence of typically 120-150 nm thick deposits (see fig. 5.16), this result clearly indicated complete removal of the TP after transfer. For larger separations, debris was observed in the holes after transfer (d)&(e). It is not known for certain if this debris was predominantly donor or residual DRL. However, the observation of some liquid material having been transferred with the deposits at these separations suggested the presence

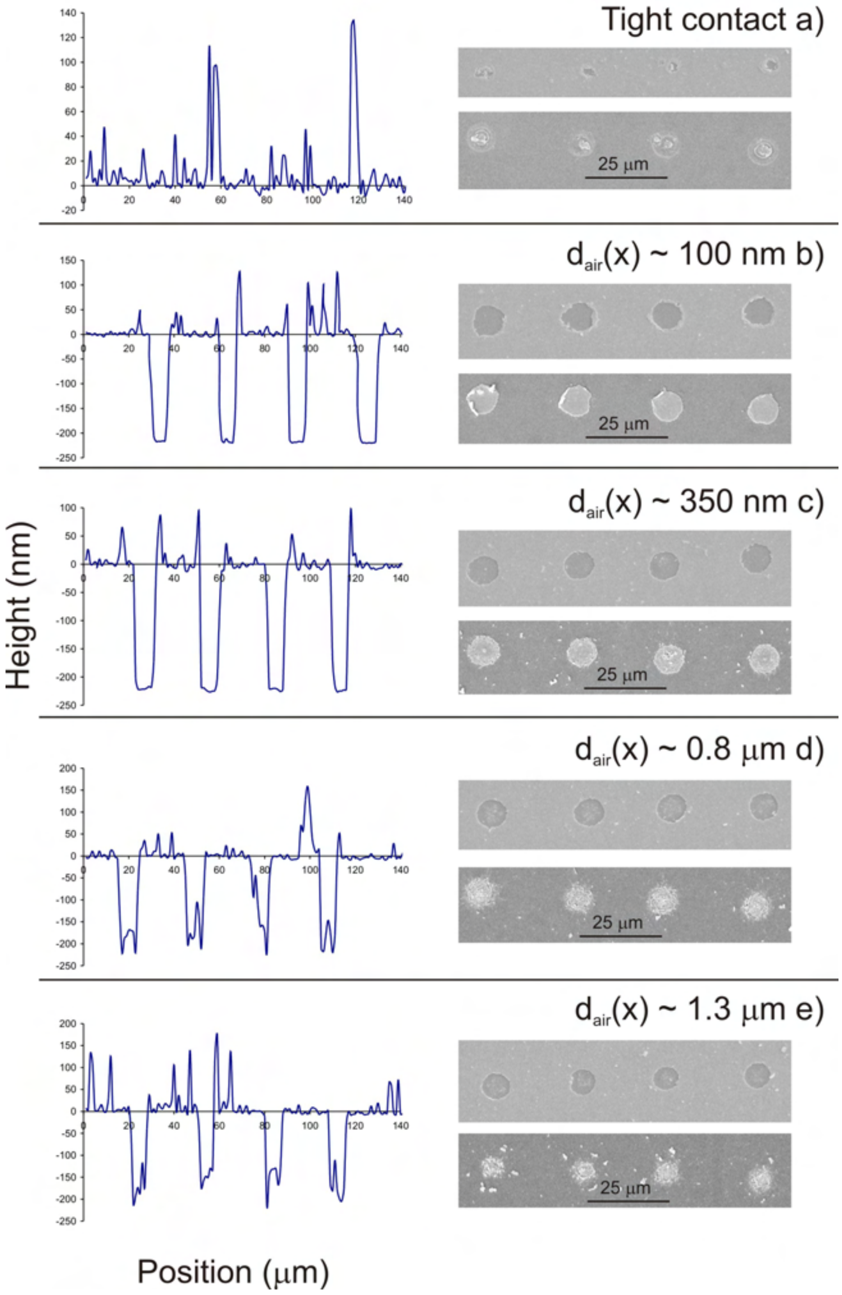

FIGURE 5.20: Stylus profiling of holes in GdGaO donor following DRL-fs-LIFT with the TP DRL at various donor-receiver separations. SEM micrographs of the corresponding donor holes and associated deposits are also shown.

of some DRL that was not fully decomposed as there was no obvious mechanism which would have resulted in the donor layer melting only at large donor-receiver separations.

Figure 5.21(a) shows a close-up SEM micrograph of a GdGaO deposit produced using the TP DRL with donor-receiver separation approximately optimal. Figure 5.21(b) and (c) show the resultant hole left in the donor film taken from above and at a viewing angle of 50°, respectively. The completeness and highly localised nature of material

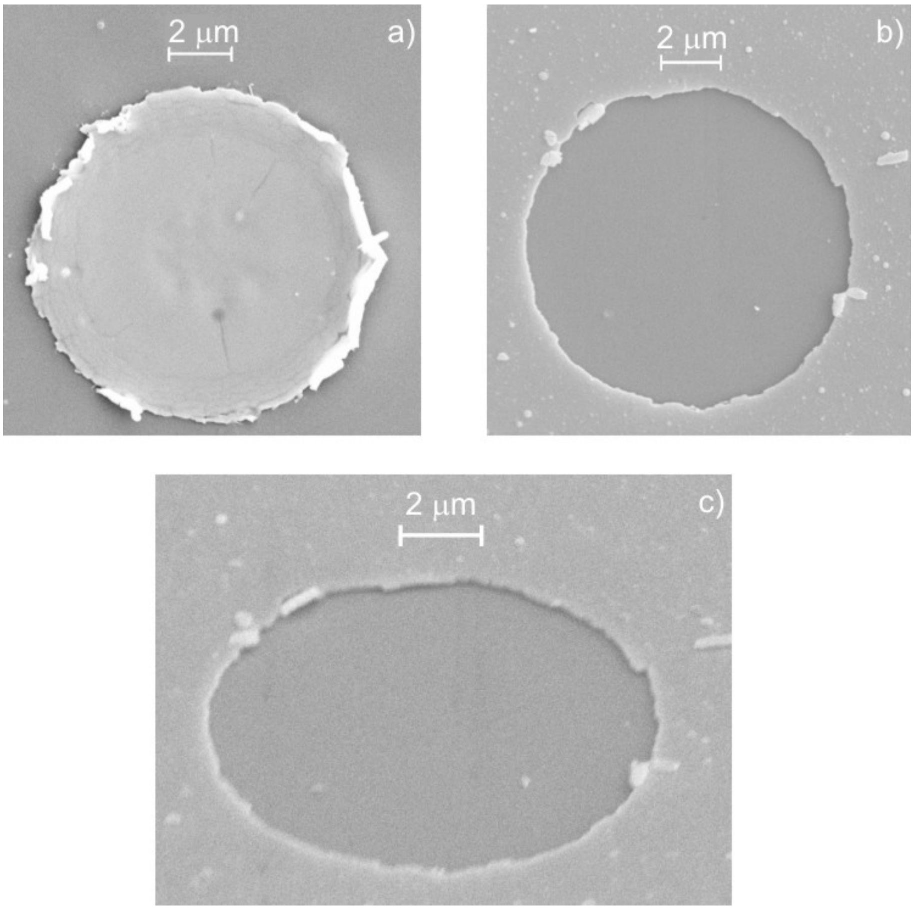

FIGURE 5.21: SEM micrographs of a deposit produced with optimal donor-receiver separation (a), and the associated hole in the donor film from above (b) and at 50° (c).

removal was apparent and clearly demonstrated the suitability of the TP for DRL-fs-LIFT applications.

5.6 Discussion

The first point to be made regarding DRL-fs-LIFT of GdGaO with Al, S1813, and TP DRLs was that all DRL materials allowed for transfer of the donor layer, apparently in solid phase, with much better uniformity than could be achieved without a DRL. The DRLs were all able to protect the donor during transfer and prevented the shattering and potential heat-induced changes that could occur without a DRL. Best quality depositions with all the DRL materials were obtained with fluences slightly above the transfer threshold.

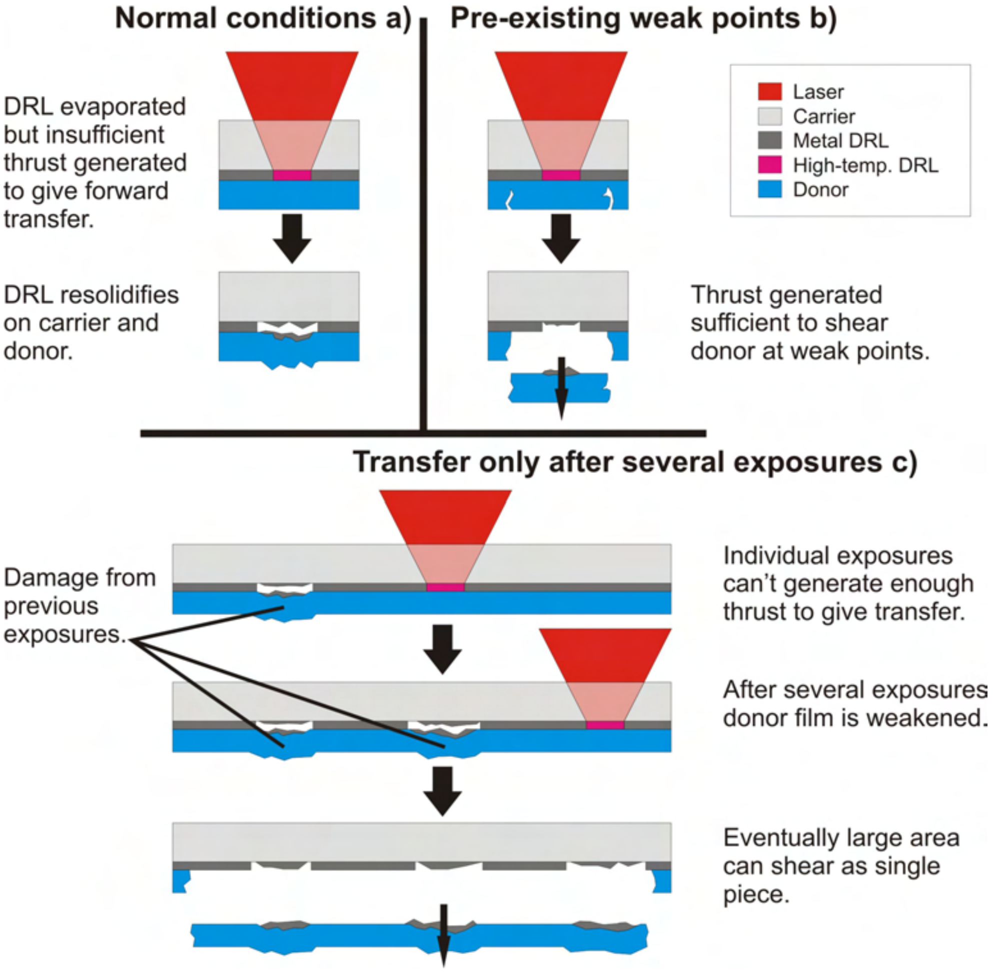

FIGURE 5.22: Hypothesised transfer processes of GdGaO donor with metallic (Al) DRL layer when there are no 'weak' areas in the donor (a), when there are weak points (b), and how successive exposures can give large area transfer (c).

5.6.1 DRL Materials

Let us now consider which material was 'best' for DRL applications. The Al layer only resulted in forward transfer in a minority of attempts and when transfer was successful the shape of resultant depositions varied significantly and there was evidence of residual DRL contamination and possibly melting of the donor film (see section 5.5.2.1). The reason for the high number of unsuccessful depositions may be hypothesised to be that the DRL was not thick enough and, even when completely vaporised, did not provide sufficient thrust to transfer the donor. Instead, transfer was determined by a combination of DRL evaporation and pre-existing weaknesses in the donor film influencing where the film sheared; the hypothesised transfer process is shown diagrammatically in fig. 5.22. Further experiments with metallic DRLs could be performed to identify more suitable DRL thickness. However, using thicker metal layers to increase the available thrust will increase the related problem of residual DRL contamination, which was observed even with the (probably) sub-optimal thickness layers investigated in this work.

The photoresist was a much more promising DRL material. Deposits obtained with this DRL exhibited a relatively uniform shape. The success rate (i.e. when material forward-transfer occurs after laser exposure) was $90 - 100\%$, much improved over the Al rate of $\approx 25\%$, although there was some evidence that the donor-receiver separation may again be very important in determining if good-quality deposits were obtained. The effect of separation was not studied because it could not be measured easily using the current setup; further work should investigate this effect. As with the Al DRL, there was also evidence of DRL contamination; this was probably due to a combination of incomplete dissociation of the photoresist and the thickness of the DRL layer. Time constraints prevented a thorough investigation with different photoresist thicknesses, but this should be performed before the S1813 is ruled out as a DRL material as it is much more readily available than more specialised polymers (e.g. the TP).

At present the TP represents the best DRL material for DRL-fs-LIFT at 800 nm that has been studied. Deposits produced using the TP (at the optimal donor-receiver separation) displayed highly reproducible shape, minimal cracking during transfer, no surrounding splatter, and little or no evidence of residual DRL contamination. As with the photoresist, the success rate was $\geq 90\%$, although the best depositions were only obtained in a well-defined, narrow range of donor-receiver separation (from $\approx 100 - 150$ nm).

5.6.2 Low Transfer Thresholds with Polymeric DRLs

A very important observation from the presented experiments that has not been discussed yet is the dramatically lower transfer threshold fluences with the polymeric DRL materials c.f. the conventional ablation thresholds of these materials at 800 nm with 130 fs pulses. The TP, for example, was transferred with fluence around 90-100 mJ/cm^2, only around 20% of the ablation threshold (≈ 500 mJ/cm^2 [Bonse et al., 2005a]). This was very different from the case of nanosecond polymer DRL-assisted LIFT where the LIFT threshold has been consistently found to be slightly above the polymer ablation threshold (see, for example, [Doraiswamy et al., 2006; Fardel et al., 2007b; Mito et al., 2001; Xu et al., 2007]). Hence a totally new process is observed when using femtosecond pulses for polymeric DRL-LIFT. This low threshold represents a major bonus for DRL-fs-LIFT over the longer pulsed regime as transfer can be effected with (much) lower energy pulses, reducing the thermal load on delicate overlying donor materials. A number of possible phenomena may explain the surprisingly low threshold; these are listed in table 5.1 (in order from most to least important) and described in more detail below.

Process	**Evidence in favour**	**Evidence against**
Abs. in carrier or donor causing indirect polymer heating	• Only a relatively small temp. increase of TP required to decompose • Evidence of Raman-Stokes process in carrier • Donor transfer threshold	• No visible evidence of laser damage to DRL or donor
Pressure increase in constrained DRL	• Complete polymer decomposition	• Damage threshold lowered without donor
3-photon abs. at 800 nm (266 nm)	• Strong abs. in S1813 and TP at 266 nm • 3-photon believed to be dominant in TP at 800 nm	• Relatively low probability for 3-photon process • Transfer fluence well below 3-photon ablation threshold
Linear abs. in DRL at 400 nm from the AC	• Strong abs. at 400 nm for S1813 • Close agreement between TP transfer threshold and white light threshold	• Abs. at 400 nm ≈ abs. at 800 nm for TP • ≤1% conversion efficiency can't explain observed threshold for TP
Impurities in DRL affecting abs. properties	• More linear abs. at 800 nm could explain lower threshold	• Doesn't explain different damage thresholds with and without donor
Partial polymer decomposition below full ablation threshold	• Constrained geometry of LIFT could allow transfer with only partial decomposition of polymer layer	• Results indicate TP is fully decomposed during transfer
Constructive interference in polymer	• Same effect seen to cause damage to donor	• Donor-receiver separation appeared to have no effect
Boiling off of solvent in polymer	• Solvent boils at lower temperatures than polymer	• Results indicate TP is fully decomposed during transfer • TP transfer threshold well below previously reported solvent boiling fluence
2-photon abs. at 800 nm (400 nm)	• Strong abs. at 400 nm for S1813	• Abs. at 400 nm ≈ abs. at 800 nm for TP • No evidence in literature for 2-photon damage of TP

TABLE 5.1: Possible processes that may explain low transfer threshold fluence with polymeric DRLs, in order from most (top) to least (bottom) important.

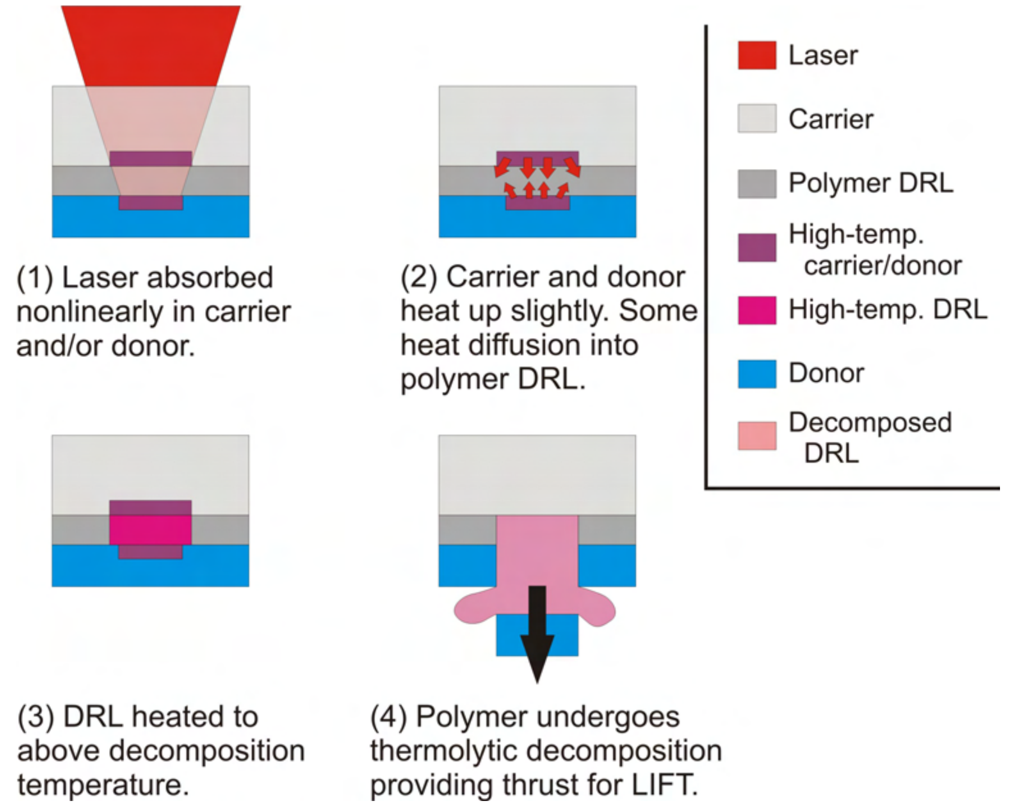

FIGURE 5.23: Schematic of how nonlinear absorption in the carrier and donor could cause heating of a polymer DRL and lead to LIFT below the polymer ablation threshold.

The first possible process leading to the lower than expected transfer thresholds with polymer DRLs involves indirect heating of the polymer layer (shown in fig. 5.23). The idea is that the laser energy is partially absorbed in one or both of the carrier and donor. Although the amount of absorbed energy is insufficient to damage the donor/carrier (hence the lack of visible damage to these materials), it could be sufficient to heat the material slightly. As was stated earlier, the thermal decomposition temperature of the TP is relatively low (≈ 250 °C), so the amount of heat energy that must be transferred to the polymer layer is small. Several of pieces of evidence support this model:

1. The donor layer was transferred with a fluence only slightly higher without a DRL than when the DRL was used; hence it was likely some absorption of laser energy in the donor could have occurred at the typical TP transfer fluences.
2. The AC spectra presented earlier indicated that some Raman-Stokes processes were occurring in the carrier, which would result in some carrier heating close to the polymer interface.
3. The lower DRL damage threshold seen with than without a donor layer can be explained by the extra heating occurring because of absorption in the donor.

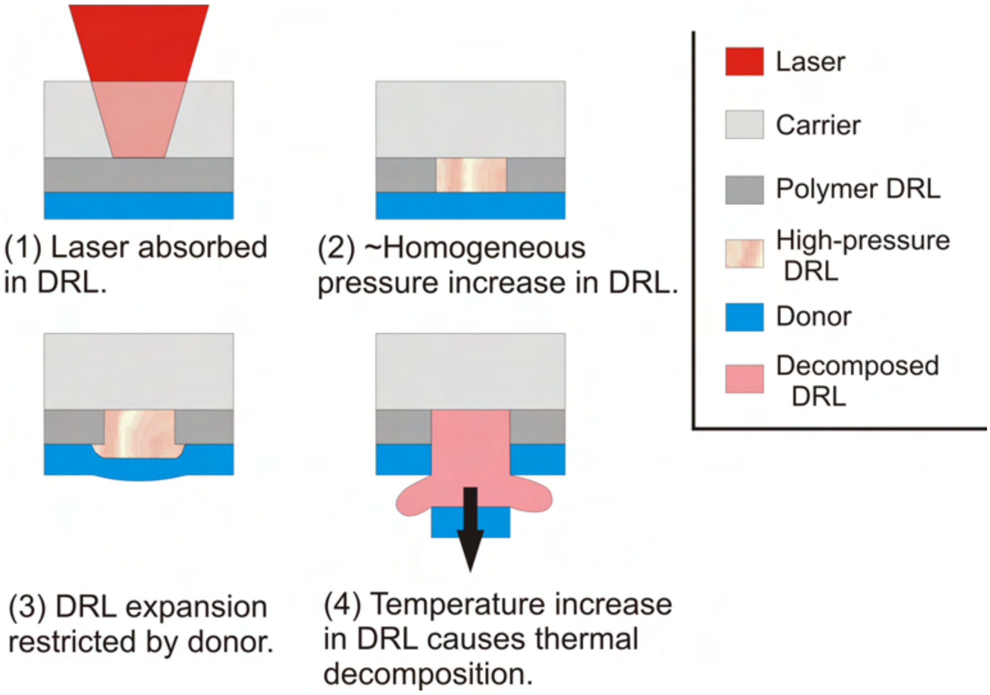

FIGURE 5.24: Schematic of how a pressure increase in a polymer DRL could lead to sub-ablation threshold thermolytic decomposition if relaxation of the pressure increase cannot occur due to an overlying donor layer.

It is difficult to relate this idea to the case of S1813 because its thermal decomposition properties (or even if thermal decomposition is possible) are unknown. This model appears to (partially, at least) explain the transfer process with the TP; however, modelling of the temperatures reached during the process will be necessary to determine if indirect heating is the primary driving force for transfer. The reason that the low threshold is only seen with femtosecond pulses can also be explained using this model because the transparent carrier/donor would not absorb nanosecond pulses. The only problem with this interpretation is that it is difficult to explain why the TP appeared to only partially decompose when donor-receiver separation was increased.

The second likely process involves a pressure increase of the polymer following absorption of the laser energy that cannot be easily relaxed by expansion due to the presence of the overlying donor. It is well known that absorption of ultrashort duration pulses in polymers initiates a rapid pressure jump in the target due to the pulse energy being deposited faster than the target can fully relax (see e.g. [Hare et al., 1995]). This is in sharp contrast to exposure to longer duration pulses, where the relatively slow rate of energy deposition predominantly results in a temperature increase. However, even with ultrashort pulses, with free surface ablation this pressure increase can be somewhat relaxed by expansion of the target. In a DRL-fs-LIFT arrangement, particularly with a hard donor film, significant expansion of the polymer is restricted by the overlying layer.

Hence in this case, the pressure of the polymer DRL is raised sharply by absorbing the femtosecond pulse. The increase cannot be easily relaxed by polymer expansion, so a sharp temperature increase in the polymer occurs. This temperature increase results in the DRL temperature rising and thermolytic decomposition can occur. The model is shown in fig. 5.24. In principle, it explains why the low transfer threshold is only seen in the femtosecond regime, and why complete decomposition of the TP DRL was observed only when the donor-receiver separation was relatively small. However, on its own, this model cannot explain the lower damage threshold observed for a TP layer with no overlying donor, and there is the point that the absorption of the TP is very low at 800 nm, so any pressure increase would be very small.

A number of other processes including multiphoton absorption, influence of the AC, absorption by impurities in the polymer DRLs, partial polymer decomposition occurring below the full ablation threshold, and interference effects in the DRL, have all been considered as possible explanations for the low threshold. However, none of them on their own can fully explain all the features of the process, namely

- why the low threshold is only seen in the femtosecond regime.
- why having an overlying donor affects the polymer damage threshold.
- why donor-receiver separation didn't affect damage threshold.
- why complete decomposition of the polymer layer was observed.

It is considered most likely that a combination of processes led to the low threshold, however the relative importance of each is not yet known. At present it appears that indirect heating of the TP by absorption in the GdGaO and the constrained expansion were the most likely causes for the low transfer threshold. Further experiments and modeling studies will be necessary to fully understand the process.

The final point to consider is the variation of deposit morphology with separation when a TP DRL was used. The observed results supported a model where transfer was effected by a relatively gentle bending and shearing of the donor film; the envisaged process is shown in fig. 5.25.

The model can be explained as follows. When donor and receiver were in tight contact, no discs of donor material were obtained. The TP decomposed due to the various reasons described previously, however the tight contact with the receiver prevented expansion of the decomposed polymer, which was necessary to shear the donor material. Instead the high pressure build up in the irradiated region just caused some damage to the underlying Si receiver. With a small donor-receiver separation, there was sufficient space to allow a

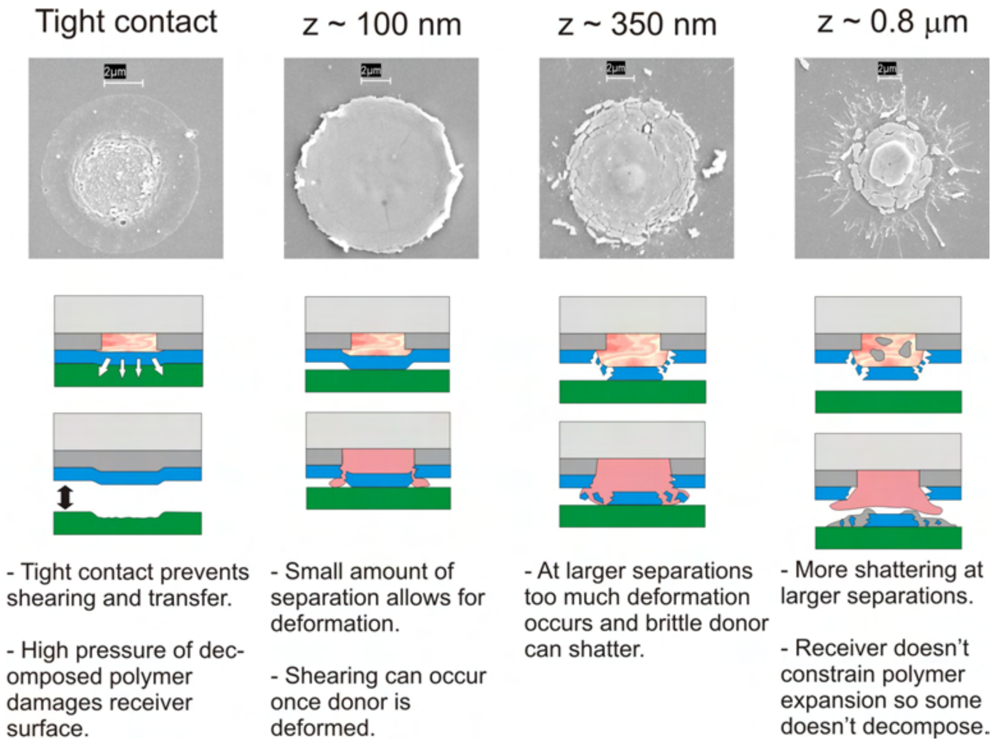

Figure 5.25: Illustration of hypothesised transfer process for polymer DRL-fs-LIFT with varying donor-receiver separation based on observed results.

small amount of expansion of the decomposed polymer which allowed for relatively clean shearing and transfer of a clean disc of donor; however excessive deformation of the donor film was prevented by the close proximity of the receiver. The slight deformation of the donor film prior to shearing also explains the slightly raised edges of the best deposits reported previously (see fig. 5.16). As the separation was increased, the brittle donor experienced increased deformation and could shatter, resulting in a more particulate deposit. It was observed that there appeared to be some liquid material transferred at larger separations; it is not obvious why an increase in separation would lead to the donor melting during transfer so it is hypothesised that this material may be DRL that did not decompose. A possible explanation for this, which supports the idea of pressure-induced decomposition proposed above (see fig. 5.24), could be that polymer expansion was not sufficiently constrained when the receiver was (relatively) far away, so full decomposition did not occur. We conclude therefore that the Si receiver also played a critical role in determining the final quality of deposited material. The receiver had to be close enough to the donor to constrain deformation of the brittle donor and prevent shattering. However, a small separation between donor and receiver was necessary to allow some deformation of the donor, ultimately leading to shearing of the donor film.

5.7 Conclusions

In this chapter, a number of important discussions related to fs-LIFT and DRL-fs-LIFT have been presented. The subject of dynamic release layers has been covered in detail, specifically the features that make a material suitable for DRL applications. Also introduced was the principle of active carriers, which may be important for future fs-LIFT studies but is not believed to have had much impact on the work in this chapter.

The experiments that were reported on concerned the DRL-fs-LIFT of an amorphous GdGaO layer with and without DRLs. Metallic and polymeric DRLs were used to investigate which were more suitable. The results presented here appeared to indicate that polymeric DRLs produced better results in terms of deposit reproducibility, uniformity, and minimising residual DRL contamination post-transfer. Of the two polymers investigated, a custom-designed triazene polymer produced better results than a commercially available photoresist, although further work is needed to optimise the photoresist thickness before this material can be completely discounted.

Arguably the most important finding of this work was that the transfer threshold fluence with polymeric DRLs was much lower than the polymer ablation threshold if and only if femtosecond pulses were used to initiate transfer. A number of processes have been considered as possible explanations for this low threshold and their relative likelihoods discussed. At present the most likely is considered to be nonlinear absorption in the carrier and donor that led to indirect heating of the polymer layer and subsequent thermolytic decomposition. Another process that may be significant concerns pressure increases in the polymer layer that cannot be relaxed due to the overlying donor and close proximity of the receiver. It is most likely that a combination of effects contributed to the low threshold; more experiments and modeling are required to fully understand the origin of the surprisingly low threshold.

Bibliography

Bahnisch, R., Gross, W., and Menschig, A. (2000). Single-shot, high repetition rate metallic pattern transfer. *Microelectron. Eng.*, 50:541–546.

Banks, D., Grivas, C., Mills, J., Zergioti, I., and Eason, R. (2006). Nanodroplets deposited in microarrays by femtosecond ti:sapphire laser induced forward transfer. *Appl. Phys. Lett.*, 89:193107.

Bera, S., Sabbah, A., Yarbrough, J., Allen, C., Winters, B., Durfee, C., and Squier, J. (2007). Optimization study of the femtosecond laser-induced forward-transfer process with thin aluminium films. *Appl. Opt.*, 46(21):4650–4659.

Bonse, J., Solis, J., Urech, L., Lippert, T., and Wokaun, A. (2007). Femtosecond and nanosecond laser damage thresholds of doped and undoped triazenepolymer thin films. *Appl. Surf. Sci.*, 253:7787–7791.

Bonse, J., Wiggins, S., Solis, J., and Lippert, T. (2005a). Phase change dynamics in a polymer thin film upon femtosecond and picosecond laser irradiation. *Appl. Surf. Sci.*, 247:440–446.

Bonse, J., Wiggins, S., Solis, J., Lippert, T., and Sturm, H. (2005b). Femtosecond laser-induced decomposition in triazenepolymer thin films. *Appl. Surf. Sci.*, 248:157–162.

Brodeur, A. and Chin, S. (1999). Ultrafast white-light continuum generation and self-focusing in transparent condensed media. *J. Opt. Soc. Am. B*, 16(4):637–650.

Doraiswamy, A., Narayan, R., Lippert, T., Urech, L., Wokaun, A., Nagel, M., Hopp, B., Dinescu, M., Modi, R., Auyeung, R., and Chrisey, D. (2006). Excimer laser forward transfer of mammalian cells using a novel triazene absorbing layer. *Appl. Surf. Sci.*, 252:4743–4747.

Fardel, R., Feurer, P., Lippert, T., Nagel, M., Nuesch, F., and Wokaun, A. (2007a). Laser ablation of aryltriazene photopolymer films: Effects of polymer structure on ablation properties. *Appl. Surf. Sci.*, 254:13321337.

Fardel, R., Nagel, M., Nuesch, F., Lippert, T., and Wokaun, A. (2007b). Fabrication of organic light-emitting diode pixels by laser-assisted forward transfer. *Appl. Phys. Lett.*, 91:061103.

Fardel, R., Nagel, M., Nuesch, F., Lippert, T., and Wokaun, A. (2007c). Laser forward transfer using a sacrificial layer: influence of the material properties. *Appl. Surf. Sci.*, 254:1322–1326.

Haight, R., Longo, P., and Wagner, A. (2003). Metal deposition with femtosecond light pulses at atmospheric pressure. *J. Vac. Sci. Technol. A*, 21(3):649–652.

Hare, D., Franken, J., and Dlott, D. (1995). Coherent raman measurements of polymer thin-film pressure and temperature during picosecond laser ablation. *J. Appl. Phys.*, 77(11):5950–5960.

Herman, I. (1989). Laser-assisted deposition of thin films from gas-phase and surface-adsorbed molecules. *Chem. Rev*, 89:1323–1357.

Hopp, B., Smausz, T., Antal, Z., Kresz, N., Bor, Z., and Chrisey, D. (2004). Absorbing film assisted laser induced forward transfer of fungi (trichoderma conidia). *J. Appl. Phys.*, 96(6):3478–3481.

Karnakis, D., Lippert, T., Ichinose, N., Kawanishi, S., and Fukumura, H. (1998). Laser induced molecular transfer using ablation of a triazeno-polymer. *Appl. Surf. Sci.*, 127-129:781–786.

Koch, J., Fadeeva, E., Engelbrecht, M., Ruffert, C., Gatzen, H., Ostendorf, A., and Chichkov, B. (2006). Maskless nonlinear lithography with femtosecond laser pulses. *Appl. Phys. A*, 82:2326.

Lippert, T. and Dickinson, J. (2003). Chemical and spectroscopic aspects of polymer ablation: Special features and novel directions. *Chem. Rev*, 103:453–485.

Mito, T., Tsujita, T., Masuhara, H., Hayashi, N., and Suzuki, K. (2001). Hollowing and transfer of polymethyl methacrylate film propelled by laser ablation of triazeno polymer film. *Jpn. J. Appl. Phys.*, 40:L805–L806.

Nagel, M., Hany, R., Lippert, T., Molberg, M., Nuesch, F., and Rentsch, D. (2007). Aryltriazene photopolymers for uv-laser applications: Improved synthesis and photodecomposition study. *Macromol. Chem. Phys.*, 208:277–286.

Nagura, C., Suda, A., Kawano, H., Obara, M., and Midorikawa, K. (2002). Generation and characterization of ultrafast white-light continuum in condensed media. *Appl. Optics*, 41(18):3735–3742.

Papakonstantinou, P., Vainos, N., and Fotakis, C. (1999). Microfabrication by uv femtosecond laser ablation of pt, cr and indium oxide thin films. *Appl. Surf. Sci.*, 151:159–170.

Serra, P., Colina, M., Fernandez-Pradas, J., Sevilla, L., and Morenza, J. (2004). Preparation of functional dna microarrays through laser-induced forward transfer. *Appl. Phys. A*, 85(9):1639–1641.

Shipley (2002). Microposit s1800 series photo resists. Data sheet.

Smausz, T., Hopp, B., Kecskemeti, G., and Bor, Z. (2006). Study on metal microparticle content of the material transferred with absorbing film assisted laser induced forward transfer when using silver absorbing layer. *Appl. Surf. Sci.*, 252:4738–4742.

Tolbert, W., Lee, I., Doxtader, M., Ellis, E., and Dlott, D. (1993). High-speed color imaging by laser ablation transfer with a dynamic release layer: fundamental mechanisms. *J. Imag. Sci. Tech.*, 37(4):411–421.

Xu, J., Liu, J., Cui, D., Gerhold, M., Wang, A., Nagel, M., and Lippert, T. (2007). Laser-assisted forward transfer of multi-spectral nanocrystal quantum dot emitters. *Nanotechology*, 18:025403.

Zergioti, I., Papazoglou, D., Karaiskou, A., Fotakis, C., Gamaly, E., and Rode, A. (2003). A comparative schlieren imaging study between ns and sub-ps laser forward transfer of cr. *Appl. Surf. Sci.*, 208-209:177–180.

Chapter 6

The Influence of Interference in Multi-Layered Stacks of Transparent Thin Films on Ablation, LIFT, and DRL-LIFT

Nomenclature

z	Global depth
t	Time
E_{In}	Incident electric field amplitude
λ	Wavelength (in air)
ω	Angular frequency

In layer j

z_j	Local depth
$\mathbf{E^+_{j,i}(z)}$	Electric field propagating in positive z-direction
$\mathbf{E^-_{j,i}(z)}$	Electric field propagating in negative z-direction
	- i distinguishes multiple reflections
$\mathbf{E_j(z)}$	Total electric field
$E_{In,j}$	Effective electric field amplitude incident on layer
$\mathbf{I_j(z)}$	Intensity
k_j	Propagation constant
$\mathbf{n_j}$	Complex refractive index
n_j	Real part of refractive index
κ_j	Imaginary part of refractive index
α_j	Absorption coefficient
d_j	Thickness of layer
τ_j	Internal transmittance - energy lost due to absorption during propagation through layer

Between layers i and j

Γ_{ij}	Interface
t_{ij}	Transmission coefficient
r_{ij}	Reflection coefficient

Coefficients in multiple thin-film structures

r'_{ij}	Effective reflection coefficient between layer i and all subsequent layers
r^*_{ij}	As r'_{ij} but looking in opposite direction ($= -r'_{ij}$)
t'_{ij}	Effective transmission coefficient at Γ_{ij} ($= 1 - r'_{ij} = 1 + r^*_{ij}$)
X_j	Term relating $r'_{j,j+1}$ and $r'_{j-1,j}$
Y_j	Term relating $r{*}_{j,j-1}$ and $r{*}_{j+1,j}$

6.1 Introduction

When monochromatic light is incident on one or more thin films sandwiched between two effectively infinite dielectric media, a standing wave pattern is produced in the film(s). The standing wave is a result of interference between forward and backward propagating light waves via reflection off the various interfaces within the multi-layered structure. At points within the films where this interference is constructive (or destructive), the local light intensity may be significantly higher (or lower) than the incident intensity. Hence, for the laser-ablation (and LIFT) of semi-transparent thin films (i.e. films where the optical penetration depth is much greater than the film thickness), these multiple reflections must be considered to determine the peak intensity within the target film, which ultimately determines the ablation threshold. This has particular relevance to the front- and rear-side ablation and LIFT thresholds of the triazene and photoresist polymer DRLs described in chapter 5.

In this chapter, the theory of standing waves in multi-layered thin film structures is developed and applied to cases like those encountered in the experiments. Selected results from the DRL-fs-LIFT study in chapter 5 are included to compare with the theoretical predictions. The derivations in the next section follow closely those of C.A. Mack [Mack, 1986] and Widmann [Widmann, 1975]. The ultimate goal of this investigation is to determine if the formation of optical standing waves can explain the surprisingly low DRL-fs-LIFT thresholds observed in the experiments in the previous chapter. It should be noted that the presented theory is for monochromatic illumination, whereas the femtosecond source used in the experiments had a bandwidth of 9-10 nm. As such, caution must be used when comparing the theoretical predictions with experimental results. However, as the bandwidth was small compared to the standing wave period, the qualitative effect of the finite bandwidth on the standing wave can be expected to be minimal.

6.2 Theory

6.2.1 Single Thin Film Case

Consider first the case shown in fig. 6.1 of a single thin film on the front-side of a relatively thick substrate. We define the air as layer 1, the thin film as layer 2, and the substrate as layer 3. The film is exposed to a normally incident monochromatic plane wave, $\mathbf{E_{In}(z)} = \mathbf{E^{+}_{1,1}(z)} = E_{In}exp(-ik_1 z)exp(i\omega t)$, i.e. a forward propagating wave of amplitude E_{In}, where k_1 denotes the propagation constant in layer 1. $\mathbf{E^{+}_{j,i}(z)}$ denotes

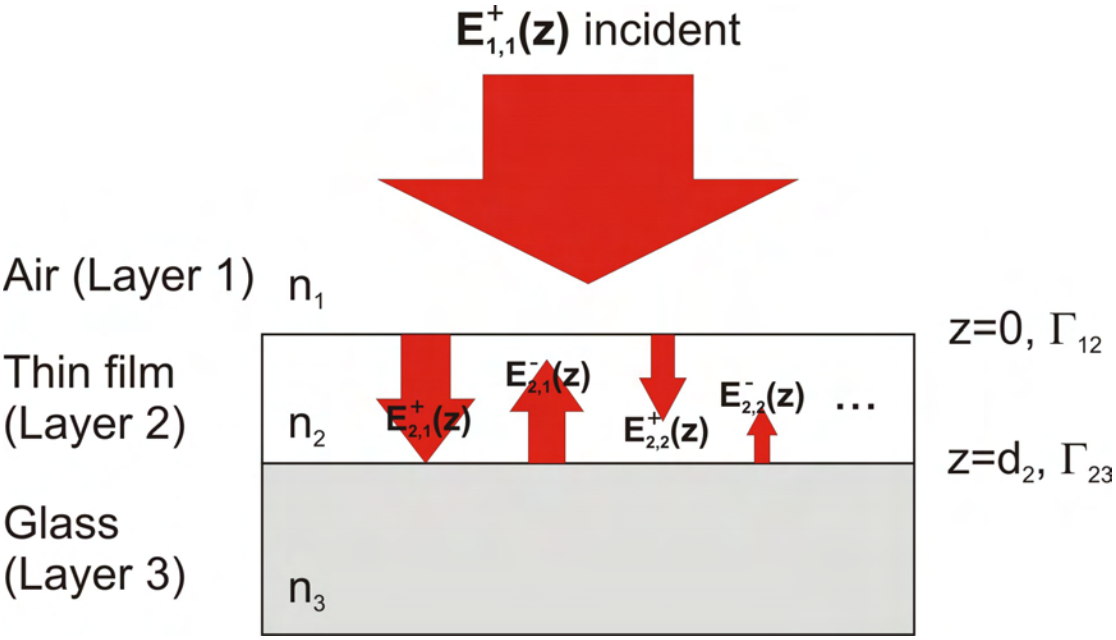

FIGURE 6.1: Schematic of the various travelling waves present in a single thin film on a glass substrate under monochromatic, plane-wave illumination. Multiple reflections have been spatially separated in the diagram for ease of viewing.

the i^{th} forward propagating wave in layer j; later $\mathbf{E^-_{j,i}(z)}$ will be used for backward propagating waves. For simplicity, it is chosen to set $z = 0$ at the first interface, Γ_{12}, i.e. the interface between layers 1 and 2; in this case the air/film interface. $\mathbf{E^+_{1,1}(z)}$ is partially transmitted by this interface, which gives rise to a transmitted wave propagating forward in the film, $\mathbf{E^+_{2,1}(z)}$, of the form

$$\mathbf{E^+_{2,1}(z)} = E_{In}t_{12}exp(-ik_2z_2)exp(i\omega t) \tag{6.1}$$

where E_{In} = the incident amplitude

$t_{ij} = 2\mathbf{n}_i/(\mathbf{n}_i + \mathbf{n}_j)$ = the transmission coefficient at Γ_{ij}

$\mathbf{n}_j = n_j + i\kappa_j$ = the complex refractive index

$k_j = 2\pi\mathbf{n}_j/\lambda$ = the propagation constant in layer j

λ = wavelength

ω = the angular frequency

and z_j is the local depth into layer j[1]; note that, as we have chosen $z = 0$ at Γ_{12}, $z_2 = z$. κ_2 can be determined from the absorption coefficient of the thin film, α_2, using $\kappa_2 = -\alpha_2\lambda/4\pi$.

---

[1] Note that, although it may seem unnecessarily complicated to refer to a local depth here, local depths will be important later for multi-layered stacks and so, for consistency, we will use the local depth here also

$\mathbf{E}^{+}_{\mathbf{2,1}}(\mathbf{z})$ is then reflected back off the film/substrate interface at $z_2 = d_2$, where d_2 is the thickness of layer 2 (i.e. the film thickness). This reflection gives rise to a new, backward propagating wave in the film, $\mathbf{E}^{-}_{\mathbf{2,1}}(\mathbf{z})$,

$$\mathbf{E}^{-}_{\mathbf{2,1}}(\mathbf{z}) = r_{23}\mathbf{E}^{+}_{\mathbf{2,1}}(\mathbf{d_2})exp[ik_2(z_2 - d_2)] \tag{6.2}$$

where $r_{ij} = (\mathbf{n}_i - \mathbf{n}_j)/(\mathbf{n}_i + \mathbf{n}_j)$ = the reflection coefficient at Γ_{ij}.

Combining equations 6.2 and 6.1 gives

$$\begin{aligned}\mathbf{E}^{-}_{\mathbf{2,1}}(\mathbf{z}) &= r_{23}E_{In}t_{12}exp(-ik_2d_2)exp(i\omega t)exp[ik_2(z_2 - d_2)]\\ &= r_{23}E_{In}t_{12}exp(-i2k_2d_2)exp(ik_2z_2)exp(i\omega t)\\ &= E_{In}t_{12}r_{23}\tau_2^2 exp(ik_2z_2)exp(i\omega t) \qquad (6.3)\end{aligned}$$

where $\tau_j = exp(-ik_jd_j)$ is the internal transmittance of layer j, i.e. the energy lost to absorption during propagation across layer j.

Multiple reflections off Γ_{12} and Γ_{23} occur, giving rise to further forward and backward propagating waves;

$$\mathbf{E}^{+}_{\mathbf{2,2}}(\mathbf{z}) = E_{In}t_{12}r_{23}r_{21}\tau_2^2 exp(-ik_2z_2)exp(i\omega t) \tag{6.4}$$
$$\mathbf{E}^{-}_{\mathbf{2,2}}(\mathbf{z}) = E_{In}t_{12}r_{23}^2r_{21}\tau_2^4 exp(ik_2z_2)exp(i\omega t) \tag{6.5}$$
$$\mathbf{E}^{+}_{\mathbf{2,3}}(\mathbf{z}) = E_{In}t_{12}r_{23}^2r_{21}^2\tau_2^4 exp(-ik_2z_2)exp(i\omega t) \tag{6.6}$$
$$\mathbf{E}^{-}_{\mathbf{2,3}}(\mathbf{z}) = E_{In}t_{12}r_{23}^3r_{21}^2\tau_2^6 exp(ik_2z_2)exp(i\omega t) \tag{6.7}$$

and so on. Hence we can write

$$\mathbf{E}^{+}_{\mathbf{2,j}}(\mathbf{z}) = E_{In}t_{12}r_{23}^{j-1}r_{21}^{j-1}\tau_2^{2(j-1)} exp(-ik_2z_2)exp(i\omega t) \tag{6.8}$$
$$\mathbf{E}^{-}_{\mathbf{2,j}}(\mathbf{z}) = E_{In}t_{12}r_{23}^{j}r_{21}^{j-1}\tau_2^{2j} exp(ik_2z_2)exp(i\omega t) \tag{6.9}$$

Of course, there are also other propagating waves in layers 1 and 3, but these are not relevant to the applications of ablation, LIFT, and DRL-LIFT that will be studied later and so are neglected.

The total electric field in the thin film, $\mathbf{E_2}(\mathbf{z})$, is then the summation of all these forwards and backwards propagating waves:

$$\mathbf{E_2}(\mathbf{z}) = \sum_{j=1}^{\infty}\left(\mathbf{E}^{+}_{\mathbf{2,j}}(\mathbf{z}) + \mathbf{E}^{-}_{\mathbf{2,j}}(\mathbf{z})\right) \tag{6.10}$$

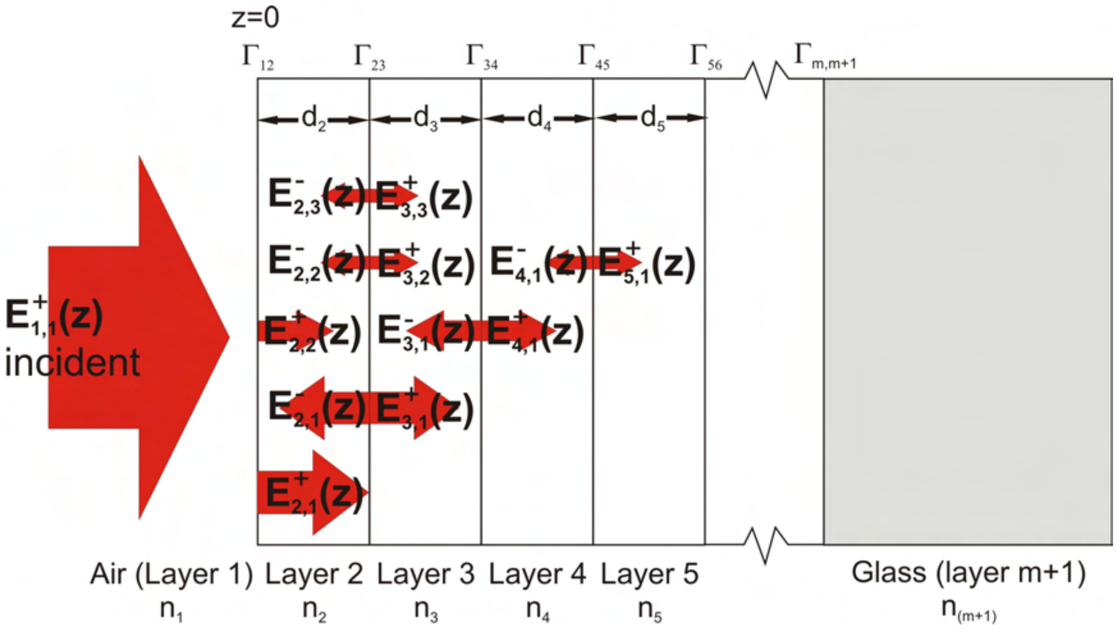

FIGURE 6.2: Schematic of the first 4 possible reflections in a stack of transparent thin films illuminated by a monochromatic, plane-wave source.

Substituting equations 6.8 and 6.9 into 6.10, it is straightforward to show that

$$\mathbf{E_2(z)} = E_{In}t_{12}[exp(-ik_2z_2) + r_{23}\tau_2^2 exp(ik_2z_2)]exp(i\omega t) \times S \tag{6.11}$$

where $S = 1 + r_{21}r_{23}\tau_2^2(1 + r_{21}r_{23}\tau_2^2(1 + \ldots))$, is a geometric series. Hence, we arrive at

$$S = 1/(1 - r_{21}r_{23}\tau_2^2) = 1/(1 + r_{12}r_{23}\tau_2^2) \tag{6.12}$$

as $r_{21} = -r_{12}$, and so

$$\mathbf{E_2(z)} = E_{In}t_{12}\left(\frac{exp(-ik_2z_2) + r_{23}\tau_2^2 exp(ik_2z_2)}{1 + r_{12}r_{23}\tau_2^2}\right)exp(i\omega t) \tag{6.13}$$

Finally, the intensity in the film, $\mathbf{I_2(z)}$, is proportional to the square of the magnitude of $\mathbf{E_2(z)}$

$$\begin{aligned}\mathbf{I_2(z)} &\propto |\mathbf{E_2(z)}|^{\mathbf{2}} \\ &= I_2\left|E_{In}t_{12}\frac{exp(-ik_2z_2) + r_{23}\tau_2^2 exp(ik_2z_2)}{1 + r_{12}r_{23}\tau_2^2}\right|^2\end{aligned} \tag{6.14}$$

Where I_2 is a constant of proportionality. Note that the time dependence has disappeared when taking the modulus of equation 6.13.

6.2.2 Multiple Film Case

It is reasonably simple to extend the above analysis for a single film to the case of multiple thin films (as shown in fig. 6.2). The derivation is performed for the general case of an $m+1$ layer system, that is $m-1$ thin films between two thicker layers for completeness. This time there are multiple reflected and transmitted waves from all the interfaces within the structure that must all be accounted for to determine the overall intensity profile in each layer. As before the incident field, $\mathbf{E^{In}(z)}$, is partially transmitted through the first interface to give $\mathbf{E^{+}_{2,1}(z)} = E_{In}t_{12}exp(-ik_2z_2)exp(i\omega t)$ in layer 2. $\mathbf{E^{+}_{2,1}(z)}$ can be reflected or transmitted at Γ_{23} to give

$$\mathbf{E^{-}_{2,1}(z)} = E_{In}r_{23}t_{12}\tau_2^2 exp(ik_2z_2)exp(i\omega t) \tag{6.15}$$

$$\text{and } \mathbf{E^{+}_{3,1}(z)} = E_{In}t_{23}t_{12}\tau_2^2 exp(-ik_3z_3)exp(i\omega t). \tag{6.16}$$

$\mathbf{E^{-}_{2,1}(z)}$ can then be reflected back from Γ_{12} (the transmitted wave into layer 1 is ignored as before), whilst $\mathbf{E^{+}_{3,1}(z)}$ can be reflected or transmitted at Γ_{34}, so

$$\mathbf{E^{+}_{2,2}(z)} = E_{In}r_{23}r_{21}t_{12}\tau_2^2 exp(-ik_2z_2)exp(i\omega t) \tag{6.17}$$

$$\mathbf{E^{-}_{3,1}(z)} = E_{In}t_{23}t_{12}r_{34}\tau_2^2\tau_3^2 exp(ik_3z_3)exp(i\omega t) \tag{6.18}$$

$$\text{and } \mathbf{E^{+}_{4,1}(z)} = E_{In}t_{23}t_{12}t_{34}\tau_2^2\tau_3^2 exp(-ik_4z_4)exp(i\omega t). \tag{6.19}$$

These fields can also reflect and transmit at Γ_{23} and Γ_{45} giving,

$$\mathbf{E^{-}_{2,2}(z)} = E_{In}r_{23}^2r_{21}t_{12}\tau_2^4 exp(ik_2z_2)exp(i\omega t) \tag{6.20}$$

$$\mathbf{E^{+}_{3,2}(z)} = E_{In}r_{23}r_{21}t_{12}t_{23}\tau_2^4 exp(-ik_3z_3)exp(i\omega t) \tag{6.21}$$

$$\mathbf{E^{-}_{2,3}(z)} = E_{In}t_{23}t_{12}r_{34}t_{32}\tau_2^2\tau_3^2 exp(ik_2z_2)exp(i\omega t) \tag{6.22}$$

$$\mathbf{E^{+}_{3,3}(z)} = E_{In}t_{23}t_{12}r_{34}r_{32}\tau_2^2\tau_3^2 exp(-ik_3z_3)exp(i\omega t) \tag{6.23}$$

$$\mathbf{E^{-}_{4,1}(z)} = E_{In}t_{23}t_{12}t_{34}r_{45}\tau_2^2\tau_3^2\tau_4^2 exp(ik_4z_4)exp(i\omega t) \tag{6.24}$$

$$\text{and } \mathbf{E^{+}_{5,1}(z)} = E_{In}t_{23}t_{12}t_{34}t_{45}\tau_2^2\tau_3^2\tau_4^2 exp(-ik_5z_5)exp(i\omega t). \tag{6.25}$$

The situation up to $\mathbf{E^{+}_{5,1}(z)}$ is shown in fig. 6.2 for clarity. As can be seen, the situation for a large number of films rapidly becomes complicated. The electric field in the top thin film (i.e. the second layer), $\mathbf{E_2}(z)$, is given by [Mack, 1986]

$$\mathbf{E_2(z)} = E_{In}t_{12}\frac{exp(-ik_2z_2) + r'_{23}\tau_2^2 exp(ik_2z_2)}{1 + r_{12}r'_{23}\tau_2^2}exp(i\omega t) \tag{6.26}$$

where

$$r'_{23} = \frac{\mathbf{n}_2 - \mathbf{n}_3 X_3}{\mathbf{n}_2 + \mathbf{n}_3 X_3}, \tag{6.27}$$

$$X_3 = \frac{1 - r'_{34}\tau_3^2}{1 + r'_{34}\tau_3^2}, \tag{6.28}$$

$$r'_{34} = \frac{\mathbf{n}_3 - \mathbf{n}_4 X_4}{\mathbf{n}_3 + \mathbf{n}_4 X_4}, \tag{6.29}$$

$$\vdots$$

$$X_m = \frac{1 - r_{m,m+1}\tau_m^2}{1 + r_{m,m+1}\tau_m^2}, \tag{6.30}$$

$$r_{m,m+1} = \frac{\mathbf{n}_m - \mathbf{n}_{m+1}}{\mathbf{n}_m + \mathbf{n}_{m+1}}. \tag{6.31}$$

r'_{ij} represents the effective reflection coefficient between layer i and all the subsequent layers.

Similarly, if it is desired to know the field in the j^{th} layer, $\mathbf{E_j}(z)$, this is given by [Mack, 1986]

$$\mathbf{E_j}(\mathbf{z}) = E_{In,j} t'_{j-1,j} \frac{exp(-ik_j z_j) + r'_{j,j+1}\tau_j^2 exp(ik_j z_j)}{1 + r^*_{j-1,j} r'_{j,j+1}\tau_j^2} exp(i\omega t) \tag{6.32}$$

where $t'_{j-1,j} = 1 - r'_{j-1,j} = 1 + r^*_{j-1,j}$ is the effective transmission coefficient at $\Gamma_{j-1,j}$ ($r^*_{j-1,j}$ is analogous to $r'_{j-1,j}$ looking from the opposite direction), and

$$r^*_{j-1,j} = \frac{\mathbf{n}_{j-1} Y_{j-1} - \mathbf{n}_j}{\mathbf{n}_{j-1} Y_{j-1} + \mathbf{n}_j}, \tag{6.33}$$

$$Y_{j-1} = \frac{1 + r^*_{j-2,j-1}\tau_{j-1}^2}{1 - r^*_{j-2,j-1}\tau_{j-1}^2}, \tag{6.34}$$

$$\vdots$$

$$r^*_{23} = \frac{\mathbf{n}_2 Y_2 - \mathbf{n}_3}{\mathbf{n}_2 Y_2 + \mathbf{n}_3}, \tag{6.35}$$

$$Y_2 = \frac{1 + r_{12}\tau_2^2}{1 - r_{12}\tau_2^2}. \tag{6.36}$$

z_j is the distance into the j^{th} layer (i.e. $z_j = 0$ at $\Gamma_{j-1,j}$ and $z_j = d_j$ at $\Gamma_{j,j+1}$) and $E_{In,j}$ is the effective field incident on the j^{th} layer, which is given by

$$E_{In,j} = E_{In} \frac{t_{12}\tau_2}{1 + r_{12}\tau_2^2} \frac{t'_{23}\tau_3}{1 + r^*_{23}\tau_3^2} \cdots \frac{t'_{j-2,j-1}\tau_{j-1}}{1 + r^*_{j-2,j-1}\tau_{j-1}^2}. \tag{6.37}$$

The intensity in the top or j^{th} layer can then be found by squaring the magnitude of 6.26 or 6.32, respectively

$$\begin{aligned}\mathbf{I_2(z)} &\propto |\mathbf{E_2(z)}|^2\\ &= I_2 \left| E_{In} t_{12} \frac{exp(-ik_2 z_2) + r'_{23}\tau_2^2 exp(ik_2 z_2)}{1 + r_{12} r'_{23}\tau_2^2} \right|^2 , \qquad (6.38)\\ \mathbf{I_j(z)} &\propto |\mathbf{E_j(z)}|^2\\ &= I_j \left| E_{In,j} t'_{j-1,j} \frac{exp(-ik_j z_j) + r'_{j,j+1}\tau_j^2 exp(ik_j z_j)}{1 + r^*_{j-1,j} r'_{j,j+1}\tau_j^2} \right|^2 . \qquad (6.39)\end{aligned}$$

Again, I_j is just a proportionality constant. Hence, the intensity profile in any layer of a multi-layered system can be found simply from the refractive indices and thicknesses of the layers.

6.3 Implications of Standing Waves for Thin Film Ablation

Consider the case of a thin film on a glass substrate ablated by a laser, as shown in fig. 6.3(a) (i.e. equivalent to a donor on the front-side of a carrier). Here, $n_1 = n_{air} \approx 1$, $\alpha_1 \approx 0$, $n_3 = n_{glass} \approx 1.47$, and $\alpha_3 \approx 0$. It should be apparent that this is simply the situation described in section 6.2.1 and so the intensity profile in the thin film is given by equation 6.14. The setup can be easily rearranged for a thin film on the rear-side of a glass substrate (i.e. conventional LIFT arrangement) by swapping $\mathbf{n_1}$ with $\mathbf{n_3}$, and α_1 with α_3 (fig. 6.3(b)).

The influence of standing waves was of interest primarily in the DRL-LIFT experiments with polymeric DRLs where it was considered that local nodes in a standing wave could explain the surprisingly low LIFT thresholds observed (see section 5.6.2). Hence here the laser wavelength was taken to be $\lambda = 800$ nm and the thin film was some material similar to the TP, so $1.6 \leq n_2 \leq 1.8$ [Bonse et al., 2005b] and $\kappa_2 \approx -0.06$ at 800 nm. The value of κ_2 has been estimated from the absorption coefficient supplied by the polymer manufacturers.

Intensity profiles in thin films on the front and back of glass substrates were calculated to investigate whether standing waves in thin films could explain the different ablation thresholds seen via front and back ablation of polymer films. Film thicknesses from $d_2 = 50$ nm - 1 μm were studied, in line with typical thicknesses used for DRLs and donor films in LIFT experiments.

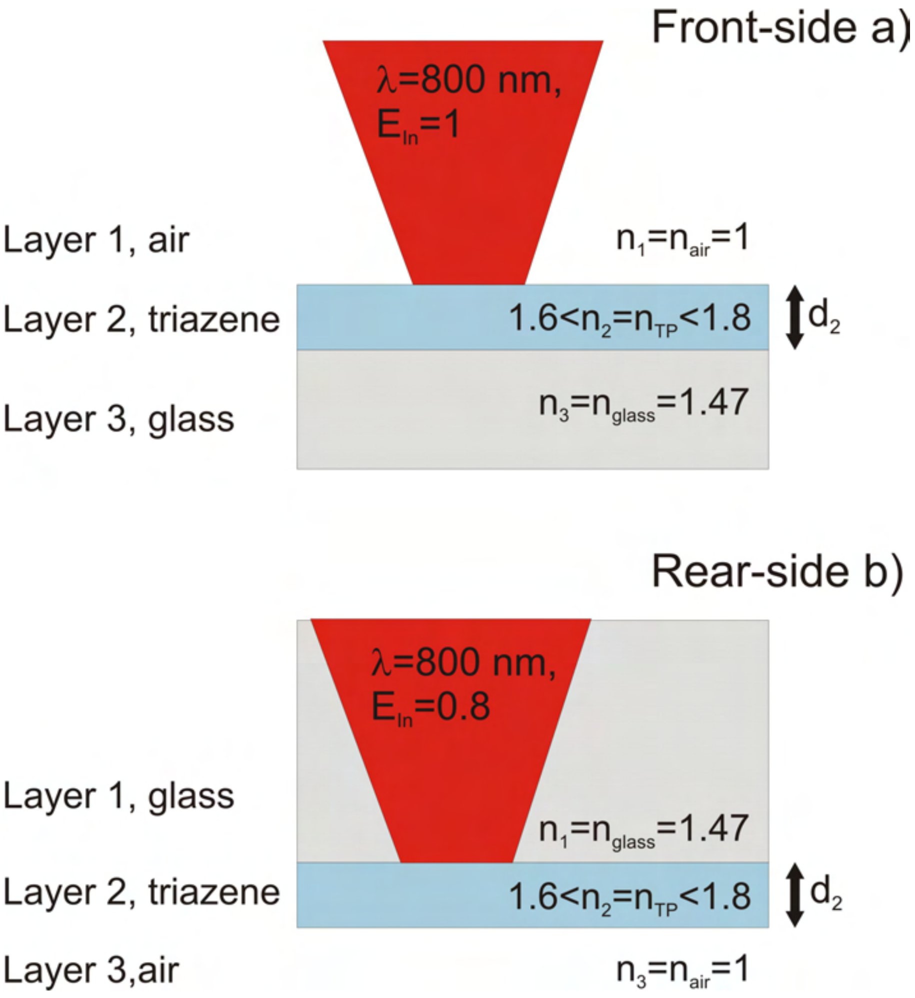

Figure 6.3: Schematic representation of the model situation used in the theoretical study of standing waves in a single thin film.

The incident amplitude for both geometries was taken to be unity for simplicity. In the case of front-side ablation, this meant setting $E_{In} = 1$, and for rear-side ablation $E_{In} = 0.8$ to account for the 0.2 reflection coefficient encountered when the incident light entered the glass substrate from air in the first place. Note that this assumes no absorption in the glass carriers; however, as was seen in chapter 5, nonlinear processes could occur in the glass at typical LIFT intensities. Hence some absorption occurred and so the calculated intensity values in rear-side films may be slightly overestimated. In all AC-LIFT experiments, no permanent modification of the carriers was observed so it can be surmised that the amount of absorption was small. I_2 was taken to be 1 as, at this point we are only interested in the positions of maxima and minima rather than absolute values.

The effect of the AC's on the laser spectrum was neglected due to the low conversion efficiency and the fact that the TP absorption over the whole white-light spectral range was approximately equal. We chose here to focus solely on the TP as this DRL material has been more extensively studied than the photoresist (the Al-DRLs were not transparent). The situation was investigated for $n_2 = 1.6$, 1.7, and 1.8, covering the whole possible range of refractive index of the TP reported in the literature [Bonse et al., 2005b]. We were also assuming perfectly smooth TP surfaces; stylus profiling suggested that this assumption was reasonable for the free surface. No data was available for the surface in contact with the glass, but there was no prior evidence in the literature to suggest this assumption was invalid.

6.3.1 Results

The intensity profiles in front- and rear-side coated, TP-like films of various thicknesses from $d_2 = 50 - 300$ nm were calculated for the cases of $n_2 = 1.6$ (fig. 6.4), $n_2 = 1.7$ (fig. 6.5), and $n_2 = 1.8$ (fig. 6.6). In the figures, the blue lines show the intensity profile in front-side illuminated films and the red lines are the profile in rear-side illuminated films. In all cases, the intensity profile in layer 2 neglecting multiple reflections is also shown by the dotted lines for comparison. Note that the intensity profile in front- and rear-side films was almost identical if multiple reflections were neglected, hence why one dotted line is difficult to see behind the other.

It was immediately apparent that the maximum intensity of the standing wave in the film was greater for rear-side than for front-side films for all studied n_2 and d_2. The peak intensity following the first reflection at Γ_{23} was higher in the rear-side films simply because the back reflection in this case was stronger (due to the higher refractive index contrast). The intensity at the rear-side of the thin film obviously dropped with increasing d_2 due to the greater absorption.

A number of other clear features could be seen also. Firstly, the intensity in the films decreased with increasing n_2; this can be explained easily by considering the transmission coefficient at Γ_{12}, $t_{12} \propto (n_2)^{-1}$, so less light energy entered films with higher n_2. Secondly, there was always a maximum in the standing wave at $z_2 = d_2$, i.e. at Γ_{23}; again this can be easily explained, this time by the fact that $n_2 > n_3$ so there was no phase shift upon reflection at Γ_{23}.

It is easy to show, considering only a single reflection at Γ_{23}, that there should have been a maximum or minimum every $\lambda/4n_2$. The final observation to be made regarding figs. 6.4, 6.5, and 6.6 was that, although the period of the standing waves decreased with increasing n_2 as expected, the maxima and minima were not at the predicted positions if only a single reflection was considered. Also the positions of maxima and minima in front- and rear-side films did not coincide and their spacing was not constant (these

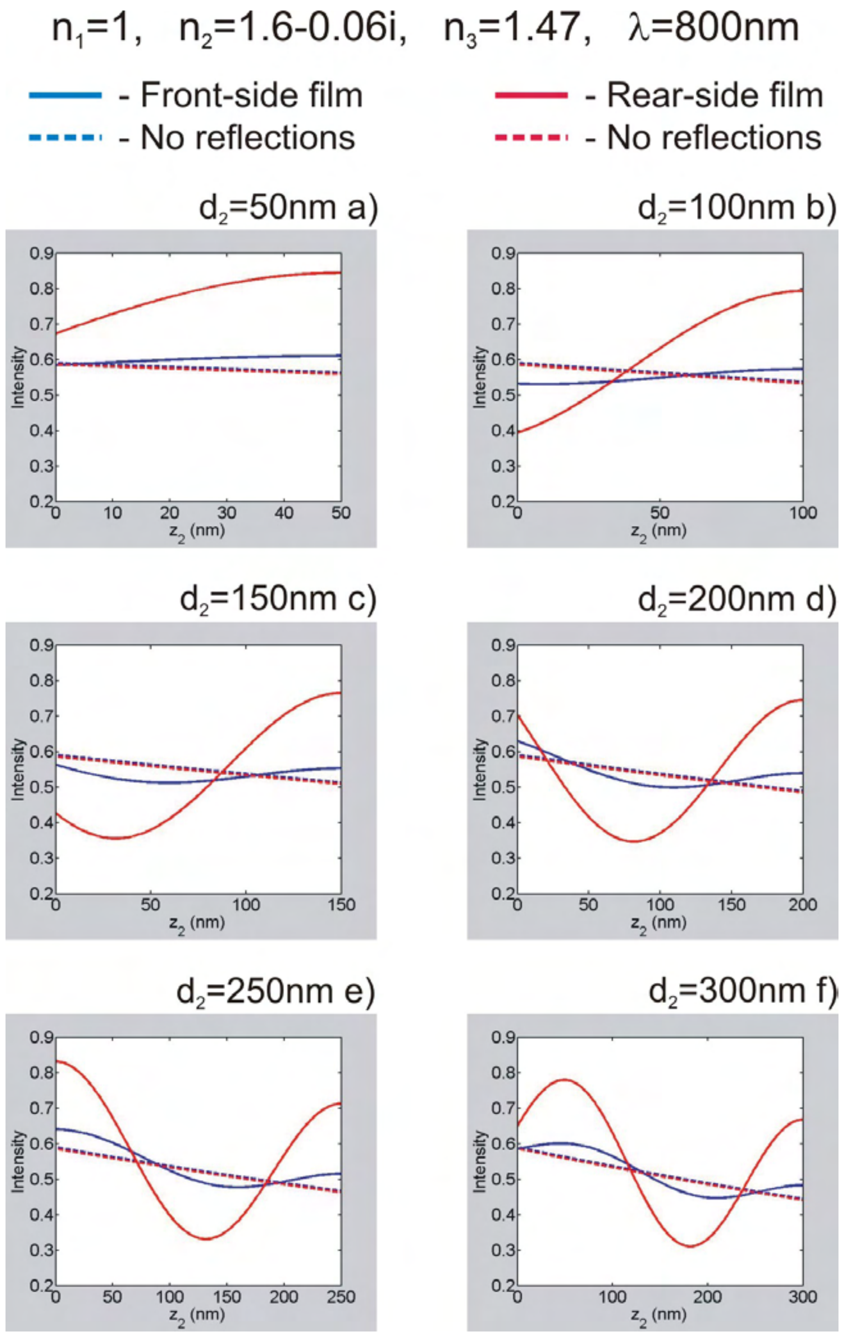

FIGURE 6.4: Intensity profiles in thin films on the front-side (blue) and rear-side (red) of glass substrates with various film thicknesses assuming $\mathbf{n_2} = 1.6 - 0.06i$. Dotted lines show the profile if multiple reflections were neglected (N.B. the profiles with no reflections were almost identical).

results are quite hard to see in the figures as the shifts were relatively small; the clearest occurrence was for the minimum in the front-side profiles). If the reflection at Γ_{12}, i.e. the second reflection, was also considered, then these observations can be explained easily. This reflection resulted in a second forward propagating wave, $\mathbf{E}^{+}_{\mathbf{2,2}}(\mathbf{z})$, which was absorbed as it passed through layer 2, hence there was a greater contribution to

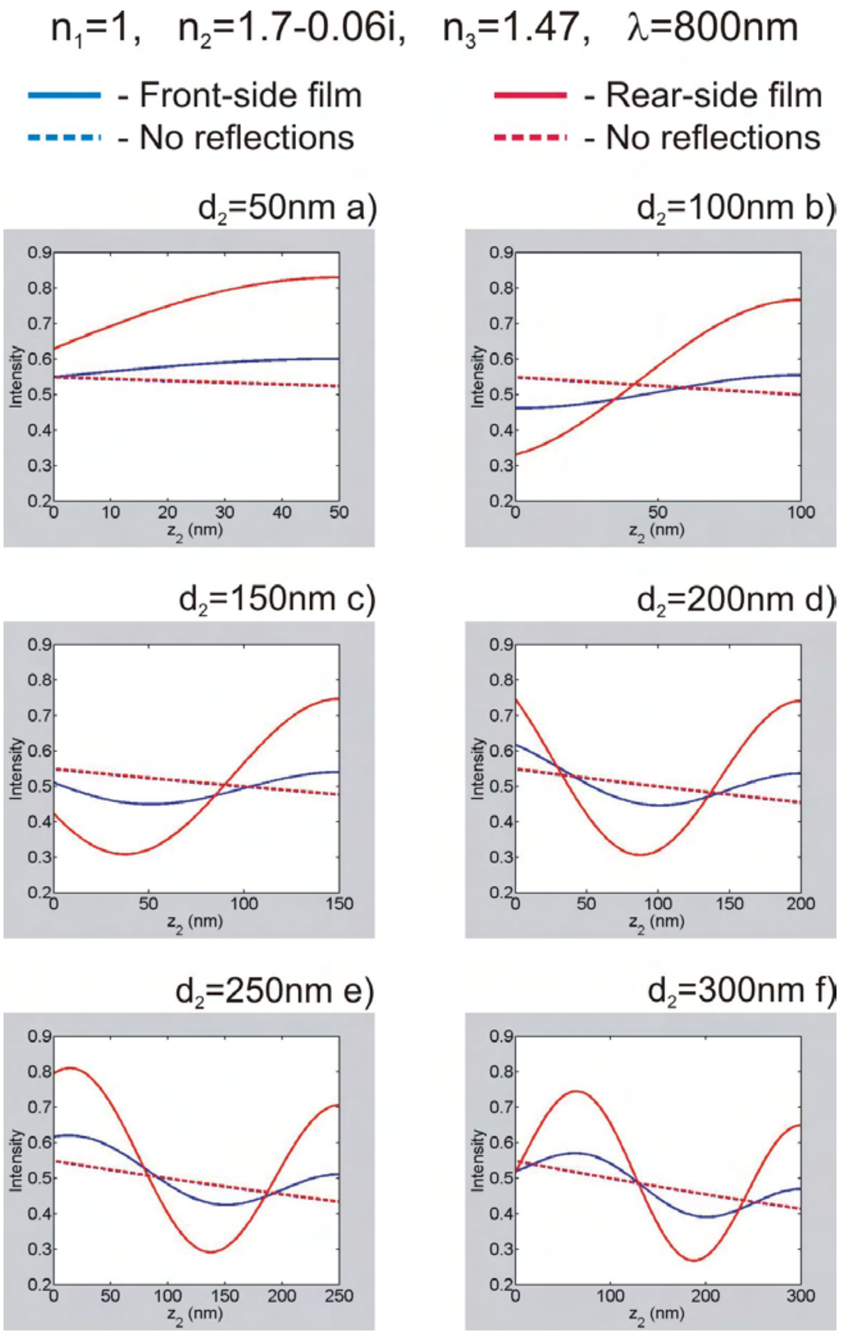

FIGURE 6.5: Intensity profiles in thin films on the front-side (blue) and rear-side (red) of glass substrates with various film thicknesses assuming $\mathbf{n_2} = 1.7 - 0.06i$.

$\mathbf{E_2}(\mathbf{z})$ from $\mathbf{E^+_{2,2}}(\mathbf{z})$ for smaller values of z_2. The overall effect of this would be to push the maxima positions to smaller values of z_2, and minima to higher values, as was seen. As r_{21} was relatively stronger in front-side films, this effect was more pronounced in these films than for the rear-side films. Due to the relatively low reflection coefficients, r_{21} and r_{23}, the third and subsequent reflections could be considered negligible.

The peak intensity, I_{Max}, in the thin film was the key parameter which would determine

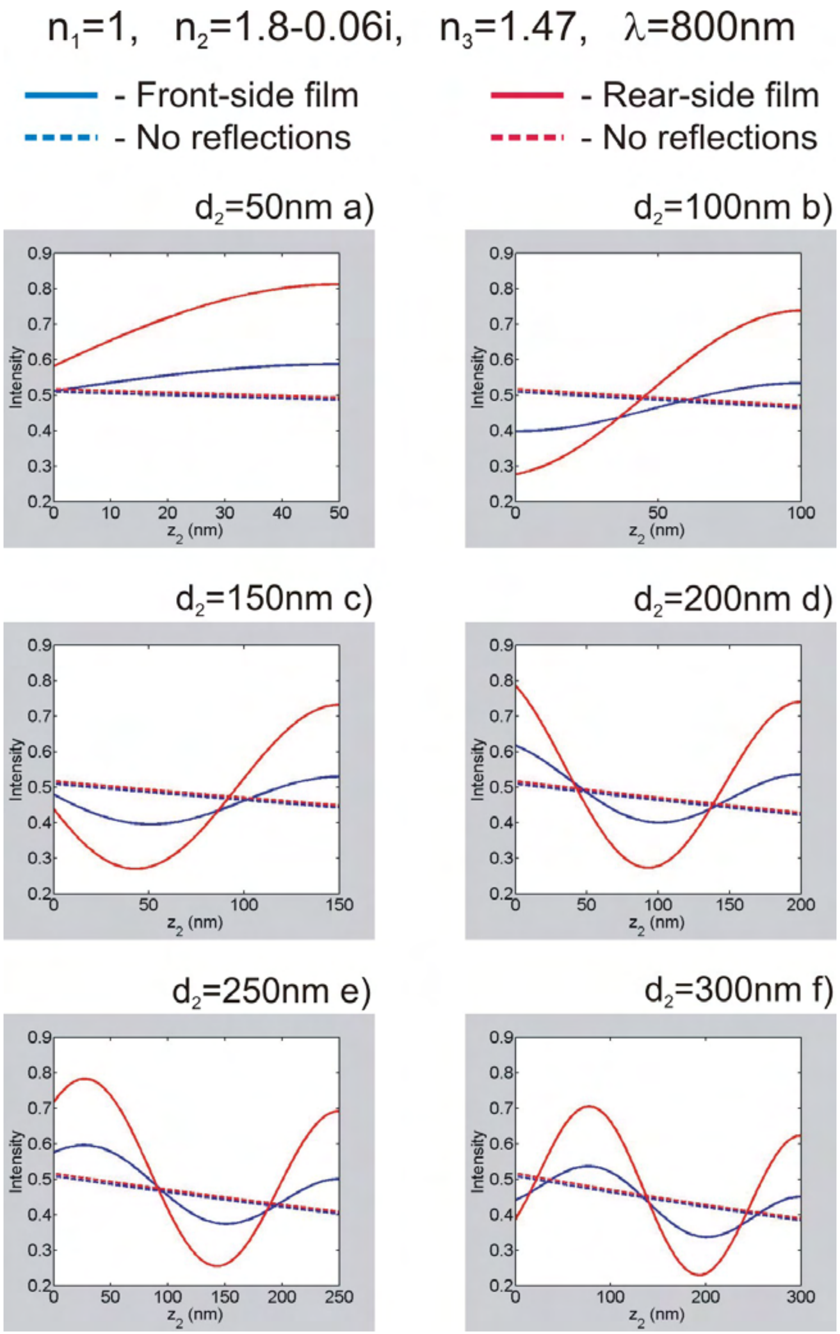

FIGURE 6.6: Intensity profiles in thin films on the front-side (blue) and rear-side (red) of glass substrates with various film thicknesses assuming $\mathbf{n_2} = 1.8 - 0.06i$.

the ablation threshold. I_{Max} is plotted for front-side (top) and rear-side (middle) films as functions of d_2 for $n_2 = 1.6$ (fig. 6.7), $n_2 = 1.7$ (fig. 6.8), and $n_2 = 1.8$ (fig. 6.9). The dashed lines show the maximum intensity assuming no reflections. It is apparent from these plots that the increased back reflections in a rear-side film c.f. a front-side film resulted in a standing wave of larger amplitude, for a given film thickness. Hence the peak intensity in a rear-side film was also greater than for a front-side film.

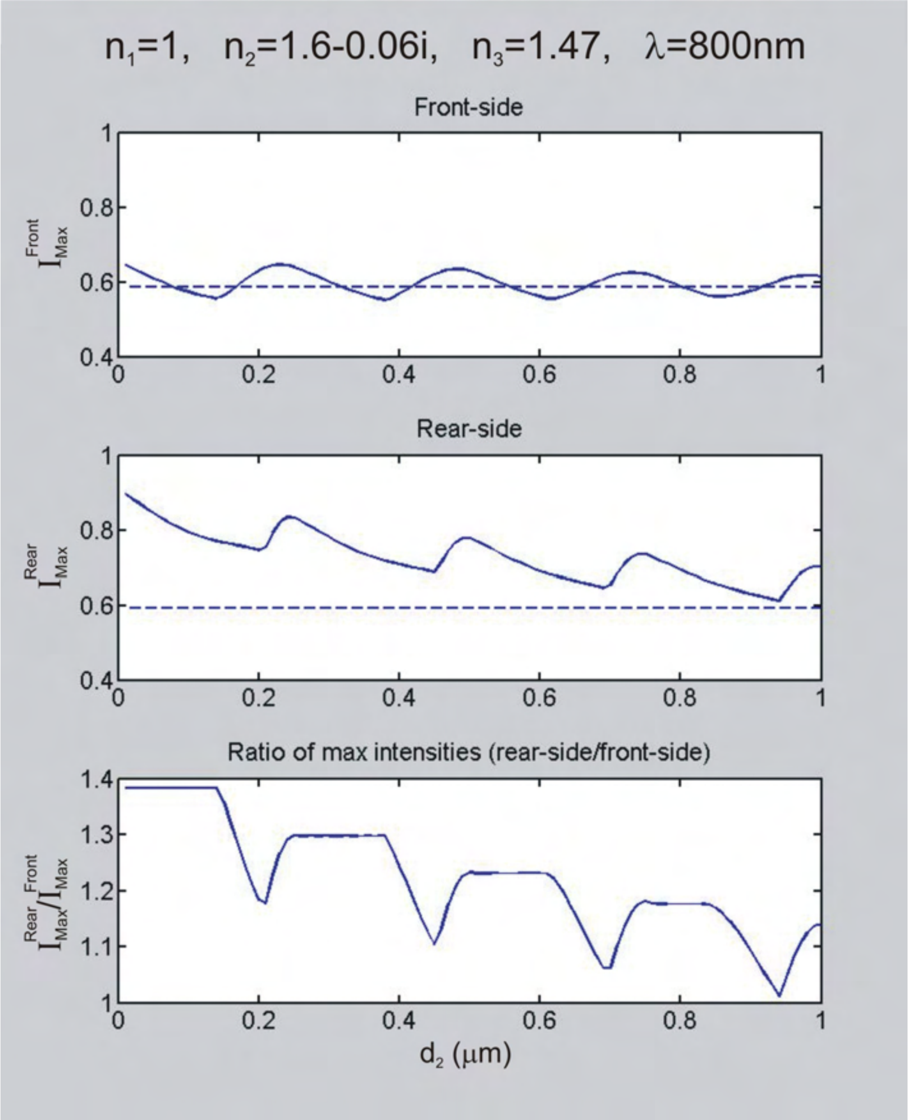

FIGURE 6.7: Plots of the peak intensity inside a front-side film (top), rear-side film (middle), and ratio of rear-side:front-side peak intensity (bottom) as functions of film thickness with $\mathbf{n_2} = 1.6 - 0.06i$. Dotted lines show the case with no reflections.

The amount by which the rear-side peak intensity was greater than the front-side peak was dependent on film thickness, refractive index, absorption, and wavelength as these determine where the nodes and antinodes occurred in the standing wave patterns. For an easily understood comparison of front and rear-side films, the ratio of I_{Max} in a rear-side film to I_{Max} in a front-side film is plotted as a function of d_2 in the bottom plots of figures 6.7, 6.8, and 6.9.

As can be seen, the rear-side peak intensity reached a maximum of ≈ 1.4 times that of the front-side due to the stronger first back reflection for $d_2 \leq 150$ nm. This result appeared to be only very weakly dependent on the film refractive index so not having an accurate value for the index of the TP should not have introduced significant errors

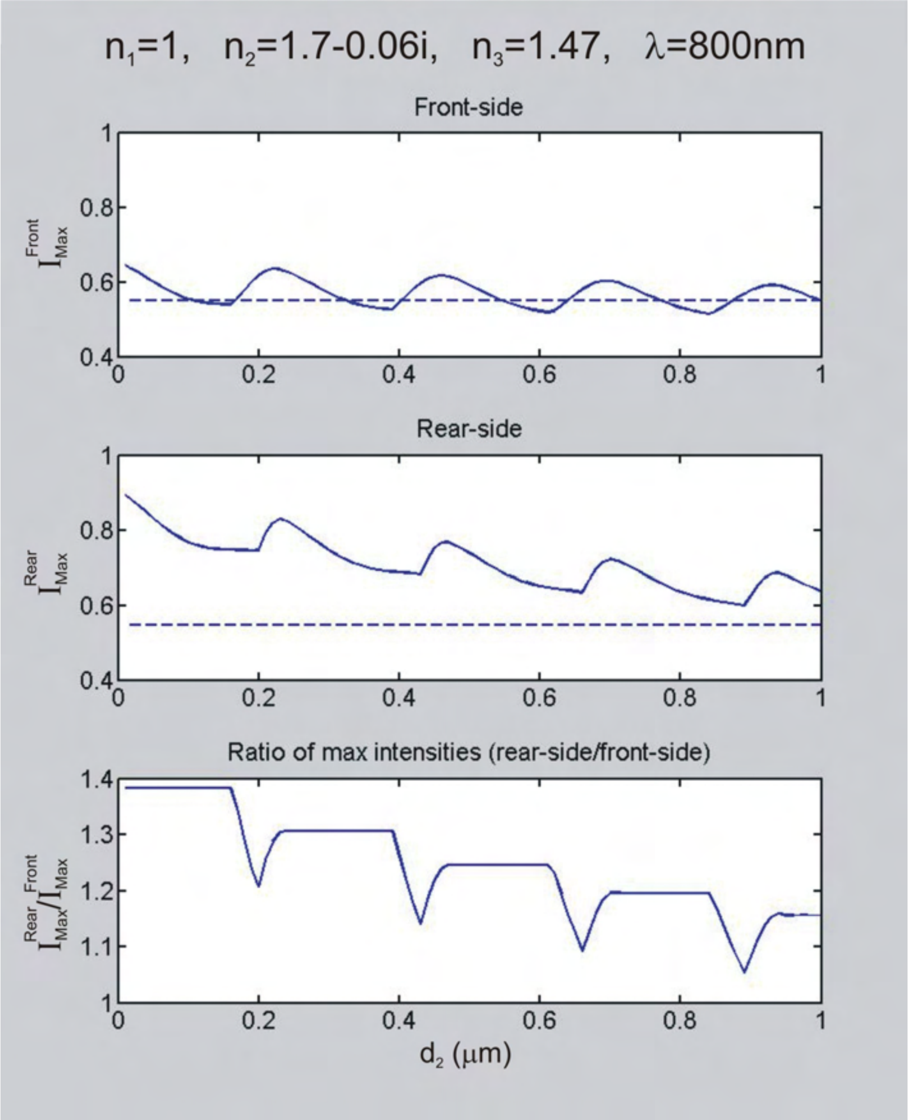

FIGURE 6.8: Plots of the peak intensity inside a front-side film (top), rear-side film (middle), and ratio of rear-side:front-side peak intensity (bottom) as functions of film thickness with $\mathbf{n_2} = 1.7 - 0.06i$.

into the model. The reason that the ratio of rear:front peak decreased in steps rather than smoothly was due to the reflection at Γ_{12} shifting the positions of the maxima and minima in front- and rear-side by different amounts, as discussed previously.

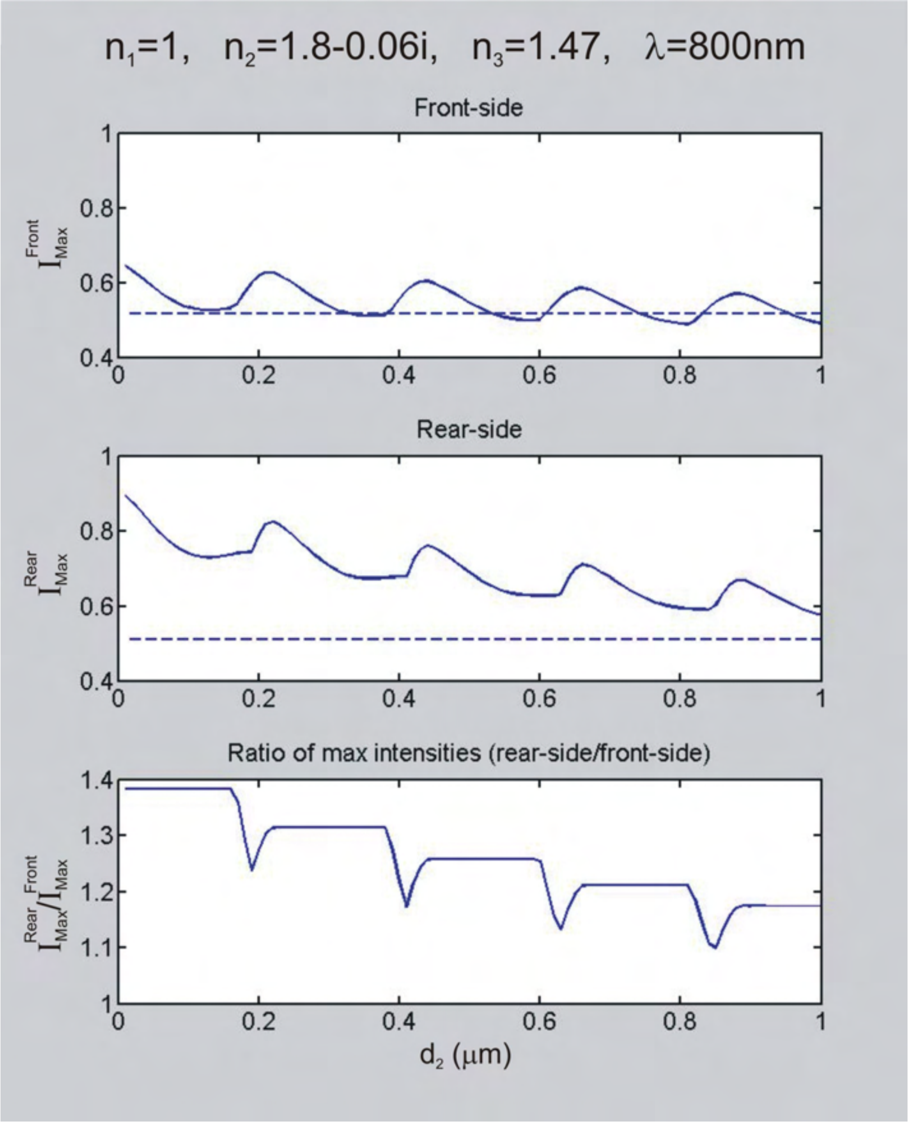

FIGURE 6.9: Plots of the peak intensity inside a front-side film (top), rear-side film (middle), and ratio of rear-side:front-side peak intensity (bottom) as functions of film thickness with $\mathbf{n_2} = 1.8 - 0.06i$.

6.3.2 Validating the Numerical Model

To check that the computer program was producing results in agreement with the theory, the behaviour of the standing wave model as the film thickness tended to infinity was studied (as this result is easy to determine analytically for comparison with the numerical results). As $d_2 \rightarrow \infty$, multiple reflections from the interfaces become negligible as the film is slightly absorbing. Hence the peak intensity in the film is simply the incident intensity, i.e.

$$I_{Max,d_2\rightarrow\infty} \propto (E_{In} t_{12})^2 \tag{6.40}$$

The ratio of maximum intensities in rear- and front-side films, ξ, is then determined by

$$\begin{aligned} \xi &= \frac{I^{Rear}_{Max,d_2\rightarrow\infty}}{I^{Front}_{Max,d_2\rightarrow\infty}} && (6.41)\\ &= \frac{(E^{Rear}_{In} t^{Rear}_{12})^2}{(E^{Front}_{In} t^{Front}_{12})^2} && (6.42)\\ &= \frac{(E^{Rear}_{In} \frac{2\mathbf{n}^{Rear}_1}{\mathbf{n}^{Rear}_1+\mathbf{n}^{Rear}_2})^2}{(E^{Front}_{In} \frac{2\mathbf{n}^{Front}_1}{\mathbf{n}^{Front}_1+\mathbf{n}^{Front}_2})^2}. && (6.43) \end{aligned}$$

Noting then

$$\begin{aligned} E^{Rear}_{In} &= 0.8, && (6.44)\\ E^{Front}_{In} &= 1, && (6.45)\\ \mathbf{n}^{Rear}_1 &= \mathbf{n}_{glass}, && (6.46)\\ \mathbf{n}^{Front}_1 &= \mathbf{n}_{air}, && (6.47)\\ and \quad \mathbf{n}^{Front}_2 &= \mathbf{n}^{Rear}_2 = \mathbf{n}_2 && (6.48) \end{aligned}$$

it is easy to show that

$$\xi = \mathbf{0.64} * \left[\frac{\mathbf{n_{glass}(1+n_2)}}{\mathbf{(n_{glass}+n_2)}}\right]^{\mathbf{2}} \tag{6.49}$$

Evaluating equation 6.49 for $n_2 = 1.6$, 1.7, and 1.8 yields $\xi = 0.9919$, 1.0033, and 1.0140, respectively. Figure 6.10 shows the value of $(I^{Rear}_{Max}/I^{Front}_{Max})$ as functions of film thickness for $0.05 \leq d_2 \leq 5$ μm with $n_2 = 1.6$ (a), 1.7 (b), and 1.8 (c). As can be seen, the numerical values of the ratios are tending to the analytically determined values of ξ (shown as a red dotted line in the figures) as d_2 increases, supporting the accuracy of the numerical model.

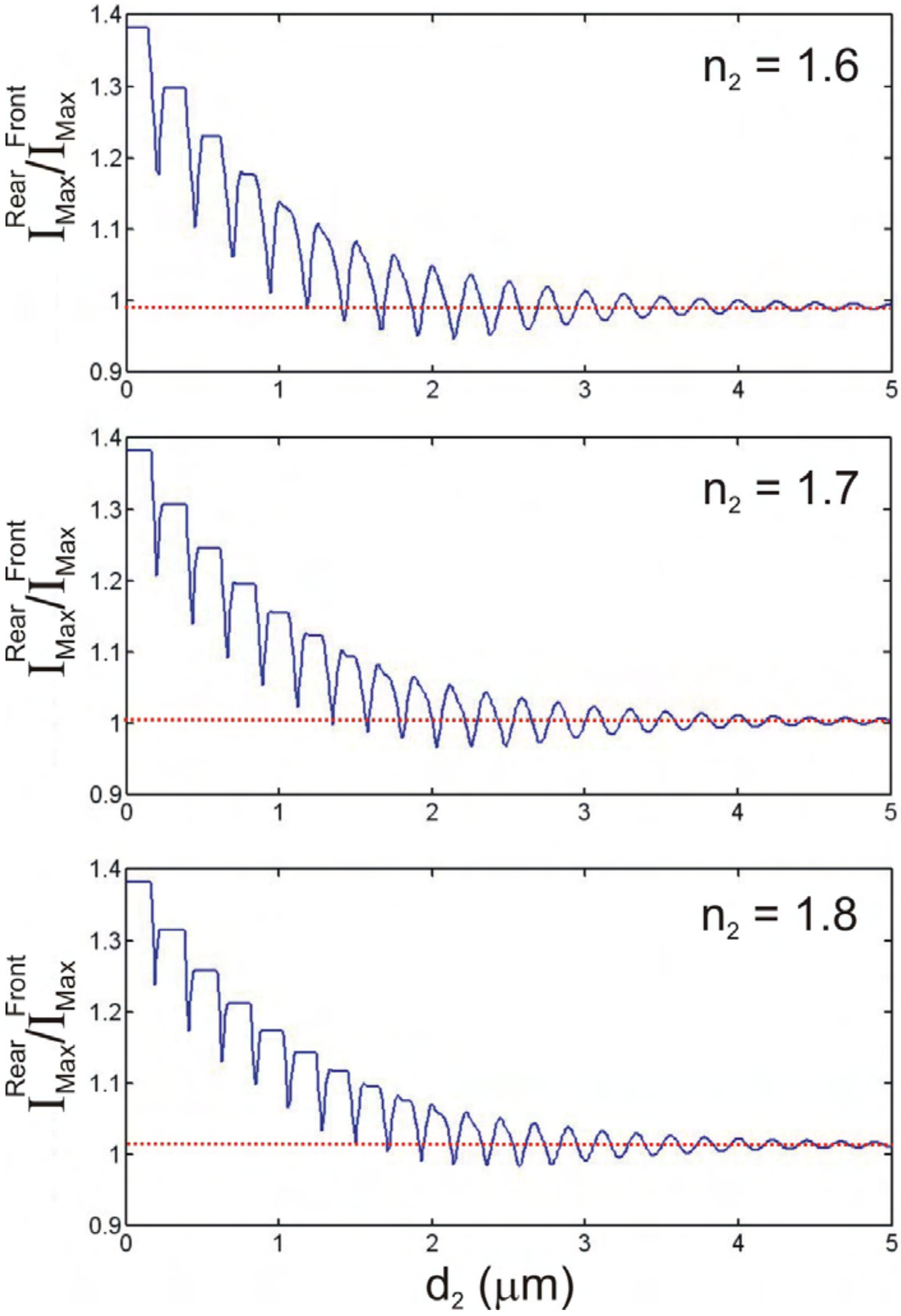

FIGURE 6.10: rear-side/front-side peak intensity as function of films thickness for $\mathbf{n_2} = 1.6 - 0.06i$ (a), $\mathbf{n_2} = 1.7 - 0.06i$ (b), and $\mathbf{n_2} = 1.8 - 0.06i$ (c). Dotted lines indicate the appropriate values of ξ.

6.3.3 Discussion

So what are the implications of standing waves for the ablation of TP and can they be used to explain the surprisingly low ablation and transfer thresholds seen in the experiments in the previous chapter? Bonse et al. have considered the effects of optical standing waves on the ablation of front-side thin TP films and determined that, with a similar laser to that used in these experiments, such waves were not the principal damage mechanism [Bonse et al., 2007, 2005a]. In their first work, an increase in thin film reflectivity was observed only in a narrow fluence range well below the permanent damage threshold fluence (i.e. ablation threshold). This was attributed to a periodic modification of the film refractive index due to localised N_2 release at peaks in the standing wave, which caused the film to act like a layered dielectric mirror [Bonse et al., 2005a].

In later work, the ablation thresholds of 50 nm and 1.1 μm thick TP films either undoped or doped with an IR-absorber were investigated [Bonse et al., 2007]. The results indicated that the presence of a dopant appeared to have little impact on the ablation threshold, suggesting that absorption in the TP was the dominant absorption mechanism leading to film damage. However, they also found that, for the doped films, the thicker films had higher damage thresholds than the thinner films; this trend was not observed in the undoped films. Permanent damage appeared as the formation of a macroscopic bubble in the films, indicating that the onset of ablation occurred at the polymer-glass interface. The proposed explanation for the process was that film damage was initiated by absorption of laser energy at the interface due to defects in the polymer films.

Although it was not discussed in Bonse's work, such a model also explains the film thickness dependence of the damage threshold that was observed. For undoped films, there was essentially zero linear absorption of the laser energy in the film, so the fluence at the polymer-glass interface, and hence the damage threshold, was essentially independent of film thickness. This was in contrast to the doped films where there was a small amount of linear absorption due to the dopant (although apparently not enough to initiate thermolytic decomposition of the TP); hence, the fluence at the polymer-glass interface was lower in the thicker than the thinner doped films.

The important point to be drawn from Bonse's work is that a standing optical wave model cannot be used to explain the ablation threshold of thin TP films on glass substrates. However, the defect-induced absorption model does not explain our observations of a significant difference in the front- and rear-side ablation thresholds for such films. As was reported in the previous chapter, the front- and rear-side ablation thresholds of a 100 nm TP film were measured to be ≈ 500 mJ/cm^2 and ≈ 330 mJ/cm^2, respectively; i.e. the rear-side threshold was ≈ 1.5 times lower than that of the front-side. The model predicted the maximum intensity in a 100 nm film to be ≈ 1.4 times higher for a film on the rear-side of a glass substrate than on the front-side. Allowing for errors in the experimentally measured ablation thresholds, the increase in intensity within the rear-side film appears to be great enough to account for the lower rear-side threshold.

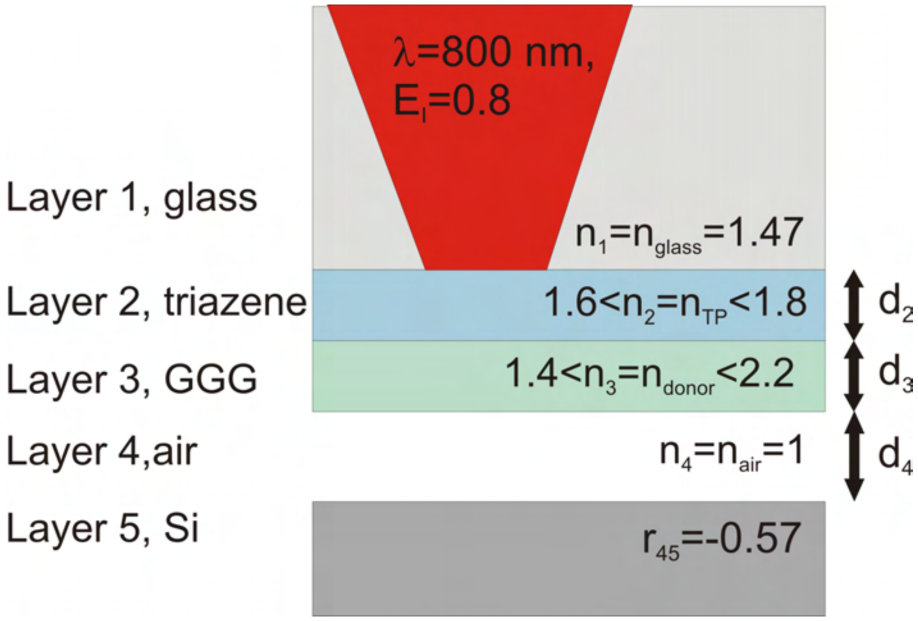

FIGURE 6.11: Schematic of the parameters used in the standing wave model of LIFT/DRL-LIFT with transparent films.

As was seen in section 6.3.1, the maximum intensity in rear-side thin TP films varied with film thickness (see figs. 6.7, 6.8, and 6.9). To determine conclusively if the formation of a standing wave was the reason for the lower threshold, it would be necessary to measure the damage threshold of rear-side films of various thicknesses experimentally and see if a similar variation occurs. Unfortunately, at the time of writing such data was unavailable, and so we are forced to conclude that, although theoretically standing waves could explain the reduced rear-side threshold, the influence of other effects discussed in section 5.6.2 cannot yet be ruled out completely.

6.4 Implications of Standing Waves for LIFT

The numerical model is now extended to the case of multiple thin films on the rear-side of a glass carrier substrate, i.e the situation described in section 6.2.2. Such an arrangement can be made analogous to a LIFT setup by setting the 1^{st} layer to be glass, the m^{th} layer (i.e. the last thin film) to be an air (or vacuum) layer, and the $(m+1)^{th}$ layer to be a typical receiver material. Any DRL and donor layers are then included between layers 1 and m. The intensity profile in the first thin film (i.e. the DRL or first donor layer) can be calculated using equation 6.38, and for all subsequent layers using equation 6.39. Note that, in the air layer (layer m), $r'_{j,j+1}$ in equation 6.32 should be replaced by $r_{j,j+1}$, i.e. the reflectivity of the receiver. The situation is shown in fig. 6.11.

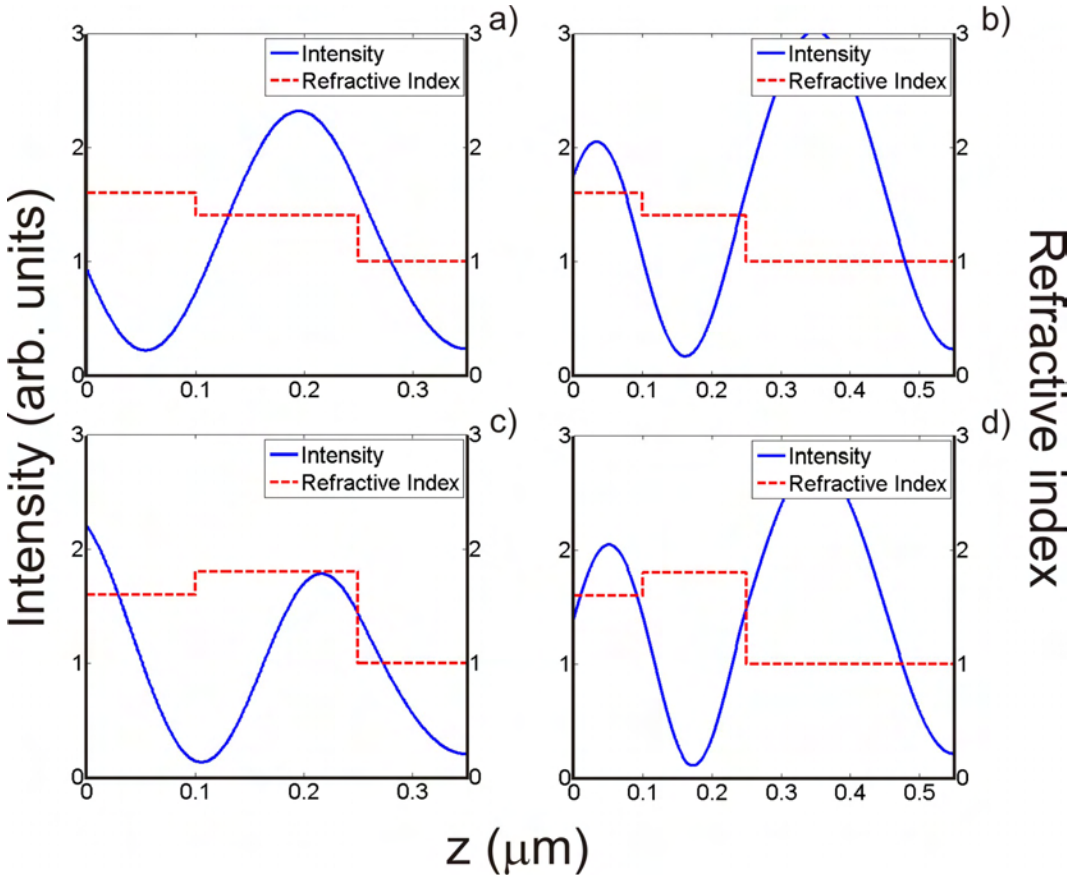

FIGURE 6.12: Sample intensity profiles when varying n_3 and d_4; other properties $n_2 = 1.6$, $\kappa_2 = -0.06$, $d_2 = 100$ nm, $d_3 = 150$ nm, $\kappa_3 = -0.03$, $n_4 = 1$, $\kappa_4 = 0$, and $r_{45} = -0.57$. (a) $n_3 = 1.4$, $d_4 = 100$ nm, (b) $n_3 = 1.4$, $d_4 = 300$ nm, (c) $n_3 = 1.8$, $d_4 = 100$ nm, and (d) $n_3 = 1.8$, $d_4 = 300$ nm.

As before, we assume unity amplitude of the incident wave $\mathbf{E_{In}(z)}$, i.e. E_{In} was set to 0.8 to account for the reflection at the carrier front surface. For the 1^{st} layer (carrier) and the 1^{st} thin film (DRL, layer 2), we assumed the properties of the glass and TP listed in section 6.3. The 2^{nd} thin film (donor, layer 3) was taken to be a material similar to the GdGaO donor in used in the DRL experiments in chapter 5. κ_3 was estimated, from spectrophotometer measurements, to be ≈ -0.03. Unfortunately no estimate of n_3 was available at time of writing so the effect of varying this parameter on the intensity profiles in the films will be investigated; the refractive index for single crystal GGG is approximately 1.95. The 4^{th} layer was the air gap between source and receiver so $n_4 \approx 1$ and $\kappa_4 \approx 0$. The receiver was taken to be silicon to fit with the experiments; this meant that the reflection coefficient at Γ_{45}, the air-receiver interface, r_{45}, was ≈ -0.57 at 800 nm.

6.4.1 Results

Figure 6.12 shows sample intensity profiles in layer 2 (DRL), layer 3 (donor), and layer 4 (air) (with the associated refractive index profiles to indicate the layer boundaries) for $(n_3, d_4) = (1.4, 100nm)$ (a), $(1.4, 300nm)$ (b), $(1.8, 100nm)$ (c), and $(1.8, 300nm)$ (d). The dominant factor in this example, at least in terms of determining the positions of maxima and minima in the layers, would appear to be d_4, the air gap (compare fig. 6.12 (a) and (c) with (b) and (d)). This finding was unsurprising as the reflection at Γ_{45} was by far the strongest reflection in the setup, and so dominated the standing wave pattern. However, to neglect the effect of varying n_3, the donor refractive index, would be to grossly oversimplify the situation. For example compare fig. 6.12 (a) and (c) and observe the difference in peak intensity in layer 2 (the DRL) or layer 3 (the donor) by increasing n_3 from 1.4 (a) to 1.8 (c); the peak intensity in layer 2 almost doubles due to the stronger back reflection off Γ_{23}.

As can be seen, the situation is relatively complex even when only considering two parameters. We have not begun to consider the effects of varying DRL refractive index (n_2), DRL thickness (d_2), donor thickness (d_3), and receiver reflectivity (r_{45}). d_2, d_3, and r_{45} are easily controlled in a real LIFT setup, so the correct combination can be chosen to suit the desired standing wave profile. However, n_2 is not well known and n_3 is not known at all. The values of n_2 and n_3 determine the reflection coefficients at the layer interfaces and so have a major influence on the standing wave profile. The peak intensities of the standing wave pattern in the DRL and donor layers would determine the ablation thresholds and so are of vital importance in the investigation of low LIFT thresholds.

Figures 6.13 and 6.14 show the peak intensities in layer 2 (DRL), $I_{Max,2}$ (a) and layer 3 (donor), $I_{Max,3}$ (b) as functions of n_3 and n_2 without (achieved by setting $r_{45} = 0$) and with a Si receiver, respectively. n_2 was varied from 1.6-1.8 in accordance with literature values, whilst n_3 was allowed to vary from 1.0-2.5. Note that the n_3 and n_2 axes are swapped in the top and bottom plots of both figures to make the curves easier to see. In all these cases, $d_2 = 100$ nm, $d_3 = 150$ nm, and d_4 was set to 50 nm. The presence of the receiver was clearly a major factor in determining the peak intensity in both films. Varying either n_2 or n_3 was observed to have significant implications for $I_{Max,2}$ and $I_{Max,3}$. The effects of varying the refractive indices of the two layers were more pronounced in the presence of the receiver.

Figures 6.15 and 6.16 show the peak intensities in layer 2 (DRL) (a) and layer 3 (donor) (b) as functions of n_3 and d_4 (with the Si receiver, $r_{45} = -0.57$), for $n_2 = 1.6$ (fig. 6.15) and $n_2 = 1.8$ (fig. 6.16). Again, n_3 varied from 1.0-2.5, and d_4 from 0-1.4 μm; as

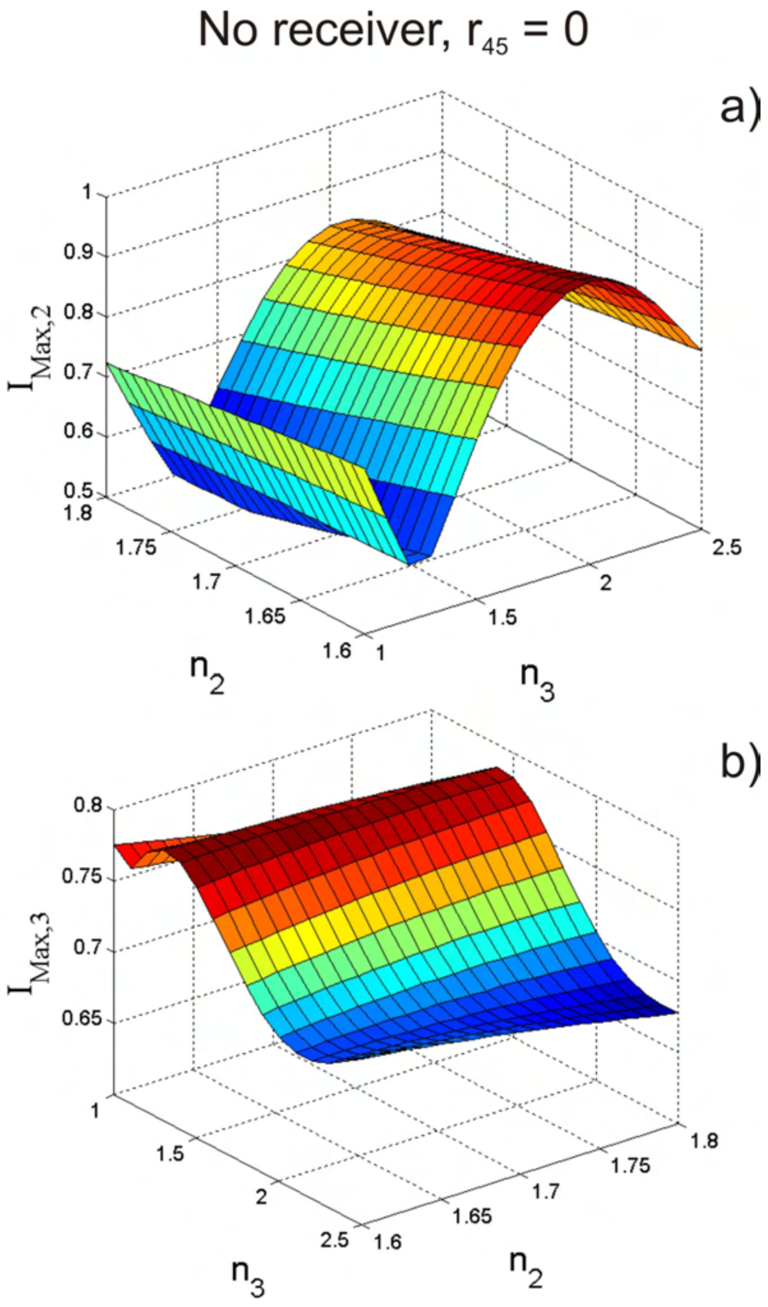

Figure 6.13: Peak intensities in layer 3 (donor) (a) and layer 2 (DRL) (b) layers as functions of n_3 and n_2 with no receiver (i.e. $r_{45} = 0$). Note n_3 and n_2 axes swapped in (a) and (b) to make curves easier to see.

before $d_2 = 100$ nm and $d_3 = 150$ nm. From these plots, a couple of trends can be noted. Firstly, for a given d_4 (source-receiver separation), increasing n_3 decreased the maximum intensity in layer 3 (donor) because of greater back reflection at Γ_{12}. This was in contrast to layer 2 (DRL), where the influence of multiple reflections meant that the values of d_4 at which peaks in $I_{Max,3}$ occurred also varied with n_3. The second observation is that the choice of n_2 appeared to have only limited influence on the peak intensities in layers 2 and 3. The final, and arguably most important, observation was

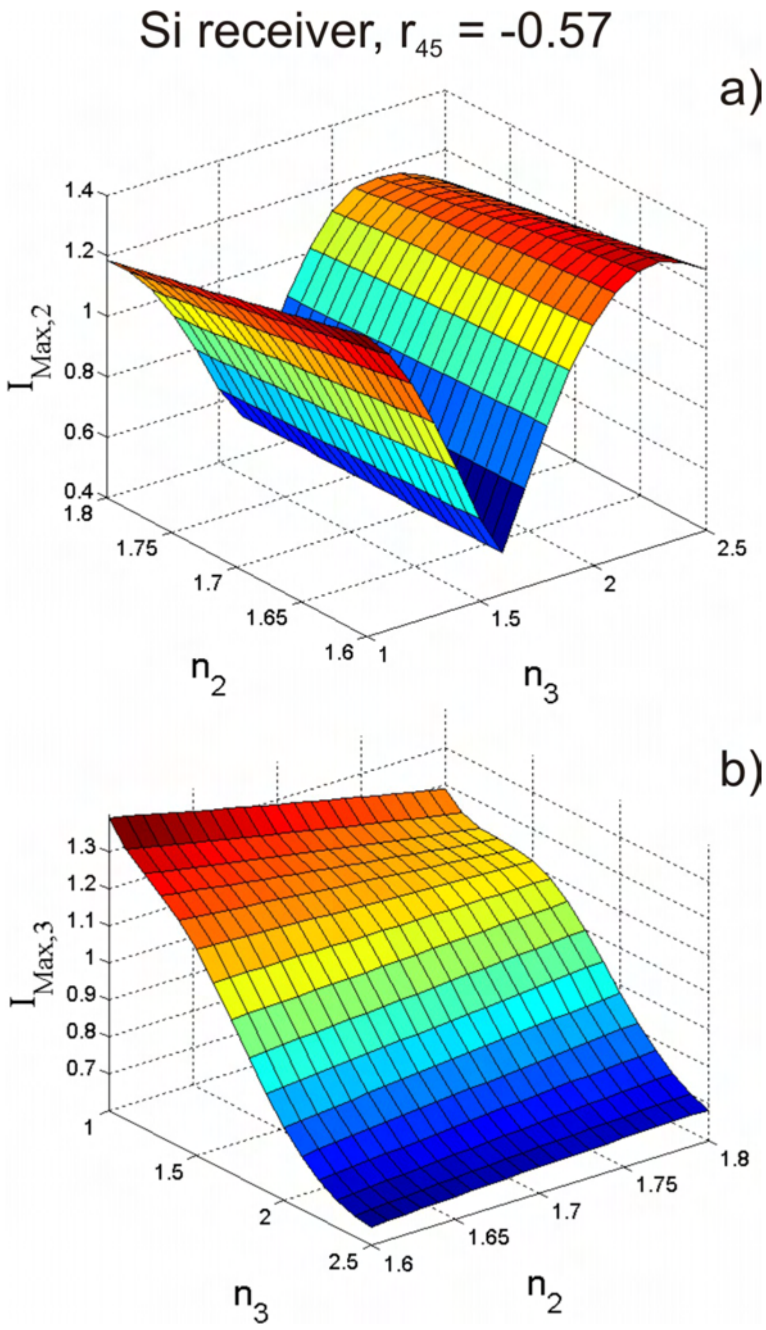

FIGURE 6.14: Peak intensities in layer 3 (donor) (a) and layer 2 (DRL) (b) layers as functions of n_3 and n_2 with a Si receiver (i.e. $r_{45} = -0.57$). Note n_3 and n_2 axes swapped in (a) and (b) to make curves easier to see.

also the most intuitive: that the peak intensities in both layers were periodic in d_4 with the periodicity independent of n_2 and n_3. This result was simply due to the fact that the back reflection off Γ_{45} was by far the strongest reflection in the setup and so its influence dominated the resultant intensity profiles.

A particularly interesting result, especially for DRL-LIFT, is how the peak intensities in DRL and donor layers varied relative to each other when other parameters were

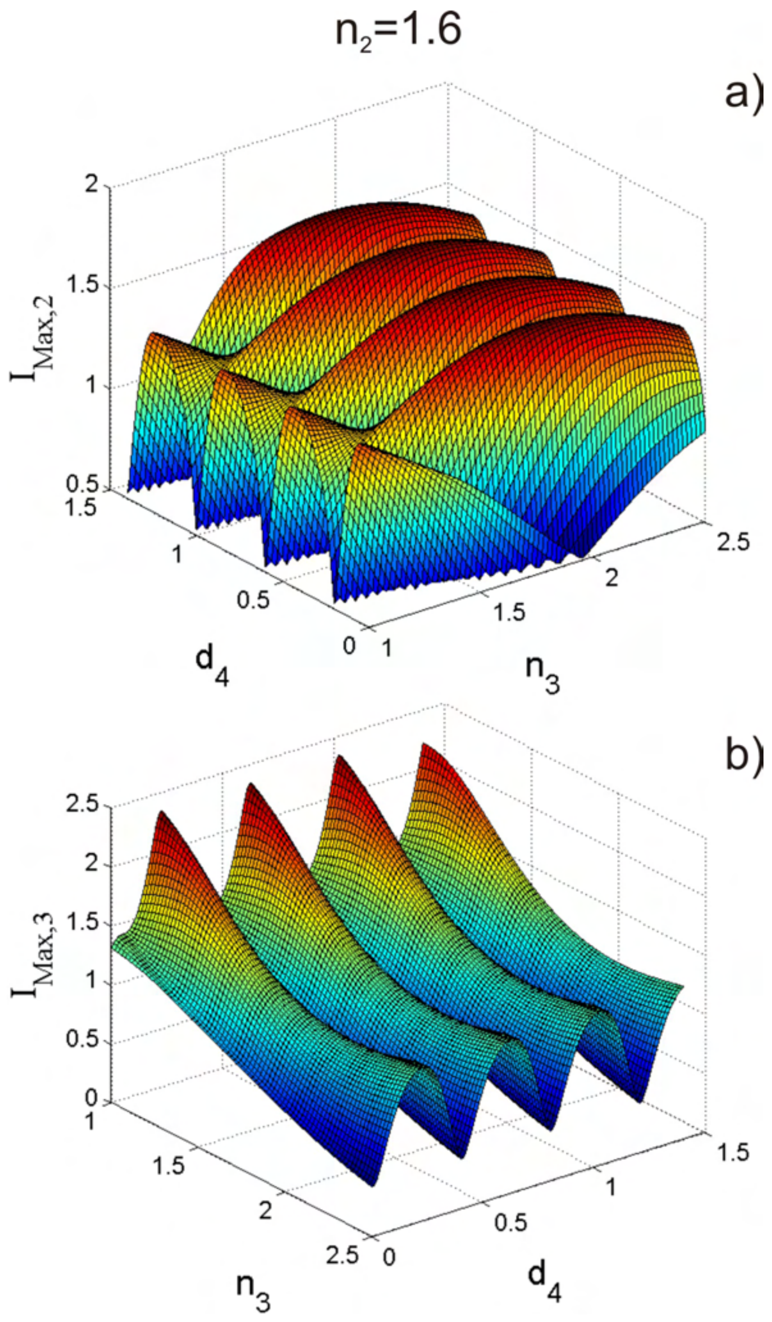

FIGURE 6.15: Peak intensities in layer 2 (a) and layer 3 (b) as functions of n_3 and d_4 with Si receiver (i.e. $r_{45} = 0.33$). Note n_3 and d_4 axes swapped in (a) and (b) to make curves easier to see.

adjusted. For example, it would be desirable to have very high intensity in the DRL and very low intensity in the donor so that the DRL was completely removed during the DRL-LIFT process whilst the donor remained undamaged by the laser energy; this could be particularly important for the DRL-LIFT of photo-sensitive donors. As such, the ratio of peak intensities in the 2^{nd} and 3^{rd} layers as functions of d_2 and d_3 are plotted in fig. 6.17 for the two cases of $n_2 < n_3$ ($n_2 = 1.6$, $n_3 = 1.9$) (a) $n_2 > n_3$ ($n_2 = 1.8$,

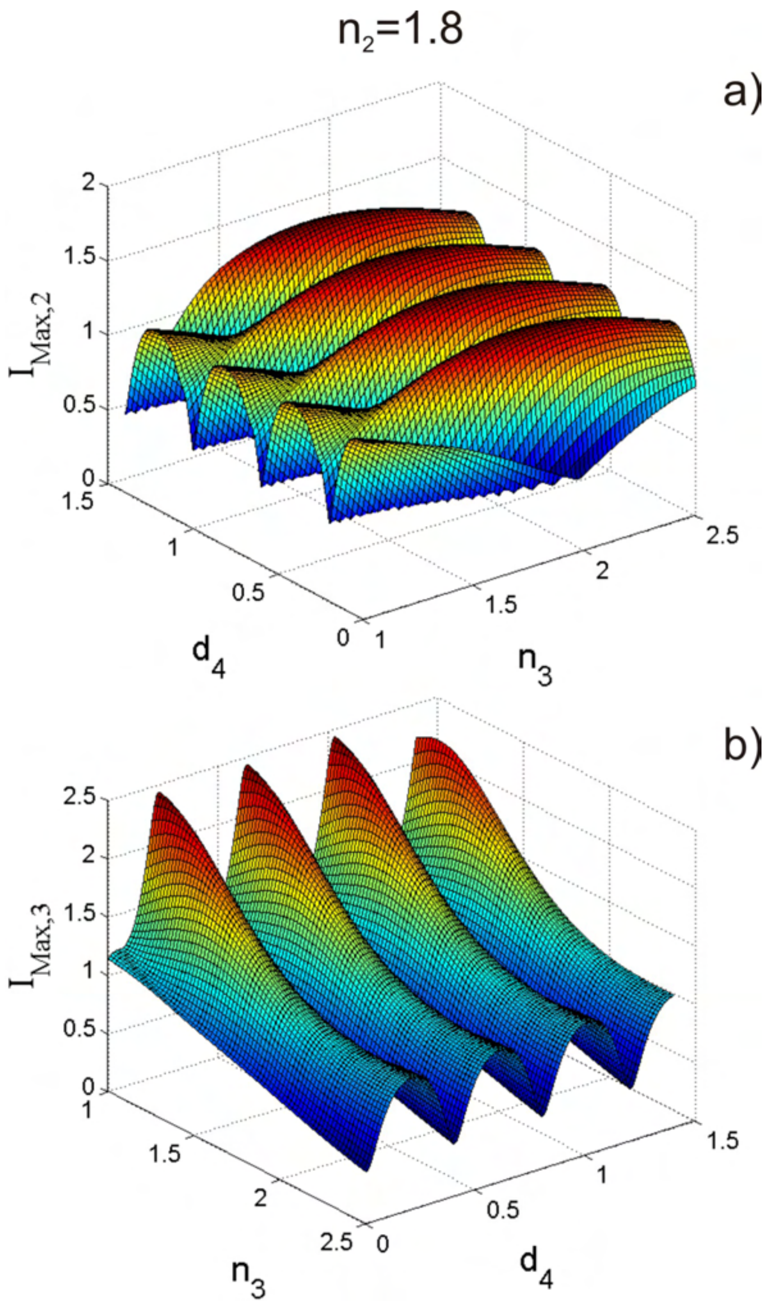

FIGURE 6.16: Peak intensities in layer 2 (a) and layer 3 (b) as functions of n_3 and d_4 with Si receiver (i.e. $r_{45} = 0.33$). Note n_3 and d_4 axes swapped in (a) and (b) to make curves easier to see.

$n_3 = 1.6$) (b); $10nm \leq (d_2, d_3) \leq 1\mu m$, $d_4 = 100$ nm, $r_{45} = -0.57$, $\kappa_2 = -0.06$, and $\kappa_3 = -0.03$. The situations for $d_4 = 200$ nm and $d_4 = 400$ nm with all other parameters the same are shown in figs. 6.18 and 6.19.

The most obvious trend that can be seen from figures 6.17, 6.18, and 6.19 is that the ratio increased with increasing d_2. This observation is easy to understand as there would be greater absorption in a thicker layer, and hence less energy incident on the subsequent

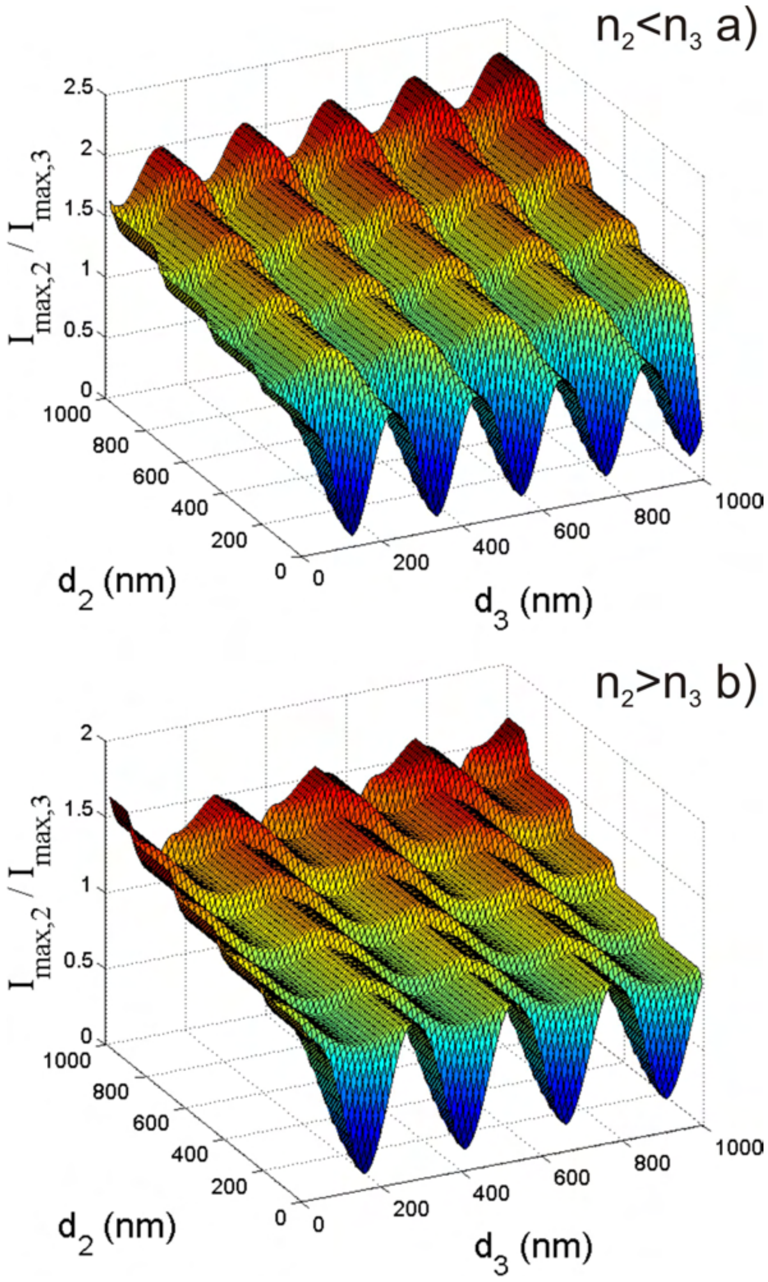

FIGURE 6.17: Ratio of peak intensity in layer 2 to peak in layer 3 as functions of d_2 and d_3 with $d_4 = 100$ nm for $n_2 < n_3$ (a) and $n_2 > n_3$ (b).

layers. In contrast, d_3 appeared to have very little effect on the ratio, particularly in the case of $n_2 > n_3$. An interesting observation is that the ratio becomes very large for small d_3 at $d_4 = 400$ nm so, in this particular case, most of the energy can be concentrated in layer 2 (i.e. the DRL). Hence, it is suggested that thicker DRLs are preferable in general to prevent high intensities in the donor material. However, care must be taken as thick DRL layers may not be removed completely during the DRL-LIFT process. Donor thickness does not appear to be particularly important (except in the special case just mentioned), although thicker donors may not transfer if a relatively thin DRL

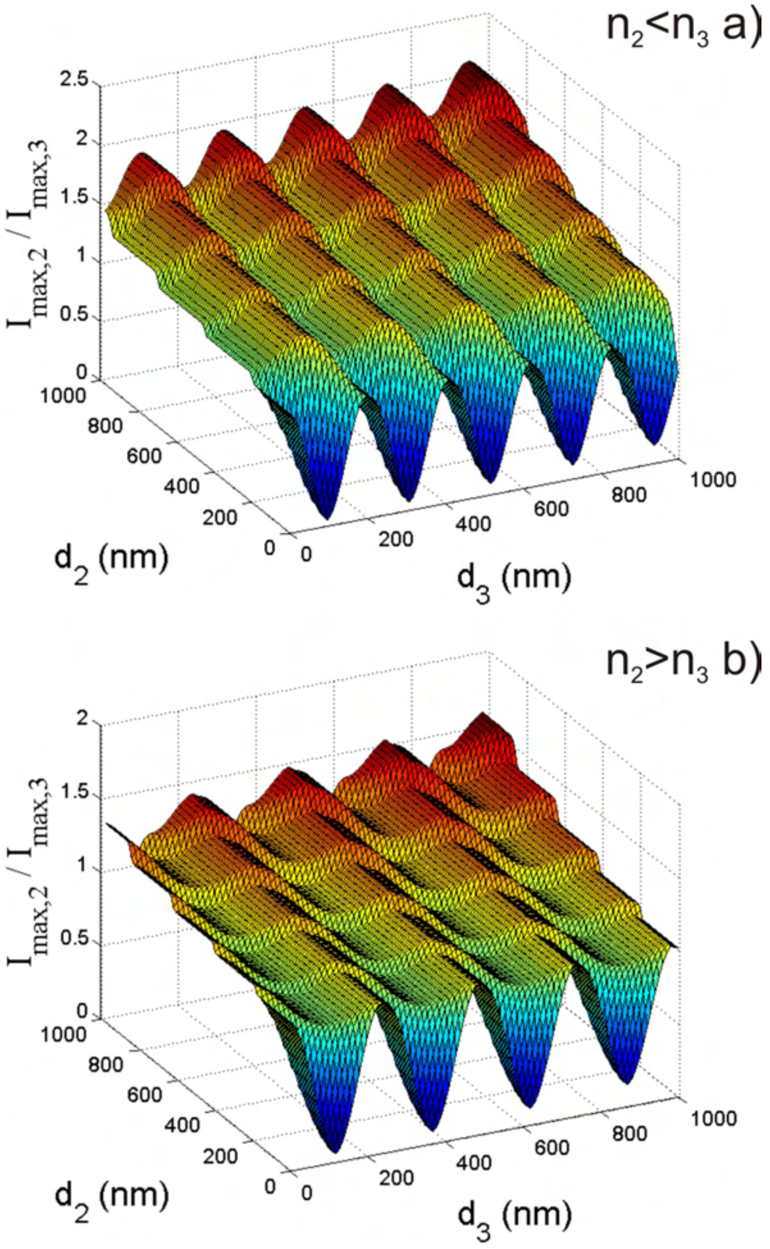

FIGURE 6.18: Ratio of peak intensity in layer 2 to peak in layer 3 as functions of d_2 and d_3 with $d_4 = 200$ nm for $n_2 < n_3$ (a) and $n_2 > n_3$ (b).

is required to provide the thrust. Once again, d_4 appeared to be the dominant parameter determining the ratio.

6.4.2 Discussion

Finally we have enough information to address the original question posed at the beginning of this chapter: can optical standing waves explain the surprisingly low DRL-LIFT thresholds observed in the previous chapter? It should be stressed at this stage that,

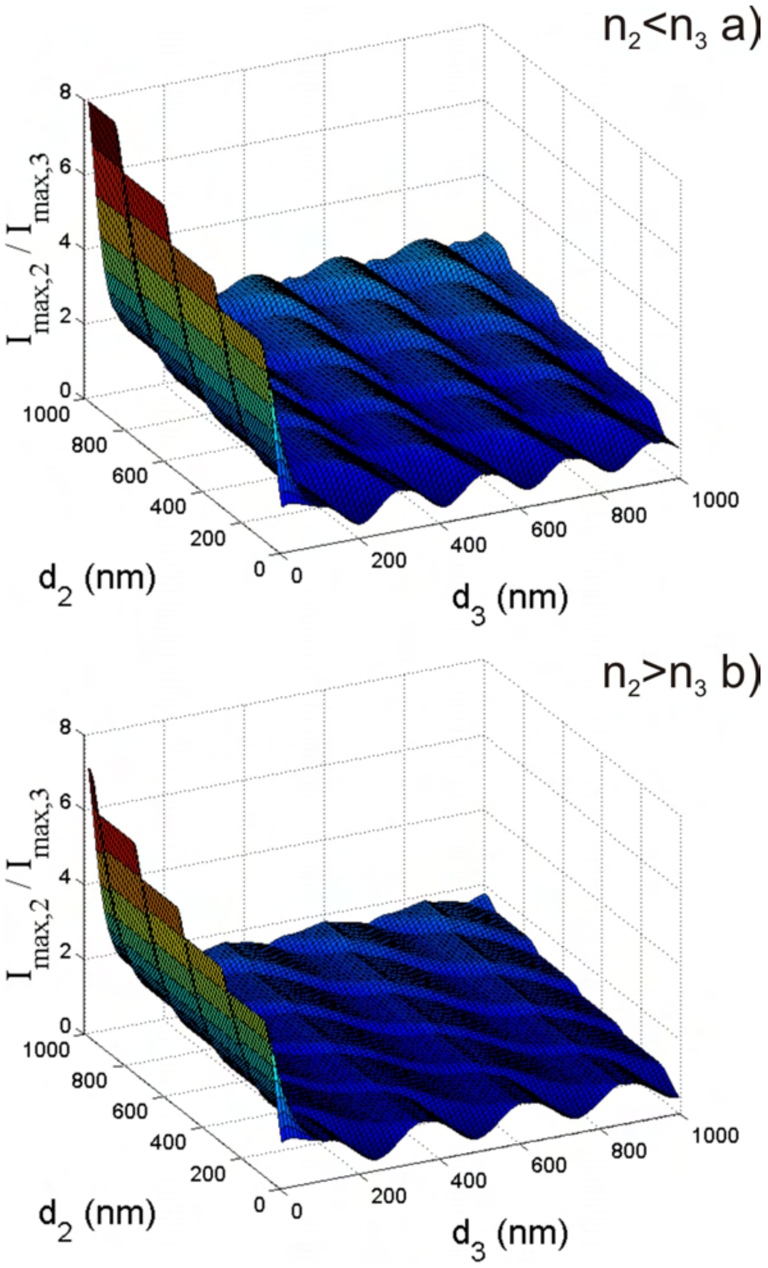

FIGURE 6.19: Ratio of peak intensity in layer 2 to peak in layer 3 as functions of d_2 and d_3 with $d_4 = 400$ nm for $n_2 < n_3$ (a) and $n_2 > n_3$ (b).

due to the relatively large uncertainties in the refractive indices of the TP and GGG, any numerical results would have large errors associated with them. The general trends which will be discussed are more enlightening.

To summarise the important results presented in chapter 5, the DRL-LIFT threshold of a 150 nm GGG donor with a 100 nm TP-DRL was found to be ≈ 90 mJ/cm^2. This value was only $\approx 20\%$ of the TP ablation threshold but was only slightly less than the LIFT threshold of a 150 nm GGG donor without a DRL (≈ 110 mJ/cm^2). The key parameter in determining the quality of depositions was the source-receiver separation (previously

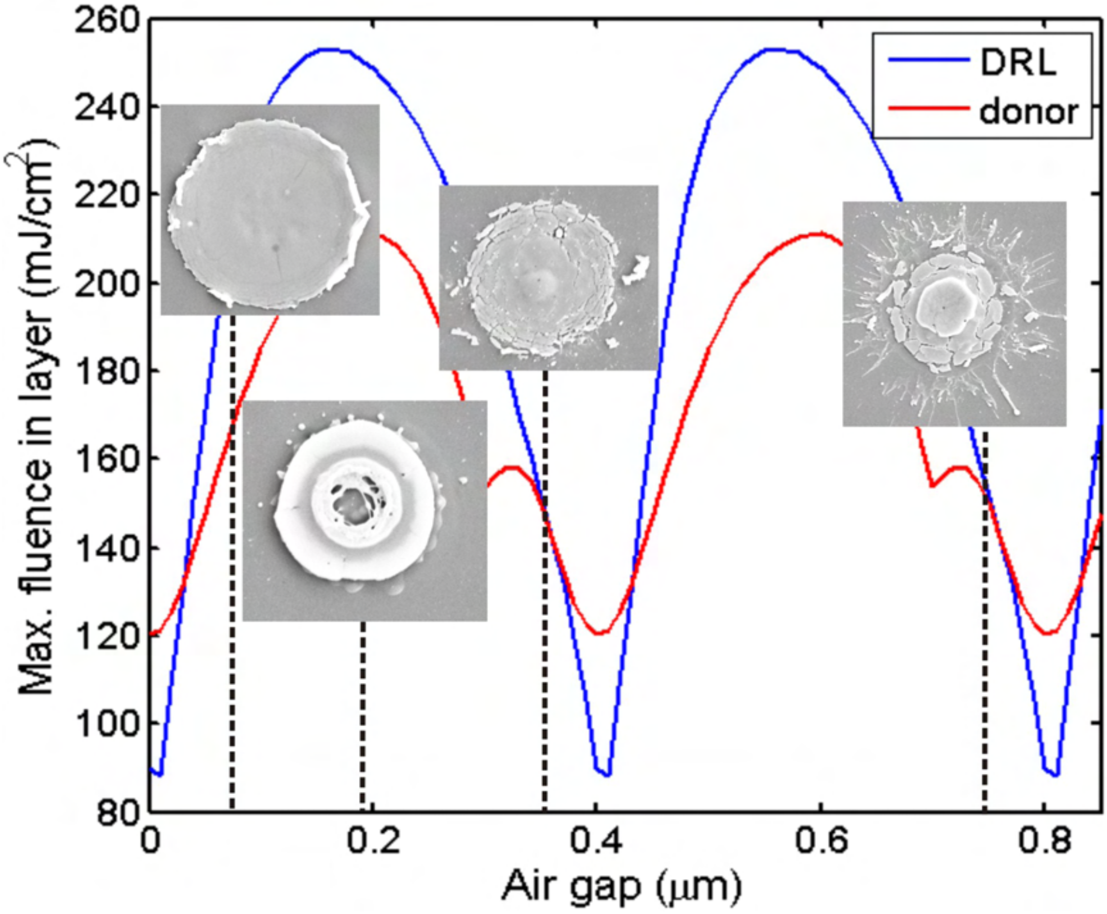

FIGURE 6.20: Plots of variation of maximum fluence (assuming incident fluence 90 mJ/cm^2) in DRL (blue) and donor (red) with d_{air}, given $n_{DRL} = 1.7$, $n_{donor} = 1.9$, $\kappa_{DRL} = -0.06$, $\kappa_{donor} = -0.03$, $d_{DRL} = 100$ nm, and $d_{donor} = 150$ nm.

defined as d_{air}, and analogous to d_4 in the previous analysis). The optimal separation was around 230-250 nm, although good deposits were also seen around $d_{air} = 600$ nm. No significant dependence of the DRL-LIFT threshold with separation was observed, although the amount of material transferred, and the extent to which transfer without melting was evident both varied dramatically (and, more crucially, periodically) with d_{air}. The TP-DRL was observed to be completely removed (decomposed) at the optimal values of d_{air}; liquid material was seen on the deposits at other values of d_{air}, but it is not known if this was residual DRL or melted donor.

The graph in fig. 6.20 shows the calculated variation of maximum fluence in DRL (blue line) and donor (red line) with d_{air} assuming an incident fluence at the glass-DRL interface of 90 mJ/cm^2 (achieved with the proper choice of E_{In}). The other parameters were taken to be $n_{DRL} = 1.7$, $n_{donor} = 1.9$, $\kappa_{DRL} = -0.06$, $\kappa_{donor} = -0.03$, $d_{DRL} = 100$ nm, and $d_{donor} = 150$ nm, i.e. in approximate agreement with the experimental conditions. Selected SEM micrographs of deposits obtained at certain values of d_{air} are included for comparison; a more complete picture of deposit variation with d_{air} will be presented later.

The first point to note is that the increase in local intensity due to the standing optical wave was insufficient to explain the $\approx 80\%$ decrease seen for the DRL-LIFT threshold fluence c.f. the TP ablation threshold. The model predicted a maximum achievable intensity in the films slightly more than double the incident intensity due to multiple reflections, i.e. a predicted transfer threshold of ≈ 250 mJ/cm^2 if the standing wave were the sole cause of the low threshold. Note also that the maximum obtainable fluence in the DRL predicted by the model (≈ 250 mJ/cm^2) was not sufficiently intense to imply localised boiling of residual solvent (predicted by Bonse et al. to occur at $\approx 350 - 400$ mJ/cm^2 [Bonse et al., 2005a]). Hence, the standing wave alone could not account for the low DRL-LIFT threshold, nor could it account for the observed complete decomposition of the TP-DRL.

To explain the observed dependence of the deposits on d_{air}, it was necessary to consider the intensity in the donor layer. It is already known that the GdGaO-donor LIFT threshold fluence without a DRL, i.e. approximately the ablation threshold, was ≈ 110 mJ/cm^2, only $\approx 20\%$ greater than the DRL-LIFT threshold with the TP-DRL. As can be seen from the graph in fig. 6.20, due to multiple reflections the fluence in the donor exceeded the ablation threshold for all values of d_{air}. Note that, because only estimates of the material properties of DRL and donor were available, it is very possible that there are significant errors in the calculated fluence values. This could explain why the fluence appeared to be great enough to ablate the donor for all values of d_{air}. Note also that we have assumed very weak absorption for the donor. As the calculated values of fluence in the donor are near the ablation threshold then it is likely that this assumption is no longer valid and that κ_{donor} was really greater than the estimated value. Increasing the value of κ_{donor} was found to decrease the maximum fluence in both layers (results not shown here), which could also explain the apparent discrepancy between the calculated fluences and amount of donor damage observed in the SEM micrographs.

Figure 6.21 shows how the deposits varied with d_{air}. An approximate d_{air} scale is included in the figure, however it should be noted that, because of the imprecise way the separation was measured (namely thin film interference in the air gap using a white-light source), and difficulty in accurately identifying deposits after transfer, a large error is attached to the given values of d_{air}. It is difficult to quantify this error and it could be as much as ±50 nm; that said, the SEM micrographs do at least correspond to a monotonic (nonlinear) increase of d_{air} across the investigated range. The reason that d_{air} did not increase linearly was that the carrier and receiver bent slightly under vacuum

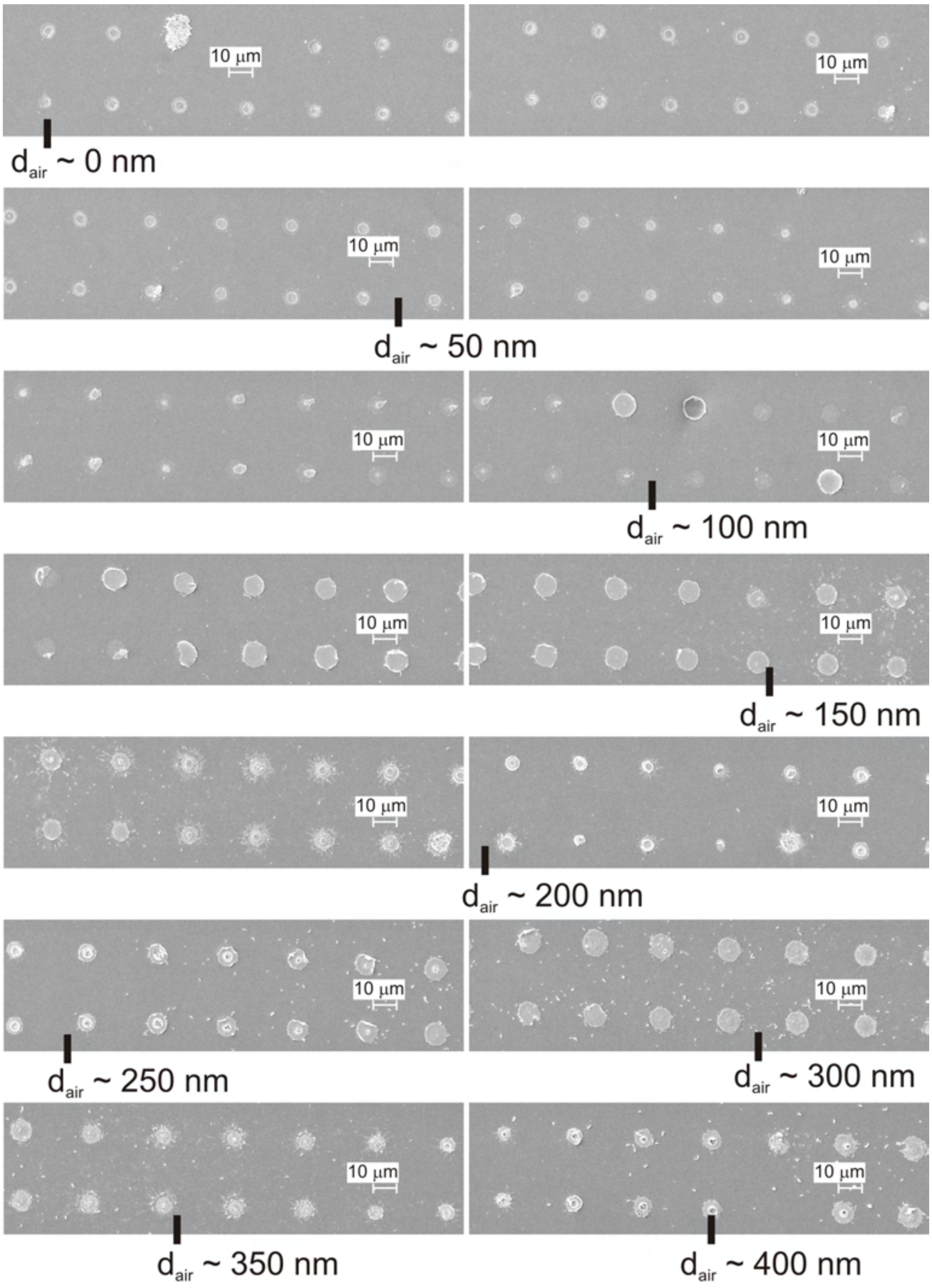

Figure 6.21: SEM micrographs of GGG deposits obtained with a TP-DRL with varying d_{air}. Marked points indicate an approximate d_{air} scale.

(the experiments were conducted at ≈ 0.1 mbar to ensure tight contact between donor and receiver).

In tight contact and for small separations, no clean deposits were obtained, probably for the reasons discussed earlier. However there was also a lot of receiver damage, possibly partially due to the high fluence in the donor, which would have caused the donor to ablate strongly. For separations around $d_{air} \approx 100$ nm and $d_{air} \approx 300$ nm, the fluence in the donor was comparatively low (see fig. 6.20), minimising laser-induced damage and allowing for the DRL-LIFT of clean discs of donor material, although at the larger separation, there was increased shattering of the transferred pellet. Around the values of d_{air} for which the fluence in the donor was maximised, i.e. $d_{air} \approx 200$ nm and $d_{air} \approx 400$ nm, the fluence in the donor was well above the ablation threshold (see fig. 6.20), hence damage to the donor was extensive, appearing in the form of liquid splatter or holes in the transferred material.

Looking at figures 6.20 and 6.21, the standing wave model appears to explain the variation of deposits with d_{air}. This observation, combined with the fact that it appears standing waves alone cannot explain direct laser-induced decomposition of the TP-DRL, allows us to conclude that absorption of laser energy in the donor layer, and subsequent back heating of the DRL (as discussed in section 5.6.2), was the key process in the DRL-LIFT experiments leading to low-threshold transfer. This conclusion indicates a problem with the current setup because the whole purpose of the DRL was to prevent exposure of the donor to the laser energy. A further problem this demonstrated was that, in a LIFT setup with the donor (and DRL in a DRL-LIFT setup) transparent to the laser wavelength, the source-receiver separation becomes another parameter (alongside fluence, film thickness etc.) that must be finely controlled to optimise the process, introducing extra complexity. Thus it is suggested that, in LIFT/DRL-LIFT experiments, a laser wavelength should be chosen that is well absorbed by the DRL or donor. In the current setup, using high intensity, ultrashort pulsed lasers and relying on multiphoton absorption in the DRL doesn't appear to be a promising route either because the damage threshold of the donor was less than that of the DRL so donor ablation occurred before DRL-LIFT. This is not to say such an approach would not work with other choices of DRL/donor material combinations.

6.5 Conclusions

The influence of optical standing waves on thin film ablation, LIFT, and DRL-LIFT has been considered theoretically. It has been found that the formation of a standing wave in a TP film coated on the rear-side of a glass carrier substrate could explain why the ablation threshold of such a film is approximately 1.5 times lower than that of a identical film on the front-side. In LIFT/DRL-LIFT setups it has been found that the formation of a standing wave introduces undesirable effects, primarily a strict dependence of deposit quality on the source-receiver separation that does not exist for the process with absorbing films.

The model was used to further investigate the TP-DRL assisted LIFT results presented in the previous chapter. It was found that the formation of a standing wave could not account for the surprisingly low forward transfer threshold. Instead the investigation supported the hypothesis that transfer was induced by absorption of laser energy in the donor layer and subsequent back-heating of the DRL, which then decomposed thermolytically. The theoretically predicted dependence of donor damage on the source-receiver separation was well matched by a study of GGG deposits obtained as a function of d_{air} using the TP-DRL.

The implications of standing waves for LIFT/DRL-LIFT have been discussed and it has been suggested that either the process should be conducted with a laser wavelength well absorbed by the DRL (or donor in conventional LIFT), or with multiphoton absorption of ultrashort pulses. However, in the latter case, care must be taken in DRL-LIFT experiments to ensure that the fluence threshold of multiphoton ionisation in the DRL is lower than the ablation threshold of the donor.

Bibliography

Bonse, J., Solis, J., Urech, L., Lippert, T., and Wokaun, A. (2007). Femtosecond and nanosecond laser damage thresholds of doped and undoped triazenepolymer thin films. *Appl. Surf. Sci.*, 253:7787–7791.

Bonse, J., Wiggins, S., Solis, J., and Lippert, T. (2005a). Phase change dynamics in a polymer thin film upon femtosecond and picosecond laser irradiation. *Appl. Surf. Sci.*, 247:440–446.

Bonse, J., Wiggins, S., Solis, J., Lippert, T., and Sturm, H. (2005b). Femtosecond laser-induced decomposition in triazenepolymer thin films. *Appl. Surf. Sci.*, 248:157–162.

Mack, C. (1986). Analytical expression for the standing wave intensity in photoresist. *Appl. Optics*, 25(12):1958–1961.

Widmann, D. (1975). Quantitative evaluation of photoresist patterns in the 1 μm range. *Appl. Optics*, 14(4):931–934.

Chapter 7

Solid-Phase Forward Transfer: Premachining and Ballistic Laser-Assisted Solid Transfer

7.1 Introduction

The deposition of intact material in solid phase is a major goal for forward transfer techniques. Conventional ns-LIFT is not well suited to achieve this as the material to be transferred is required to act as its own propellant and, as was discussed in chapter 3, the ns-LIFT process tends to result in a complete melting of the donor film during transfer. The previous chapters and several reports in the literature (particularly those of Fardel et al. [Fardel et al., 2007]) demonstrate the ability of DRL-LIFT to meet this goal, but challenges remain. Other LIFT variants such as MAPLE-DW (section 2.2.1), LP-LIFT (section 2.2.5), or the others described in chapter 2, tend to focus on intact or solid transfer but not both.

For reasons discussed in chapter 3, fs-LIFT may offer advantages for solid and intact transfer. Intact, particulate transfer of biomaterial has already been demonstrated by Zergioti et al. [Zergioti et al., 2005a,b]. In this chapter we shall present results demonstrating the first reproducible solid transfer without a DRL. Section 7.2 provides a discussion on the motivation for solid and intact (and ultimately both) transfer. Next, in section 7.3, some typical fs-LIFT results are presented to show that the use of femtosecond pulses alone appears to be insufficient to achieve solid transfer. Section 7.4 introduces the concept of premachining, whereby the pattern to be transferred is written into the donor prior to fs-LIFT to circumvent the challenge of having to shear the transferred material from the donor film for solid transfer. Premachining is also

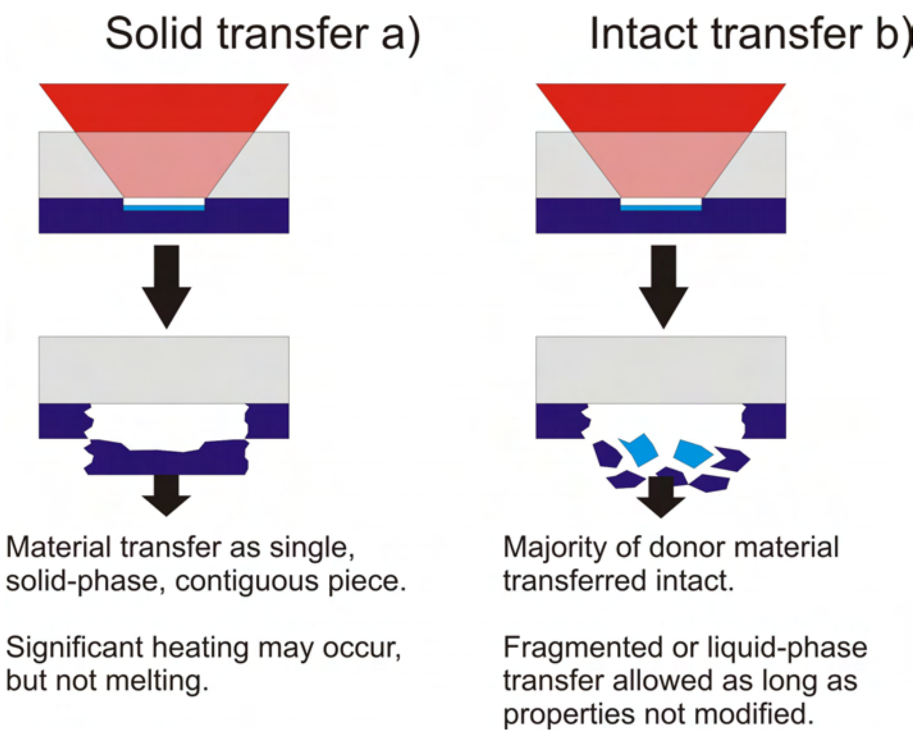

FIGURE 7.1: Diagrammatic representation of what is meant by "solid" (a) and "intact" (b) transfer in the text.

found to be incapable of allowing solid transfer, so in section 7.5 a new forward transfer technique is introduced, Ballistic Laser-Assisted Solid Transfer (BLAST) [Banks et al., 2008a]. BLAST utilises multiple, low-energy femtosecond pulses to gradually remove the material to be transferred from the carrier and allows, for the first time, solid-phase forward transfer. Finally, in section 7.6, results using spatially shaped pulses for BLAST, thus combining the advantages of this new technique with those of premachining are presented.

7.2 Motivation for Solid and Intact Transfer

Before moving on to discuss why the forward transfer of solid and intact material is such an important goal, it is necessary first to define clearly what is meant by each term.

solid transfer: By solid transfer we refer not just to the forward transfer of material in solid phase, but to the transfer of the entire irradiated area as a single, solid-phase, contiguous piece, as shown in fig. 7.1(a). Significant heating may occur, as long as the material remains in solid phase.

intact transfer: Intact transfer indicates material that exhibits the same properties (physical, chemical etc.) after forward transfer as the original donor film, as shown

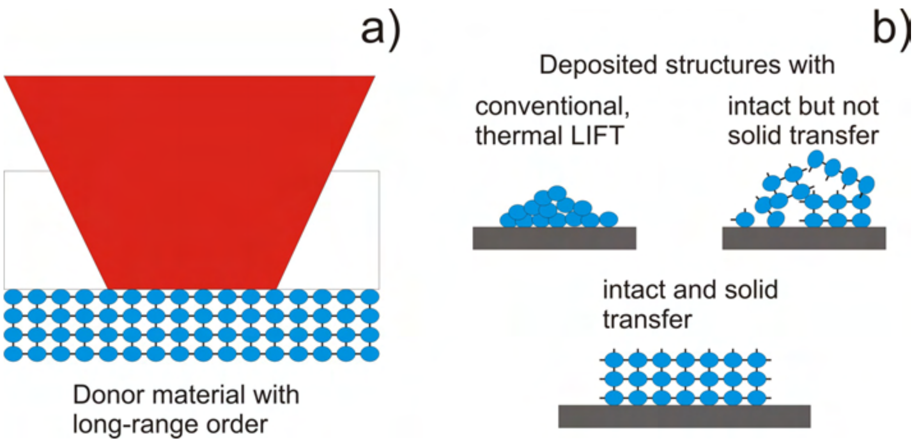

FIGURE 7.2: Illustration of why certain types of donors require both solid and intact transfer.

in fig. 7.1(b). Note that intact transfer may also imply solid transfer for certain materials that exhibit long-range order, e.g. single crystal or oriented.

Different kinds of materials have different transfer requirements. For example, biological materials or functional polymers require intact transfer or their functionality may be lost or altered during transfer. Metallic donors, particularly those intended for electronic applications, may benefit from solid transfer to avoid depositing porous structures with resistivity much greater than that of the bulk material (as was seen when using MAPLE-DW to deposit conductive lines [Pique et al., 1999]). Certain applications (e.g. micro- and nanodroplet deposition) may require that neither of the above processes occurs, and then there is a final category that requires both solid AND intact transfer. Donor films that are single crystalline, single-domain, or oriented fall into this final, and most challenging, category (as shown in fig. 7.2, reproduced from chapter 3). Such materials must be transferred in solid phase to preserve their underlying structure, but may also exhibit other, temperature-dependent changes (e.g. a glass transition). Hence, they must also be transferred intact if the deposited material is to display the same properties as the donor film. Let us now consider the history of solid and intact forward transfer.

7.2.1 Solid Transfer

A review of successful solid transfer experiments is necessarily short. The only notable results (besides our own [Banks et al., 2008a]) are those of Kantor et al. [Kantor and Szorenyi, 1995; Kantor et al., 1994a,b] using LP-LIFT (see section 2.2.5). This technique requires a significant amount of heating of the donor to induce transfer and so may not be readily applicable to the intact transfer of materials with other, temperature-dependent property changes, as discussed above. Also, because transfer of donor in LP-LIFT depends on annealing of material to the receiver, the choice of receiver material is limited. For example, it would not be possible to use LP-LIFT to deposit onto plastics for flexible display applications. However, for materials where only solid-phase transfer is necessary, onto receivers that can withstand significant heating, LP-LIFT is a viable and simple method of achieving this.

7.2.2 Intact Transfer

The majority of forward transfer studies in recent years have been concerned with the intact transfer of a variety of functional materials. Usually these works have involved the use of sacrificial materials to absorb the laser energy and provide the thrust for forward transfer without (significant) direct damage to the material of interest. The most widely used techniques are those described in chapter 2: DRL-LIFT, MAPLE-DW, LMI, LITI, and a-Si:H LIFT. These techniques have allowed for the forward transfer direct-writing of a number of functional devices including organic LED's [Fardel et al., 2007], microbatteries [Arnold et al., 2004], solar cells [Kim et al., 2004], phosphor screens [Fitz-Gerald et al., 2000], sensors [Pique et al., 1999, 2002], DNA microassays [Serra et al., 2004], bacteria [Hopp et al., 2004], cells [Doraiswamy et al., 2006], light-emitting polymers [Blanchet et al., 2003], and various fluorescent molecules [Fukumura et al., 1994]. Recently, nanosecond LIFT was shown to allow for the intact transfer of luciferase [Tsuboi et al., 2007].

fs-LIFT has also been shown to be capable of intact transfer without the use of a sacrificial material. Zergioti et al. have deposited biomaterial [Zergioti et al., 2005a], Koundourakis et al. have produced active optical microstructures [Koundourakis et al., 2001], and Thomas et al. have deposited conducting polymers [Thomas et al., 2007].

7.2.3 Solid and Intact Transfer

Problems begin to arise when trying to combine solid and intact transfer. MAPLE-DW, LMI, and LITI are designed for the transfer of particulate or liquid donors and cannot, by definition, be used for solid and intact transfer. MAPLE-DW has been used for the transfer of metallic powders to form electrical connections, but the resultant structures were porous and had resistivity 10^3 times higher then the bulk value [Pique et al., 1999].

DRL-LIFT, most notably the work of Fardel et al. [Fardel et al., 2007] and our own results ([Banks et al., 2008b] and chapters 5 and 6), is so far the only technique shown to be capable of solid and intact transfer. Even then it is necessary to use specially designed materials, such as the TP, for the DRL to allow for good quality transfer and avoid residual DRL contamination. Such materials are not readily available and also place limitations on the available donors, e.g. donors requiring high temperatures or lattice matching to deposit cannot be grown onto the polymer. That said, for a wide variety of applications requiring solid and intact transfer, DRL-LIFT with the TP is the technique of choice.

It would be highly desirable to have a forward transfer technique that combined the simplicity of conventional LIFT with the ability to deposit virtually any solid-phase material offered by solid and intact transfer, without the limitations imposed by having to include a DRL. It was suggested in chapter 3, that fs-LIFT might offer such a capability because of the reduced heated volume and shock-induced (rather than thermolytic) transfer mechanism. In practice however, there are still challenges, as illustrated next.

7.3 fs-LIFT for Solid and Intact Transfer

As a simple demonstration of the capabilities of fs-LIFT for solid and intact transfer, forward transfer experiments with Cr were conducted. The experimental setup was identical to that described for the nanodroplet experiments in chapter 4 with the sole exception that the Cr donor film was 80 nm thick. This donor thickness was chosen to be significantly greater than the skin depth of Cr at $\lambda = 800$ nm ($\delta \approx 20$ nm [Kim and Na, 2007]) to try and avoid complete melt-through of the donor.

The transfer threshold was measured to be around 350 mJ/cm^2, in good agreement with the onset of evaporation in the Cr donor found in the nanodroplet experiments (see section 4.4). For fluence above ≈400 mJ/cm^2, the deposited structures were typically fragmented and appeared to have been completely melted during transfer.

Figure 7.3 shows SEM micrographs of the best (in terms of solid transfer) kind of deposits typically obtained with this setup. The fluence was around 380 mJ/cm^2, but similar deposits were obtained for 370-390 mJ/cm^2. The contiguous nature and smooth appearance of the deposits suggested transfer of a significant portion of the donor in solid-phase. Comparing these results with typical structures obtained with ns-LIFT (see e.g. [Bohandy et al., 1986, 1988; Nakata et al., 2002; Pimenov et al., 1995]) clearly demonstrates the potential benefits of using femtosecond duration pulses for achieving solid transfer. However, there was still evidence of significant melting, as demonstrated by the splashed droplets around the main deposits.

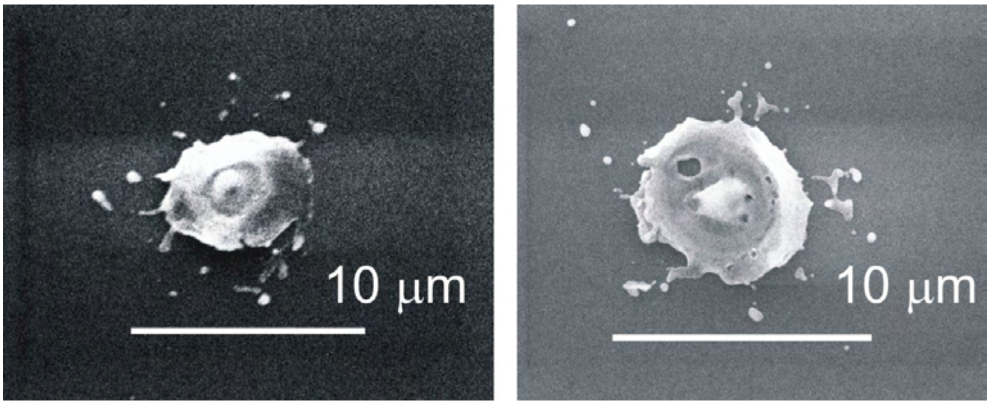

FIGURE 7.3: SEM micrograph of typical Cr deposits obtained with 380 mJ/cm^2.

Clearly the above results do not represent an exhaustive study of fs-LIFT for solid transfer. Further optimisation of the choice of the experimental parameters would be highly likely to produce improved solid transfer results. However, our objective was to develop a general solid transfer technique applicable to a range of donors. Hence, it was decided that fine-tuning of the fs-LIFT process to find the optimal experimental conditions was not the correct avenue to pursue. Instead we proceeded to investigate variations on fs-LIFT that could be reasonably expected to produce more promising results.

7.4 Premachining

To induce solid transfer, there are essentially two processes that must occur (as shown in fig. 7.4(a)):

- the stiction of the donor to the carrier must be overcome, and
- a whole pellet of donor must be sheared from the film without shattering.

The first process is easily achieved with ablation or evaporation induced by focused lasers. The second process can be circumvented by etching or machining the donor prior to LIFT to define the area for transfer as a freestanding structure on the carrier, as shown in fig. 7.4(b). This technique can be referred to as *premachining*. In principle, the resultant structures on the carrier can then be LIFTed without having to be sheared from the remaining film. Hence, they shouldn't shatter during transfer, and can be deposited as a single piece. It would be tempting to expect that premachining may also allow for LIFT with lower fluence, thus reducing the amount of melting and evaporation. However, the film must still be evaporated at the donor-carrier interface to overcome

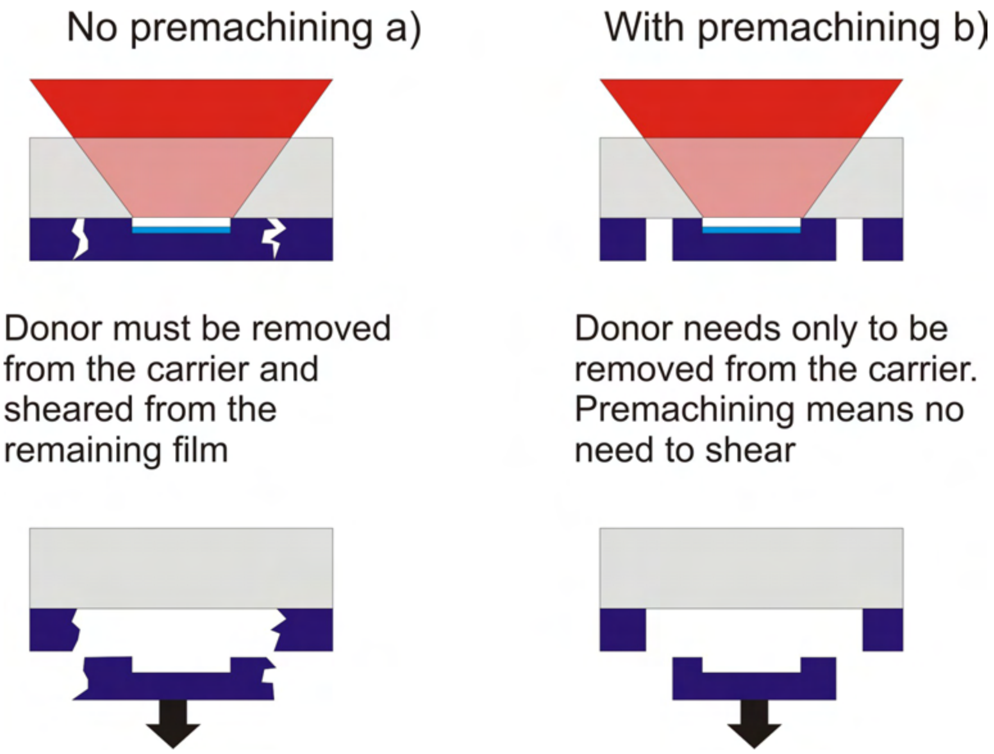

FIGURE 7.4: Diagram showing the processes that must occur to enable solid transfer without (a) and with (b) premachining.

the stiction, and so the transfer fluence is, in fact, likely to be similar for premachined and unstructured films.

7.4.1 Premachining Transfer Results

To investigate the potential of fs-LIFT of premachined films in practice, focused ion beam (FIB) machining was used to write structures into a 200 nm Cr donor film. The FIB was used to write a 2D raster pattern into the donor, resulting in a grid of freestanding rectangular structures ranging from 1x1 μm to 10x10μm, as shown in fig. 7.5(a).

The threshold fluence for forward transfer of the premachined donor was found to be around 350 mJ/cm^2. Sample structures transferred around this fluence are shown in fig. 7.5(b). The laser spot size was around 8 μm in diameter, resulting in multiple freestanding structures being transferred with a single pulse. Clearly solid transfer was not achieved. Indeed, the deposited structures more closely resembled those seen in the nanodroplet studies in chapter 4 when the fluence was increased to a level corresponding to the onset of phase explosion in the donor.

One possible explanation for the poor quality of the depositions could have been damage to the carrier by machining too deep with the FIB, however similar results were seen

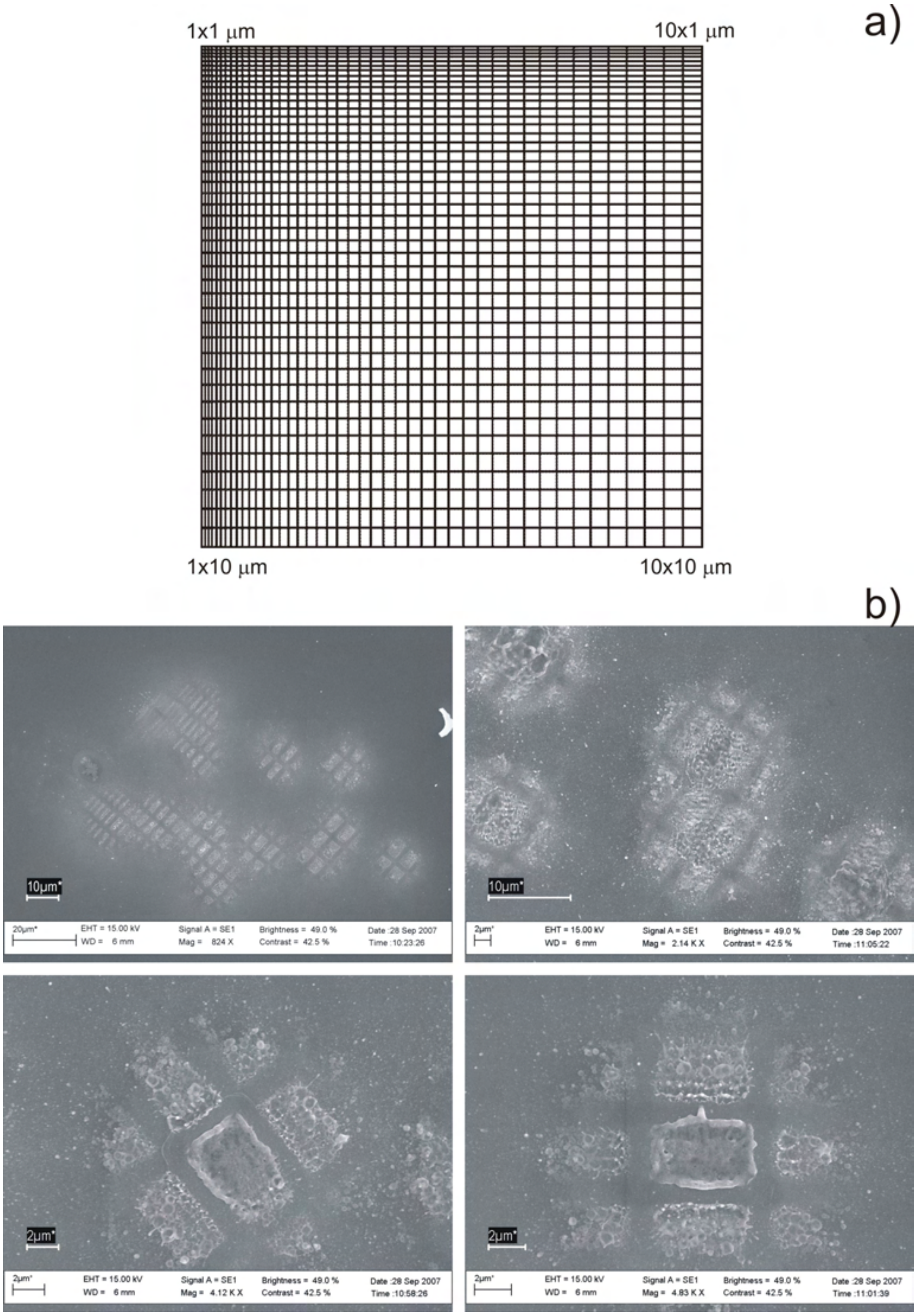

FIGURE 7.5: SEM micrographs of Cr deposits on Si from the premachined donor. The laser spot size was around 8 μm.

when fs-laser micromachining was used instead of FIB to define the structures into the donor. Hence, we can conclude that damage to the carrier was not the cause of the poor quality depositions as the laser intensity was too low to have damaged the carrier. Instead it is believed that, by defining freestanding structures into the donor, lateral heat diffusion in the film was prevented. Hence, for a given incident fluence, the premachined

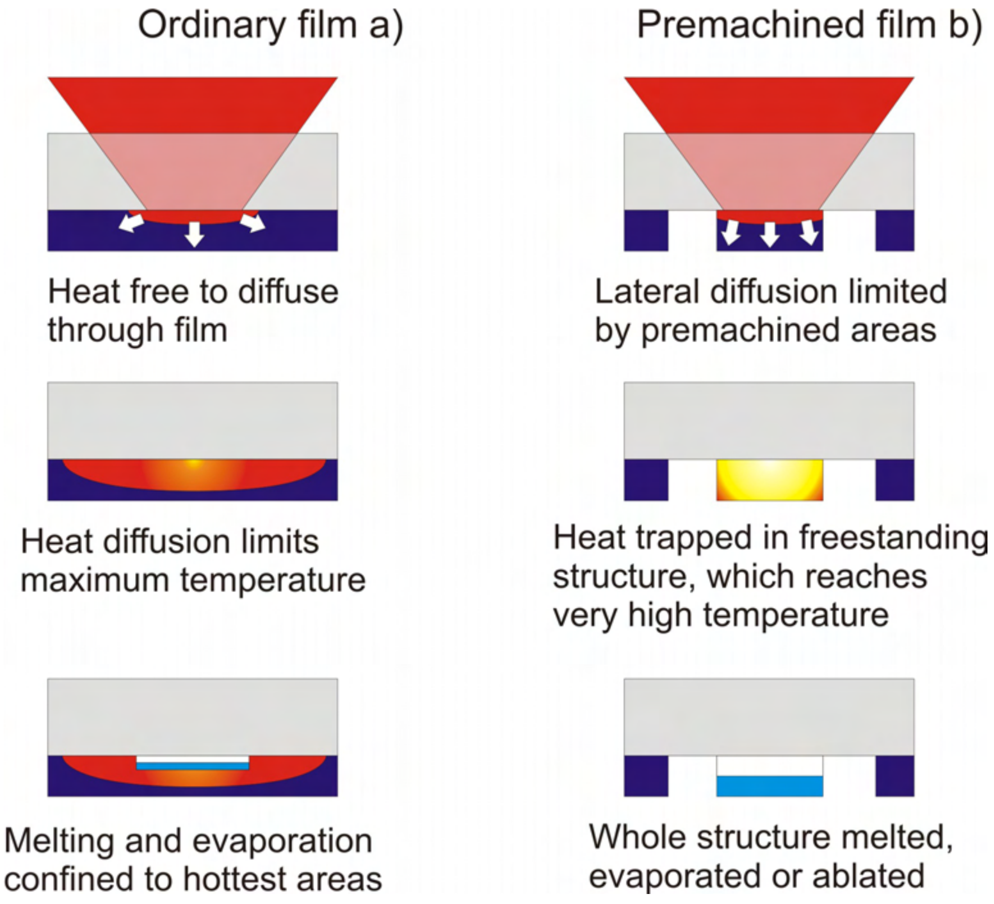

FIGURE 7.6: Illustration of how a premachined donor (b) reaches higher temperatures during LIFT than a non-machined one (a).

film reached a higher temperature than the film that had not been machined (see fig. 7.6). Hence, it is possible that, when the fluence was sufficient to cause evaporation at the carrier-donor interface (as was required for transfer), the film was unavoidably melted through.

These results suggested that premachining does not appear to be an encouraging technique to achieve solid transfer either. It is possible that thicker donors may transfer better, because the lack of lateral heat diffusion can be offset by diffusion perpendicular to the carrier-donor interface. Further experiments would be necessary to investigate this. However, it is apparent that the premachining technique introduces undesirable extra complexity to LIFT and, in the light of these unpromising initial results, it was decided not to pursue these experiments further.

7.5 Ballistic Laser-Assisted Solid Transfer

In these last 2 sections, we present initial results from a further complementary LIFT technique for solid transfer of 'hard' donor films. This technique we have termed Ballistic Laser-Assisted Solid Transfer (BLAST). BLAST does not require a DRL and so is potentially applicable for the forward transfer deposition of any 'hard' donor without the possibility of contamination by the DRL.

It is well known that LIFT has a well-defined laser fluence threshold, dependent on the specifics of the donor film (e.g. thickness, absorption, and thermal properties) and patterning laser (e.g. wavelength and pulse duration), below which no forward transfer occurs [Banks et al., 2006]. However, it is also known that evaporation of small amounts of material from a laser-irradiated surface can occur below the fluence threshold for significant bulk modification [Xu et al., 1999]. Whilst the amount of evaporation is small enough to be considered insignificant for micromachining, in a LIFT environment any evaporated material would be trapped between donor film and carrier.

The idea behind BLAST (see fig. 7.7) is to use one pulse with sufficient energy to cause a small amount of evaporation only, without forward transfer of the donor, to delaminate the film in the irradiated region. One or more subsequent pulses, again only energetic enough to evaporate very small amounts of the donor, add more evaporated material to the trapped gas pocket until the pressure builds up sufficiently to shear the irradiated region from the donor film. The advantage of this process is that, as low energy pulses are used, laser-induced damage of the donor is reduced compared with conventional LIFT. Also the release of material from the film is a more gentle process as the donor is delaminated from the carrier prior to transfer, so shattering of material on lift-off can be prevented.

7.5.1 Experimental Setup

The output from the regenerative amplifier (800nm, 110fs, 250Hz rep rate) was used for BLAST experiments. The use of femtosecond duration pulses for BLAST was considered to be necessary to avoid melt-through of the donor. Laser pulses of $\approx$ 4mm diameter were centrally incident on an $\approx 450\mu$m circular aperture in the micromachiner, resulting in an approximately uniform circular beam. An image of the aperture was relayed to the target using the micromachiner fitted with the 5x microscope objective lens, resulting in an $\approx 12\mu$m diameter circular spot at the carrier-film interface, as measured by the laser damaged area. A high-speed, computer controlled shutter (Uniblitz LS3) was used to control exposure of the target to the laser.

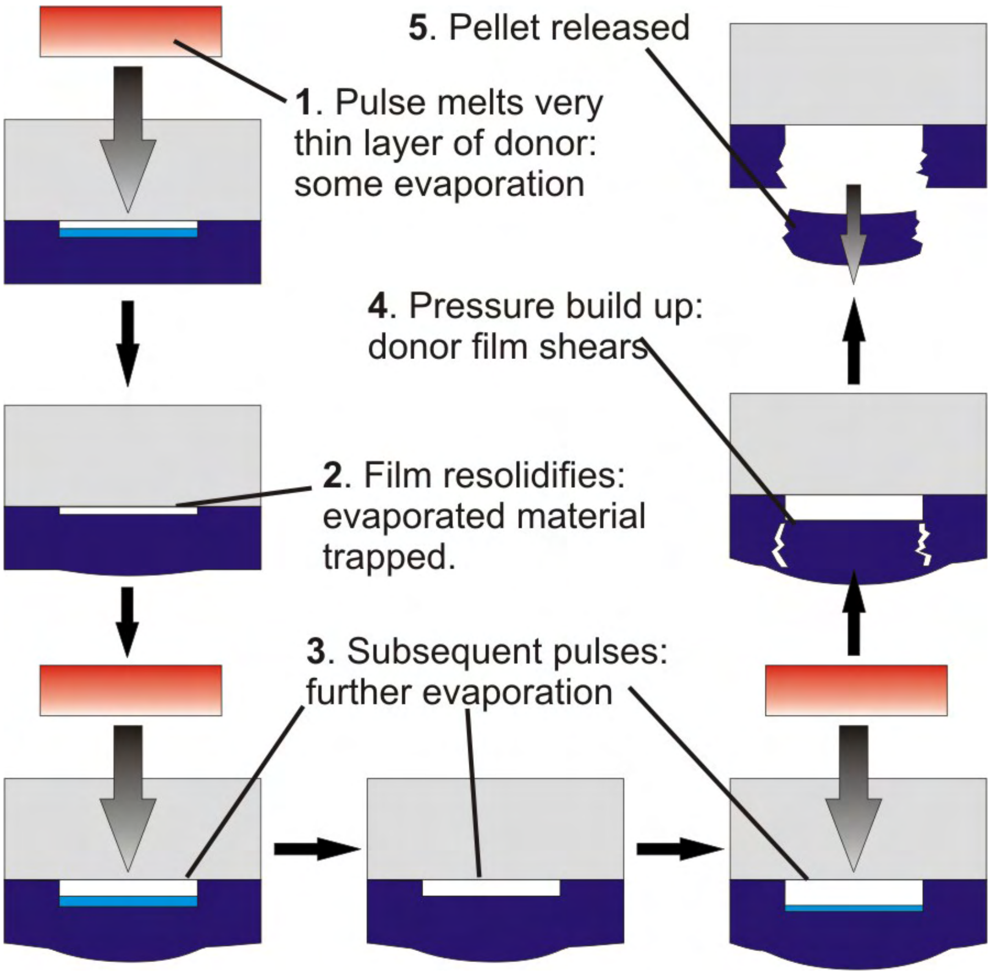

FIGURE 7.7: Representation of the principle of operation of the BLAST technique.

Cr films 80 and 160nm thick were evaporated onto fused silica for BLAST targets. Si wafers were used as receivers and target-receiver separation was controlled by Mylar spacers as with the DRL experiments (see chapter 5). It was not possible to measure d_{air} interferometrically as before because the Cr films were opaque, but we estimate that for all the experiments presented here $1 \leq d_{air} \leq 5$ μm. All experiments were performed under vacuum at $\approx$ 0.1mbar, although BLAST has also been observed to work in air also. The LIFT chamber was again mounted on the micromachiner translation stages.

7.5.2 Results

Figure 7.8(a) shows SEM micrographs of typical deposits obtained from the 80nm donor film using 10 pulses with fluence of 310 mJ/cm^2, well below the single pulse transfer threshold of around 350 mJ/cm^2. The well-defined edges and a complete lack of surrounding debris clearly indicated forward transfer in solid phase (compare with fig. 7.3).

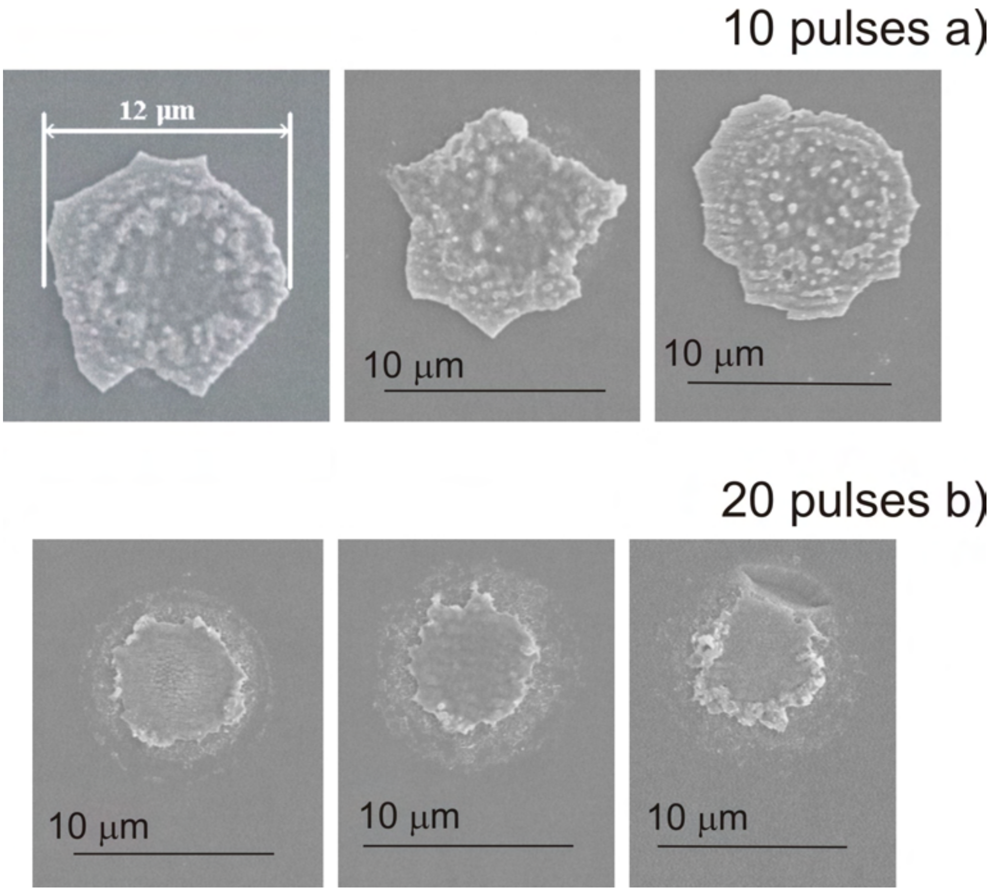

FIGURE 7.8: Cr deposits on Si transferred by BLAST with fluence 310 mJ/cm^2 using 10 pulses (a) and 20 pulses (b).

Note that fluence was even below that measured previously for the onset of significant melting in a Cr film (see chapter 4 and [Banks et al., 2006]).

Figure 7.8(b) shows the effect of using too many pulses for BLAST (in this case 20). Obviously, after transfer (at around 10 pulses), any subsequent pulses just damaged the transferred material further. Hence, care had to be taken to use only the correct number of pulses to induce solid transfer. Note that, in the right hand image, there appeared to be a hole in the Si at the top of the deposit. The hole appeared to have fairly smooth sides, suggesting that material had been chipped out of the receiver. The controlled fabrication of such holes will form the subject of the next chapter.

Deposits like that shown in fig. 7.8(a) clearly demonstrated the ability of multiple-pulse induced BLAST to forward transfer donor material in solid phase. However, the shapes of such deposits varied considerably and there was still evidence of significant damage to the top surface (i.e. the part of the film that was irradiated). The final step was then to combine BLAST with some simple beam shaping to produce a technique with the advantages of both premachining and BLAST.

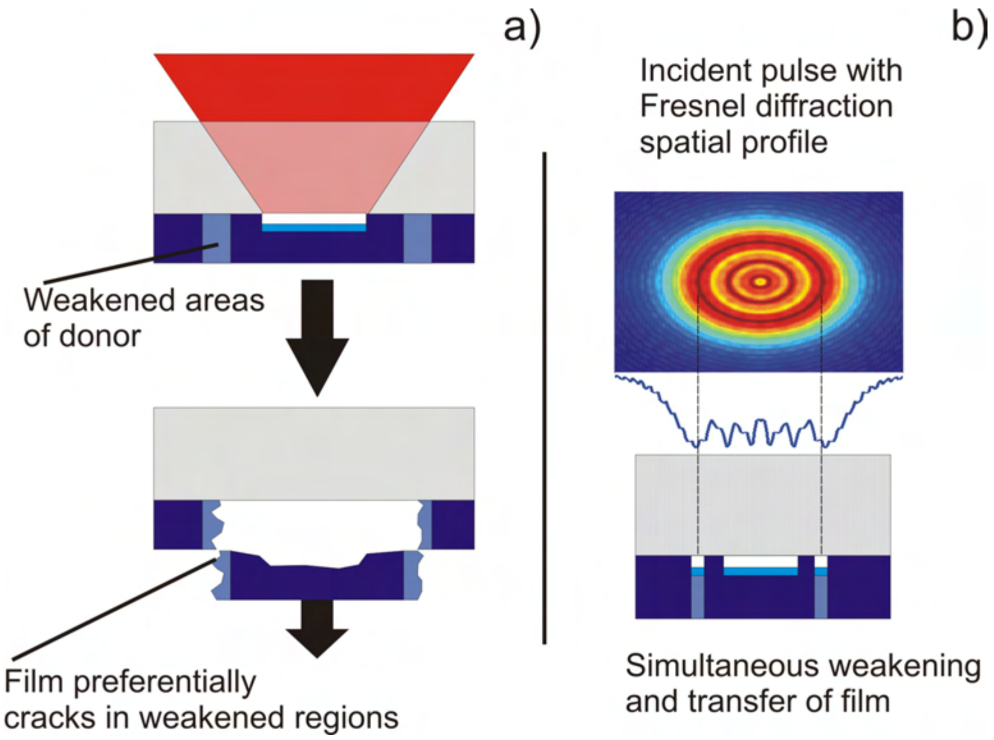

FIGURE 7.9: Schematic of how controllable weakening of the donor film may be expected to give solid transfer (a) and how such weakening can be achieved with spatial pulse shaping (b).

7.6 BLAST with Shaped Pulses

It was demonstrated before that defining freestanding structures into the film prior to transfer was not a viable way of achieving solid transfer because removing film material inhibited heat diffusion away from the irradiated area. But what if the donor could be controllably weakened to define the area for transfer instead, without creating actual gaps in the film? In principle, we could then have most of the benefits of premachining, in that the desired area of donor to be transferred would easily shear from the remaining film. The idea is shown in fig. 7.9(a).

7.6.1 Beam Shaping and its Impacts on Solid Transfer

One way to achieve controlled weakening of the donor is to use spatial pulse shaping. For example, a laser pulse displaying an intense outer ring to define the weak region, and sufficient intensity in the centre to just evaporate (and hence transfer) the donor can simultaneously weaken and transfer the film, allowing for solid transfer, as shown in fig. 7.9(b). Such pulse profiles were, conveniently, very easily achieved using our setup. By displacing the carrier-donor interface slightly away from the best image plane of the laser (usually a few 10's of μm displacement was sufficient), the pulse profile at the interface was the Fresnel diffraction pattern of the aperture. Typically, the Fresnel profile displays exactly the kind of beam profile we require, i.e. an intense outer ring with lower intensity inside.

To calculate theoretically the beam profile used when performing BLAST with Fresnel-diffraction spatial profiles, a simple model using fast Fourier transforms (FFT) was constructed [Saleh and Teich, 1991]. Assuming an input beam profile, b, and an aperture defined by the step function, ap, then the beam profile within the aperture is simply $b \times ap$. By considering the best image at the film as an aperture of diameter a, equivalent to the image size, i.e. $\approx 12\mu$m in this case, then the beam profile at a perpendicular distance z_F from the best image plane, $I(z_F)$, can be calculated using FFTs. We define the beam to be $b = exp(-(x^2/w^2 + y^2/w^2))$, where the carrier-donor interface lies in the plane defined by x and y and the parameter w is chosen to give an energy distribution across the imaged spot equivalent to that in the experiments ($w = 0.003$). The aperture was defined by

$$ap = \begin{cases} 0, & |x|, |y| \geq a/2 \\ 1, & \text{otherwise} \end{cases}$$

$I(z_F)$ was then given by

$$I(z_F) = |iFFT\{H(z_F) \times FFT(b \times ap)\}|$$

where $iFFT$ denotes an inverse FFT and $H(z)$ is the transfer function,

$$H(z) = exp\left(\frac{-i2\pi z_F}{\lambda}\right) \times exp\left(-i\pi\lambda z_F F^2\right)$$

where F is the associated frequency scale of the FFT.

Figure 7.10(a) shows a cross-section of how the calculated intensity distribution varies with z_F for $0 \leq z_F \leq 50$ μm ($\lambda = 800$ nm). Figure 7.10(b) shows plots of the intensity distribution for indicated values of z_F. As can be seen, for certain values of z_F, e.g. $z_F = 2, 14, 32$ μm, the laser profile displayed an outer ring, whilst the intensity across the rest of the laser spot was appreciably lower. We believe that beam profiles at relatively large values of z_F (≥ 30 μm) were better for shaped pulse forward transfer as the difference in intensity between the outer ring (to do the weakening) and in the centre (to induce transfer) was more pronounced. The central intense peak (see e.g. $z_F \approx 30$ μm in fig. 7.10(b)) was relied on the initiate some evaporation to induce forward transfer. It should be noted at this stage that the diameter of the ring region was typically around 5 - 7 μm for $30 \leq z_F \leq 50$ μm.

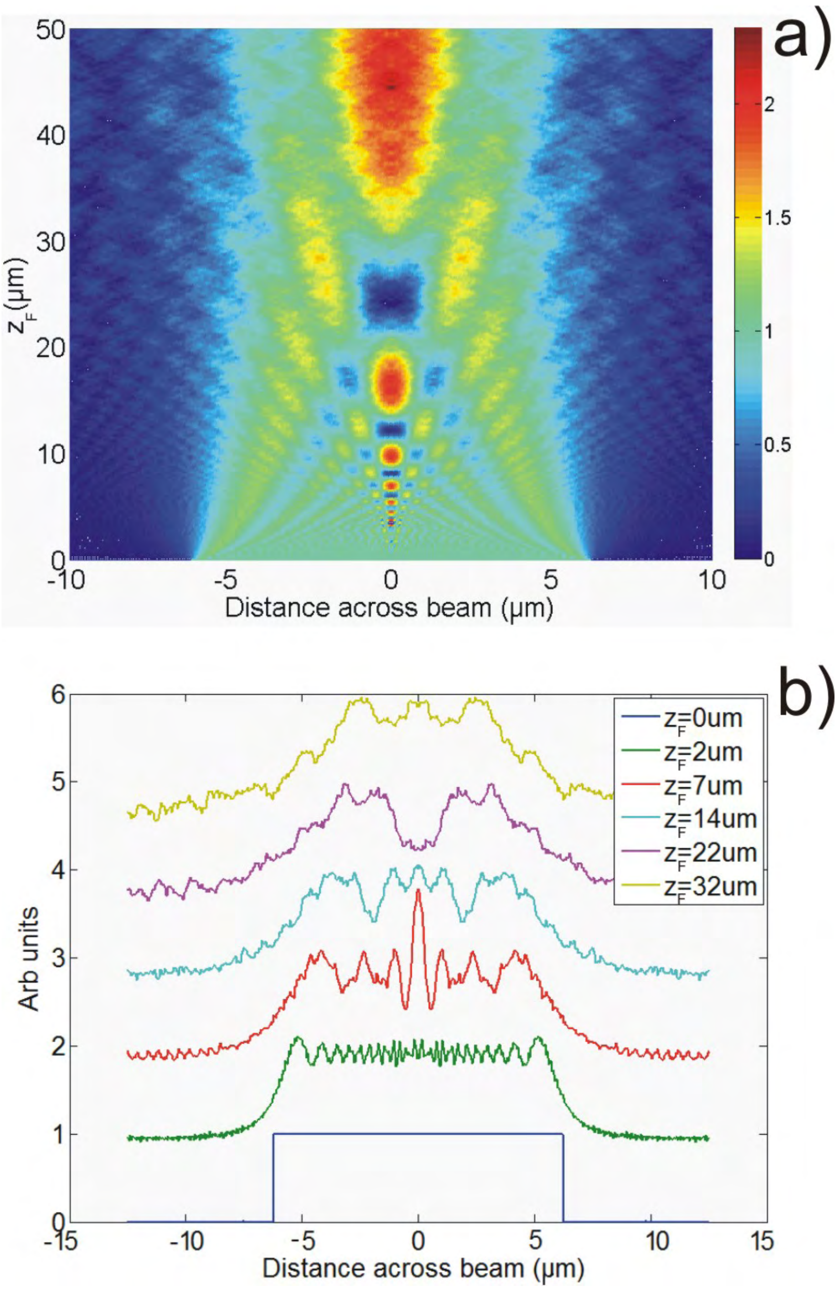

FIGURE 7.10: Cross-section (a) and line-plots (b) of the calculated intensity profile with distance from the best image plane (at $z_F = 0$).

7.6.2 Results with Shaped Pulses

The single-pulse threshold fluence for forward transfer of the 80 nm donor when $z_F \approx 50$ μm was estimated to be around 340 mJ/cm^2. Of course, this value is only approximate as the intensity varied significantly across the laser spot; in reality the ring region would have possessed higher fluence than this, whilst the central region would be lower. It was virtually impossible to give very accurate values as the real beam profile used was

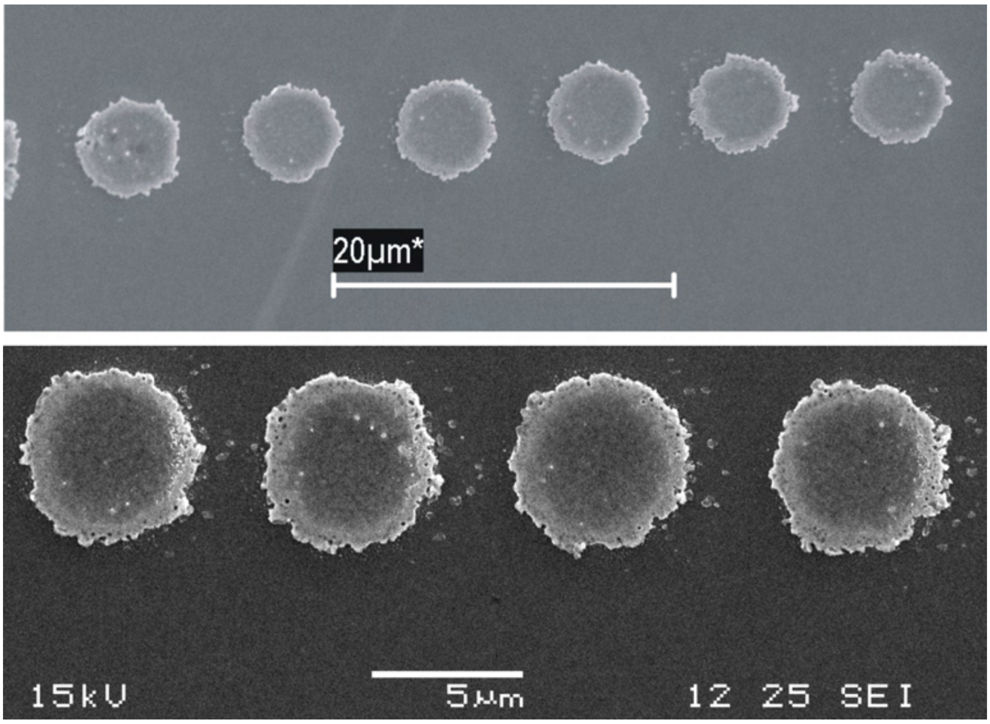

FIGURE 7.11: Cr deposits on Si obtained with single shaped pulses ($z_F \approx 50$ μm) with fluence around the transfer threshold (≈ 340 mJ/cm^2).

difficult to determine and, in truth, high accuracy was not particularly important. Recall, however, that this is slightly less than the value of 350 mJ/cm^2 found with uniform intensity pulses (i.e. $z_F = 0$), demonstrating that the weakening was probably having a small effect, reducing the amount of thrust required for transfer.

Figure 7.11 shows typical Cr deposits obtained with single shaped pulses ($z_F \approx 50$ μm) with fluence around the transfer threshold (≈ 340 mJ/cm^2). Comparing these with the deposits in fig. 7.3 clearly demonstrates the benefits of beam shaping for fs-LIFT in terms of reducing melting and surrounded splatter, and transferring material as a single piece. However, AFM profiling revealed a significant thinning in the centre of the deposits c.f. the donor film thickness, and thickening around the edge. This suggested that there was still significant melting occurring during transfer and associated flow of material towards the edges of the deposits.

The final experiments combined BLAST with beam shaping. Multiple shaped pulses were used to gently remove the donor from the carrier as before, but now these early *pre-pulses* were also simultaneously defining the weakened region. Figure 7.12 shows typical deposits obtained from the 80 nm donor (fig. 7.12(a)) and 160 nm donor (fig. 7.12(b)) using 10 pulses. The fluence for the deposits was ≈ 310 mJ/cm^2 and ≈ 340 mJ/cm^2, respectively. Comparing these with the single shaped pulse (fig. 7.11) and unshaped

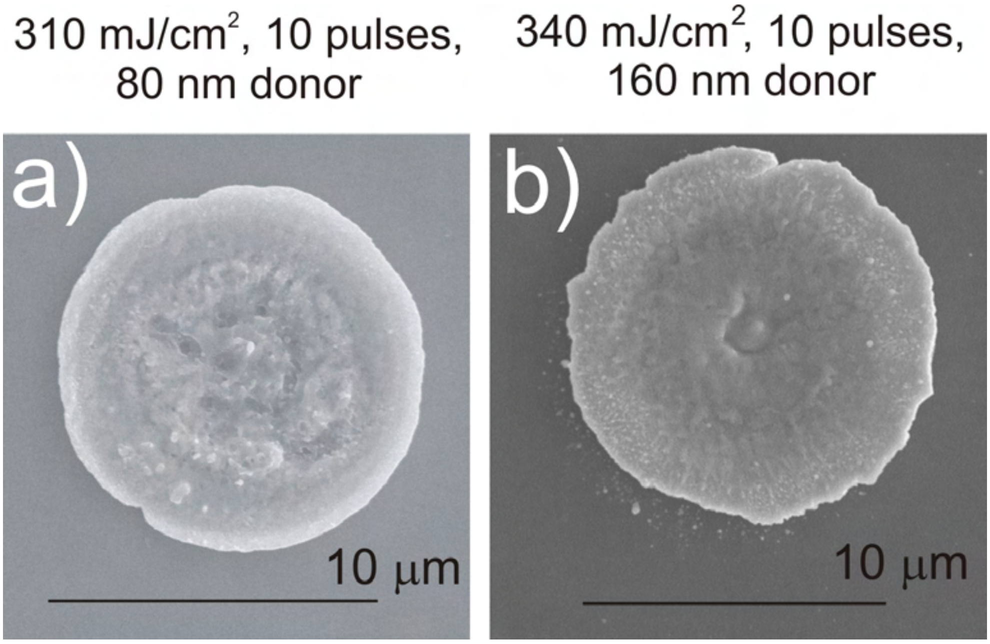

FIGURE 7.12: SEM micrographs of Cr deposited from the 80 nm (a) and 160 nm (b) donor using 10 pulses with fluence ≈ 310 mJ/cm^2 and ≈ 340 mJ/cm^2, respectively.

BLAST results (7.8) clearly shows the major benefits for solid transfer that the BLAST technique with shaped pulses provides in terms of solid transfer.

Evidently the deposits in fig. 7.12 were transferred in solid phase, but the thicker donor film, and hence greater force required for shearing, resulted in pellets with slightly less regular edges and required slightly higher fluence. However, the thicker donor also provided increased capacity for heat to diffuse away from the irradiated region, lessening damage to the pellet compared with similar deposits from the thinner film.

Despite the good quality of the results, there was still evidence of significant damage to the centre of both deposits, even at the optimal transfer conditions. This damage was the result of exposure of the entire area to the multiple weakening pulses. Pulse-to-pulse control of the beam profile may be expected to reduce this damage further. For example, if it were possible to have a few ring shaped pulses incident first to do the weakening, and then a few low intensity, top-hat profile pulses to BLAST the weakened region, we would expect damage to be minimised.

A full parameter scan in terms of z_F, fluence, and number of pulses, N_p, for the 160 nm donor is shown in fig. 7.13. The fluence was varied from ≈ 320 mJ/cm^2 to ≈ 370 mJ/cm^2 in 10 mJ/cm^2 steps, and z_F from the carrier-donor interface 60 μm beyond the best image plane to 200 μm in front of it in 20μm steps. N_p was set to 1, 2, 3, 5, . . ., 21 and for each set of (fluence, z_F, N_p), 3 transfers were attempted.

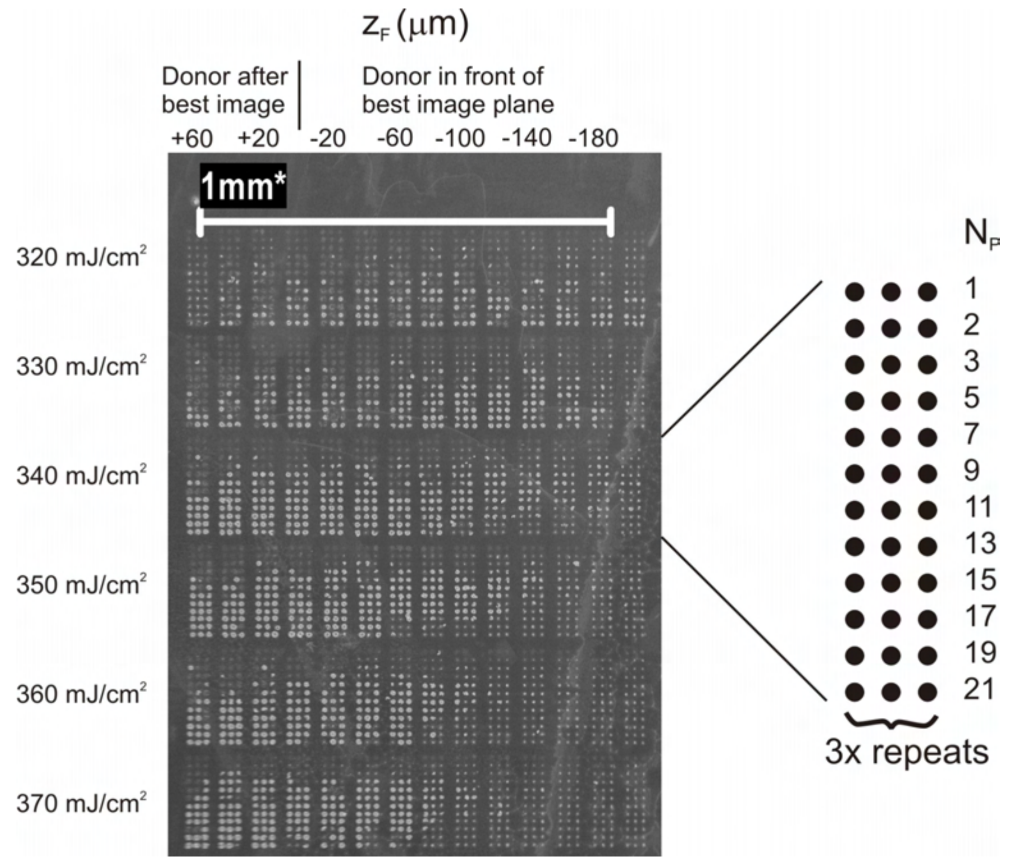

FIGURE 7.13: SEM micrograph of pellets of Cr transferred from the 160 nm donor with varying fluence, beam profile, and number of pulses.

From fig. 7.13, it can be seen that deposits could be obtained with as few as 3 pulses in some cases. However, reproducible transfer was only typically achieved for $N_p \geq 9$. The majority of the best deposits were obtained for $|z_F| \lesssim 50$ μm and fluence around $340 - 350$ mJ/cm^2. The deposit already shown in fig. 7.12(b) represents about the best that could typically be achieved from the 160 nm donor.

Lastly, fig. 7.14 shows SEM micrographs of a couple of attempted shaped-pulse BLAST transfers that failed (the image is of the donor after transfer). The way the donor preferentially sheared in the weakened region is obvious from the figures.

7.7 Conclusions

We have presented a thorough description of attempts to achieve solid transfer in a forward transfer environment without a DRL. fs-LIFT has been shown to offer some advantages in terms of solid transfer over ns-LIFT, but there was still unavoidable melting during transfer. Premachining patterns into the film to circumvent the problem of

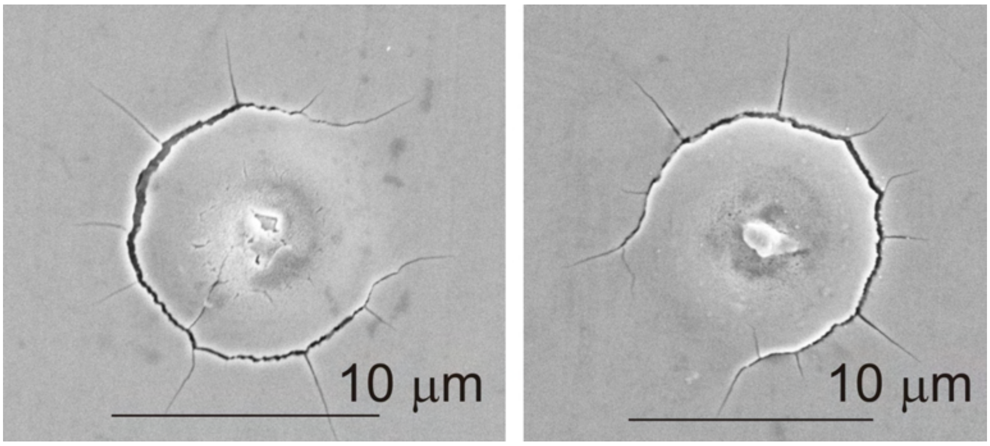

Figure 7.14: SEM micrographs the 160 nm Cr donor after failed BLAST. The shearing of the donor in the weakened region is apparent.

having to shear solid material from the remaining film was proposed as a promising technique for solid transfer, but at a cost of increasing the complexity of the process. However, it was found that limitation of the ability of heat to diffuse away from the irradiated area in fact resulted in molten transfer.

A new forward transfer technique was demonstrated that used multiple, low-energy pulses to transfer the donor. BLAST was seen to offer clear advantages in terms of solid transfer. Only a few (≈ 10) pulses were required to induce transfer, and the fluence required was slightly lower than that for conventional fs-LIFT. However, the shape of the resultant deposits was seen to vary significantly from one transferred pellet to another.

Lastly, pulses exhibiting a Fresnel diffraction profile were used to improve the reproducibility of pellet shape and to reduce the force required for lift-off, by defining a weakened region into the film prior to transfer, resulting in a further decrease in deposit damage. The results obtained indicated that the BLAST technique has potential for the forward transfer printing of a range of potentially delicate or heat-sensitive, solid donor films, in applications where existing techniques are not applicable.

Bibliography

Arnold, C., Kim, H., and Pique, A. (2004). Laser direct write of planar alkaline microbatteries. *Appl. Phys. A*, 79:417–420.

Banks, D., Grivas, C., Mills, J., Zergioti, I., and Eason, R. (2006). Nanodroplets deposited in microarrays by femtosecond ti:sapphire laser induced forward transfer. *Appl. Phys. Lett.*, 89:193107.

Banks, D., Grivas, C., Zergioti, I., and Eason, R. (2008a). Ballistic laser-assisted solid transfer (blast) from a thin film precursor. *Opt. Express*, 16:3249–3254.

Banks, D., Kaur, K., Gazia, R., Fardel, R., Nagel, M., Lippert, T., and Eason, R. (2008b). Triazene photopolymer dynamic release layer-assisted femtosecond laser-induced forward transfer with an active carrier substrate. *Europhys. Lett.*, 83:38003.

Blanchet, G., Loo, Y.-L., Rogers, J., Gao, F., and Fincher, C. (2003). Large area, high resolution, dry printing of conducting polymers for organic electronics. *Appl. Phys. Lett.*, 82(3):463–465.

Bohandy, J., Kim, B., and Adrian, F. (1986). Metal deposition from a supported metal film using an excimer laser. *J. Appl. Phys.*, 60(1):1538–1539.

Bohandy, J., Kim, B., Adrian, F., and Jette, A. (1988). Metal deposition at 532 nm using a laser transfer technique. *J. Appl. Phys.*, 63(4):1158–1162.

Doraiswamy, A., Narayan, R., Lippert, T., Urech, L., Wokaun, A., Nagel, M., Hopp, B., Dinescu, M., Modi, R., Auyeung, R., and Chrisey, D. (2006). Excimer laser forward transfer of mammalian cells using a novel triazene absorbing layer. *Appl. Surf. Sci.*, 252:4743–4747.

Fardel, R., Nagel, M., Nuesch, F., Lippert, T., and Wokaun, A. (2007). Fabrication of organic light-emitting diode pixels by laser-assisted forward transfer. *Appl. Phys. Lett.*, 91:061103.

Fitz-Gerald, J., Pique, A., Chrisey, D., Rack, P., Zeleznik, M., Auyeung, R., and Lakeou, S. (2000). Laser direct writing of phosphor screens for high-definition displays. *Appl. Phys. Lett.*, 76(11):1386–1388.

Fukumura, H., Kohji, Y., Nagasawa, K., and Masuhara, H. (1994). Laser implantation of pyrene molecules into poly(methyl methacrylate) films. *J. Am. Chem. Soc.*, 116:10304–10305.

Hopp, B., Smausz, T., Antal, Z., Kresz, N., Bor, Z., and Chrisey, D. (2004). Absorbing film assisted laser induced forward transfer of fungi (trichoderma conidia). *J. Appl. Phys.*, 96(6):3478–3481.

Kantor, Z. and Szorenyi, T. (1995). Dynamics of long-pulse laser transfer of micrometer-sized metal patterns as followed by time-resolved measurements of reflectivity and transmittance. *J. Appl. Phys.*, 78(4):2775–2781.

Kantor, Z., Toth, Z., and Szorenyi, T. (1994a). Metal pattern deposition by laser-induced forward transfer. *Appl. Surf. Sci.*, 86:196–201.

Kantor, Z., Toth, Z., Szorenyi, T., and Toth, A. (1994b). Deposition of micrometer-sized tungsten patterns by laser transfer technique. *Appl. Phys. Lett.*, 64(25):3506–3508.

Kim, H., Kushto, G., Arnold, C., Kafafi, Z., and Pique, A. (2004). Laser processing of nanocrystalline tio_2 films for dye-sensitized solar cells. *Appl. Phys. Lett.*, 85(3):464–466.

Kim, J. and Na, S. (2007). Metal thin film ablation with femtosecond pulsed laser. *Opt. Laser Technol.*, 39:14431448.

Koundourakis, G., Rockstuhl, C., Papazoglou, D., Klini, A., Zergioti, I., Vainos, N., and Fotakis, C. (2001). Laser printing of active optical microstructures. *Appl. Phys. Lett.*, 78(7):868–870.

Nakata, Y., Okada, T., and Maeda, M. (2002). Transfer of laser dye by laser-induced forward transfer. *Jpn. J. Appl. Phys.*, 41:L839–L841.

Pimenov, S., Shafeev, G., Smolin, A., Konov, V., and Vodolaga, B. (1995). Laser-induced forward transfer of ultra-fine diamond particles for selective deposition of diamond films. *Appl. Surf. Sci.*, 86:208–212.

Pique, A., Chrisey, D., Auyeung, R., Fitz-Gerald, J., Wu, H., McGill, R., Lakeou, S., Wu, P., Nguyen, V., and Duignan, M. (1999). A novel laser transfer process for direct writing of electronic and sensor materials. *Appl. Phys. A [Suppl.]*, 69:S279–S284.

Pique, A., Weir, D., Wu, P., Pratap, B., Arnold, C., Ringeisen, B., McGill, R., Auyeung, R., Kant, R., and Chrisey, D. (2002). Direct-write of sensor devices by a laser forward transfer technique. *Proc. SPIE*, 4637:361–368.

Saleh, B. and Teich, M. (1991). *Fundamentals of Photonics.* Wiley Interscience, Hoboken, New Jersey, 2 edition.

Serra, P., Colina, M., Fernandez-Pradas, J., Sevilla, L., and Morenza, J. (2004). Preparation of functional dna microarrays through laser-induced forward transfer. *Appl. Phys. A*, 85(9):1639–1641.

Thomas, B., Alloncle, A., Delaporte, P., Sentis, M., Sanaur, S., Barret, M., and Collot, P. (2007). Experimental investigations of laser-induced forward transfer process of organic thin films. *Appl. Surf. Sci.*, 254:1206–1210.

Tsuboi, Y., Furuhata, Y., and Kitamura, N. (2007). A sensor for adenosine triphosphate fabricated by laser-induced forward transfer of luciferase onto a poly(dimethylsiloxane) microchip. *Appl. Surf. Sci.*, 253:8422–8427.

Xu, X., Chen, G., and Song, K. (1999). Experimental and numerical investigation of heat transfer and phase change phenomena during excimer laser interaction with nickel. *Int. J. Heat Mass Trans.*, 42:1371–1382.

Zergioti, I., Karaiskou, A., Papazoglou, D., Fotakis, C., Kapsetaki, M., and Kafetzopoulos, D. (2005a). Femtosecond laser microprinting of biomaterials. *Appl. Phys. Lett.*, 86:163902.

Zergioti, I., Karaiskou, A., Papazoglou, D., Fotakis, C., Kapsetaki, M., and Kafetzopoulos, D. (2005b). Time resolved schlieren study of sub-pecosecond and nanosecond laser transfer of biomaterials. *Appl. Surf. Sci.*, 247:584589.

Chapter 8

Laser-Induced Solid Etching: A Novel Solid-Phase Simultaneous Etching and Deposition Technique

8.1 Introduction

This chapter describes briefly results obtained during BLAST and fs-LIFT experiments that point to a possible new solid-phase laser etching technique for solid, brittle materials. Although this technique does not fit strictly with the forward transfer results that make up the majority of this thesis, it does use an identical setup and so it makes sense for these results to be included.

The descriptions presented here are necessarily brief because neither the time nor the facilities were available for a systematic study of the process. In this chapter we present a description of how the technique, which we have termed Laser-Induced Solid Etching (LISE), is envisaged to work (section 8.2), discuss how it might bring new capabilities not available with other techniques (section 8.3), and show some initial results (section 8.4).

8.2 LISE: How it Works

The principle of LISE could be thought of as laser-induced carving, in that a short, sharp application of high pressure in a localised area initiates the propagation of a crack

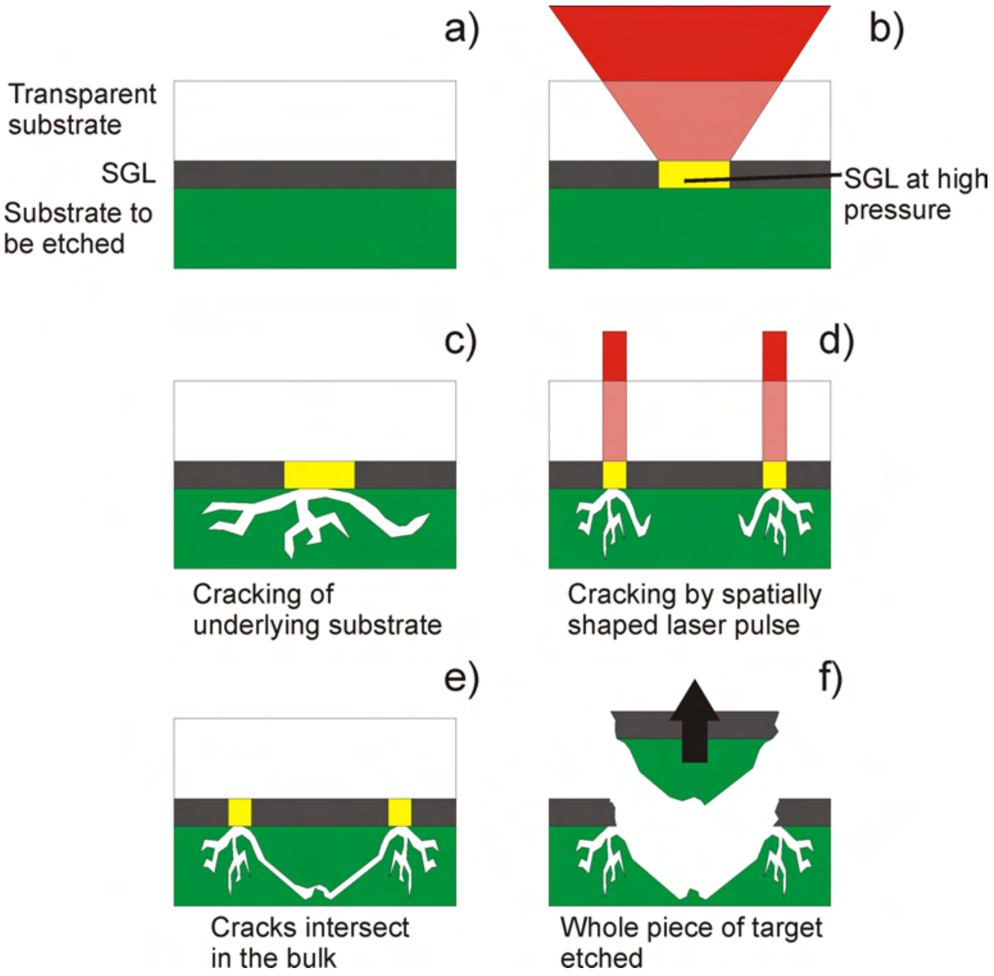

FIGURE 8.1: Illustration of the LISE technique. A thin shock generation layer is coated onto the substrate to be etched (a). Illumination of the SGL induces a sharp pressure increase (b) and can initiate crack propagation in the substrate (c). Using pulse shaping, multiple cracks can be initiated (d), which can intersect (e), allowing for solid phase etching (f).

in a brittle material. In this case, the pressure is generated by the absorption in a shock generation layer (SGL) of a femtosecond duration pulse.

Figure 8.1(a) shows a typical LISE setup. The very thin (perhaps < 100 nm) SGL is sandwiched between two bulk substrates. It should be apparent that this is identical to a forward transfer setup with donor and receiver in tight contact. The absorption of a femtosecond pulse in the SGL causes a large and rapid pressure increase, as has also been seen in ablation [Hare et al., 1995] and fs-LIFT studies [Zergioti et al., 2005], (fig. 8.1(b)). This sudden, localised pressure jump in the SGL causes cracking of the underlying substrate (fig. 8.1(c)). By spatially shaping the laser pulse (as was seen in chapter 7), it is possible to initiate multiple cracks in the substrate with a single pulse (fig. 8.1(d)). If these cracks can be made to propagate in such a way that they intersect in the substrate (fig. 8.1(e)), then a whole section can be etched away in solid phase (fig. 8.1(f)).

8.3 LISE: The Competition

There are a great many techniques for subtractively structuring solid materials (see, for example [Franssila, 2004; Madou, 2002]). Some, such as laser micromachining, are very simple single-step, DW processes that can be carried out in ambient atmosphere, but typically produce rough structures and may have difficulty processing transparent materials. Other, more complex, DW techniques, such as particle beam milling, offer improved resolution and cleaner etched features, but require high vacuum environments and expensive equipment. Also, there are many lithographic techniques capable of feature sizes as small as a few 10's of nm [Mappes et al., 2007; Robinson et al., 1999] and very smooth structured surfaces. However, these are multi-step, usually time-consuming and expensive processes involving the use of harmful substances and requiring a clean-room environment.

LISE potentially offers a new approach of etching solid materials without inducing a phase change. The technique is DW, can be performed in an ambient atmosphere, and does not require any harmful chemicals. As will be reported in this chapter, LISE has so far been shown to be capable of single, micron-scale structures or continuous writing of micron-deep features at speeds of mm/s. LISE also offers, should this be required, the simultaneous deposition of the etched material onto another nearby substrate, with the transferred material remaining in solid phase throughout. As the etching is via a cracking of the substrate rather than boiling or ablation, the etched features are typically very smooth compared to other laser-DW techniques, especially when cracking can be initiated along cleavage planes (as will be seen in Si later). Finally, because no phase change is involved (except possibly of the SGL), the risk of redeposition of etched material around the etched feature, as is often seen using laser-machining, is minimised. Possible applications of LISE include the etching of smooth pits and channels for microfluidics, as an alternative to DRL-LIFT for the solid and intact LIFT of hard donors with the SGL replacing the DRL to crack an overlying, solid-phase donor, or for the DW of strip-loaded waveguides [Grivas et al., 2004].

One obvious application for LISE is the etching of transparent materials. A widely applied technique for this is Laser-Induced Backside Wet Etching (LIBWE) [Wang et al., 2000]. This technique has been observed to yield very smooth etched features, and a recent demonstration based on immersion interferometry produced 100 nm period arrays [Vass et al., 2007]. However, LIBWE does have disadvantages too; it is very complicated procedure requiring a well insulated liquid chamber, and the liquid absorber is often harmful. To combat these problems, a variant technique was developed, Laser-Induced Backside Dry Etching (LIBDE). LIBDE relies on explosive boiling of a thin solid film to etch the transparent material. Although the process has so far allowed for the writing of sub-micron structures, these features were quite rough [Hopp et al., 2006]. Also, neither of these etching processes allow for simultaneous deposition of the etched material.

8.4 LISE: Initial Results

The following results were obtained during studies of the BLAST technique, hence the experimental setup was identical to that described in section 7. The 80 nm thick Cr donor was the equivalent of the SGL described previously. The pulse shaping was accomplished using slight mis-imaging of the aperture, as described before, resulting in a slightly higher intensity at the edge of the laser spot (exactly how much higher is hard to quantify, but crude estimates suggest around 5%). Multiple pulses were incident at 1 kHz or 250 Hz, with the actual number controlled by shuttering of the laser beam, as before. Donor/SGL and receiver were kept in tight contact throughout.

According to the description in section 8.2, the Si receiver should have been the substrate to be etched, but we found that etching of both the Si and the silica carrier were possible. It was not obvious what determined which substrate was etched, and so far we have not been able to identify a single critical parameter and it is probable that a number of parameters, including laser fluence, beam profile, number of pulses, and donor/SGL-receiver separation, influenced the outcome.

8.4.1 LISE of Holes and Pits

Figure 8.2 shows a series of structures produced on a Si receiver after LISE with fluence around 380 mJ/cm^2 with increasing number of pulses, N_p, from 1-10000. The structures were observed from an angle of about 50° to the surface normal. A number of different processes can be seen to have occurred.

- With a small number of pulses ($N_p \lesssim 20$), there was evidence of surface damage to the Si, most likely due to the repeated heating of the donor/SGL and associated high pressures. The donor material was sometimes seen on the receiver ($N_p = 3, 4, 20$) or could remain on the carrier ($N_p = 1, 2, 5, 10$, not shown).
- When more pulses were applied ($20 \lesssim N_p \lesssim 1000$), the result was usually either a clean pit in the Si or in the silica (seen here as a deposited silica dome on the

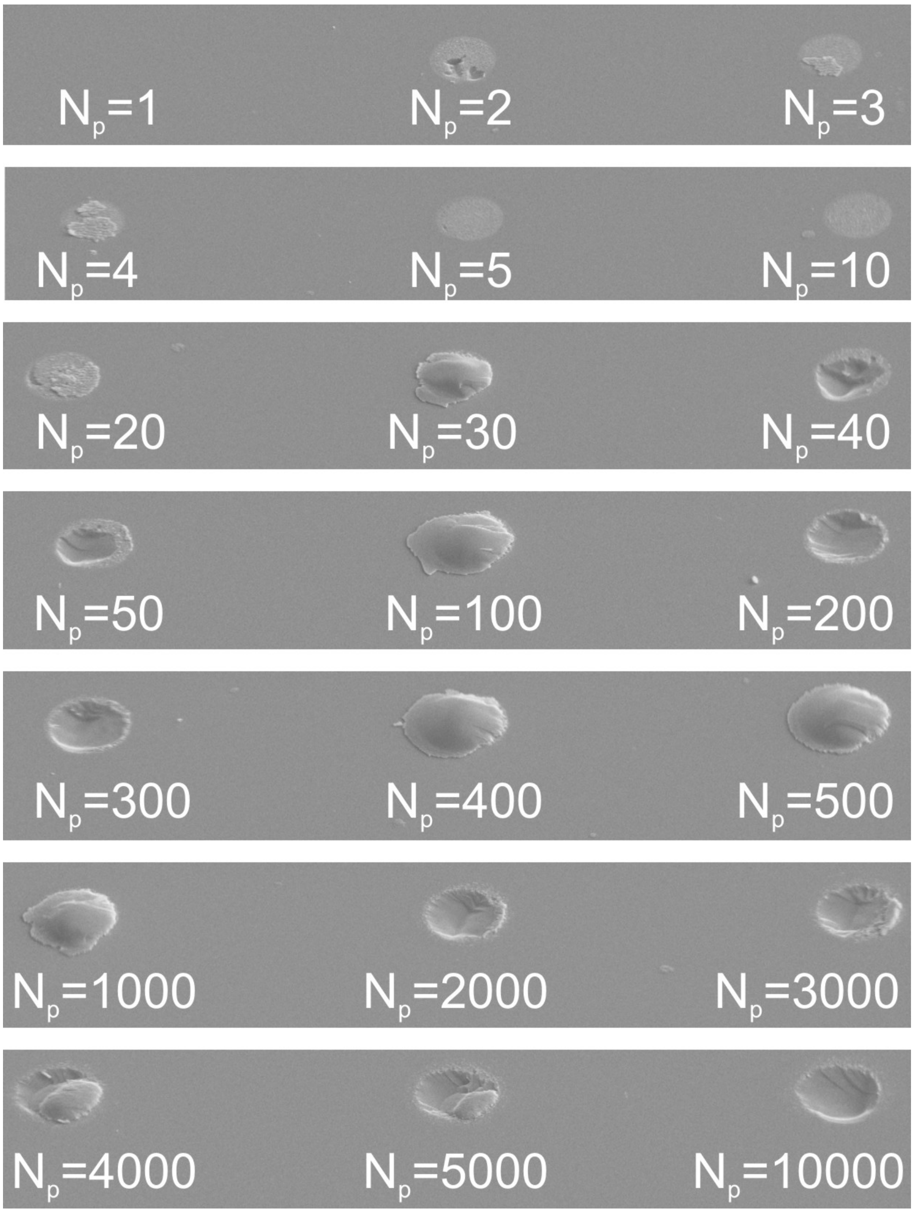

FIGURE 8.2: SEM micrographs of the Si receiver following LISE with fluence around 380 mJ/cm^2 with varying number of pulses, N_p.

receiver). Repeated scans did not reveal any systematic behaviour governing which material was etched; it appeared to be random. An interesting observation was that the holes in the silica appeared to be slightly larger in diameter than those in the Si. In both materials the holes were on the order of a few microns deep.

- If the number of pulses was increased further, we began to see damage to both the Si and the silica substrates ($N_p = 4000, 5000$).

Similar dependence on number of pulses was observed over repeated experiments. Figure 8.3 shows the variation of LISE structures with number of pulses, and with position of

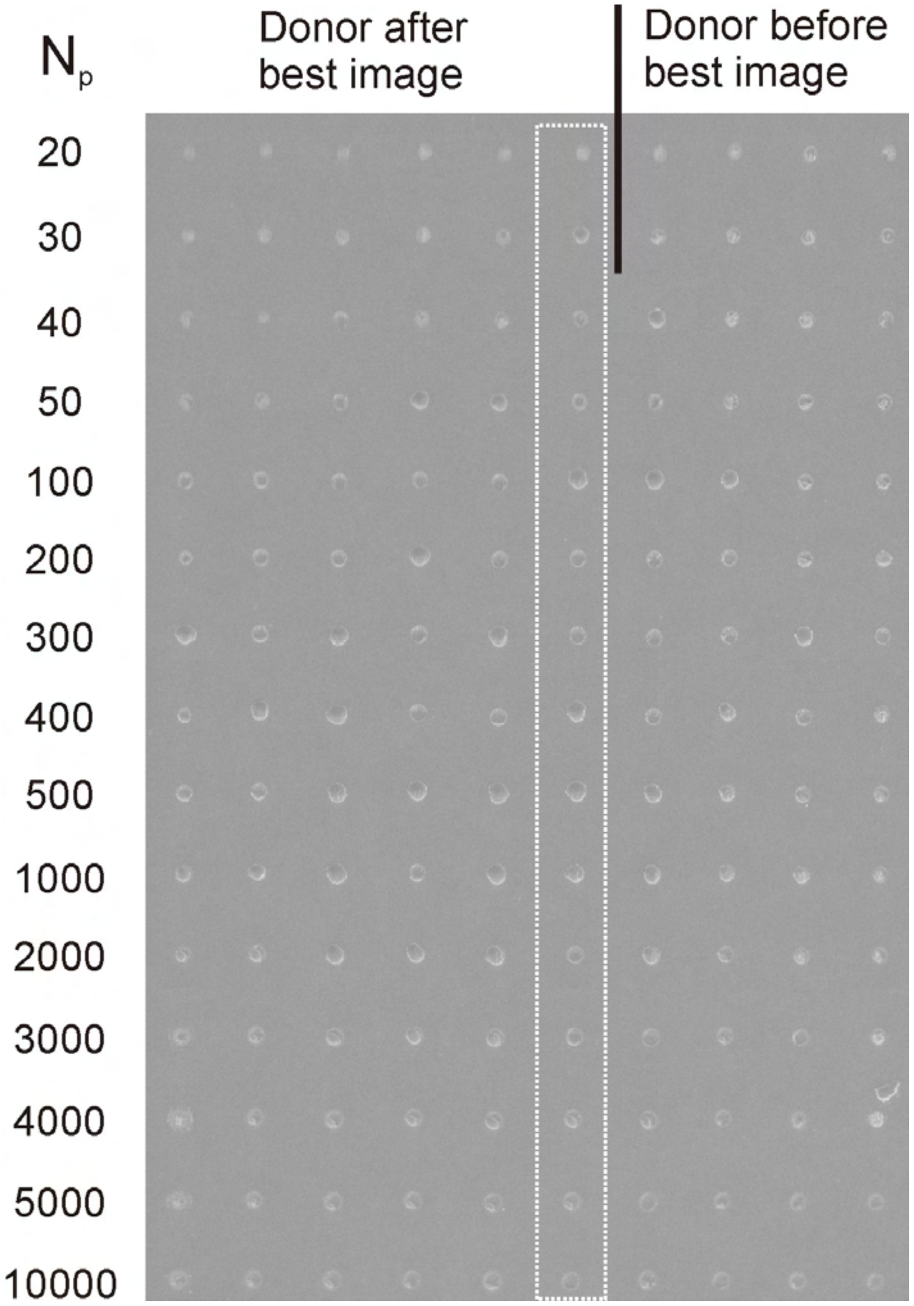

FIGURE 8.3: SEM micrograph of an array of LISE exposures at fluence around 380 mJ/cm^2. The number of pulses for each spot is indicated on the left and the deposits shown in fig. 8.2 are marked by the white box. Also indicated is the position of the donor/SGL-carrier interface relative to the best image plane of the laser. Spot separation: 60μm.

the donor/SGL-carrier interface relative to the best image plane of the laser (i.e. varying beam profile as described in chapter 7). It was observed that good quality etching of either Si or silica was only readily observed when the donor/SGL-carrier interface was placed just offset from the best image plane (within 50-100 μm). Recall that this was the same finding as with the BLAST deposits (section 7.5). Why this was the case is

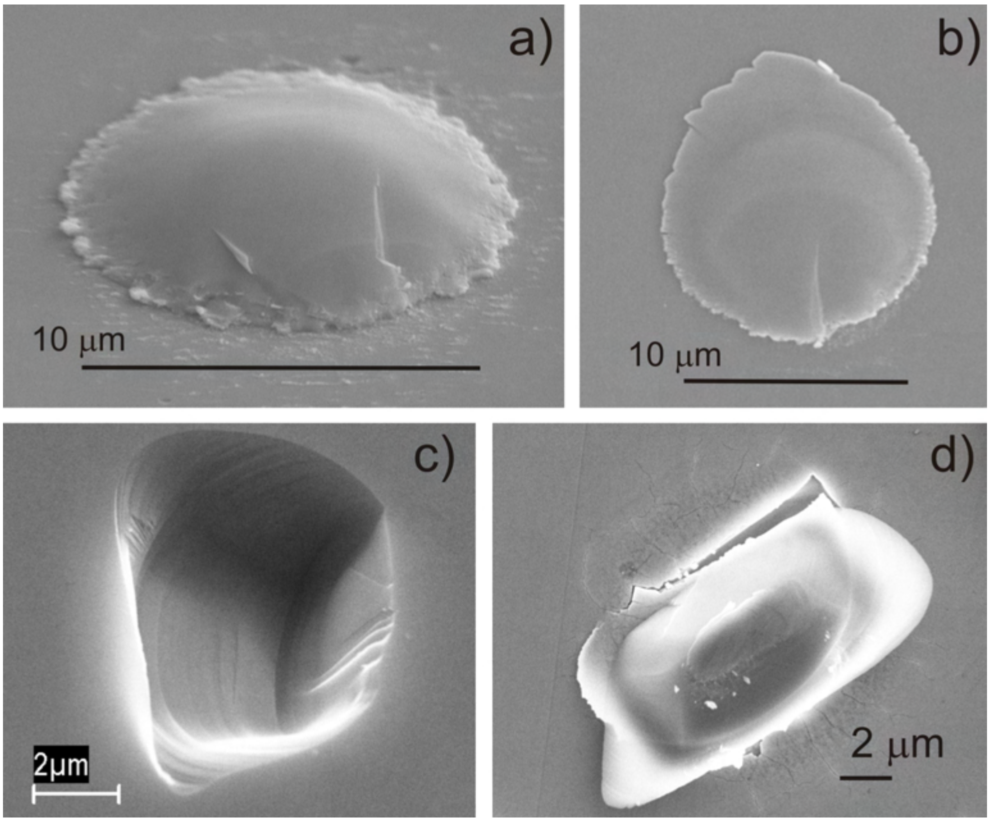

Figure 8.4: SEM micrographs of angled (a) and top down (b) views of silica etched from the carrier and deposited onto the Si. Also shown is a view of the Si receiver after LISE with the etched Si pieces scattered around the experimental area (c).

not known, but the most likely explanation would seem to be related to the beam profile as this is the only parameter that should vary significantly over this range.

It would be tempting to conclude from the presented results that the etching process was the result of a gradual shattering of the substrates under exposure of the SGL to many pulses, and not the removal of a single, solid-phase piece as discussed at the beginning of this chapter (i.e. just LIBDE). However, closer inspection of the etched material suggests that this explanation is not correct. Figure 8.4 shows angled (a) and top down (b) close-up views of a piece of etched silica deposited onto the Si receiver. Also shown is the result of another LISE experiment where the Si receiver was etched; fig. 8.4(c) shows an etched pit in the Si receiver and fig. 8.4(d) shows the etched Si on the carrier (it is believed that the donor melting and resolidifying in tight contact stuck the etched Si to the carrier). The pit was not round as in the silica most likely because the Si wafer had well-defined planes which could be cleaved; the silica was obviously amorphous so exhibited no preferential cleaving direction, hence the circular pits and deposits.

Looking at the material deposited after etching in fig. 8.4 confirms the etching of whole solid pieces of the substrates. The silica deposits in (a) and (b) display clear cracks

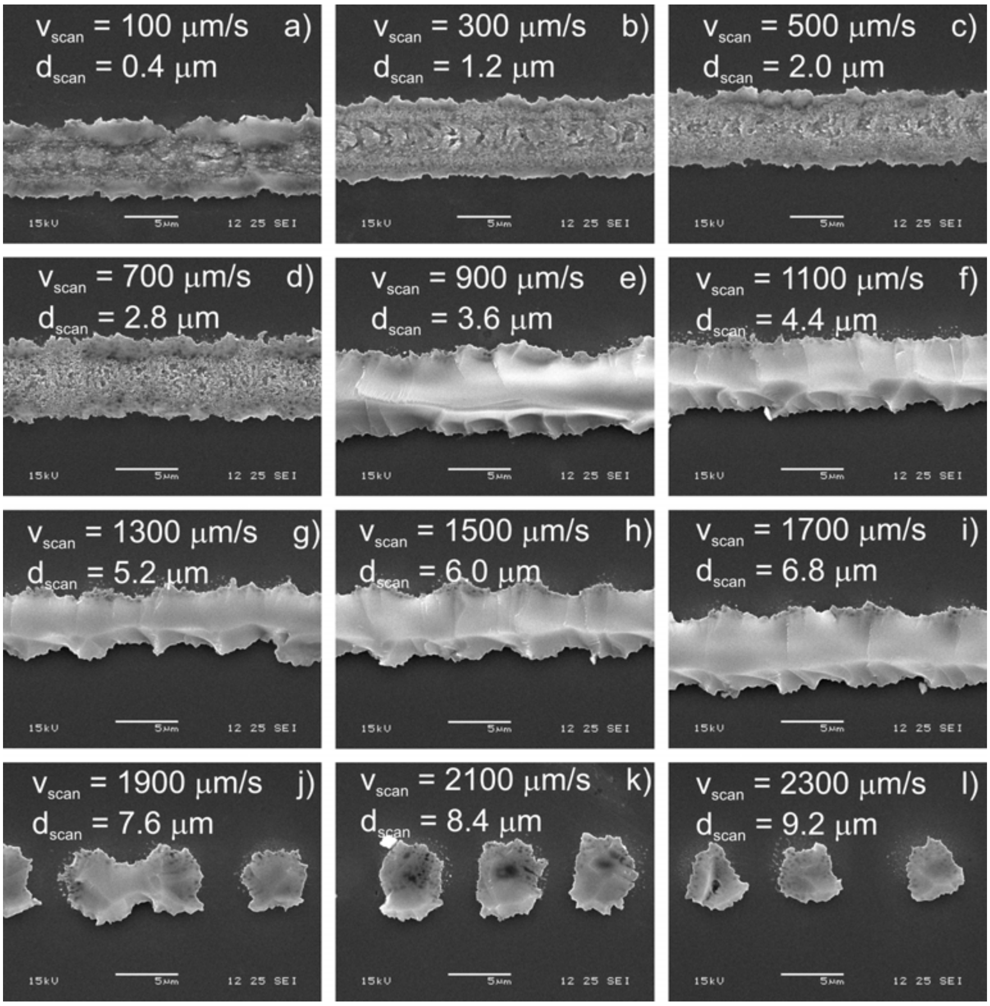

FIGURE 8.5: SEM micrographs of lines of silica deposited onto Si after etching from the carrier with fluence 700 mJ/cm^2. Laser scanning speed and associated separation between successive exposures are shown.

and sharp edges that could only be the result of a solid-phase process. Similarly, the Si etched material in (c) and (d) had obviously remained contiguous during etching, giving rise to the very angular shapes of the pieces and the identical shapes of pit and deposit.

8.4.2 LISE of Continuous Line Structures

As a further test of the LISE technique, continuous line structures were produced by raster scanning the laser across the target at speeds from 100-2300 μm/s (the fastest available) with the laser repetition rate set to 250 Hz. The laser fluence was varied from $\approx 300 - 1100$ mJ/cm^2. Figure 8.5 shows SEM micrographs of all the lines produced with 700 mJ/cm^2. In each image, the scan speed, v_{scan} and the corresponding distance separating successive exposures, d_{scan} is indicated; bear in mind that the laser spot size was around 8 μm. The images are of the silica lines deposited onto the Si receiver after

LISE, but of course these also corresponded to trenches in the carrier. 3 distinct regimes could be observed:

- Low scan speeds (100-700μm/s (a)-(d)) - With significant overlap between successive pulses, clean etching was not observed. Instead the Cr donor/SGL was transferred to and deposited onto the receiver in continuous lines. The well-defined edges of these lines suggested some solid-phase transfer so the process in this regime was more akin to BLAST than LISE.
- Moderate scan speeds (900-1700μm/s (e)-(i)) - As the separation between successive pulses reached approximately the spot radius (i.e. each area of the target experienced at most 2 laser pulses), etching of the silica carrier was observed. Clean, continuous lines of silica were forward transferred to the receiver. An interesting point to note here is that etching was being seen with only a couple of pulses, far fewer than were required to etch the pits in the previous section. We conclude, therefore that cracking of the silica was initiated at the start of the scanned lines, where the translation stages were still accelerating and so the pulse overlap was much greater. Subsequently, each successive pulse served to propagate the cracks along the scanning direction. However, this model doesn't appear to explain the lack of etching seen at low scan speeds (more overlap). The etching threshold at around 900 μm/s was seen repeatedly with varying fluence, suggesting that it was the amount of overlap that was the key parameter.
- High scan speeds (1900+μm/s (j)-(l)) - When the scan speed was increased such that d_{scan} was approximately equal to or greater than the spot size, there was little or no overlap between successive pulses. As a result, continuous lines were no longer obtained, instead a series of pits were etched into the silica. Note that we were getting etching with only a single pulse, so there must have been some cumulative effect from the multiple exposures contributing to the etching.

The continuous line formation was observed to occur over a wide range of fluence. Figure 8.6 shows silica lines on Si following LISE with fluence varying from $\approx$ 300 mJ/cm^2 - $\approx$ 1 J/cm^2. For all the lines $v_{scan} = 1100$ μm/s. A clear fluence threshold for the onset of LISE could be seen around 600 mJ/cm^2. Clearly there was both a fluence threshold and a scan speed threshold for silica etching with LISE.

So far the results shown have only been of small segments of lines. This has just been to show the detail and was not to disguise that these sections were lucky results. The experiments involved writing lines 2 mm long and the etched lines were typically continuous and uniform along the entire writing length (fig. 8.7 shows an SEM micrograph

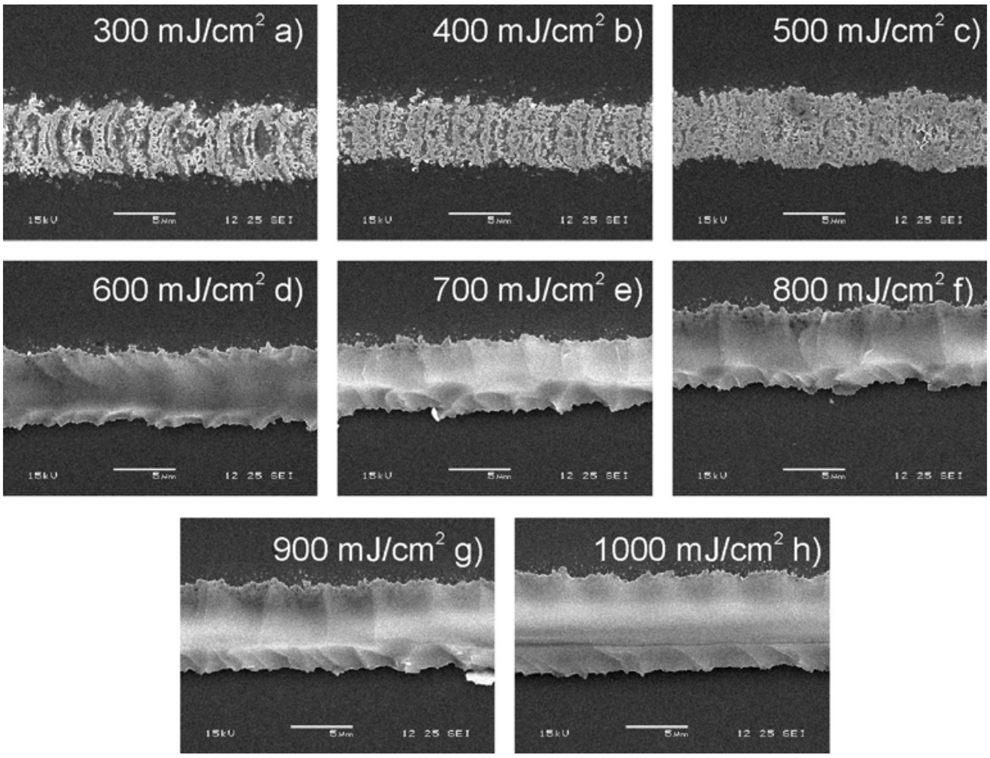

FIGURE 8.6: SEM micrographs of LISE-deposited silica lines on Si with varying applied laser fluence with $v_{scan} = 1100$ μm/s.

of lines 100's of μm in length produced with fluence 1 J/cm^2 and v_{scan} = 900 (left), 1100, 1300, 1500, and 1700 (right) μm/s). Hence the technique appears to be capable of direct-writing macroscopic length, microscopic cross-section lines and trenches.

Lastly, the height of the lines was measured using stylus profiling. Figure 8.8 shows cross-sectional stylus scans over lines produced with fluence of 700 mJ/cm^2 (a) and 1 J/cm^2 (b). Again, the results for the lower fluence can be divided into 3 categories which approximately coincide with those identified previously:

- Low scan speeds (100-500μm/s) - The deposited lines of Cr were typically around 600-800 nm in height. These values were significantly thicker than the donor film and were consistent with material transferred partially in solid-phase protruding slightly from the surface.
- Moderate scan speeds (700-1500μm/s) - The etched features were between 1.5-2 μm in height. There was a suggestion of a weak dependence on scan speed with higher structures being produced at quicker speeds, but this trend was not seen for lines deposited at other fluences, so was probably just coincidence.
- High scan speeds (1700+μm/s) - The deposited structure height was very small, on the order of 200 nm. This may have been due to the fact that, because d_{scan}

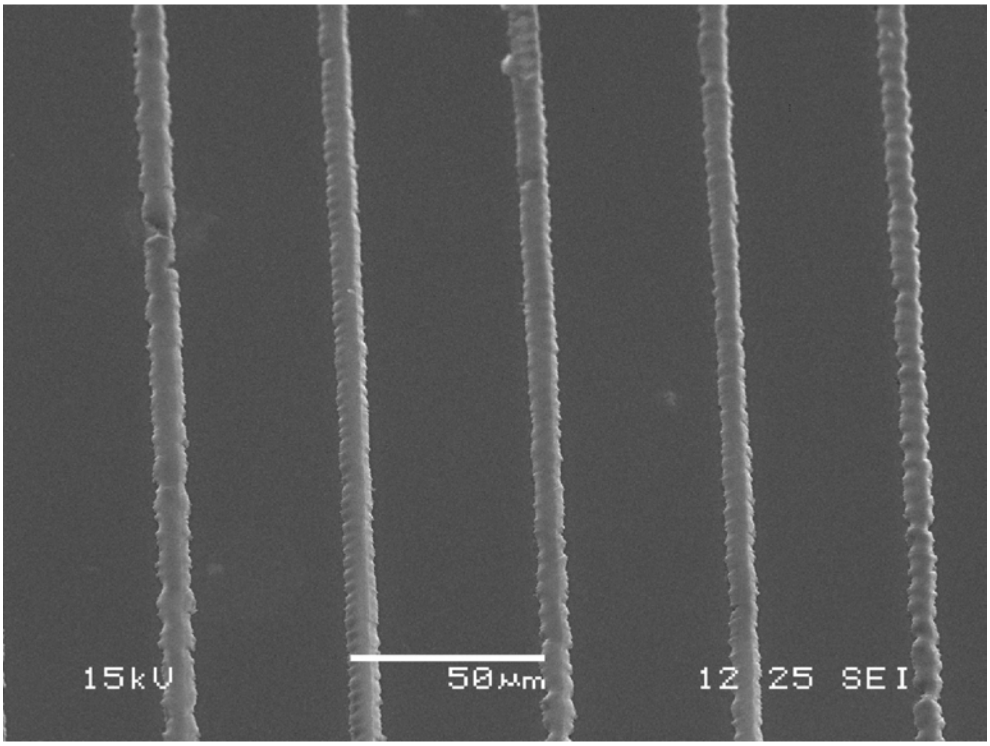

FIGURE 8.7: SEM micrograph of macroscopically long, LISE-deposited silica lines on Si with laser fluence 1 J/cm^2 and v_{scan} = 900 (left), 1100, 1300, 1500, and 1700 (right) μm/s. Image taken at 45° to surface normal.

was large, the cumulative effect of multiple pulses incident close to each other was reduced, allowing only shallow features to be etched.

For the higher fluence (fig. 8.8(b)) the thickness was much more uniform, but much smaller (around 200 nm for most scan speeds). The reason for the thickness dependence on fluence is not yet known.

8.5 Conclusions

We have presented initial observations of what appears to be a novel, solid phase etching technique. Spatially shaped femtosecond duration laser pulses were used to generate high pressures in a shock layer sandwiched between two bulk substrates. The localised and constrained high pressure could initiate crack propagation in one or both substrates. By careful control of the laser spatial profile, the cracking process could be tailored to etch pits and trenches into the substrates. The technique is unique in microfabrication in that the etched material is removed as a single, solid piece and can, if desired, be deposited onto another substrate.

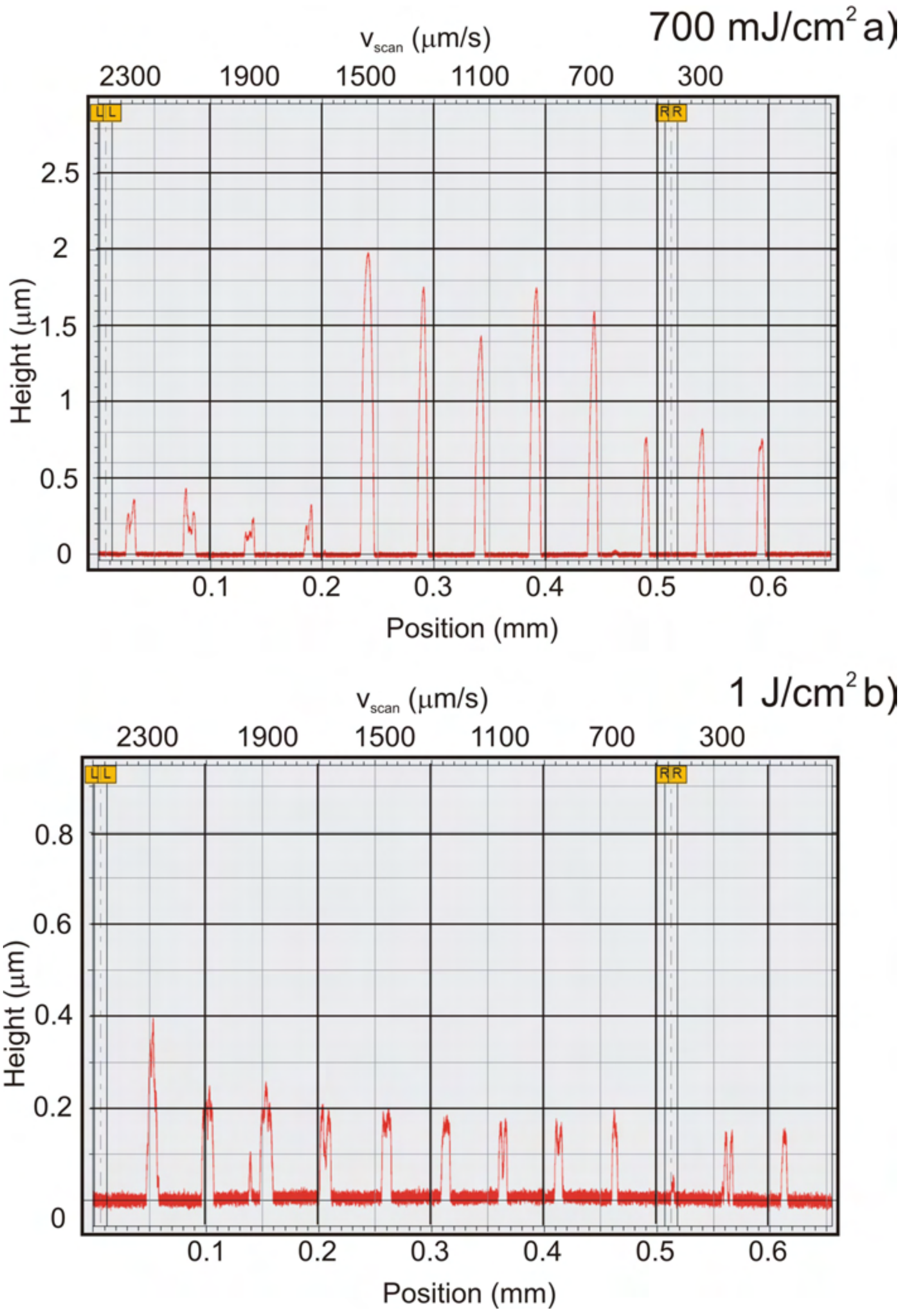

FIGURE 8.8: Stylus profiling of LISE-deposited lines produced with fluence of 700 mJ/cm^2.

Using simple beam shaping (Fresnel diffraction), we were able to etch micron-scale pits in silica and Si, and macroscopic trenches in silica with the shocks generated in a thin Cr film. The process appeared to be highly reproducible with trenches mm's in length produced with a range of fluences and laser scanning speeds, up to mm/s.

A detailed understanding of the process is still lacking due to time and facility constraints. For example, arbitrary control of the laser spatial profile was not available, which can be expected to be key for optimising the process. Also, the results presented here represent only a brief parameter scan. There are many parameters, including fluence, beam profile, number of pulses, laser scan speed, substrate materials, shock layer material and thickness, and any separation between shock layer and the substrates that must be investigated before the LISE technique will be more fully understood. Nonetheless, we have been able to demonstrate that it is a viable etching technique.

Bibliography

Franssila, S. (2004). *Introduction to Microfabrication.* Wiley, Hoboken, NJ, USA.

Grivas, C., May-Smith, T., Shepherd, D., Eason, R., Pollnau, M., and Jelinek, M. (2004). Broadband single-transverse-mode fluorescence sources based on ribs fabricated in pulsed laser deposited ti:sapphire waveguides. *Appl. Phys. A*, 79:1195–1198.

Hare, D., Franken, J., and Dlott, D. (1995). Coherent raman measurements of polymer thin-film pressure and temperature during picosecond laser ablation. *J. Appl. Phys.*, 77(11):5950–5960.

Hopp, B., Vass, C., Smausz, T., and Bor, Z. (2006). Production of submicrometre fused silica gratings using laser-induced backside dry etching technique. *J. Phys. D: Appl. Phys.*, 39:48434847.

Madou, M. (2002). *Fundamentals of microfabrication: the science of miniaturization.* CRC Press, Boca Raton, FL, USA.

Mappes, T., Achenbach, S., and Mohr, J. (2007). X-ray lithography for devices with high aspect ratio polymer submicron structures. *Microelectron. Eng.*, 84:12351239.

Robinson, A., Palmer, R., Tada, T., Kanayama, T., amd J.A. Preece, M. A., and Harris, K. (1999). 10 nm scale electron beam lithography using a triphenylene derivative as a negative/positive tone resist. *J. Phys. D: Appl. Phys.*, 32(16):L75–L78.

Vass, C., Osvay, K., Hopp, B., and Bor, Z. (2007). 104 nm period grating fabrication in fused silica by immersion two-beam interferometric laser induced backside wet etching technique. *Appl. Phys. A*, 87:611613.

Wang, J., Niino, H., and Yabe, A. (2000). Micromachining of transparent materials with super-heated liquid generated by multiphotonic absorption of organic molecule. *Appl. Surf. Sci.*, 87:45–53.

Zergioti, I., Karaiskou, A., Papazoglou, D., Fotakis, C., Kapsetaki, M., and Kafetzopoulos, D. (2005). Time resolved schlieren study of sub-pecosecond and nanosecond laser transfer of biomaterials. *Appl. Surf. Sci.*, 247:584589.

Chapter 9

Conclusions and Future Work

9.1 Introduction

In this chapter, conclusions from the previous chapters are drawn together and discussions are made of future work that could (should?) proceed from this work.

9.2 Conclusions

We began, in chapter 3, by considering some of the potential benefits of using femtosecond pulses for LIFT. In principle, fs-LIFT should offer advantages in terms of depositing smaller structures, and transferring intact and solid material due to the reduced heat affected volumes. However, due to the necessary presence of the overlying carrier substrate, it was considered that non-thermal ablation, so often characteristic of femtosecond laser-materials interactions, was not available for fs-LIFT. There was some evidence in the literature that fs-LIFT may be a shock-driven, rather than thermolytic, process. If this were true, it would offer further advantages in terms of using fs-LIFT for solid and intact transfer over ns-LIFT. However, so far only circumstantial evidence of this exists and none of our results add support to this model.

9.2.1 Nanodroplets

Chapter 4 presented results of nanoscale droplets of Cr transferred from a 30 nm donor. The smallest reproducible features were found to be $\approx$ 300 nm which, at the time of writing, are the smallest LIFT-fabricated structures. The transfer process is believed to be purely thermal, with droplet formation and transfer occurring when the donor film was just melted through. Previously the smallest features with both fs-LIFT and ns-LIFT were around 0.5 μm [Narazaki et al., 2008; Papakonstantinou et al., 1999] and it was not immediately apparent whether the improved resolution achieved here was a result of using fs-duration pulses or simply the choice of other experimental parameters.

The effect of laser fluence on nanodroplet diameter and morphology was studied in detail. The transfer threshold fluence was found to be around 330 mJ/cm^2. We observed greater flattening (and, hence, larger diameters) of the deposited droplets with increasing fluence due to larger impact momentum on the receiver. At around 400 mJ/cm^2, we began to see the transfer of multiple droplets per laser shot. This was attributed to the onset of phase explosion in the donor film, a hypothesis that was supported by investigating the number of droplets transferred as a function of fluence over 400 mJ/cm^2.

It would be reasonable to expect that reducing the laser spot size and using Gaussian spatial profiles (such that only the centre of the laser spot was sufficiently intense to induce transfer) might lead to reduced droplet sizes. However, there is some evidence in the literature to suggest that there may be a fundamental limit to the size of droplets grown in this way due to surface tension effects [Seifert and Betz, 1998]. The droplet sizes reported here are on the order of the fundamental limits suggested by Seifert et al. so it is possible that significantly smaller sizes may not be achievable.

One application where reducing the laser spot size would definitely have a beneficial effect would be in the high-speed writing of microarrays. Our results suggested that the nearest two droplets could be transferred from the donor film was around the laser spot radius. This result was perhaps unsurprising as the donor film would be damaged by the first droplet transfer, thus negatively influencing any subsequent transfers from that area. Of course, it would always be possible to move the donor film between each droplet transfer to produce arbitrarily small period arrays on the receiver, but this would introduce a great deal of extra complexity to the technique and significantly increase processing times.

9.2.2 Solid and Intact Transfer

A number of approaches to solid and intact transfer have been considered here. In chapters 5 and 6 the DRL-LIFT technique using a triazene polymer DRL for the forward transfer of a gadolinium gallium oxide. This was the first time fs-duration pulses had been used for TP-DRL-LIFT. The transfer threshold fluence of the GdGaO was measured to be $\approx$ 90 mJ/cm^2, well below the measured ablation threshold of the DRL but only slightly below the donor ablation threshold. Our observations suggested that it was absorption in the donor and back-heating of the TP-DRL that was the reason for the very low transfer threshold. Nonetheless, it was observed that this process allowed for the deposition of oxide material in single, solid phase pellets, with no evidence of residual TP-DRL. Thus far, we have not been able to ascertain if the transferred material was intact.

Other DRL materials were also studied. Thin films of photoresist and Al were used and compared to the TP for DRL applications. Despite being the only material to linearly absorb the laser radiation, the Al-DRL produced the poorest results. Although transferred material was solid, it displayed significant surface damage, lack of reproducible deposit shape, and a lot of DRL material was still present after transfer. The photoresist was more promising. Good quality, round deposits were produced, and again the transfer threshold was well below the DRL ablation threshold. There was evidence of significant amounts of residual DRL; however, this problem can be expected to be reduced by using thinner photoresist-DRL's. The results suggested that polymers appear to be better suited for DRL applications than metals.

With the TP-DRL we observed a periodic dependence of transferred donor damage on the donor-receiver separation. This was attributed to back reflections of the laser off the Si receiver causing localised high intensities in the donor layer at certain separations. A simple numerical model of the standing wave intensity profile in the DRL-LIFT setup was developed and the predicted points of high intensity were found to agree extremely well with the observed donor damage in the experiments. These results have implications for the LIFT of any transparent material.

For a number of reasons it would be desirable to achieve solid and intact transfer without a DRL. As such we investigated a number of techniques to achieve this. Neither femtosecond LIFT nor premachining of the donor were found to be particularly promising and so we focused on a new technique known as Ballistic Laser-Assisted Solid Transfer (BLAST). BLAST utilises multiple, low energy pulses to gently transfer material without significant melting or shattering.

We found that BLAST with around 10 pulses using fluence ≈ 310 mJ/cm^2 produced solid transfer from an 80 nm thick Cr donor. However, the deposits still displayed evidence of significant damage as a result of the transfer process. A simple refinement of BLAST using pulses with a Fresnel diffraction profile allowed for the reproducible deposition of sub-10 μm scale solid phase material; again, typically around 10 laser pulses were necessary to induce transfer. We have so far not been able to demonstrate solid and intact transfer with BLAST.

9.2.3 Solid Phase Etching

During BLAST experiments, a new etching technique was discovered that uniquely allows for the simultaneous etching and deposition of material in solid phase. This technique, which we have called Laser-Induced Solid Etching (LISE), relies on controlled cracking of a brittle substrate to initiate transfer. Cracking of Si and silica substrates was achieved using absorption in a thin Cr film to generate high pressure shock waves.

As the geometry for LISE was identical to a LIFT setup, there was by definition another substrate nearby that the etched material could be deposited onto. In this way we were able to simultaneously etch trenches and deposit ridges of silica, or etch holes and deposit pellets. The process is not yet well understood but dependences on number of incident pulses, laser beam profile, and fluence have all been observed.

Typically the structures produced by LISE were on the order of a couple of microns deep, but this is predicted to vary with applied beam size. A threshold fluence for etching was observed around 600-700 mJ/cm^2 in the current geometry. The technique was highly reproducible, with repeatable pit shapes and lines on the order of mm long being produced.

9.3 Future Work

The results presented here leave many avenues of study still open to further investigation. For the nanodroplets, it may still be possible to produce smaller droplets and smaller period microarrays through optimisation of the laser spot size. Other donor materials may yield smaller structures due to differing material properties in the liquid phase. It would also be desirable to be able to achieve sub-micron period microarrays as these would be more useful for plasmonic applications. Also, the use of UV wavelengths, and hence tighter focusing, may offer a route to smaller nanodroplets and smaller period microarrays.

From a DRL point of view, the photoresist DRL requires further investigation. Although the TP-DRL produced the best results here, the photoresist is a much more readily available material and the initial results were quite promising. The next step will be to try DRL-LIFT with thinner photoresist DRLs. It will also be necessary to ascertain to what degree transferred material is still intact after LIFTing with all the DRL materials, particularly the polymers. The TP was designed for use at 308 nm and so displays strong absorption in the UV. Hence, future experiments should focus on TP DRL-fs-LIFT at UV wavelengths for comparison with the $\lambda = 800$ nm (where linear absorption is extremely weak) results here. Also, donor materials with more obvious applications should be tested. The GdGaO is fine as a sample 'hard' material, but it lacks any obvious applications, although we will be investigating post-transfer crystallisation of the GdGaO pellets as a route for micro-depositing crystalline material. Other, more functional materials, such as piezoelectrics, will be used as donors in the future.

The photoresist may also prove a useful material for further investigation of the active carriers seen during the DRL experiments. Exposed and unexposed photoresist display markedly different absorption coefficients at $\lambda = 400$ nm, where the active carrier emission was strongest. Hence, it would be interesting to compare DRL-LIFT with the two photoresist states to get a better idea of the impact of the active carrier on the LIFT process. In the future it may be possible to design custom active carriers to optimise the LIFT process. For example, one could imagine a process where the laser wavelength was optimised to induce transfer, whilst the AC also generated a secondary wavelength to perform some other function, such as annealing or initiation of photo-chemical reactions.

The early BLAST results were very promising, but we believe that the current results are about the best that can be expected with the available setup. To improve on these results, shot-to-shot beam shaping capabilities will be required to offer precision control over the weakening and transfer processes. In this way it may be possible to significantly reduce the damage seen to have occurred to the centre of the transferred material, even at the optimal printing conditions. Once the quality of transfer has been improved the next step, as with the DRL experiments, will be to achieve intact transfer. Only then can the technique be applied to the deposition of more interesting materials than Cr.

The initial results of the LISE technique were also very promising. Again, this technique would benefit from the ability to arbitrarily control the laser pulse profile shot-to-shot. However, in the meantime, the line structures produced appear well-suited to the DW of strip-loaded waveguides [Grivas et al., 2004]. The next steps with LISE will involve attempting the deposition of materials that would be suitable for this goal, e.g. Ti:sapphire. Then, hopefully, we may be able to demonstrate waveguiding.

Femtosecond time-resolved microscopy [Sokolowski-Tinten et al., 1998a,b] has been shown to be a powerful technique for studying the ablation behaviour of a number of materials under femtosecond irradiation. In the near future, and funding permitting, we hope to use this technique to study nanodroplet formation and transfer, DRL-LIFT, and BLAST.

The author is also involved in a side project in collaboration with researchers at the Department of Automatic Control and Systems Engineering (ACSE) at the University of Sheffield, UK. The project is aimed at using control theory to optimise the laser-induced heating of targets and control phase-change fronts in those targets. This work has produced 2 conference publications to date (see Appendix A). Further work is also dedicated to the design of a cellular automata-based model for the nanodroplet growth and transfer process. This project is now producing results that will soon be written up for a journal submission.

Bibliography

Grivas, C., May-Smith, T., Shepherd, D., Eason, R., Pollnau, M., and Jelinek, M. (2004). Broadband single-transverse-mode fluorescence sources based on ribs fabricated in pulsed laser deposited ti:sapphire waveguides. *Appl. Phys. A*, 79:1195–1198.

Narazaki, A., Sato, T., Kurosaki, R., Kawaguchi, Y., and Niino, H. (2008). Nano- and microdot array formation of fesi$_2$ by nanosecond excimer laser-induced forward transfer. *Appl. Phys. Exp.*, 1:057001.

Papakonstantinou, P., Vainos, N., and Fotakis, C. (1999). Microfabrication by uv femtosecond laser ablation of pt, cr and indium oxide thin films. *Appl. Surf. Sci.*, 151:159–170.

Seifert, N. and Betz, G. (1998). Computer simulations of laser-induced ejection of droplets. *Appl. Surf. Sci.*, 133:189194.

Sokolowski-Tinten, K., Bialkowski, J., Boing, M., Cavalleri, A., and von der Linde, D. (1998a). Thermal and nonthermal melting of gallium arsenide after femtosecond laser excitation. *Phys. Rev. B*, 58(18):805–808.

Sokolowski-Tinten, K., Bialkowski, J., Cavalleri, A., von der Linde, D., Oparin, A., ter Vehn, J. M., and Anisimov, S. I. (1998b). Transient states of matter during short pulse laser ablation. *Phys. Rev. Lett.*, 81(1):224–227.

Appendix A

Publications

A.1 Journal Papers

D.P. Banks, K. Kaur, R. Gazia, R. Fardel, M. Nagel, T. Lippert, and R.W. Eason, "Triazene photopolymer dynamic release layer-assisted femtosecond laser-induced forward transfer with an active carrier substrate," *Europhys. Lett.* **83**, 38003 (2008).

D.P. Banks, C. Grivas, I. Zergioti, and R.W. Eason, "Ballistic laser-assisted solid transfer (BLAST) from a thin film precursor," *Opt. Express* **16**, 3249-3254 (2008). *A summary of this paper appeared in Laser Focus World, May 2008*

D.P. Banks, C. Grivas, J.D. Mills, I. Zergioti, and R.W. Eason, "Nanodroplets deposited in microarrays by femtosecond Ti:sapphire laser induced forward transfer," *Appl. Phys. Lett.* **89**, 193107 (2006). *This paper was reproduced in the December 2006 issue of the Virtual Journal of Ultrafast Science*

A.1.1 In preparation

D.P. Banks and R.W. Eason, "The Effect of Standing Waves on Laser Induced Forward Transfer of Transparent Thin Films" *(working title)*

D.P. Banks and R.W. Eason, "Simultaneous Micro-Etching and Deposition of Brittle Materials by a Novel Femtosecond Laser-Induced Cracking Technique" *(working title)*

X. Xu, **D.P. Banks**, R.W. Eason, and S.P. Banks, "Modeling of nanodroplet growth and transfer in femtosecond Laser-Induced Forward Transfer using cellular automata" *(working title)*

A.2 Conferences

D. Banks, X. Xu, R. Eason, and S. Banks, *"Optimal Control of a Moving Boundary by Laser Heating in a 2-Phase Stefan Problem,"* Proc. of WCNA, Orlando, Florida, July 2008.

D.P. Banks, C. Grivas, I. Zergioti, and R.W. Eason, *"Femtosecond Laser-Induced Forward Transfer (LIFT): A Technique for Versatile Micro-Printing Applications,"* CLEO Europe, Munich, Germany, July 2007. *(Oral presentation)*

D. P. Banks, C. Grivas, I. Zergioti, and R.W. Eason, *"Ballistic Laser-Assisted Solid Transfer (BLAST),"* EMRS Spring Meeting, Strasbourg, France, May 2007. *(Oral presentation)*

D. Banks, R.W. Eason, and S. Banks, *"Control of Phase Boundary in a 2-Phase Stefan Problem by Linear Heating,"* ICCC, Štrbské Pleso, Slovakia, May 2007. *(Oral presentation)*

K. Kaur, **D.P. Banks**, R. Gazia, C. Grivas, R. Fardel, M. Nagel, T. Lippert and R.W. Eason, *"Femtosecond Laser-Induced Forward Transfer of thin Films using a Triazene Polymer Sacrificial Layer and an Active Carrier,"* EMRS Spring Meeting, Strasbourg, France, May 2008 (Poster).

A. Canagasabey, J. Canning, J. Mills, **D.P. Banks**, and M. Ibsen, *"Fibre Bragg fabrication in germanosilicate fibres with 244nm femtosecond laser light,"* PICALO, Melbourne, Australia, April 2006. *(Oral presentation)*